CVR JOURNAL OF SCIENCE AND TECHNOLOGY

Vol.No. 22, June 2022
P-ISSN 2277 - 3916
DOI 10.32377/CVRJST22
E-ISSN 2581 - 7957

CVR COLLEGE OF ENGINEERING

In Pursuit of Excellence

PATRONS

Dr. Raghava V. Cherabuddi, President & Chairman

Dr. K. Rama Sastri, Director

Dr. K. Ramamohan Reddy, Principal

Editor : **Dr. K. Lal Kishore, Professor and Dean - Research, CVRCE**

Associate Editor : **Dr. S. Venkateshwarlu, Professor & Head, Dept. of EEE, CVRCE**

Technical support : **Mr. K. Veeranjaneyulu, Asst. Prof., Dept. of CSE, CVRCE**

CVR JOURNAL OF SCIENCE AND TECHNOLOGY

Indexed by

- Google Scholar
- Directory of Research Journals Indexing (DRJI)
- Scientific Indexing Services (SIS)
- International Institute of Organised Research (I2OR)
- Scholar Impact - Journal Index
- Citefactor
- Member Crossref / DOI

Accredited by NAAC with 'A' GRADE

CVR COLLEGE OF ENGINEERING

(UGC Autonomous - Affiliated to JNTU Hyderabad)
Mangalpalli (V), Ibrahimpatnam (M),
R.R. District, Telangana. – 501510
http://cvr.ac.in

EDITORIAL

The Editorial Team of CVR Journal of Science and Technology is very happy to bring out Vol.22, due in June 2022. This is yet another accomplishment of bringing out the Journal in time. After the impact of pandemic in March 2020, things are returning to normal. This Volume is brought out under this situation compared to Vols 18. to 21.

We are taking care to see that standard practices are followed in the publication of the Journal. Blind review is done, and number of iterations are done till the reviewers are fully satisfied with the standard of the research paper. Senior faculty of English language Department, take care of the language issues. Template verification and typographical errors are checked before the articles go for publishing. This preparation work takes more than six months, before the volume is brought out. Hope the researchers appreciate this effort. This volume is carrying a research article received from University in France. Many research articles published in the journal are being referred by other researchers across the globe, as indicated by DOI, crossref data.

This Volume covers research articles in the following disciplines:

CSE – 2 , CSIT – 2 , ECE –3 , EEE –3 , EIE – 1 , IT – 1 , MECH – 7, CIVIL – 5, H & S –1.

The Volume has e-ISSN number along with print ISSN number. Every research article published is given DOI number and they can be accessed on-line. On-line portal is also created for the Journal. This Volume is also brought out in time, with the co-operation of all the authors and editorial team. We are thankful to the Management for supporting this activity, and permitting to publish the journal in color print, using quality printing paper.

In this issue, also there is one research article related to COVID. As the COVID pandemic dominated the world events for the last two years, researchers also tuned their work towards the pandemic related issues. This Journal carried COVID related research articles in the last three issues. In this Volume also, another research article “Supervised Learning for COVID Mortality Span Prediction” must make interesting reading. Another research article “Predicting Diabetic Retinopathy using Deep Learning techniques” may also be useful for many from other branches as well, apart from computers related areas. Another research article “Designing of Blind Navigation System using GSM and RFID Technology in Indoor Environments” must also enthuse interest of many researchers. There is another research article published, on the Wing design for Jet model Dassault FALCON 7X aircraft. These research articles indicate the urge of the researchers to address the problems with practical applications through research.

I am thankful to all the members of the Editorial Board for their help in reviewing and short listing the research papers for inclusion in the current Volume of the journal. I wish to thank **Dr. S. Venkateshwarlu, HOD, EEE** for the effort made in bringing out this Volume. Thanks are due to **HOD, H & S, Dr. G. Bhikshamaiah** and the staff of English Department for reviewing the papers. I am also thankful to **Smt. A. Sreedevi, DTP Operator** in the Office of Dean Research for the preparation of research papers in Camera - Ready form.

For further clarity on waveforms, graphs, circuit diagrams and figures, readers are requested to browse the soft copy of the journal, available on the college website www.cvr.ac.in wherein a link is provided. Authors can also submit their papers through our online open journal system (OJS) www.ojs.cvr.ac.in or www.cvr.ac.in/ojs

Prof. K. Lal Kishore
Editor

International Review Board:

CONTENTS

E-ISSN 2581 – 7957
P-ISSN 2277 – 3916

CVR Journal of Science and Technology, Volume 22, June 2022
DOI: 10.32377/cvrjst2201

A Scheme for Verifying Integrity of SQL Query Processing on Encrypted Databases

K. Srinivasa Reddy[1] and K. Pranitha Kumari[2]
[1]Assoc. Professor, CVR College of Engineering/CSE Department, Hyderabad, India
Email: k.srinivasareddy@cvr.ac.in
[2]Assoc. Professor, CVR College of Engineering/CSE Department, Hyderabad, India
Email: k.pranithakumari@ cvr.ac.in

Abstract: **In the database-as-a-service model, a service provider hosts the clients' data and allows access to the data through the Internet. Database-as-a-service model offers considerable benefits to organizations with data management needs by allowing them to outsource their data management infrastructures. Yet, the model introduces many significant challenges, that of data privacy and security. Ensuring the integrity of the database, which is hosted by a service provider, is a critical and challenging problem in this context. We propose a novel Query Result Integrity Guarantee (QRIG) scheme over encrypted databases, which allow a database enquirer to verify that their queries were faithfully executed by the server. The experimental results obtained in this paper show the performance of proposed scheme.**

Index Terms: **data integrity, query result, database, encryption, security**

I. INTRODUCTION

Nowadays outsourced IT services have become very popular. Users no longer need to be concerned about providing infrastructure or scaling up software for their computation. With the advent of outsourced IT services like cloud computing any required infrastructure, software or services can be provided to users by third persons. Users can speed up their computation based on the load by boosting the software without the rise in cost, because using 1000 hours of a server does not cost more than using 1000 servers for an hour [1]. Mobility is the other advantage of cloud computing. Users can run their computation by logging into their account in cloud via their cell phones on their way to work. Cloud computing also reduces cost for users. Users will pay for the services that they receive during the service time. The other costs like software (in our case database licensing costs), hardware and maintenance are associated with service providers which makes cloud computing more attractive for users [2]. Although outsourced IT services and cloud computing are desirable for users but there is a concern that prevents most of users from using these services. Security is the main concern that stops users to delegate their computation to the cloud. Users want to ensure that services provided by third party are secure and trusted. Recent study on 500 IT administrators and IT managers in 17 countries revealed that 80% of them tend to use existing internal systems rather than using cloud infrastructures. The fear of losing control over protecting data was the main reason for them to stay with existing internal systems [3].

In this paper we focus on providing security for the outsourced database. Outsourced database security has two aspects: privacy and data integrity. Privacy in databases were studied in many research works and different approaches have been presented [4][5]. Data integrity recently became an interesting challenge for researchers. Data integrity can be provided at different levels of granularity. In principle, integrity checks can be at the level of a table, a column, a row (a record or a tuple of the table), or an individual attribute value. Providing integrity checks at the table (or column) level implies that the entire data pertaining to that table (or column) should be returned in the query reply for the client to verify the integrity of the query response. This is clearly impractical as it requires transferring large amounts of data to the client. Hence, we do not consider this to be a viable approach. On the other hand, computing integrity checks at the level of individual attribute values yields a very large number of signatures which is very expensive for the signer (owner) in terms of computation as well as for the server in terms of storage.

Therefore, the optimal choice is to provide integrity at the record level. This enables the server to return in response to a query any set of matching records along with their respective integrity checks. Of course, computing integrity checks over the entire record, as opposed to individual attributes, inferred that the smallest unit of data returned as a query reply is an entire record, even when the querying client is only interested in a single field.

Query result integrity has three aspects: Correctness, Completeness and Freshness. Correctness means that the results returned by server must be genuine records. Genuine records are those records that exist in original database and have not been modified by server. Completeness means that returned records are the results of executing the query over the entire database and all the possible records that satisfy the query are included. Freshness means that query result contains the records based on executing the query over the most updated database. In this paper, we propose a novel Query Result Integrity Guarantee (QRIG) scheme for verifying integrity of query processing over encrypted databases and to satisfy the three aspects of query result integrity: correctness, completeness, and freshness.

In this paper, we consider insert, delete, and update queries and the standard SQL queries involving *SELECT* clauses such as equality, range, join and aggregate queries. This paper focuses on providing *correctness* and *freshness* of query replies returned by the server. A related, and

Received on 09-08-2021, Revised on 18-10-2021, Accepted on 30-10-2021.

CVR Journal of Science and Technology, Volume 22, June 2022
DOI: 10.32377/cvrjst2201

equally important, issue is the *completeness* of query replies. Although we consider it debatable whether *completeness* is a security concern, we acknowledge that it poses a challenge which needs to be addressed in the outsourced databases. However, we consider *completeness* of query only with respect to SCOPE scheme [32], in which any sensitive column is encrypted and stored at trusted proxy.

The remaining part of this paper is structured as following. Section II describes the related work. Section III describes the proposed system model. Section IV describes the proposed scheme in detail. In Section V the results of experiments are summarized, and our conclusions are presented in Section VI.

II. Related Work

The problem of assuring query integrity in the context of outsourced data was fundamentally related to the concept of certified data structures [27], which presents some results that are conceptually important but not efficient. The state-of-the-art solutions to query integrity are due to [13][23], which are the only solutions that support selection, projection and join queries simultaneously. These two solutions follow two respective approaches to the query integrity problem.

The tree-based approach: Basically, this approach uses the Merkle hash tree [15] or its variants to index search keys [11][17][13][7][16][31][20][21]. As a result, this approach leads to logarithmic complexity in terms of both communication and verification, possibly with some further tricks (e.g., using the Merkle hash tree to maintain signatures at multiple hash tree levels [11]). The best solution in this approach is due to [13], which uses the Merkle B-tree and the Embedded Merkle B-tree to reduce I/O operations.

The signature-based approach: Basically, this approach uses the signature aggregation technique [5][18] to aggregate the validity of query answers [18][19][23][22]. As a result, this approach can lead to low (even constant) communication complexity but may require special treatment for handling more powerful (e.g., projection) queries and often leads to large storage and computational complexities. The best solution in this approach is due to [23], which uses aggregate signatures to sign each attribute and returns a single signature as the validity proof for projection queries. This solution uses a chaining signing technique to build the index for the search key to facilitate range queries and publishes a certified bitmap corresponding to every update to facilitate dynamic updates. These cause a large storage and communication overhead while including many enfolding and pairing operations.

There are studies that are somewhat related to the theme of the present paper as well [33][34][35]. These include authenticating the answers to set operations using accumulator [25], authenticating the answers to aggregate queries using authenticated prefix-sums trees [14], authenticating the answers to join queries [30], authenticating count queries with respect to multi-dimensional data while preserving privacy [29], and assuring probabilistic integrity in selection and join operations [28]. Query integrity is also somewhat related to outsourced verifiable computation [1][6][10].

III. System Model

The proposed system model is shown in Fig. 1 in which the trusted proxy hosts the creation and management of the encrypted database. All tenant database users can submit SQL queries directly to the encrypted cloud database. The whole tenant organization data is stored in an encrypted form in the cloud database. By using SQL-aware encryption schemes, the cloud database server can process user's SQL queries on encrypted data without decryption. The key management module at proxy handles generation, derivation, and revocation of cryptographic keys.

The trusted proxy has four significant responsibilities:

1. **Key Management:** The trusted proxy generates and manages the keys required to decrypt the data.
2. **Query Rewrite:** The queries written by the user contain plain text. Therefore, the plain text in the query has to be encrypted by the trusted proxy. Moreover, depending on the encryption scheme used to encrypt the data in the cloud, the queries written by the user might need to be restructured using metadata information.
3. **Decryption and Post-Processing:** Depending on the encryption scheme, the trusted proxy needs to decrypt and possibly post-process the encrypted query results.
4. **Verify query result integrity:** Proxy authenticates the origin and verifies the integrity of data returned by the service provider in response to a posed query.

The system model works as follows: The Trusted Proxy (TP) translates the tenant organization's access control policies into an access control matrix. TP distributes unique secret keys to the users at the creation of their accounts according to the access control matrix. These keys enable the users to access all and only the subsets of encrypted tenant data on which the users have legitimate access. When a user enters his credentials, TP validates the user's credentials. The TP takes as its input the original plaintext database and generates the tuple integrity code and produces the

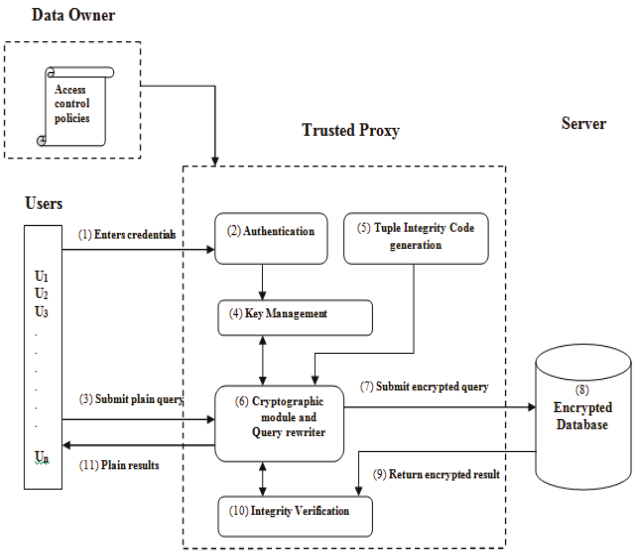

Figure 1. System model

CVR Journal of Science and Technology, Volume 22, June 2022
DOI: 10.32377/cvrjst2201

encrypted tenant data. Each user can execute SQL operations through the TP. The TP takes as its inputs the user credentials and the encrypted metadata and translates plaintext SQL queries into encrypted SQL queries that can be executed on encrypted data at server. The TP decrypts the encrypted results returned by the server and verifies the integrity of the results. Finally, the verified plain results are returned to the user.

A. Generic Assumptions

Various assumptions that are made in this paper are as follows:

1. Server is not trusted. Hence proxy does not share its secret encryption keys with server.
2. Proxy is fully trusted and won't be compromised. If we remove this assumption, then security can never be guaranteed since adversary can compromise proxy and see all the data.
3. The communication channel between client, proxy and server is secure. This can be ensured by using various techniques such as TLS (Transport Layer Security) and SSL (Secure Sockets Layer).

All the encryption schemes used here are individually secure.

B. Adversary Model

The model used in this work is "malicious" adversary model. The assumption of this model is that the server can misbehave in any way, such as returning incorrect answers to the user query.

The assumptions made here allow our scheme to protect the data against:

1. An adversary that eavesdrops network traffic cannot access any plaintext information because SQL operations issued to the cloud database are protected by using standard encryption protocols (e.g., SSL).
2. An adversary that has breached the cloud database cannot access confidential information, because our scheme encrypts client data with semantically secure algorithms and the cloud provider never obtains the decryption keys.

IV. Query Result Integrity Guarantee Scheme

The proposed QRIG scheme works in two phases, the first phase is called the Tuple Integrity Code generation and the second phase is called Query Result Integrity Verification.

A. Tuple Integrity Code Generation

The tuple-level integrity represents that the content of a record has not been manipulated in an unauthorized manner. Although it may not be apparent, data encryption does not provide data integrity automatically. The owner of the decryption key can decrypt the encrypted messages, which were encrypted with the same key. But this does not guarantee that the encrypted message has not been manipulated by the adversary. The discussion of how encrypted messages can be manipulated undetectably can be found in [12]. This motivates the need for data integrity measures over encrypted data.

To provide tuple-level integrity we propose a scheme based on *Tuple Integrity Codes (TICs)*. TICs are specially computed representative images for each record with certain security and uniqueness measures. Fig. 2 shows the procedure that provides tuple-level data integrity. The data owner/user has a record r that will be inserted into the database, which is maintained by the server. The trusted proxy first computes the hash code of the record $H=h(r)$ by using a TIC algorithm [8], which produces *Tuple Integrity Code* (TIC). After this step, the trusted proxy integrates the

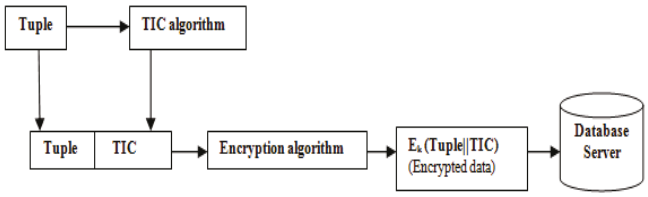

Figure 2. Tuple integrity code generation

hash code H with the original record text r and encrypts them together by using any deterministic encryption algorithm E [9] with secret key k i.e., the trusted proxy computes ciphertext $C= E_k (r||h(r))$ where || represents concatenation. The trusted proxy inserts ciphertext C as an *encTuple* into the database.

B. Query Result Integrity Verification

Whenever the user requests a record, the server sends back the corresponding *encTuple* in encrypted form to trusted proxy. To verify the integrity of the record, the trusted proxy first decrypts the *encTuple* recovering r' and H', which is the TIC, parts. Since only the trusted proxy has the secret key k for encryption algorithm no one else can decrypt. Then the trusted proxy independently computes $h(r')$ of received record r' and compares that with the hash code H'. If they are equivalent, this verifies that the received record is authentic and has data integrity, i.e., has not been manipulated in an unauthorized manner. The query result integrity verification process is depicted in Fig. 3.

C. Query Processing

Here, we discuss how a trusted proxy uses the QRIG scheme

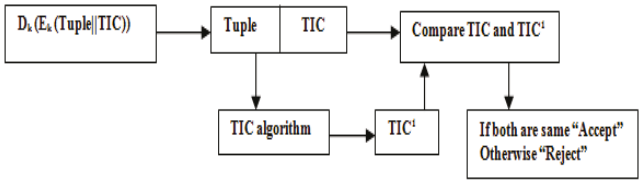

Figure 3. Query result integrity verification

and verifies the integrity of query results returned by the server when a user executes various SQL queries over an encrypted database. For example, consider an employee table in a database consisting of name and salary columns as given in Table I. The employee table is mapped to a corresponding encrypted table, shown in Table II, at the server. TID represents tuple identifier, the second column *encTuple* contains the string corresponding to the encrypted tuples in employee table.

For instance, the first tuple is encrypted to Enc (John, 32,000 || TIC), where *Enc* is a deterministic encryption algorithm [24] with key k. The third column corresponds to

the *eName* which is encrypted with deterministic encryption algorithm such as AES [26]. The fourth column represents the *eSalary* which is encrypted with SCOPE scheme [32], since order operations are usually applied on it.

SELECT Query

Suppose the user sends the select query Q = "select * from employee where salary ≥ x and salary ≤ y" to server. We consider correctness, completeness and freshness of Q while verifying the query result integrity.

The QRIG scheme for verifying the correctness of Q results works as follows:

1. The trusted proxy rewrites the Q using SCOPE scheme [32], to an encrypted query Q_E and sends it to server.
2. The server processes Q_E and returns the encrypted tuples result to the trusted proxy.
3. The trusted proxy applies the query result integrity verification process given in Section 4.2.
4. The trusted proxy returns the plaintext results to the user.

The QRIG scheme for verifying the completeness of Q results works as follows:

1. The trusted proxy temporarily stores the count of the data items that satisfies the condition in Q while rewriting the Q using SCOPE scheme. In SCOPE scheme, the trusted proxy stores the sensitive column (i.e., salary) in encrypted form.
2. The trusted proxy rewrites Q to an encrypted query Q_E and sends it to server.
3. The server processes Q_E and returns the encrypted tuples result to the trusted proxy.
4. The trusted proxy computes the count of the encrypted tuples returned by the server and compares it with the count value stored with it. If both count values are same then it accepts the result, otherwise it rejects the result.
5. The trusted proxy returns the plaintext results to the user.

If the SELECT query result satisfies correctness and completeness, then it automatically satisfies the freshness. The SELECT query includes equality, range, join and aggregate queries. Therefore, the QRIG scheme is

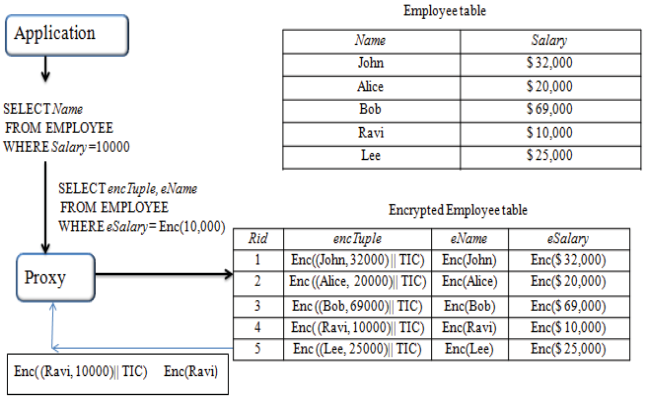

Figure 4. Equality query result integrity verification

applicable for verifying correctness, completeness, and freshness of all SELECT queries.

The example given in Fig. 4 shows how the QRIG scheme is applicable for verifying correctness, completeness, and freshness of equality query result.

The trusted proxy temporarily stores the count of the data items that satisfies the condition in the equality query EQ (count=1). The trusted proxy rewrites EQ to an encrypted query EQ_E and sends it to server. The server processes EQ_E and returns the encrypted tuples result to the trusted proxy. The trusted proxy applies the query result integrity verification process given in Section 4.2 for correctness and computes the count of the encrypted tuples returned by the server and compares it with the count value stored with it for completeness and returns the plaintext results to the user. Since the equality query result satisfies correctness and completeness then it automatically satisfies the freshness.

UPDATE Query

The trusted proxy interacts with the server to update the stored table with the update information. The following are the different cases of update operation:

1. *Insertion*: Suppose update is "insert the tuple *r* into table". The trusted proxy applies the tuple integrity code generation process given in Section 4.1. The trusted proxy delivers update information to the server and the server inserts *r* into table. The trusted proxy maintains the count *c* of the existing tuples in the table. The trusted proxy updates *c* whenever new tuples *t* is inserted into the table (i.e., c = c + t). Therefore, the trusted proxy can verify the completeness and freshness of tuples by getting the count *c′* of the total tuples from the server and comparing *c′* with *c*.
2. *Deletion*: Suppose update is "delete the tuple *r* from table". The trusted proxy delivers update information to the server and the server deletes *r* from table. The trusted proxy gets the count *d* of the tuples that are deleted from the table. The trusted proxy maintains the count *c* of the existing tuples in the table. The trusted proxy updates *c* whenever new tuples *t* is deleted from the table (i.e. c = c - t). Therefore, the trusted proxy can verify the completeness and freshness of tuples by getting the count *c′* of the tuples from the server and comparing *c′* with *c*.
3. *Modify*: Suppose update is "update the tuple *r* with *r′* ". The trusted proxy applies the tuple integrity code generation process given in Section 4.1 for *r′*. The trusted proxy delivers update information to the server and the server updates *r* to *r′*. The trusted proxy maintains the count *c* of the existing tuples in the table. Therefore, the trusted proxy can verify the completeness and freshness of tuples by getting the count *c′* of the tuples from the server and comparing *c′* with *c*.

The correctness of the tuples present in the table is verified during the data retrieval process which is described in Section 4.2.

V. Experimental Evaluation

In this section we evaluate the performance of QRIG scheme on an encrypted database. QRIG is implemented in Java over MySQL database server. We measured the performance of QRIG on a machine with a 2.27 GHz Intel Core i5 processor running with Windows 7 with only a single core enabled for consistency, running both the client and the server on the same machine and with 2GB of memory.

In the experiments, we consider employee database consisting of one table with two columns. Here the table columns are encrypted with AES and SCOPE to support equality and ordering operations over encrypted data respectively. The database columns not requiring any computation can be encrypted through standard algorithms such as AES with random initialization vectors.

QRIG scheme performances are examined by considering insert and retrieve operations on encrypted employee database. In our experiments, we varied the total database size between one hundred and one lakh entries. We were able to run experiments up to one lakh entries, limited only by the RAM size available on our workstation. The efficiency of QRIG is measured in terms of the time taken to generate tuple integrity codes during insert operations. During the retrieval operation, the efficiency of QRIG is measured in terms of the time taken for verifying query result integrity by applying a set of retrieval queries on encrypted employee database.

A. Database Insert And Retrieve

During the experiment, an insert query is applied on employee table by inserting 10^2,10^3,10^4 and 10^5 records at a time using QRIG scheme and the corresponding user time, system time, and CPU time are calculated and is clearly depicted in Table III. Next, a set of M range queries where M=10, 20, 30…100 are applied on 1000 records present in an encrypted employee database and the corresponding user time, system time, and CPU time are calculated. The results are described in Table IV.

Here, "user time" is the time spent running the application code, "system time" is the time spent running OS code on behalf of the application (such as for IO) and "CPU time" is user time plus system time. It is the total time spent using a CPU for your application. Here, the total insertion time (CPU time) = User time + System time.

VI. Conclusions

We propose a novel Query Result Integrity Guarantee scheme over encrypted databases, which allow a database querier to verify that their queries were faithfully executed by the server. The proposed scheme provides the security of the stored data against the malicious attacks as well as the database integrity features, which ensure the correctness, completeness and freshness of the data stored at the server. Our approach is efficient, and it only introduces small storage overhead.

TABLE I.
Employee Table

Name	Salary
John	$ 32,000
Alice	$ 20,000
Bob	$ 69,000
Ravi	$ 10,000
Lee	$ 25,000

TABLE II.
Encrypted Employee Table

Tid	encTuple	eName	eSalary
1	Enc (John, 32,000 || TIC)	Enc (John)	Enc (32,000)
2	Enc (Alice, 20,000 || TIC)	Enc (Alice)	Enc (20,000)
3	Enc (Bob, 69,000 || TIC)	Enc (Bob)	Enc (69,000)
4	Enc (Ravi, 10,000 || TIC)	Enc (Ravi)	Enc (10,000)
5	Enc (Lee, 25,000 || TIC)	Enc (Lee)	Enc (25,000)

TABLE III.
Applying Insertion Query on Employee Table

Number of Records Inserted	User time (seconds)	System time (seconds)	CPU time (seconds)
100	0.03	0.01	0.04
1000	0.09	0.02	0.11
10000	0.22	0.02	0.24
100000	1.05	0.08	1.13

TABLE IV.
Applying Insertion Query on Employee Table

Number of Records Inserted	User time (seconds)	System time (seconds)	CPU time (seconds)	Number of Records retrieved
10	0.15	0.01	0.16	5382
20	0.22	0.01	0.23	10764
30	0.24	0.02	0.26	16137
40	0.27	0.03	0.30	21430
50	0.30	0.04	0.34	26326
60	0.35	0.04	0.39	31708
70	0.40	0.04	0.44	37090
80	0.46	0.04	0.50	42463
90	0.49	0.05	0.54	47756
100	0.53	0.05	0.58	52652

References

[1] B. Applebaum, Y. Ishai, and E. Kushilevitz, "From secrecy to soundness: Efficient verification via secure computation," *Automata, Languages and Programming*, vol. 6198, pp. 152–163, 2010.

[2] G. Ateniese, R. Burns, R. Curtmola, J. Herring, L. Kissner, Z. Peterson, and D. Song, "Provable data possession at untrusted stores," *In Proceedings of the 14th ACM conference on Computer and communications security*, pp. 598–609, 2007.

[3] G. Ateniese, S. Kamara, and J. Katz, "Proofs of storage from homomorphic identification protocols," In Proceedings of the 15th International Conference on the Theory and Application of Cryptology and Information Security: Advances in Cryptology, pp. 319–333, 2009.

[4] M. Bellare and G. Neven, "Multi-signatures in the plain public-key model and a general forking lemma," *In ACM Conference on Computer and Communications Security*, pp. 390–399, 2006.

[5] D. Boneh, C. Gentry, B. Lynn, and H. Shacham, "Aggregate and verifiably encrypted signatures from bilinear maps," *In Proceedings of the 22nd international conference on Theory and applications of cryptographic techniques*, pp. 416–432, 2003.

[6] K.-M. Chung, Y. Kalai, and S. Vadhan, "Improved delegation of computation using fully homomorphic encryption," *In Proceedings of the 30th annual conference on Advances in cryptology*, pp. 483–501, 2010.

[7] P. Devanbu, M. Gertz, C. Martel, and S. G. Stubblebine, "Authentic data publication over the internet," *J. Computer Security*, vol. 11(3), pp. 291–314, 2003.

[8] C. Erway, A. Küpçü, C. Papamanthou, and R. Tamassia, "Dynamic provable data possession," *In Proceedings of the 16th ACM conference on Computer and communications security*, pp. 213–222, 2009.

[9] A. Fiat, "Batch rsa," *In Proceedings on Advances in cryptology*, pp. 175–185, 1989.

[10] R. Gennaro, C. Gentry, and B. Parno, "Non-interactive verifiable computing: outsourcing computation to untrusted workers," *In Proceedings of the 30th annual conference on Advances in cryptology*, pp. 465–482, 2010.

[11] M. Goodrich, R. Tamassia, and N. Triandopoulos, "Super-efficient verification of dynamic outsourced databases," *Topics in Cryptology*, vol. 4964, pp. 407–424, 2008.

[12] A. Juels and B. S. Kaliski, Jr., "Pors: proofs of retrievability for large files," *In Proceedings of the 14th ACM conference on Computer and communications security*, pp. 584–597, 2007.

[13] F. Li, M. Hadjieleftheriou, G. Kollios, and L. Reyzin, "Dynamic authenticated index structures for outsourced databases," *In Proceedings of the ACM SIGMOD international conference on Management of data*, pp. 121–132, 2006.

[14] F. Li, M. Hadjieleftheriou, G. Kollios, and L. Reyzin, "Authenticated index structures for aggregation queries," *ACM Trans. Inf. Syst. Secur.*, vol. 13(4), pp. 1–32, 2010.

[15] R. C. Merkle, "A certified digital signature," *In Proceedings on Advances in cryptology*, pp. 218–238, 1989.

[16] K. Mouratidis, D. Sacharidis, and H. Pang, "Partially materialized digest scheme: an efficient verification method for outsourced databases," *The VLDB Journal*, vol. 18(1), pp. 363–381, 2009.

[17] E. Mykletun, M. Narasimha, and G. Tsudik, "Providing authentication and integrity in outsourced databases using merkley hash trees," *In UCI-SCONCE Technical Report*, 2003.

[18] E. Mykletun, M. Narasimha, and G. Tsudik, "Authentication and integrity in outsourced databases," *Trans. Storage*, vol. 2(2), pp. 107–138, 2006.

[19] M. Narasimha and G. Tsudik, "Authentication of outsourced databases using signature aggregation and chaining," *In Proceedings of the 11th international conference on Database Systems for Advanced Applications*, pp. 420–436, 2006.

[20] G. Nuckolls, "Verified query results from hybrid authentication trees," In Proceedings of the 19th annual IFIP WG 11.3 working conference on Data and Applications Security, pp. 84–98, 2005.

[21] B. Palazzi, M. Pizzonia, and S. Pucacco, "Query racing: fast completeness certification of query results," *In Proceedings of the 24th annual IFIP WG 11.3 working conference on Data and applications security and privacy*, pp. 177–192, 2010.

[22] H. Pang, A. Jain, K. Ramamritham, and K.-L. Tan, "Verifying completeness of relational query results in data publishing," *In Proceedings of the 2005 ACM SIGMOD international conference on Management of data*, pp. 407–418, 2005.

[23] H. Pang, J. Zhang, and K. Mouratidis, "Scalable verification for outsourced dynamic databases," *Proc. VLDB Endow.*, vol. 2(1), pp. 802–813, 2009.

[24] C. Papamanthou, R. Tamassia, and N. Triandopoulos, "Authenticated hash tables," *In Proceedings of the 15th ACM conference on Computer and communications security*, pp. 437–448, 2008.

[25] C. Papamanthou, R. Tamassia, and N. Triandopoulos, "Optimal verification of operations on dynamic sets," *In Proceedings of the 31st annual conference on Advances in cryptology*, pp. 91–110, 2011.

[26] H. Shacham and B. Waters, "Compact proofs of retrievability," In Proceedings of the 14th International Conference on the Theory and Application of Cryptology and Information Security: Advances in Cryptology, pp. 90–107, 2008.

[27] R. Tamassia and N. Triandopoulos, "Certification and authentication of data structures" *In AMW*, 2010.

[28] M. Xie, H. Wang, J. Yin, and X. Meng, "Integrity auditing of outsourced data," *In Proceedings of the 33rd international conference on Very large data bases*, pp. 782–793, 2007.

[29] J. XU and E.-C. CHANG, "Authenticating aggregate range queries over multidimensional dataset," *Cryptology ePrint Archive*, 2010.

[30] Y. Yang, D. Papadias, S. Papadopoulos, and P. Kalnis, "Authenticated join processing in outsourced databases," *In Proceedings of the 35th SIGMOD international conference on Management of data*, pp. 5–18, 2009.

[31] Y. Yang, S. Papadopoulos, D. Papadias, and G. Kollios, "Spatial outsourcing for location-based services," *In Proceedings of the 2008 IEEE 24th International Conference on Data Engineering*, pp. 1082–1091, 2008.

[32] Srinivasa Reddy, K. and Ramachandram, S, "A secure, fast insert and efficient search order preserving encryption scheme for outsourced databases," *Int. J. Advanced Intelligence Paradigms*, Vol. 13, Nos. 1/2, pp.155–177, 2019.

[33] Reddy, K.S. and Ramachandram, S, "Cryptographic key management scheme for supporting multi-user SQL queries over encrypted databases," *Int. J. Computer Aided Engineering and Technology*, Vol. 12, No. 4, pp.461–479, 2020.

[34] Srinivasa Reddy, K. and Ramachandram, S, "A new randomized order preserving encryption scheme," *International Journal of Computer Applications*, Vol. 108, No. 12, pp.41–46, 2014.

[35] K.Srinivasa Reddy and Sirandas Ramachandram, "A Novel Dynamic Order-Preserving Encryption Scheme*," IEEE First International Conference on Networks & Soft Computing*, 2014.

E-ISSN 2581 – 7957
P-ISSN 2277 – 3916
CVR Journal of Science and Technology, Volume 22, June 2022
DOI: 10.32377/cvrjst2202

Architecture of Multi-Processor Systems using Networks on Chip (NoC): An Overview

M. Swami Das
Assoc. Professor, CVR College of Engineering/CSE Department, Hyderabad, India.
Email: msdas.520@gmail.com

Abstract: **Network on chip (NoC) is an integrated chip component system with a large scale of integration of components. NoC is an integrated solution in architecture multiprocessor chip. It has metallic wires, ICs, core modules, and components that are used to make products. Specific Integrated Circuits can be classified into three types namely First, Standard IC, second ASSP, and third ASIC. System on chip (SoC) architecture uses communication elements, processors, energy, design applications, modularity, and complexity of the system. The NoC architecture provides operation communication and micro-network components. The NoC architecture is used for processing the data, with multicore on chips (SoC), processing elements(routers), Hardware, network elements, and components. NoC routing chip resources in microprocessor, memory, and Input/Output operations. The SoC chip design is a complex application that requires the design of system components based on requirements, and application specific. The applications are connected to the backbone of the network which uses network topology, NoC chip design, architecture, processors, and it depends on needs and applications. In this study the overview of NoC Architecture elements, topology, routing, flow control, and applications are mentioned. The architecture elements according to the needs to design and development of high-performance systems with optimal utilization of resources. The Future work can be extended to design and develop application-specific standard components in Network on chips.**

Index Terms: **NoC, SoC, Multi-Processor, High-Performance computing, Integrated circuit, Multicore systems, Integration Chip, Communication, Computing**

I. Introduction

Network on-chip communication-based Integrated Chip, the subsystems based on Integrated chip components of the system. NoC is a microprocessor that provides the method to send or receive data. NoC is an approach used to implement VLSI systems. Large scale design, network on a chip is used in the message flow. It contains hardware (routing and switching), topology in different areas of the network.

It minimizes complexity and provides a well-controlled structure with reliability, speed, and High-end systems. Network on-chip is the best integrated solution. Network on Chip (NoC) is an emerging significant on chip design, communication architecture which is used for multi-processor systems where parallel NoC systems are costly and consumes more energy. NoC chip communication scaling is based on application usage, computing advanced integration technologies. The NoC is used in various applications like Artificial Intelligence, big data analytics.

Optical energy with 3D Integrated Circuit solution improves the performance by reducing interconnect length. Section 2 describes the Literature survey, Section 3 deals with the Architecture of NoC and applications, section 4 has discussions, and Section 5 ends with the conclusion and future scope

II. Literature Survey

3D Optical Networks-on-chip (NoC) for Multiprocessor Systems-on-chip (MPSoC), the complexity of multiprocessor system on chip (MpSoc), global communication on the chip is a challenging performance.

Yaoyao Ye et.al[1] studied network communication architecture, which has parallel metallic wires and authors proposed a high bandwidth data transmission in the optical domain. 3D electronic chip integrates optical data transmission network.

Avi Kolodny [2] studied NoC essentials, communication, routing through hops, switches and parallelism. The authors studied a generic architecture with network on chip that route the packets by chip when interconnection is needed. The design model and its characteristics are most important architecture are sensitive to cost, area and power consumption. The custom network design specifications based on requirements like traffic, load, application.

Pingqiang Zhou et. al [3] studied the 3D silicon integration techniques, Network on chip (NoC)architecture design with the 3D environment. The NOC components are used in the building model, the power saving, latency reduction, chip temperature reduction are the parameters.

Mostafa S.Sayed et.al [4] studied the NoC bus architecture, performance and scalability. In NOC design, the authors introduced the architecture which is flexible router with available buffer. The flexible design can achieve better performance by Hotspot, nearest neighbor traffic uniform traffic patterns.

Daniel Gebhardt et.al[5] studied NoC with the interconnection of a large number of Intellectual property cells in the network communication where each cell clock domain has power, latency, and overhead. The authors described asynchronous NoC using flow control, topology, router placement, NOC design, topology, and routing for large routers with network communication latencies.

Adesh Kumar et. al[6] presented chip implementation NOC router by algorithms of architecture with FPGA, VHDL programming and optimized with timing parameters, maximum frequency, and memory.

Youhui Zhang et.a[7] addressed software, hardware hybrid simulation chip multiprocessor system. The NoC simulated FPGA resource. NoC simulation, hardware,

Received on 08-09-2021, Revised on 23-10-2022, Accepted on 07-02-2022.

software-implemented flexible simulation high-performance compact on-chip design, with Xilinxsvirtex 5155T chip. The advantage is increasing the injection rate with the help of hybrid method and improve performance of Chip core by executing CPU.

NoC is the most significant way of communication in Multiprocessor System on Chip (MPSoC). Salma Hesham et.al [14] discussed challenges, design and overview of real time NoC architecture, QoS and fault tolerance.

3D network on Chip problem, the quality mapping methods improve communication efficiency. The IP cores plays most important role in power optimizations. Cui Huang et.al [15] proposed a quantum behaved particle swarm optimization method, where speed and low power consumption in 3D NoC systems. IoT and cloud computing demand, scaling computing with highly efficient, low power process, the NoC is done with packet switched communication. Juan Fang et.al [16] proposed a hybrid NoC framework by buffering and buffer less NoC.

SoC revolution, NoC engineers to designing, dynamic, scalable reliable networks. M.Sujathaet.al [17] reviewed on various NoCs , wired, and wireless and hybrid networks by considering parameters such as adaptability, power and latency and throughput etc.

NoC development on topologies, routing problems Aleksandr Yu et.al [18] proposed a 2D circulant topology design for NoC, characteristics of mesh, torus topologies. Routing NoC with circulant topology and other methods are used. AyasKanta Swain et.al [19] studied a review on demand for home products automation, information sharing, social networks for consumer electronic devices. Multiprocessor SoC and NoC solution helps to improve performance of CE devices.

Parisa Mazaheri Kalahroudi et.al [20] proposed IAM (IWO algorithm mapping), to enhance 2D mesh based NoC mapping IP cores to routers.

III. The Architecture of NoC and Applications

Architectural specification implementation is classified into two types 1) bus-based design 2) NoC-based Design. architectural specification chip, gates and optimize the routing, area, wires, and components in a design where all the things are connected to a bus. Network switches or routers, are capable to take the data and send it to another router, change the locations and send packets to another location. Logical network uses routing methods packet transmissions that has physical design identical to NoC.

Network on chip has following characteristics topology, routing algorithms, switching strategy, and flow control. Metrics: bisection bandwidth, node degree/ diameter. Routers or buffers, wiring delay grow quadratically, buffer insertion can make it linear, but at the heavy cost of buffers, multicycle hops.

Network on Chip architecture: Chip communication improves bandwidth, power efficiency, and scalability. Optical NoC Hybrid architecture was used in optical data transmission at high-speed electronic networks in distributed applications. Optical on-chip router is the most significant component of Optical NoCs. NoC architecture on three-dimensional (3DiC) improves performance by CMOS technology, which supports higher density, and attainment of mixed chip technology interconnections.

System on a Chip (SoC) combines elements in a silicon chip has Very-large-scale integration (VLSI) complex, and high performance core modules and the components technologies used to make the products. SoC processing elements, international technology uses around 4 billion transistors. SoC chip on communication architecture, the processing elements are configured into a single processor. Features of SoC are Physical constraints, bandwidth, synchronization, scheme access pattern, throughput parallel computing, energy consumption proximity, non-determination energy constraints, design specifications general-purpose communication, modularity, and complexity

NoC separated computation from communication, Network on Chip Architecture is shown in Fig.1. Functional Layers: Network on chip architecture, design solution, communication on NoC communication system uses OSI Model, application API and software applications.

Network on Chip architecture: NoC architecture has multiple wires, routes, logic process cores, network interface with clients. ISO/ISI layer has seven layers and functions are described here.

Physical layer. The Communication is done with wire connectivity data link, energy, micro-networks. The physical layer has signal representation with wires, repeaters, circuits, and drivers

***Datalink layer*:** It consists of bits, protocols, error detection, protocols used in network operation. This layer manages system resources, network resources, and quality of services. The data link layer takes the data from the Physical layer as bits and makes into frames. It supports functions like flow control, handing of continuation, correction of transmission errors for the data, The data link layer requires a reliable, signal drivers and receivers, the design technologies are used to restoring signal as technology, error control, utilizing of high bandwidth.

Flow control: Upstream router should know the buffer availability of downstream router and router micro-architecture

Network Layer: Network topology, architecture, which use network resources such as routers, host, heterogenous, cores, architecture. Network layer handles and provides routing algorithms used in message packets transmissions. It provides circuit switch, controller, switch design, virtual channel, channel utilization, multiprocessor networks for end-to-end delivery control Switching is a technique used in a communication network, it needs buffer, store forward virtual circuit needs a buffer, packet has limited buffer size, virtual channels will increase the buffer size. The switching algorithms (i.e., circuit, packet, cut-through switching) were used to another networks.

Routing has deterministic, adaptive routing logic order. In NoC, static routing is used. A Generic Architecture for On-chip route packets interconnections, is the network on Chips where two packets trying to use the same link at same time

will buffer one, maintaining the drop the other is misroute one (deflection).

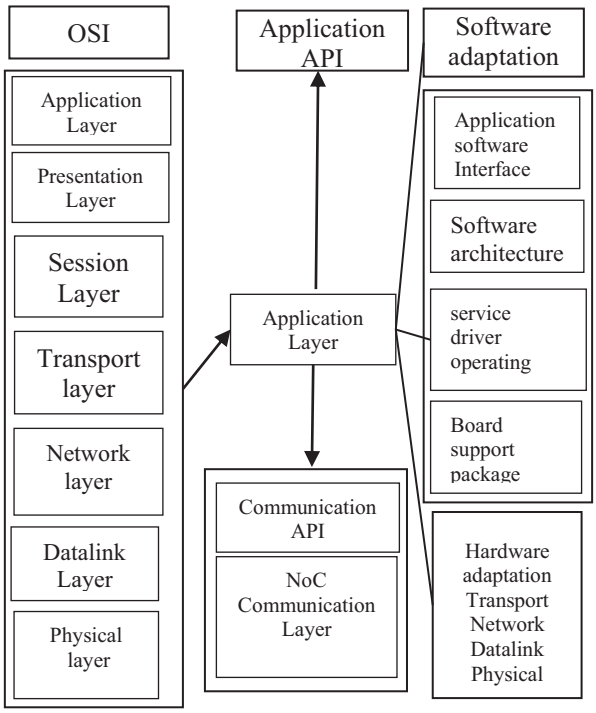

Figure1. NoC architecture (Ref 6)

Transport layer: Transport layer messages decompose the data into a sequence of a message to the destination. The packet standardization, in SoC micro-networks, the traffic management, transportation of packets in NoC, flow control routing algorithms are used for better communication performance. Architecture network, control algorithms are used to provide communication services.

Session Layer: It provides session management, opening, closing sessions between the end-user application process. It provides connections from local to remote system applications.

Presentation Layer: It serves as data translator for the network, mainly concentrating on syntax of user, formatted data, translation with data services. For example, data compression, decomposition, encryption, and decryption.

Application Layer*:* The set of computation, communication tasks, like speed, energy are optimized. Total communication energy is used to recognize service limitations to provide application.

Software Layer: Provided operating system and application layers services. Uniprocessor cannot provide efficient power, and performance.

System software: The system programs on SoC operation.

The NoC architecture provides communication protocols, scalability.

Topology: Topology is the physical organization medium network most common in NoC architecture. Architecture, communication devices have routing and synchronization. The channel communication (if it is asynchronous) then the data is reconstructed. Synchronization of two or more operations can be done at the same time. A direct network is a point-to-point network to each node directly linked with several neighboring nodes. The indirect network is switch-based network nodes that must go to a set of switches. A hybrid network is tightly integrated /connected to computational units with multiple backplanes hierarchical buses.

Topologies, network with new constraints for example 2D mesh has processing element/router link Torus. It shortens distance end to end in either direction into shorter path

The linear set of connection is Hypercube (2 ary,3 cubes), Ring, Octagon etc. The topology in node network connected as bus, mesh, star, etc. The routing algorithms network traffic from node links the data from data link layer to network layer as packets. Network layer uses topologies bus, mesh, tree, torus etc. The switching circuit provides addressing the physical to logical flow of transactions which avoids the distributed deadlocks and improves quality of service. The best services such as best effort, assured throughput, congestion control, flow control end to end communication.

Internet the performance is based on Service Level Agreement (SLA). The RISC, AISC architecture models used Network in Chip, and finds a shortest path routing which optimizes resource scheduling, fast transmission of data. The communication protocols, scalability, topology, computing operations of each process in processor. Network On-chip uses a micro-network protocol which is critical in architecture communication. For SoC design used NoC schemes, SoC architecture.

NoC architecture proposal companies use Free scale, IBM, Intel. The companies to sell it, Sonic (USA),NoC research communities, VLSI/CAD architects, experts use new models, interconnection via transmission message using wires virtual through the NoC. These models' interconnection requires bandwidth, timing, topology, software application, hops that use a router design etc.

NoC platform is scalable, use of billions of transistor chips, many use model VLSI systems with multicore architecture models will improve performance and speed. The 3D Silicon integration technology is a new opportunity design for Network on Chip (NoC) architecture which is developed on System on Chip (SoC). The NoC architecture design uses a 3 D environment and its topology design, 2D, 3D circuits, critical interconnect, all flexibilities are enabled in new system and improve performance system on chip (SoC) structures by 3 D technology. The 3D integrated circuits, with multiple tiers, latency, critical interconnect structure. 2D design rather than 3D circuits give a new high-performance system on chip (SoC) structure 3 D with communication, bandwidth, and parameters.

Architecture of Network on Chip (NoC) is more secured system, the multicore system which depends on switching strategy, topology, and routing methods. The NoC architecture has secured the router. The cryptography message encryption is a Key, the most important in channel security, for multiprocessor systems on chip (MPSoC) and NoC. The secret key encryption algorithms are used in NoC. NoC approach design a network subsystem which has cores,

CVR Journal of Science and Technology, Volume 22, June 2022
DOI: 10.32377/cvrjst2202

SoC, the software application layer in NoC uses resources, microprocessor, OSI layer, network interface, switch, resource for example. connection resources. Network on chip (NoC) uses IP cores, system on chip (SoC), NoC communication stack, chip regions areas each other connected in circuit. A resource in microprocessor, memory, I/O request, ISO /OSI layer model and network services.

NoC based on packet communication, reliable distributed transmission from higher layers to lower layers of abstractions a multi-process chip has hundreds of thousands of cores (ie. Multi-core) has high performance. The traditional systems interconnection with bus interface where network on chip (NoC), communication, architecture, design solve the issues and improve performance, power consumption, scalability, and integrity. The computation time is dominated by gate delay, computer, and unit on ad-hoc basis. The Transistors gates has wire delay. Scalable, structures architecture on-chip is more important design-centric communication design. The Moore's law used in SoC, Chip core chip processing design, the processor is making with hardware designing use application tasks multiple processing elements On /off to save power. Each processing element is optimized to frequency and voltage. And use of load balancing, reliable methods algorithms used for improving performance.

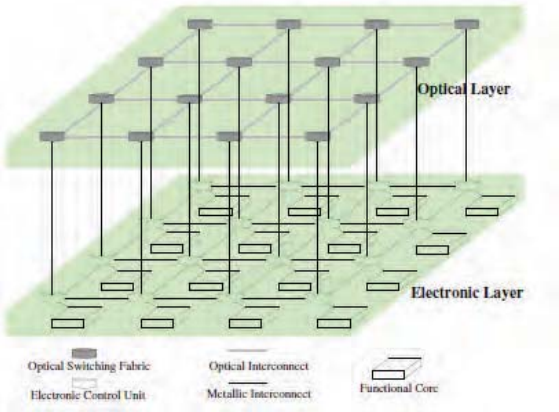

Figure 2. 4X4 mesh-based 3 D optical NoC architecture

The SoC chip designer is a complex application. The communication interconnection with the backbone of the network. The SoC designer uses communication devices that are connected to the backbone of the network which consists of layers, physical interfaces, protocols. The Protocols are used in data transmission, where the network layer routes the Packets from source to destination in a physical path. The routing is forwarded on a per-hop basis, set up optical path, control packets, routing, source-target address etc., The high speed without buffering, is obtained using NoC mesh-based design. Implement physical design is used to control the network Pins. The action of modules provides internal connections, components of SoC multimedia system provides more data transmission on-chip, multi-processor huge data on-chip where a Set of applications on-chip links to modules signals are carried out with global wires. The Architecture-based reusability, scalability for Multiple chip hierarchical processor has more cores on a single chip. SoC architecture has low latency, high throughput, reliable global services. The modern silicon devices shrink to 50 nanometers. For example, network topology 4X4 mesh 3 D optical architecture is shown in Figure.2. which has an optical layer and electronic layer.

NoC has regularity in higher-level abstraction which is like road system, or telephone network systems consisting of Computing module, Network switch, Network links. The network architecture with multiple cores is shown in Figure.3 the resources manager handles tasks.

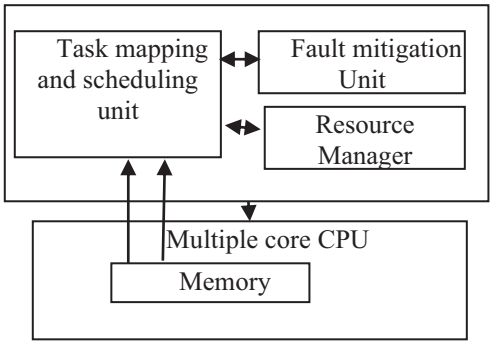

Figure 3. NoC architecture with multiple cores

NoC fundamental concept is a Module where communication packet of bits, point to point link in modules, and the modules are connecting with switch (or router) which sends the packets into several hops via using of switches, which is an efficient use of sharing wires to implement parallelism in communication. The NoC module communication is shown in figure.4. routing the packets through switch control.

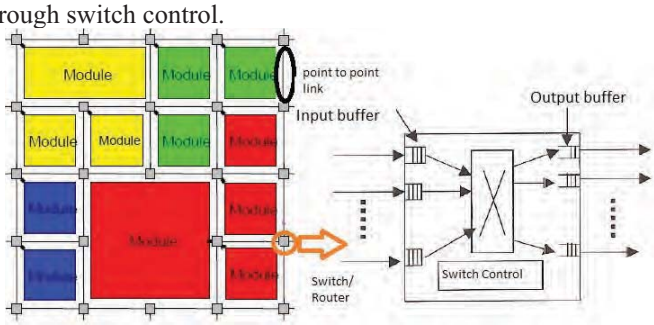

Figure 4. NoC module communication packets connecting to Router.

NoC architecture uses various topologies of interconnections for example bus, advanced bus and multilevel bus are discussed here. Bus Networks: The feature of bus has limited bandwidth, low cost, synchronous, central arbiter. The shared bus architecture is shown in figure.5.

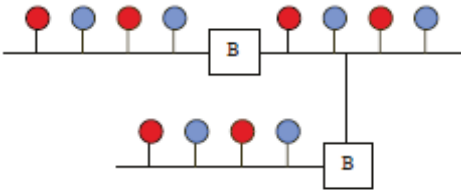

Figure 5. Shared Bus architecture.

Advanced Bus is a segmented One, transaction processed in central arbiter, where it uses limited bandwidth, transfer,

E-ISSN 2581 – 7957
P-ISSN 2277 – 3916
CVR Journal of Science and Technology, Volume 22, June 2022
DOI: 10.32377/cvrjst2202

pipelining features split transactions, with overlapped arbitration, transactions preemption, and resumption transaction reordering. The multilevel segmented bus is shown in figure.6

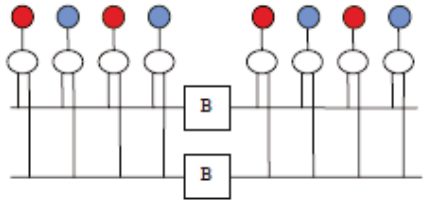

Figure 6. Multilevel segmented Bus

Paradigm architecture will replace with wire by a network to new infrastructure as shown in figure.7. The figure has network link, router link, computing module and bus, power grim clock grid are the components.

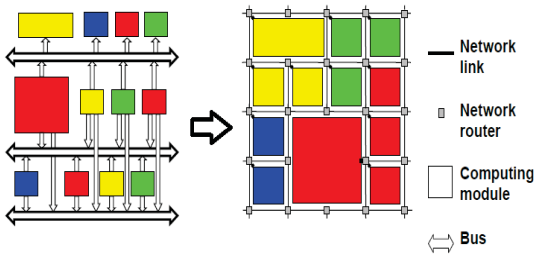

Figure 7. Paradigm the architecture with replacing with wire by packets new infrastructure

The problems are addressed by NoC Global design, system integration and chip multiprocessor with efficient computing. NoC scalability

TABLE I.
NETWORK ON-CHIP AND COST COMPLEXITY

Network on chip	Complexity
NoC	O(n)
Simple Bus	$O(n^3\sqrt{n})$
Point to point	$O(n^2\sqrt{n})$
Segmented Bus	$O(n^2\sqrt{n})$

Table.1 describes Network on chip design and cost complexity of NoC, Simple bus, point to point, and segmented bus and its architecture and cost complexities. NoC and Global wire delay: The wire design for NoC uses NoC links that connects regular, point to point, transmission path with layout and are optimized with power, speed, and noise.

The NoC and GALS system modules may use synchronization method, Asynchronous system has no waste of power in lines where routers are idle in the architecture Chip Multi-Processor (CMP), application-specific standard product (ASSP), application-specific integrated circuit (ASIC)), field-programmable gate arrays (FPGA), the choice depends on the system needs, single application, general-purpose application, configuration during run time, boot time and design time is shown in figure.8. The architecture is based on purpose of application, flexibility with required parameters.

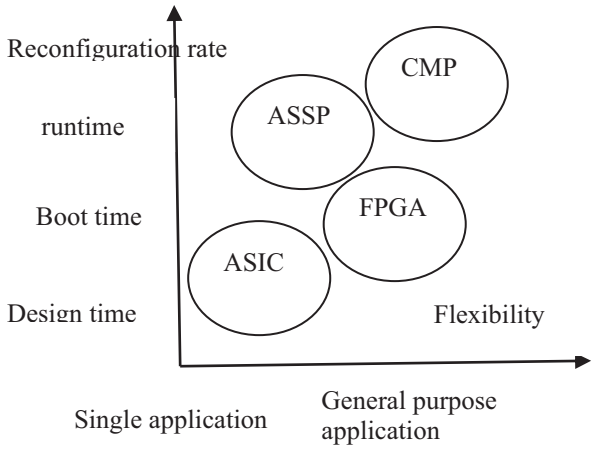

Figure 8. Architecture choice depends on system needs (Ref.12)

Chip multiprocessor (CMP) is a logic design architecture that has multiple processing (i.e., CPU cores) that are integrated onto a single Integrated Circuit. MP figure is shown in figure 9. Single, shared and I/O interfaces.

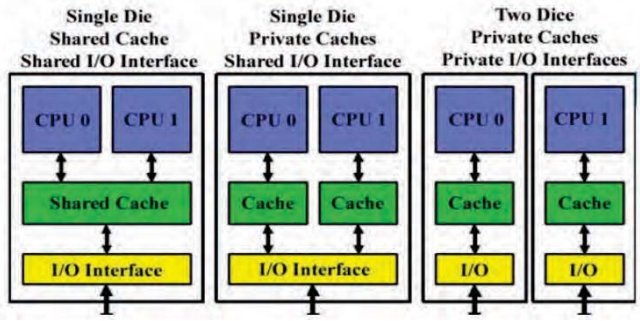

Figure 9. CMP chip Multiprocessor

The application-specific Integrated Circuits can be into three types namely 1) Standard IC 2) ASSP and 3) ASIC
The ASIC figure is shown in figure. 10. ASSP (application-specific standard product) is a product that has a semiconductor device with an integrated circuit. It is used for specific applications in the market. ASIC design built by the specific company.

ASIC design methodology can be designed into full custom design that is extremely slow and expensive. FPGA design is cost effective and fast. The AISC has improved performance with use of mix of analog to digital design, IC, HDL, the limitations are it cannot be upgraded, redesign is complex and expensive.

FPGA is IC programming gateway using semiconductor devices. It is used in application desired functionality requirement after manufacturing. FPGA are available, devices, software, configurable, ready to use IP cores in the market, for example, Defense and aerospace, ASIC prototyping, used in embedded software, SoC systems and in medical, industrial, automotive, broadcast, and consumer electronics applications.

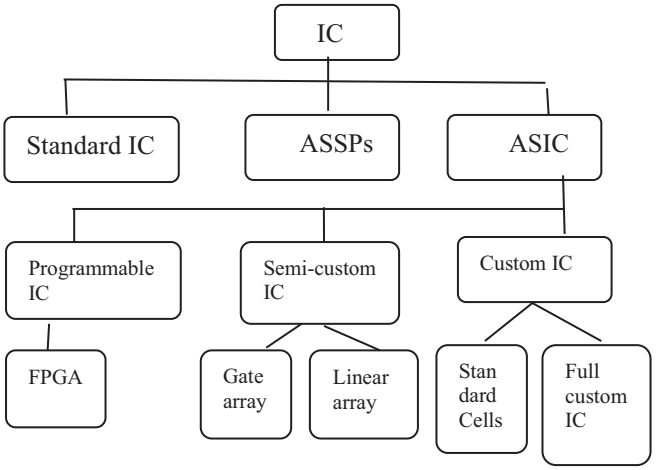

Figure 10. Application-specific Integrated Circuits (ASIC)

Choice of topology can be tree, tours, mesh, ring, bus, star, BFT, Spin, Interconnection. Simple mesh fits planar chip, short links routing, switching, blocking, delay, load, quality of service. NoC aggregate Bandwidth growth, link speed, current spatial reuse, pipelining, distributed arbitration, and separated abstraction layers. sensitivity area of the parameters for example traffic, wires, cost also plays significant role in designing time specialization for custom NoC system.

Bus is off-chip network where the bandwidth is limited, shared, speed grows down if there are more connections, no concurrency, pipelining is difficult, no layer abstraction, cost of links, latency is tolerable, traffic is unknown, changes at run time, Adherence to network standards. To solve critical problems set up connection design we use new tools which minimize the complexity, and design productivity. VLSI problems are mapping application, routing, buffering, timing closure, simulation, and testing. VLSI problems are reframed to NoC application mapping (the task by cores), Placement/Floor planning (is within the network), message routing, buffer sizing (FIFO queue in router), Timing closure(Bandwidth link allocation capacity), simulation(Network simulation, delay/traffic/Modeling power)

Testing and combined problems in the design of NoC(with topology, switching, virtual channels, flow control, arbitration, etc.). Network on the chip is a microprocessor that enables the method to send/receive data in combination. Embedded FPGA interconnections are shown in the figure.11, it has embedded FPGA, input/output connected to Network interconnection, this connects to CPU of the systems and access the memory.

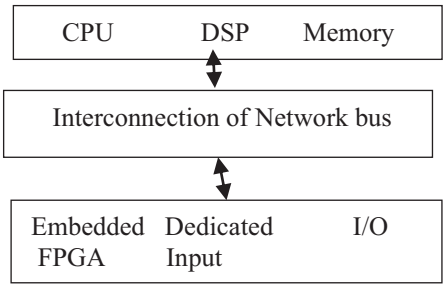

Figure 11. Embedded FPGA interconnection to components operations

Resources: Chip communications improves the bandwidth, power efficiency, and scalability. The optical NoC, Hybrid architecture are used in optical data transmission, it has high speed with distributed operations. The NoC architecture on three-dimensional (3DiC) improves performance by CMOS technology, which supports higher density with mixed chip design technology

The elements are used in NoC which is based on packet communication, interconnects to large IP cells, this can be used in SoC.

Network communicates with cells by clocks, domains, with minimum power, space, latency. NoC elastic protocol, which helps to generate topology, router. SoC design uses binary tree topology. The Process scaling, complex design, fits on System on Chip (SoC). Design is difficult due to multiple clocks, domains are increasing and integrated chip is used in design.

Network of Chip is communication point to point maintaining global clock. NoC design includes topology (star, mesh, etc.), Packet-switched or circuit switch parameters. The design of NoC, topology is mesh, star, tours, packet-switched or circuit-switched

NoC buffer uses optimized buffer size, length of the link, bandwidth NoC design uses Network topology, Heuristic algorithms, Linear programing, capability to topology design, router link, bandwidth, the sender sends the valid data, the receiver receives the data with Network components, Network based protocols, elastics system design with clock, communication channel and sender, receiver's module.

Network fabric work uses Network on Chip (NoC), design, Topology uses packet transmission in routing, throughput, router buffer with NoC fabric, the transmission of data by routing buffer, Network hardware and improves performance. The most important factors are network, topology, design, communication traffic, clocks, IP block, design, topology, router, high bandwidth, minimization function.

In Topology CTG design, each group data structure used is Graph Group where two groups joined by the router. Algorithm. 1 describes NoC topology a path of network routing.

Topology: T (V, E) v is vertices, in physical link E.Map the edge width. The path is critically weights with Network components, the methodology of repeated routing algorithms is used which is described in algorithm.2., Routing algorithm represented in algorithm.3.

CVR Journal of Science and Technology, Volume 22, June 2022
DOI: 10.32377/cvrjst2202

Algorithm:1 NoC Topology a path of network routing

Begin
Step1. IP router Initialize T, V
Step2. while Vc two or more vertices
find the highest edge
Step3. Create a new router. Group to form new Vc
Step4. Combine both the edges
Step5.Remove route directly
End

The Network router step minimizes the latency in critical paths of communication. Use the directed method to determine router locations by router with path physical length.
Procedure repeated router is represented in algorithm.2.

Algorithm:2 Algorithm for repeated router

begin
Step1.For each edge find the path topology assign router for each router all vectors, move the router in direction.
Step2. Router R
R is sorted in descending area block. Move overlapping router block.
Step3. consider replacement of router on the overlapping block. Block overlapping routers each.
Step4. Move router IP block
Step5. For each router make a new router.
Step6. Find minimum distance move a neighbor while each step run the router if not allowed in the block areas top the edge
Step 7. return
end

NoC framework, bandwidth, pace linked, packet direction data, packets direction total capacity of the link, bandwidth will be considered with needed available systems.

Design SOC for Routing algorithms: The proposed router, Functionality, Module.

Algorithm:3 network routing algorithm FIFO

begin
Input data and output. FIFO flexibility.
Step1. Find the FIFO router to store the incoming packet. FIFO buffer.
Step2. Receive packets from input to output with use of Routing methods packet data with use of routers.
Step3. The operation of the router with FIFO request
Step4. Free slot request, find free hop
Step5. Packet transmission operation
Step6 If deadlock problem, Packet buffer direction, deadlock, avoid deadlock, where the router can store incoming packets,
Step7. Transmit the packets in a specified route.
end

The Communication and Programming model improves performance by Network operations and optimal network. System on chips (SoCs) complexity pushes researchers to come up with NoC bus architecture, the advantages are the scalability, performance, throughput, utilization, and power consumption. In NoC design the overall network design uses the availability of buffer, Virtual channels with power consumption. The NoC performance increase by use of the number of buffers, Router buffer in NoC. If Router increases by use of buffer size, then go for FIFO method and reduce the size of buffers.

The high-performance system increases buffering resources, increase buffer size, Number of VCs, by use of optimization methods. The router uses a large optimization size of the switch, buffer. The architecture use mesh topology, traffic conditions. Finally Analyze dynamic buffer resize with new technique, new router architecture, buffer structure, VC incoming traffic. Flexibility and buffer size. The new router architecture: Flexible router, Buffer, VCs, port. The Router architecture with Input controller, requests, transfer data. Input controller router grants and send internal request transfer packets.

Routing logic is packer director with FIFO, according to designation address the Arbiter receives all requests, grants according to pre specified logic. The router design shown in figure 12.

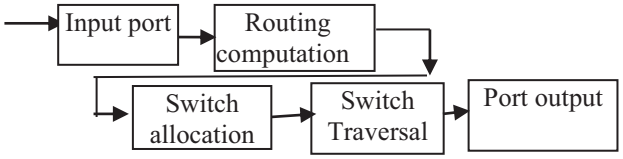

Figure 12. Flow control by Router

For example, Let us take input (N, S, W, PE) with the input port, the input is in the input buffer, the router accepts the input and allocates the channel to process and allocating packets switch and path to outport (N, SW, PE) flow control.

The flow control of networks which improves efficiency by allocation, buffer, packets, control networks and which ensure packet delivery, allocation of adjacent channels without buffer. Flow pipeline, routing, channel allocation, switch, switch traversal will improve the performance. Routing quality of design, reliability, failures, task processing, algorithms, and requirements to be considered based on the design (i.e., correctness, high performance, low hardware cost) etc. helps to improve performance.

IV. Discussions

SoC architecture uses technology and components, NoC address the features, several designs, System on chip(SoC), combine the elements in the chip. The VLSI projects are time to market, high complexity, high performance, Module use of cores, complexity reduced for current digital systems components in the product. The network techniques, VLSI implementation by high throughput with reduced complexity, routing algorithm, packet delivery, message passing, efficiency and the design Network on Chip architecture feasible by satisfying all requirements.2D, 3D meshes, applied SoC developments parameters.

Computation is an intensive application requires high performance, low power, adding many computing resources, CIP, Ips, on System on chip, interconnection of resources, applications can use bus aces communication, control architecture, utilize efficient resources. The environment bus has large, bandwidth, interconnection. The network on chip architecture is the scalable support chip communication leads to NoC-based solution for many researchers, developers develop a model architecture, circuit-based architecture, on packet-based architecture using routing algorithms incoming outgoing data on control flow.

The figure. 13. The high-level view of Network on Chip architecture, networks with PES, IP, host, memory, and processor cores. The Good algorithms maintains network balancing, design cost.

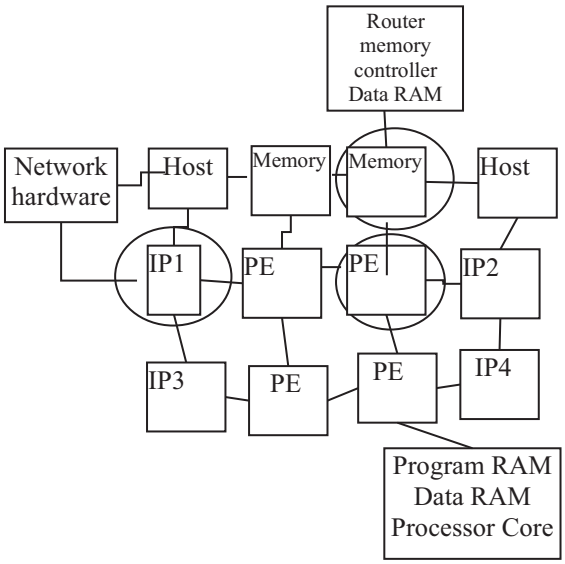

Figure 13. NoC Chip- High level view -Architecture.

The proposed NoC architecture figure14.has feasibility of hardware complexity, protocols, networks controller router capabilities. The cores of communication uses a packet-based network. The performance of system is based on multi-processor, memory modules, several IP-specific processing elements.

Router architecture: Network interconnection requires each PE, data communication, routing algorithm, Virtual channels, Router design, Physical channel, Routing algorithms. Packet is a collection of data received from the data link layer, the message is transmitted through the communication channel, router packet control, flexible for handling, designation of data.

Transfer the packets are flexible with multiple data, has better performance over single data transmission. Network simulation, packet generation traffic patterns using routing algorithm performance. Mesh topology, 8X8 each routing has better performance in each pattern, traffic pattern gives best performance with average latency. Protocol design, router FIFO per input port.

HAL is archive used in scientific documents are used in Hardware, software hybrid simulation technique for system model with chip Multiprocessor. It uses software-hardware interaction modules. Chip design and software with the use of hybrid software in host CPU.

NoC is a time-consuming, high-speed, reconfigurable resources that provides a degree of flexibility. In Hybrid design for hardware and software the resource interface, the performance of CPU improves by multicore architecture framework. CPU speed, NoC phase, design, flow, mesh network, NOC multiple routers, NoC module, the designers are with system software. Levels of the micro-architecture of CMPs Network on the chip has packet-switched, the router design uses Virtual channel flow control, communication access from CPUs cores, are transferred to all cores by local cache. chip memories, parameters, topology, data width, packet length, the latency of router, VC number, FIFO length. NoC module function call, hardware, software interfaces are used in the NoC simulation cycle. The NoC uses multiple nodes which allows communication mode all to all. communication interconnect, design, topology, in current design has required points.

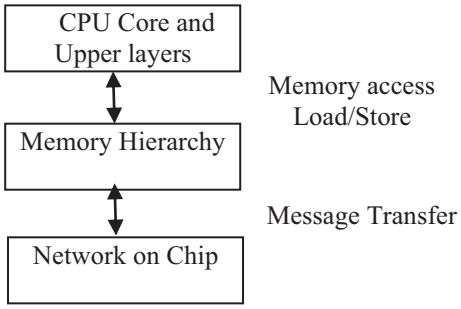

Figure 14. Levels of the micro-architecture of CMPs

The communication each direction which has a node using FIFO channel traffic with the router. Traffic Model, source-destination is with packet transmission. Latency, flow control on the router is controlled with buffer.

Timing model: Each FIFO has multiple channels (VCs), control number of VCs, design, each incoming, queue with internal timing, queue time stamping. The router module has flow control where each router connects to four channels of FIFO, traffic generator. Mesh topology, configuration Interface: Packet injection, which is packet control FIFO, access point, source designation, route the packets. The traffic generator, number of packets received through each route is used to analyze the spots, the clock signal with clock frequency to promote NOC stimulation cycle.

The Signal configuration simulation use of VC number, packet length fields and the Performance model with software, hardware. The NoC sequentially and it is widely used simulator and the simulation cycle is represented in the equation.1

$$simulation\ cycle = HTime + ETime + HStime \quad (1)$$

Where HTime is Hardware time, ETime is Elapsed time and HStime is hardware and software simulation time (interaction time)

The implantation of NoC emulator provides hardware and software interface, topology, mesh comparisons, running chip resources, on-chip resources, NoCscale. For example, 4X4 mesh, NoC, memory hierarchy level, functions, software processor on a chip, the memory space all cores, CPU core, memory access for reading/write from randomly. Memory hierarchy level with L2 cache, NoC design used in different configurations. Input design use target process, 16 core memory hierarchy. NoC computation, access trace CHIP trace for NoC.

V. Conclusions

NoC on chip integration of system components is based on requirement and application. The elements processing, memory, components, I/O, Processing Units, all involved in design, the complexity is minimized by use of software applications like AI, bigdata, and hardware components. NoC functional network architecture uses communication model for ISO/OSI reference model. For multicore systems used in handling tasks, the NoC architecture use various components and network elements, topologies, routing, and other elements. Integrated Chip can be classified into three major categories namely Standard IC, Application specific Standard Product (ASSP), and Application specific Integrated Circuit (ASIC). NoC design combine the Hardware elements such as embedded components, elements, and application software. The high-level micro architecture uses CMPS, CPU cores, and configurations channels, and software applications. In Future we can implement the SOC – Network on Chip for design and develop application-specific standard components in Network on chips.

References

[1] Y. Ye, L. Duan, J. Xu, J. Ouyang, M. K. Hung and Y. Xie, "3D optical networks-on-chip (NoC) for multiprocessor systems-on-chip (MPSoC)," 2009 IEEE International Conference on 3D System Integration, San Francisco, CA, 2009, pp. 1-6, DOI: 10.1109/3DIC.2009.5306588.

[2] AviKolodny, "Networks on Chips (NoC) – Keeping up with Rent's Rule and Moore's Law", Technion – Israel Institute of Technology International Workshop on System-Level Interconnect Prediction (SLIP), 2007

[3] Pingqiang Zhou, Ping-Hung Yuh and S. S. Sapatnekar, "Application-specific 3D Network-on-Chip design using simulated allocation," 2010 15th Asia and South Pacific Design Automation Conference (ASP-DAC), Taipei, 2010, pp. 517-522, DOI: 10.1109/ASPDAC.2010.5419830.

[4] Mostafa S. Sayed, Ahmed Shalaby, Mohamed El-Sayedand Victor Goulart, "Flexible router architecture for network-on-chip", Computers and Mathematics with Applications, Elsevier, 2012, pp. 1301-1310

[5] Daniel Gebhardt, "Elastic Flow in an Application Specific Network-on-Chip", Electronic Notes in Theoretical Computer Science 200 (2008), pp 3–15

[6] Adesh Kumar, Piyush Kuchhal and Sonal Singhal, "Secured Network on Chip (NoC) Architecture and Routing with Modified TACIT Cryptographic Technique", ICCC-2015, Elsevier, Procedia Computer Science 48, 2015, pp. 158 – 165

[7] Youhui Zhang, Peng Qu, Ziqiang Qian, Hongwei Wang, Weimin Zheng. "Software/Hardware Hybrid Network-on-Chip Simulation on FPGA". 10th International Conference on Network and Parallel Computing (NPC), Sep 2013, Guiyang, China. pp.167-178, 10.1007/978-3-642-40820-5_15. Hal-01513775

[8] [Maria Elisabete Marques Duarte, "Networks on Chip (NOC): Design Challenges", Session 4: Embedded Systems ICCA'03, pp. 121-128

[9] [Maria Elisabete Marques Duarte, "Networks on Chip (NOC): Design Challenges", Session 4: Embedded Systems ICCA'03, pp. 121-128

[10] Wen-Chung Tsai, Ying-Cherng Lan, Yu-Hen Hu, and Sao-Jie Chen, "Networks on Chips: Structure and Design Methodologies", Hindawi Publishing Corporation, Journal of Electrical and Computer Engineering, Volume 2012, Article ID 509465, pp. 1-15,doi:10.1155/2012/509465

[11] Jun Ho Bahn, Seung Eun Lee, and Nader Bagherzadeh," On Design and Analysis of a Feasible Network-on-Chip (NoC) Architecture", International Conference on Information Technology (ITNG'07), IEEE, 2007, pp, 1-6

[12] Cidon and K. Goossens, in "Networks on Chips", G. De Micheli and L. Benini, Morgan Kaufmann, 2006

[13] E. Bolotin at al. , "Cost Considerations in Network on Chip", Integration, special issue on Network on Chip, October 2004

[14] Salma Hesham, Jens Rettkowski,,Diana Göhringer, and Mohamed A. Abd El Ghany,"Survey on Real-Time Network-on-Chip Architectures",Springer International Publishing Switzerland 2015, K. Sano et al. (Eds.): ARC 2015, LNCS 9040, pp. 191–202

[15] Cui HUANG, DakunZHANG ,Guozhi SONG, "A novel mapping algorithm for three-dimensional network onchip based on quantum-behaved particle swarm optimization", Front. Comput. Sci.2017, pp. 1-10

[16] Juan Fang ,Sitong Liu, Shijian Liu, Yanjin Cheng and Lu Yu,"Hybrid Network-on-Chip: An Application-Aware Framework forBig Data",HindawiComplexity,Volume 2018, Wiley Hindawi, 2018, pp. 1-12

[17] M.Sujatha,R.Jayagowri ,"A Review on Hybrid Network on Chip", 2018 IEEE, pp. 1-11

[18] Aleksandr Yu. Romanov, "Development of routing algorithms in networks-on-chip based on ring circulant topologies", Heliyon Elsevier, 2019, pp. 1-23

[19] AyasKanta Swain, Anil Kumar Rajput, and Kamala KantaMahapatra, "Network on Chip for Consumer Electronics Devices", IEEE consumer Electronics, 2019, pp. 50-54

[20] Parisa MazaheriKalahroudi, Elham Yaghoubi and BehrangBarekatain,"IAM: an improved mapping on a 2-D network on chip to reducecommunication cost and energyconsumption", Photonic Network Communications, Springer,2020,pp 1-15

E-ISSN 2581 – 7957
P-ISSN 2277 – 3916

CVR Journal of Science and Technology, Volume 22, June 2022
DOI: 10.32377/cvrjst2203

Protecting Medical Data Over Cloud using an Effectual Authentication Model

C. Raghavendra[1] and R. Raja[2]
[1]Assoc. Professor, CVR College of Engineering/ CSIT Department, Hyderabad, India
Email: drraghavendra@cvr.ac.in
[2]Assoc. Professor, CVR College of Engineering/ CSIT Department, Hyderabad, India
Email: r.raja@cvr.ac.in

Abstract- Tele-medicine provides better on-demand service from various places. This technology is modelled to get rid of the distance based barriers and to enhance service accessing process in various rural communities. With cloud computing advancements, Medical based on-demand services (MoDS) in tele-medicine system are offered by Cloud Service Providers (CSP). CSP associates patients and medical personalities from various places with fidelity and confidentiality. However, healthcare data outsourcing over public cloud offers certain novel confronts on security. Even though, attribute based encryption process provides flexible access control, huge amounts of subscribed or unsubscribed patients are connected with cloud based medical services; offering membership management is expensive. Here, Secure-MoDS based protocol (S-MoDS) is anticipated to acquire dynamic authorization and authentication with improved efficiency and flexibility for medical services over telemedicine system. Subsequently, when patients intend to change their ordering service, it does not require any parameter updating for those patients. Here, a secure authentication mechanism has been constructed for distributed tele-medicine system that attempts to update patients' private key separately. As well as, multiple authorities are involved to handle this system even in real time environment. However, private healthcare data, distributed database that are placed in cloud should show protection integrity. This may eliminate accidental misdiagnosis from inappropriate electronic health records that are circumvented by malicious users of internal cloud. Here, simulation is performed in MATLAB environment. The anticipated S-MoDS provides better trade off in contrary to prevailing attribute based encryption model in key generation and protocol performance.

***Index Terms*- Telemedicine, authentication, medical services, integrity, public cloud**

I. Introduction

When population grows higher, medical resource requirements may increase drastically in various healthcare systems [1]. Patients' who resides in under-developmental regions, where traffic is considered to be more inconvenient, extreme mobility lack and access authority towards high quality healthcare are complex for disabled and aged persons [2]. Tele-medicinal services may facilitate a way for fulfilling the gap [3]. This system may consumes huge information technological and telecommunication advantages to provide remote healthcare resources that resolves distance barriers to enhance medical services in remote rural communities [4], and may saves life in emergency and critical situations.

On demand, medical services are aroused with advancements in telemedicine system [5]. As depicted in fig. 1, patients are provided to communicate with most available specialists or doctors in distance devoid of visiting them directly [6]. In accordance to medical certificate from specialist of very large scale hospitals, patients may undergo certain laboratory based tests and physical examination with needed demand in community or local hospital, whose major role is to upload electronic health care records to database in cloud [7]-[8]. After receiving the consultation reports, remote doctors may perform accurate diagnosis for them. With this modelling, telemedicine system provides prescription verification and remote diagnosis that may save prior medical resources and diminish overall healthcare cost for poverty stricken individuals [9]-[10]. However, this system may facilitate healthcare consultant in various location to share information and examines predictive outcomes as remains in meeting room. In case of diverse serious illness, this may avoid infectious disease transmission or parasites among medical staffs and infectors[11]-[12].

Telemedicine system is generally provided with cloud service providers who offers virtual platform that facilitates patients and doctors to function together with complete health and wellness and assisted with home care services [13]. With this, it may construct communication link between storage server and medical staff. Patient may be subscribed with certain medical services over demand for superior quality care accessibility and enhancing their experiences [14]-[15]. Cloud servers are accountable for storing electronic records and health related data. For research specialist, they may access physical data that are provided in cloud to carry put appropriate diagnosis and perform certain scientific researchers. Cloud computing may also changes conventional model for medical care in digital format.

Based on confidentiality and access authority over cloud, the predominant cryptographic model is attribute based encryption model that offers encryption and decryption in accordance to user attributes [16]. In this model, it is executed in one to many bases. Anyone who possesses the ability of decrypting protected data with data owner attribute, partial elements of encrypted data are fixed with private key component. With these characteristics, data holder may upload information to server devoid of doubt. With respect to various relationships among access

Received on 12-11-2021, Revised on 04-03-2022, Accepted on 28-04-2022.

CVR Journal of Science and Technology, Volume 22, June 2022
DOI: 10.32377/cvrjst2203

structures, private keys and cipher texts are related to secure authentication. Here, Secure-MoDS is anticipated for performing data encryption and decryption. Here, users' private keys are related to designed policies and cipher texts are labelled using various attribute sets. This may facilitates users to decrypt cipher text whenprivate key access standardization is fulfilled by embedded cipher text may eliminate user permissions. Therefore, this authentication is generally used to safeguard outsourced data confidentiality. With secure MoDS- cipher text is connected with certain standards and private key is depicted by attribute set. Users may decrypt cipher text with access tree iff attributes are related with private key to fulfil access structure, that may rejects certain decryptors requirements. This provides ability to medical service tagging by telemedicine attributes and private key distributionduring tagging user subscription. Subsequently, secure MoDS is superior for offering access confidentiality and authority of MoD than ABE.

II. Related Works

Lightweight based mutual authentication protocol for sensor and IoT devices and application is anticipated in [17]. This protocol is used among two lightweight models that work on key encryption strategy. It may utilize response and challenge strategy for mutual authentication by encryption. This kind of strategy is specified as n-pass protocol for security and encryption factors may describe various rounds. This protocol may consider participants who are previously aware of public key identities respectively. This protocol is provided to carry out when comparing with ECC, RSA and other protocol version as in contrary to optimal scheme.

There are various investigations that some efforts are provided to attribute based cryptography to blockchain. In [18], EHR's system, utilized attribute dependent signature strategy with multi-authority to validate blocking facility. It is stored with individual patient data. With this protocol, patient may provide physical data block anonymously, and provide access policy for appropriate personals to acquire those data. In [19], author used ABE approach to provide encrypt and secrete key shared data over cloud. In this approach, block chain technology may facilitate keyword search function on cipher text can be executed. In [20]-[21], author merged IBS, IBE, ABE and blockchain over crypto-system to offer system management. To facilitate privacy and data sharing, author [22] anticipated block chain dependent privacy preserving distribution for EMRs, that are stored in cloud indexes are reversed in tampered consortium proof based block chain. In [23]-[24], author offered an access control factors for block chain EMR exchange that eliminated gate way to authorize individuals access with block chain granularity. In [25], author provided a novel verification strategy for patient authentication among node database and enrolment devices. Blockchain approach may fulfil traceability and integrity of medical data.

III. Methodology

The mutual authentication operation includes two communication parties that may establish two protective authentication and communication server to start various processes. It may fulfil confidentiality with public key encryption usage; one directional has function integration and authentication using mutual agreement among communication parties for determining last session key for communication. System identity is essential for validating accuracy of transmitted message, where time stamp may fulfil message that works on current function. Every public key may be placed in server that assists in authentication and system registration.

A. Secure MoDS protocol

1) Each end user wants to establish protected communication with cloud server, may request for public key from server authority. Here, C is client, AS is service authority, P is public key, I is request, S is storage in cloud, t is time, E is encryption and D is decryption.

$$C \rightarrow AS: I_c, PK_c \quad (1)$$

2) The authority may consider the end user as valid client and responses with public key request for cloud server.

$$AS \rightarrow c: PK_s \quad (2)$$

3) Client may generate pseudo random number and timestamp XOR. Client then computes session key using $K_{c,s} = H\,(t_c \otimes R_c)$.These factors are then encrypted with cloud server based key provided by cloud authority. It is given as input to lightweight encryption process. Here, t_c, R_c, PK_c are provided for computation of $k_{c,s}$ and validating corresponding identity.

$$C \rightarrow s: E_{PKs}\left((t_c, R_c), K_{c,s}, PK_c\right) \quad (3)$$

4) When receiving encryption from client, cloud server decrypts with private key D_{SKs} and validate computation of $K_{c,s} = H(t_s \otimes R_s)$. Cloud server network address and validation message is also used here. All these factors are encrypted with client public key and transmitted to end users.

$$s \rightarrow c: E_{PKc}\left(K_{s,c}, (t_s, R_s), a_s, v\right) \quad (4)$$

5) User decrypts message with private key D_{SKc} and verification for re-computation of session key using hashing, stores timestamp message and network address validation by v. Absolutely, user may re-computes session key using $K_{c,s} = H(t_c \otimes R_c)$. In initial message part, new session key is encrypted using cloud server public key E_{PKs}, where next message is encrypted in public key E_{PKs} comprising plain text message clustered with clients' timestamp, network address, random number which is validated with cloud server by evaluating hash $H(t_c \otimes R_c)$ with user's session

CVR Journal of Science and Technology, Volume 22, June 2022
DOI: 10.32377/cvrjst2203

key $k_{c,s}$. With message encryption and key are attained and transmit as single message to server.

$$c \rightarrow s: E_{PKS}(K_{c,s}), E_{PKS}(M, (t_c, R_c), a_c) \quad (5)$$

Assume that pseudo random variables are generated with above discussed number. This protocol considers ransom values as input, therefore encryption is not usually with similar parameter.

B. S-MoDS in Tele-medicine

Telemedicine holds various informational and communicational benefits to get rid of geographical constraints and enhances access to various healthcare services. Telemedicine execution is measured as specific benefits for enhancing client experience and protecting constrained medical cost and resources. Merging various cloud computing technologies, data distribution in telemedicine model assists physicians to provide appropriate prediction in proper time and offer superior quality to all individuals.

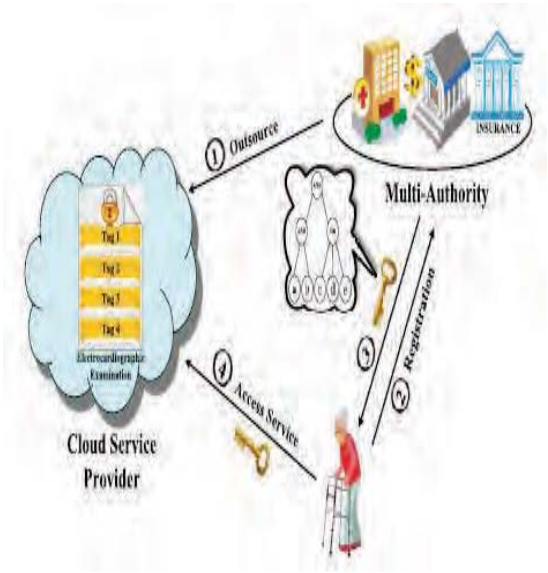

Figure 1. Generic Medical on Demand protocol

Healthcare data over telemedicine system comprises sensitive and personal information that are more attractive to cybercriminals. Henceforth, huge confronts for certain system to depict how to share, store and use data to privacy divulging server. However, integrity and privacy of healthcare data are safe guarded from external malicious users, however also from unauthorized access from insider cloud users of this system, for instance, (CSP and authority). They may assist in developing protected telemedicine system to provide integrity and privacy of healthcare data to various medical resources and fulfil data confidentiality. As depicted in Fig. 2, medical service is labelled with certain attribute in tag formats like examination of electrocardiographic tagging in heart disease, arrhythmia, angina pectoris, and price and so on. Various telemedicine authorities may merge with distributed keys with diverse standards to every patient. For example, cloud authorities

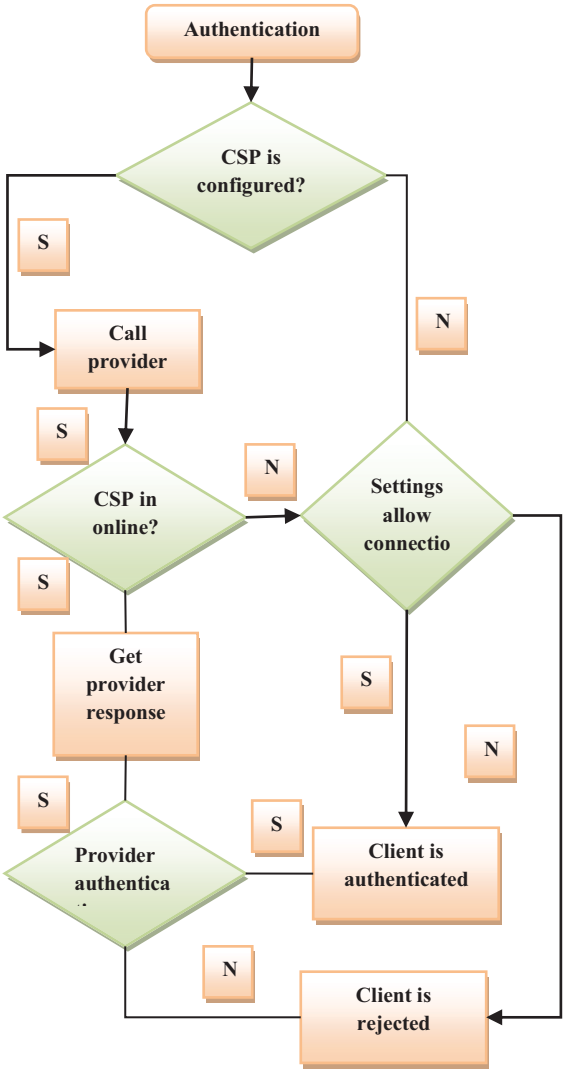

Figure 2. Flow diagram of proposed model

are accountable for registration, e-payment, and healthcare subsidies. They construct key for decrypting protected on demand services as the attributes are fulfilled with cardiology, heart disease, pectoris and arrhythmia. Therefore, Secure MoDS protocol may offer data confidentiality and access control in telemedicine system.

While considering integrity consortium based block chain is used for managing these multiple authorities as in fig. 2. More specifically, after performing private key, users may perform electrocardiographic analysis with wearable medical devices by their own in house or more sophisticated professional equipment in community care taking centre nearby. After performing this, analysis results of Electrocardiograph (ECG), physical status video, ultrasound, colour Doppler are uploaded CSP to database and data were indexed by keywords and abstracts of outcomes that are provided in block. For specialists and doctors, analysis was downloaded and provide medical certificate to user with CSP. Services may vary in diverse days; it may produce block chronologically to save indexes

CVR Journal of Science and Technology, Volume 22, June 2022
DOI: 10.32377/cvrjst2203

of associated healthcare data when appropriate data is placed. Blocks that are available in MoD services are associated with series into block chain that belongs to user. As smaller size of index, it will not exceed storage space limitation in all blocks. Based on this model, changes concerning original healthcare information in cloud may cause due to appropriate index in block chain that are altered and every entity comprising all authorities may discover corresponding variations. This approach may acquire global perspective in medical history in verifiable, efficient and permanent methodology. Therefore, block chain approaches is beneficial for offering protection integrity on healthcare data in cloud.

C. Security evaluation

This section provides a detailed security analysis on the proposed model. The S-MoDS model provides secure mutual authentication and key agreements. The trust relationship is established via the authentication process. The following are the security related steps:

1) Generate pair-wise private and public keys;

2) Randomly select the prime numbers;

3) Generate encrypted medical file or records;

4) Make the essential medical information to be encrypted;

5) Compute the cipher text;

6) Perform proxy re-encryption;

7) Compute the complexity of the private and public key;

8) Decrypt the hospital data;

9) Evaluate the essential information.

IV. Numerical Results and Discussions

The ultimate objective of this work is to examine the prevailing and the anticipated protocol model experimentally, where mutual authentication efficacy is dependent on pseudo random functionality and key exchange among cloud server. From this, experimentation is carried out using various factors. Execution time of anticipated model is demonstrated at various time instances. Simulation was carried out in MATLAB environment and key size, execution time is considered to be a major performance metrics. Here, Intel core i3 processor with 3.10GHz RAM and 16 GB internal memory.

TABLE I.
Order of Computation

Encryption cost	Decryption cost	Registering	Updating	Revoking
$O(m_c)$	$O(m_c)$	$O(m)$	$O(n\ X\ m)$	$O(n\ X\ m)$
$O(m_c)$	$O(m_c)$	$O(m)$	$O(n\ X\ m)$	$O(n\ X\ m)$
$O(m_c)$	$O(m_c)$	$O(m+m_u+n)$	$O(m+m_u+n)$	$O(m)$
$O(m_c)$	$O(m_c)$	$O(m_u)$	$O(n\ X\ m_u)$	$O(n\ X\ m)$
$O(m_c)$	$O(m_c)$	$O(m+m_u+n)$	$O(m+m_u+n)$	$O(m)$
$O(N\ X\ m_c)$	$O(N\ X\ m_c)$	$O(N\ X\ m)$	$O(N\ X\ m)$	$O(n\ X\ m)$
$O(m_c)$	$O(m_c)$	$O(m)$	$O(n\ X\ m)$	$O(n\ X\ m)$
$O(N\ X\ m_c)$	$O(N\ X\ m_c)$	$O(N\ X\ (m+m_u+n)$	$O(m+m_u+n)$	$O(m)$

TABLE II.
Encryption Time

Number of experiments	Secure data sharing scheme	S-MoDS
1	3428	3400
2	3505	3500
3	3420	3350
4	3381	3280
5	3306	3200
6	3346	3246

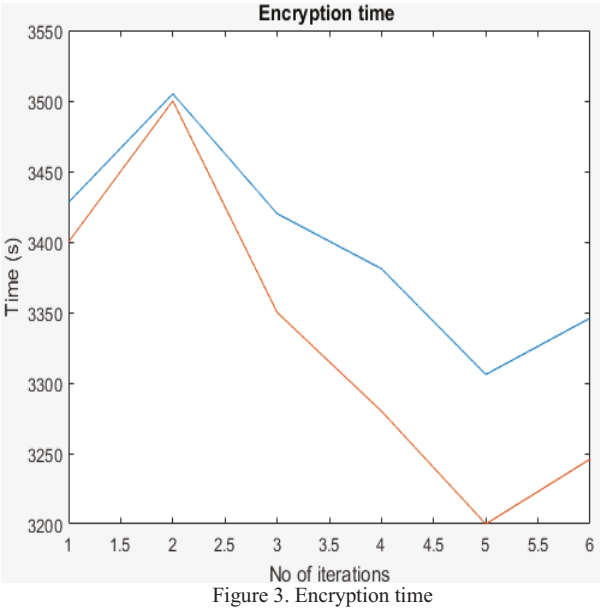

Figure 3. Encryption time

TABLE III.
DECRYPTION TIME

Number of experiments	Secure data sharing scheme	S-MoDS
1	113	110
2	104	100
3	156	150
4	189	180
5	145	140
6	108	103

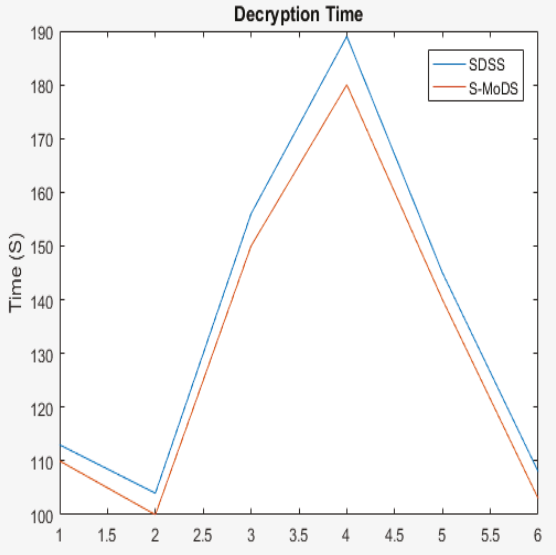

Figure 4. Decryption time

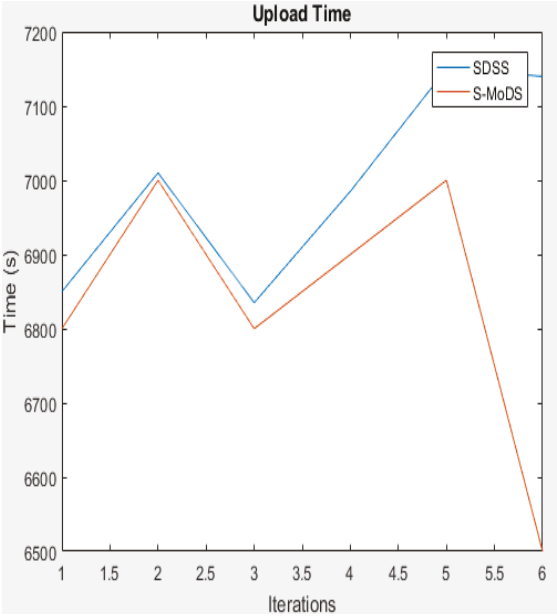

Figure 5. Uploading time

TABLE IV.
UPLOAD TIME

Number of experiments	Secure data sharing scheme	S-MoDS
1	6850	6800
2	7010	7000
3	6835	6800
4	6985	6900
5	7150	7000
6	7140	6500

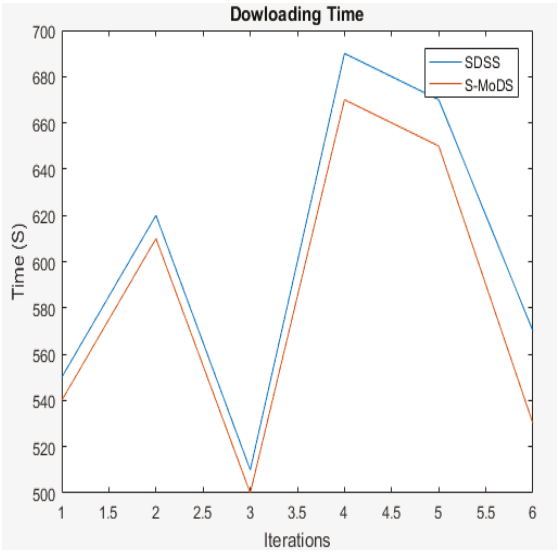

Figure 6. Downloading time

TABLE V.
DOWNLOAD TIME

Number of experiments	Secure data sharing scheme	S-MoDS
1	550	540
2	620	610
3	510	500
4	690	670
5	670	650
6	570	530

TABLE VI.
KEY GENERATION TIME

Number of experiments	Secure data sharing scheme	S-MoDS
1	1010	1005
2	1110	1100
3	1150	1130
4	1200	1100
5	1180	1080
6	1200	1050

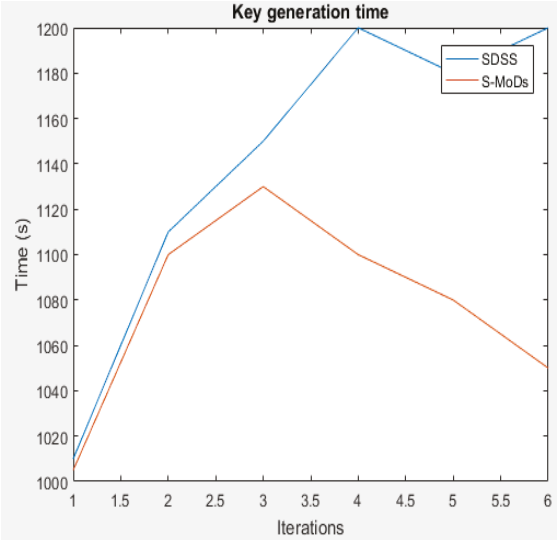

Figure 7. Key generation time

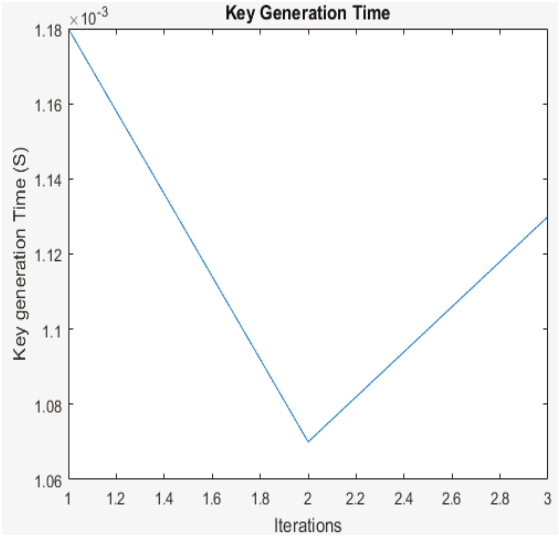

Figure 8. Key generation time

D.

TABLE VII.
KEY GENERATION TIME(S)

256 bit hash	Key generation time (s)
Session Key S_{k1}	0.001180
Session Key S_{k2}	0.001070
Session Key S_{k3}	0.001130

TABLE VIII.
COMPUTATIONAL TIME

Protocol	MPAKE	S-MoDS
Computational Time (s)	9.30	5.90

From figure given above, the performance analysis was performed with various parameter sets. Time needed for 100 key generation with available system is quite complex. Therefore, generation of millions of keys are measured to be a standalone factor for examining server that is done with reduced amount of time. Table I depicts various order of computation and complexity for performing various computation. Generation of more keys are more appropriate for time needed for all devices. Generation of session keys as in Table VI is provided 'H' timestamp.

Table VII depicts computational time of proposed versus existing model. Here, S-MoDs is compared with MAPKE where computation time of MPAKE is 9.30 while in S-MoDs computation time is 5.90 seconds. From Fig 3- Fig 8 various computations has been performed for key generation, uploading time, downloading time, encryption time, decryption time. Performance is quite similar to key generation from various set of parameter values. Table II depicts the comparison of the encryption time of proposed S-MoDS with existing secure data sharing scheme. The encryption time is measured in seconds. The execution time of proposed model is 3400s, 3500s, 3350s, 3280s, 3200s and 3246s which is comparatively higher than secure data sharing scheme, i.e. 3428s, 3505s, 3420s, 3381s, 3306s and 3346s. Table II to Table VI depicts corresponding values associated with Encryption, decryption, uploading and downloading time. Some features are more essential in protocol design such as update, Authorities, Integrity, traceability. Update is specifically for revoking and updating with standardized policies. When users joins or leaves cloud network, service authority may be raised with version number. Each authority is accountable for managing various kinds of data associated with S-MoDS authentication protocol. In traceability, it merges cloud storage and blockchain for managing original data as it is stored in cloud. It protects medical data from distortion. It will also reduce medical disputes and accidents. By evaluating various factors, protocol has to fulfil revoking, updating, integrity, traceability and multiple authority management in cloud storage.

V. CONCLUSIONS

This research intends to model a novel approach for provisioning authentication to the medical data. S-MoDS protocol is appropriate for performing against diverse attacks and outcome session offers superior performance on huge amount of devices that are to be authenticated in reduced time. Here, Secure-MoDS based protocol (S-MoDS) is anticipated for establishing authentication over telemedicine system. A secure authentication mechanism has been constructed for distributed tele-medicine system to update patients' private key where multiple authorities are involved to handle this system. Private healthcare data is placed in cloud and gives protection integrity. It eliminates accidental misdiagnosis from inappropriate electronic health records. This is extremely appropriate for cloud architecture that included IoT that are used in various labs, universities, vehicles, industries where secured environment is extremely prioritized. Regrettably, this work has attained an effectual protocol model in contrary to benchmarks like RSA, ECC and so on. As future extension, this work may carry out experimentation with multiple high level end users from various channels for approximating resource availability. As well, authentication backup is offered to eliminate single point of failure in connected network.

REFERENCES

[1] Y. Karaca, M. Moonis, Y.-D. Zhang, and C. Gezgez, “Mobile cloud computing based stroke healthcare system," Int. J. Inf. Manage., vol. 45, pp. 250_261, Apr. 2019.
[2] O. Ali, A. Shrestha, J. Soar, and S. F. Wamba, “Cloud computing-enabled healthcare opportunities, issues, and applications: A systematic review," Int. J. Inf. Manage., vol. 43, pp. 146_158, Dec. 2018.
[3] M. Armbrust, A. Fox, R. Grif_th, A. D. Joseph, R. Kaz, A. Konwinski, G. Lee, D. Patterson, A. Rabkin, I. Stoica, and M. Zaharia, “A view of cloud computing," Commun. ACM, vol. 53, no. 4, pp. 50_58, 2010.
[4] V. Casola, A. Castiglione, K. K. Choo, and C. Esposito, “Healthcare-related data in the cloud: Challenges and opportunities," IEEE Cloud Comput., vol. 3, no. 6, pp. 10_14, Apr. 2016.
[5] S. H. Lee, J. H. Song, and I. K. Kim, “CDA generation and integrationfor health information exchange based on cloud computing system," IEEE
[6] Trans. Services Comput., vol. 9, no. 2, pp. 241_249, Mar. 2016.
[7] S. Sharma, K. Chen, and A. Sheth, “Toward practical privacy-preservinganalytics for IoT and cloud-based healthcare systems," IEEE InternetComput., vol. 22, no. 2, pp. 42_51, Mar. 2018.
[8] V. Goyal, O. Pandey, A. Sahai, and B.Waters, “Attribute-based encryptionfor _ne-grained access control of encrypted data," in Proc. 13th ACMConf. Comput. Commun. Secur., Alexandria, VA, USA, Oct./Nov. 2006,pp. 89_98.
[9] K. He, J. Chen, Y. Zhang, R. Du, Y. Xiang, M. M. Hassan, and A. Alelaiwi,“Secure independent-update concise-expression access control for video
[10] on demand in cloud," Inf. Sci., vol. 387, pp. 75_89, May 2017.
[11] J. Garay, A. Kiayias, and N. Leonardos, “The Bitcoin backbone protocol:Analysis and applications," in Proc. Annu. Int. Conf. Theory Appl. Cryp-tograph. Techn.,So_a, Bulgaria, 2015, pp. 281_310.
[12] Y. Zhang and J.Wen, “The IoT electric business model: Using blockchaintechnology for the Internet of Things," Peer PeerNetw. Appl., vol. 10, no. 4,pp. 983_994, Jul. 2017.
[13] M. Li, S. Yu, Y. Zheng, K. Ren, and W. Lou, “Scalable and securesharing of personal health records in cloud computing using attribute-basedencryption," IEEE Trans. Parallel Distrib. Syst., vol. 24, no. 1,pp. 131_143, Jan. 2013.
[14] J. Wei, W. Liu, and X. Hu, “Secure and ef_cient attribute-based accesscontrol for multiauthority cloud storage," IEEE Syst. J., vol. 12, no. 2,pp. 1731_1742, Jun. 2018.
[15] H. Wang and Y. Song, “Secure cloud-based EHR system usingattribute-based cryptosystem and blockchain," J. Med. Syst., vol. 42, no. 8,p. 152, 2018.
[16] C.-H. Hong and B. Varghese, “Resource management in fog/edgecomputing: A survey," 2018, arXiv:1810.00305. [Online]. Available:https://arxiv.org/abs/1810.00305
[17] S. Khan, S. Parkinson, and Y. Qin, “Fog computing security: A review ofcurrent applications and security solutions," J. Cloud Comput., Adv., Syst.Appl., vol. 6, no. 1, p. 19, 2017.
[18] S. Khan, S. Parkinson, and Y. Qin, “Fog computing security: A review ofcurrent applications and security solutions," J. Cloud Comput., Adv., Syst.Appl., vol. 6, no. 1, p. 19, 2017.
[19] M. V.Pawar and J. Anuradha, “Network security and types of attacks innetwork," ProcediaComput. Sci., vol. 48, pp. 503_506, 2015.
[20] K. Stouffer, J. Falco, and K. Scarfone, “Guide to industrial control systems(ICS) security," NIST, Gaithersburg, MD, USA, Tech. Rep., Jun. 2011.
[21] R. Mahmud, R. Kotagiri, and R. Buyya, “Fog computing: A taxonomy,survey and future directions," Internet Everything, pp. 103_130, Oct. 2017.
[22] N. Chen, Y. Yang, T. Zhang, M.-T. Zhou, X. Luo, and J. K. Zao, “Fog asa service technology," IEEE Commun. Mag., vol. 56, no. 11, pp. 95_101,Nov. 2018.
[23] A. Kattepur, H. K. Rath, A. Simha, and A. Mukherjee, “Distributedoptimization in multi-agent robotics for industry 4.0 warehouses," inProc. 33rd Annu. ACM Symp. Appl. Comput., Pau, France, Apr. 2018,pp. 808_815.
[24] K. Piotrowski, P. Langendoerfer, and S. Peter, “How public key cryptography in_uences wireless sensor node lifetime," in Proc. 4th ACMWorkshopSecure Ad Hoc Sensor Netw., 2006, pp. 169_176
[25] V. L. Shivraj, M. A. Rajan, M. Singh, and P. Balamuralidhar, “One timepassword authentication scheme based on elliptic curves for Internet ofThings (IoT)," in Proc. 5th IEEE Nat. Symp. Inf. Technol., Towards SmartWorld, Feb. 2015, pp. 1_6.
[26] M. Mukherjee, R. Matam, L. Shu, L. Maglaras, M. A. Ferrag,N. Choudhury, and V. Kumar, “Security and privacy in fog computing:Challenges," IEEE Access, vol. 5, pp. 19293_19304, 2017.
[27] C.-H. Hong and B. Varghese, “Resource management in fog/edgecomputing: A survey," 2018, arXiv:1810.00305. [Online]. Available:https://arxiv.org/abs/1810.00305

E-ISSN 2581 – 7957
P-ISSN 2277 – 3916

CVR Journal of Science and Technology, Volume 22, June 2022
DOI: 10.32377/cvrjst2204

Supervised Learning for COVID Mortality Span Prediction

A. Srinivasa Reddy
Assoc. Professor, CVR College of Engineering/CSIT Department, Hyderabad, India
Email: srinivas.asr@gmail.com

Abstract: **The covid-19 outbreak is causing concern among the world's population. Because there are no preventative precautions in place, current treatment approaches are limited to treating patients who tested positive for covid-19. In this case, determining the severity of the patient's disease is critical in lowering the covid-19-related death rate. The pathology findings are used by clinical professionals to scale the severity of the condition. Clinical specialists' diagnosis is strongly dependent on their level of competence. Unlike the other dimensions, sensitivity, or accuracy in disease-prone situations, is extremely important in clinical practice. This paper describes a supervised learning strategy for performing computer-assisted covid-19 mortality scope using the target patient's pathology records. The experimental investigation shows the utility of the proposed strategy in predicting death with the least amount of false alerting.**

Index Terms: **COVID-19, Computed Tomography, Feature Optimization, World Health Organization, Machine Learning.**

I. Introduction

There have been several pandemic diseases that have afflicted humans in the past. The WHO (World Health Organization) is collaborating with numerous national authorities as well as professionals to combat these pandemics. As soon as the first instance of COVID-19 sickness was identified in the Wuhan district of China in December 2019, it spread throughout the world until it was ultimately eradicated on January 30th, 2020.COVID-19 has been classified as an infectious disease caused by a new coronavirus and found in WUHAN, China, according to the research in [1]. SARS-CoV-2 (severe acute respiratory syndrome coronavirus-2) is a new form of virus that has never been seen before in humans. Furthermore, the virus is spread primarily through respiratory difficulties, droplets from sneezing, coughing, or when people meet one another. When these droplets are inhaled or land on surfaces that other people touch with their hands, they become infected with the virus. If their hand meets their nose, eyes, or mouth, they become infected with the virus.

The coronavirus, which has become an epidemic disease, may exist for a few days on a variety of surfaces such as plastic and stainless steel, and for a few hours on copper and cardboard. Nonetheless, the number of potential viruses may decrease over time and may not always be there to induce infection. Furthermore, in the case of people, the viral symptoms might appear anywhere from 1 to 14 days after infection. Later, it spreads quickly, leaving no time to prepare for a newly discovered renowned and contagious virus, prompting the WHO to declare COVID-19 a pandemic, as mentioned in [2], because to its rapid transmission among humans.

Various trials have been conducted in the medical labs in distinct phases to assess the efficacy of covid-19, but no findings have been released too far. Because it is a new virus, there is no vaccination available. Even though multiple pharmaceutical and research companies have begun to work on a vaccine, it may be months or even years before the vaccine is available to the public. Because there aren't enough ventilators, hospital beds, kits, or oxygen tanks, and there's no proper treatment or vaccination available, it's important to investigate the number of positive cases, the number of recovery cases, and other factors that could influence virus proliferation. Everyone should be aware of the virus and take the appropriate steps to avoid infection.

II. Related Work

For gaining insights and spreading the sources of disease, effective outbreak estimation methodologies must be used. As mentioned in [1,3] various legislative and political organizations rely on insights from estimating methods for adopting fresh policies and monitoring the efficiency of implemented rules. The current worldwide pandemic disease COVID-19 has been envisioned as intricate and non-linear, according to the work [4].

Furthermore, the outbreak differs from other recent epidemics, raising the question of whether established methodologies can produce reliable results, as noted in [3].In addition, as noted in [1,5], various unknown as well as recognized variables included in the spread, the complexities of large population behavior in several geopolitical areas, and variances in containment systems all exacerbated technique uncertainty. As a result, traditional epidemiological methodologies face new hurdles in producing more reliable results. As indicated in [3-5], multiple unique ways have arisen to overcome this difficulty. These methods add diverse assumptions into modeling.

Machine learning has been used to improve the screening and diagnosis of identified patients using a radio imaging scheme that is like clinical data from blood samples and CT scans (computed tomography). Radiology imaging such as CT scans and X-rays are routinely used by healthcare experts to supplement traditional screening and diagnosis. Inappropriately, the performance of such devices is moderate during the peak of the SARS-CoV-2 pandemic. In this regard, the work [6] demonstrates feasible ML devices by providing a unique technique that includes both valid and quick SARS-C detection.

As mentioned in [7], the current investigations propose an accessory device for improving COVID-19 diagnosis accuracy with a novel Automatic COVID-19 identification model based on a deep learning algorithm. The proposed

Received on 04-08-21 Revised on 04-11-2021, Accepted on 04-02-2022.

CVR Journal of Science and Technology, Volume 22, June 2022
DOI: 10.32377/cvrjst2204

method makes use of raw chest x-ray pictures from 127 affected patients. The binary class has a performance accuracy of 98.08 percent, and the multiclass has a performance accuracy of 87.02 percent. The forecast approach used a judgment rule to forecast fast and estimate the number of infected people at high risk; patients who have been declared infected should be considered for intensive care, and the shortness rate should be reduced. By employing a deep-learning algorithm over a large short-term network, a forecasting approach based on Canadian time-series has been built.

III. Supervised Learning

Supervised learning is a sort of machine learning in which machines were trained using well-labeled training data and then predict the output based on that data. The labelled data indicates that some of the input data has already been tagged with the appropriate output.

In supervised learning, the training data presented to the machines acts as a supervisor, instructing the machines on how to correctly predict the output. It uses the same notion as when a student learns under the guidance of a teacher. The process of supplying input data as well as proper output data to the machine learning model is known as supervised learning. A supervised learning algorithm's goal is to discover a mapping function that will map the input variable(x) to the output variable(y).

Supervised learning can be utilized in the real world for things like risk assessment, image categorization, fraud detection, spam filtering, and so forth.

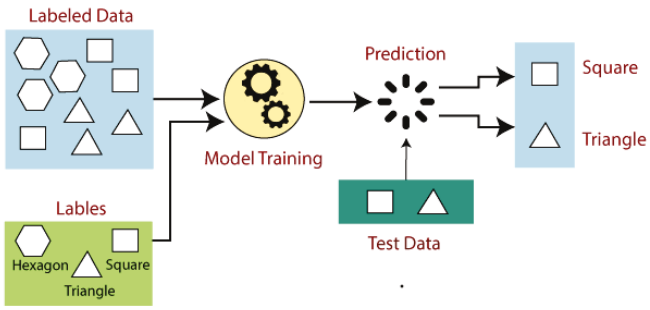

Figure 1. Model of Supervised Learning

The Process of Supervised Learning:

1. Determine the type of training dataset you'll be using.
2. Obtain the tagged training data by collecting/gathering it.
3. Divide the training dataset into three parts: training, test, and validation.
4. Determine the training dataset's input characteristics, which should contain enough information for the model to accurately predict the output.
5. Choose an appropriate algorithm for the model, such as a support vector machine or a decision tree.
6. Use the training dataset to run the algorithm. Validation sets, which are a subset of training datasets, are sometimes required as control parameters.
7. By giving the test set, you may assess the model's correctness. If the model correctly predicts the outcome, then our model is accurate.

There are two types of algorithms from supervised learning:

1. Classification
2. Regression

Regression:

If there is a relationship between the input and output variables, regression procedures are applied. It's used to predict continuous variables like weather forecasting, market trends, and so on. These algorithms include Regression trees, Linear regression, Bayesian linear regression and Polynomial regression.

Classification:

When the output variable is categorical, meaning there are two classes, such as Yes-No, Male-Female, True-False, and so on, classification methods are utilized. These algorithms include Logistic regression, Random Forest, Support Vector Machine and Decision trees.

IV. Proposed Method

This section delves into the specifics of the data, methodologies, and materials used in the suggested statistical evaluation method for predicting the mortality scope of covid-19-positive patients.

A. The Data

Age, gender, weight, and clinical reports connected to pathological reports related to blood tests are among the demographic parameters. The information gathered from clinical reports is a subset of the pathology reports for diabetes types I and II. Each record has 31 qualities, one of which is the mortality scope, which can be either positive or negative.

B. The Features

The training datasettD is bipartite as two sets i.e. tD_+ , $tD_-$with entries labeled positive and negative in the order they appear in the training dataset. Allow the set to include all attributes (excluding mortality scope) that indicate the anticipated values in each record of both sets. Additionally, all potential subsets of size 1 to $|aL|$ of the setaL size are discovered. These subsets are referred to as n-gram feature labels, and the projected values are referred to as n-gram feature labels.

The frequency of each n-gram feature in datasets tD_+ , tD_- indicates their level of confidence in the positive and negative labels, in that order. The discovery of n-grams, on the other hand, is complicated and proportional to the count of feature attributes. As a result, lowering the attribute count optimizes the number of n-grams needed in the learning phase.

CVR Journal of Science and Technology, Volume 22, June 2022
DOI: 10.32377/cvrjst2204

C. Feature Optimization

The values projected to an attribute with significant confidence in the labels positive and negative are produced as ideal attributes. The t-test [24], a distribution diversity assessment measure, was used to determine the degree of diversity between the values of an attribute in records classified as positive and the values of the same attribute in records labeled as positive and the values of respective attribute in records labelled as negative. The mathematical model of feature optimization explored in following description. The algorithm is explained as follows.

Step 1: for each attribute a_i of the attribute list aL,

$$\forall_{i=1}^{|aL|} \{a_i \exists a_i \in aL\} \tag{1}$$

Let the vectorsaf_i^+, af_i^- denote the values of the attribute a_i in positive and negative label setstD_+ , tD_-

Step 2: mean of the values listed in the vectoraf_i^+

$$\langle af_i^+ \rangle = \frac{1}{|af_i^+|}\left(\sum_{j=1}^{|af_i^+|}\{e_j \exists e_j \in af_i^+\}\right) \tag{2}$$

Step 3: mean of the values listed in the vectoraf_i^-

$$\langle af_i^- \rangle = \frac{1}{|af_i^-|}\left(\sum_{j=1}^{|af_i^-|}\{e_j \exists e_j \in af_i^-\}\right) \tag{3}$$

Step 4: deviation of the values listed in the vectoraf_i^+

$$\sigma(af_i^+) = \frac{1}{|af_i^+|}\left(\sum_{j=1}^{|af_i^+|}\left\{\sqrt{\left(\langle af_i^+ \rangle - e_i\right)^2}\right\}\right) \tag{4}$$

Step 5: deviation of the values listed in the vectoraf_i^-

$$\sigma(af_i^-) = \frac{1}{|af_i^-|}\left(\sum_{j=1}^{|af_i^-|}\left\{\sqrt{\left(\langle af_i^- \rangle - e_i\right)^2}\right\}\right) \tag{5}$$

Step 6: The t-score is calculated by ordering the vectors af_i^+, af_i^-representing attributea_i values toward positive and negative labels.

$$ts = \frac{(\langle af_i^+ \rangle - \langle af_i^- \rangle)}{\sqrt{\sigma(af_i^+) + \sigma(af_i^-)}} \tag{6}$$

D. Mortality Span Prediction

The coefficients used to scale the mortality scope will be discovered using the mathematical model below. The mean and root-mean-square-deviation (RMSD) of the positive and negative confidence of the diversified n-gram feature values are the coefficients. The required steps for this process are:

Step 1: The mean of predictive confidence of the n-gram feature values of the positive label.

$$\langle pc_+ \rangle = \frac{1}{|pc_+|}\left(\sum_{i=1}^{|pc_+|}\{c_i \exists c_i \in pc_+\}\right) \tag{7}$$

Step 2: The mean of predictive confidence of the n-gram feature values of the negative label.

$$\langle pc_- \rangle = \frac{1}{|pc_-|}\left(\sum_{i=1}^{|pc_-|}\{c_i \exists c_i \in pc_-\}\right) \tag{8}$$

Step 3: The deviation$RMSD$ of the predictive confidence of the n-grams of the positive label.

$$pc_+^\sigma = \frac{1}{|pc_+|}\left(\sum_{j=1}^{|pc_+|}\left\{\sqrt{\left(\langle pc_+ \rangle - c_j\right)^2} \exists c_j \in pc_+\right\}\right) \tag{9}$$

Step 4: The deviation of the predictive confidence of the n-grams of the negative label.

$$pc_-^\sigma = \frac{1}{|pc_-|}\left(\sum_{j=1}^{|pc_-|}\left\{\sqrt{\left(\langle pc_- \rangle - c_j\right)^2} \exists c_j \in pc_-\right\}\right) \tag{10}$$

Step 5: The lower-bound of the positive prediction scale is the difference between mean and respective deviation of the positive confidence of n-gram feature values.

$$lb_+ = \langle pc_+ \rangle - pc_+^\sigma \tag{11}$$

Step 6: The cumulative of mean and deviation denotes the upper-bound of the prediction scale of the positive label.

$$ub_+ = \langle pc_+ \rangle + pc_+^\sigma \tag{12}$$

CVR Journal of Science and Technology, Volume 22, June 2022
DOI: 10.32377/cvrjst2204

Step 7: The lower-bound of the negative prediction scale is the difference between mean and respective deviation of the positive confidence of n-gram feature values.

$$lb_{-} = \langle pc_{-} \rangle - pc_{-}^{\sigma} \tag{13}$$

Step 8: The cumulative of mean and deviation denotes the upper-bound of the prediction scale of the negative label.

$$ub_{-} = \langle pc_{-} \rangle + pc_{-}^{\sigma} \tag{14}$$

Step 9: Coefficient of n-grams has been returned, corresponding upper and lower-bounds in the form of Heuristics regression.

$$\text{Return } (ss, ssl, ssu) \tag{15}$$

E. Prediction of Label

The input record r was given to predict if the mortality span is positive or negative. Collect all the n-gram feature values of all optimal n-gram features from the given record r. Find the mean of the positive and negative confidence $< c_{+} >, < c_{-} >$ of all n-gram feature values of the given input record towards training corpus.

Further, predict the mortality scope of the record as follows,

1. $if\,(\langle c_{+} \rangle \geq ub_{+})$

   //If the mean confidence$\langle c_{+} \rangle$of the n-gram feature values discovered from the given input record r is greater than or equals to positive upper-boundub_{+}, the mortality scope against the given record$r$ is positive

2. $if\,(\langle c_{+} \rangle \geq \langle pc_{+} \rangle \&\& \langle c_{-} \rangle < \langle pc_{-} \rangle)$

   // The condition mean confidence$\langle c_{+} \rangle$is greater than the mean of the positive confidence$\langle pc_{+} \rangle$and mean confidence$\langle c_{-} \rangle$is lesser than the negative confidence$\langle pc_{-} \rangle$ also recommends labelling the given record as positive (prone to mortality).

3. $if \langle c_{+} \rangle \geq lb_{+} \&\& \langle c_{-} \rangle < lb_{-}$

   //The condition that denotes mean$\langle c_{+} \rangle$of the confidence discovered for positive label of given record r is greater than lower-bound$lb_{+}$of the positive label prediction scale and mean$\langle c_{-} \rangle$of the negative confidence of the n-gram feature values of given record r is lesser than the lower-bound$lb_{-}$of the negative label prediction scale

Under the conditions contradicting to above stated conditions, the given input record shall be labeled as negative (not prone to mortality scope).

V. Results & Discussion

Using demographic and pathological parameters of covid19 positive patients, an experimental investigation was done on a projected model of this contribution and other corresponding methods. Furthermore, the accuracy, specificity, f-measure, precision, and Mathew's correlation coefficient (MCC) have all been used to evaluate the performance of the projected model for this contribution.

The dataset used in the experiment comprises 1000 entries divided evenly between two labels: positive and negative. Each entry in the collection contains anonymized patient demographic and pathological information. There are 31 features in total, including the label. Among the 30 attributes, the optimal feature selection algorithm identified 17 as ideal.

$$Accuracy = \frac{TP + TN}{TP + TN + FP + FN} \tag{16}$$

$$Specificity = Selectivity = \frac{TN}{TN + FP} \tag{17}$$

$$Sensitivity = Recall = \frac{TP}{TP + FN} \tag{18}$$

$$Precision = \frac{TP}{TP + FP} \tag{19}$$

$$F - measure = \frac{2 * TP}{2 * TP + FP + FN} \tag{20}$$

$$MCC = \frac{TP * TN - FP * FN}{\sqrt{(TP + FP)(TP + FN)(TN + FP)(TN + FN)}} \tag{21}$$

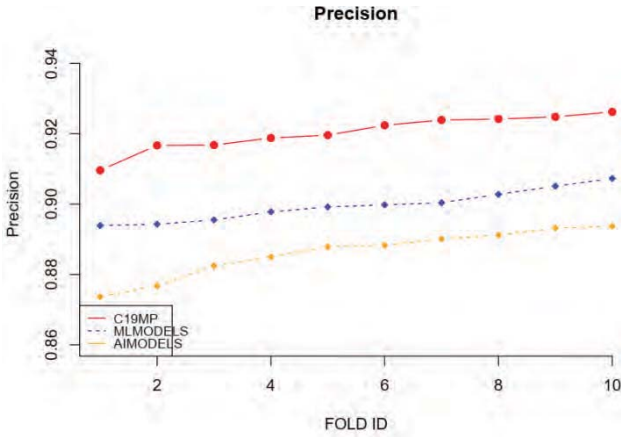

Figure 2. Precision obtained from tenfold cross validation

E-ISSN 2581 – 7957
P-ISSN 2277 – 3916

CVR Journal of Science and Technology, Volume 22, June 2022
DOI: 10.32377/cvrjst2204

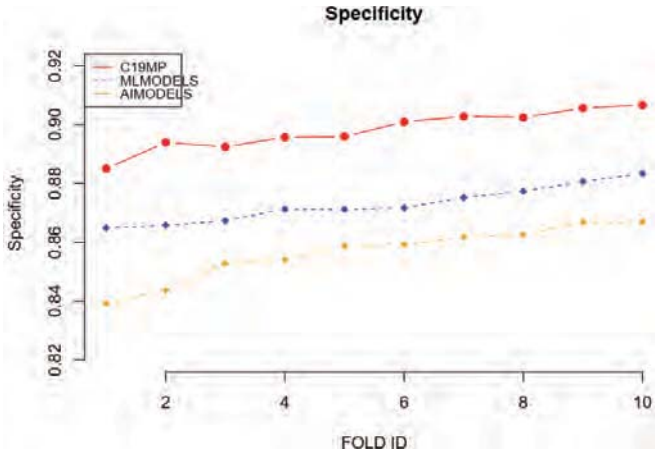

Figure 3. Specificity obtained from tenfold cross validation

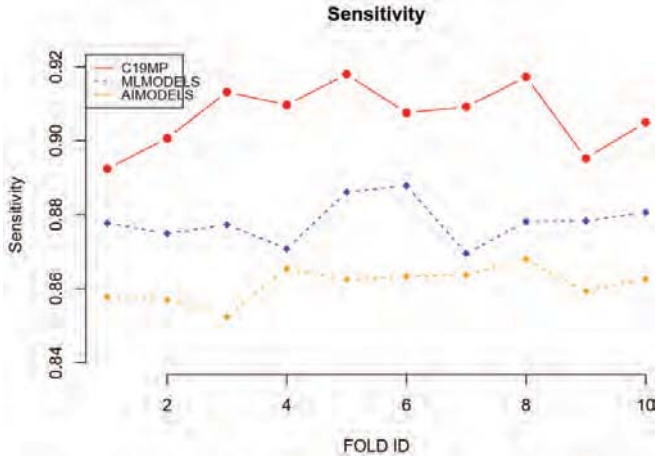

Figure 4. Sensitivity obtained from tenfold cross validation

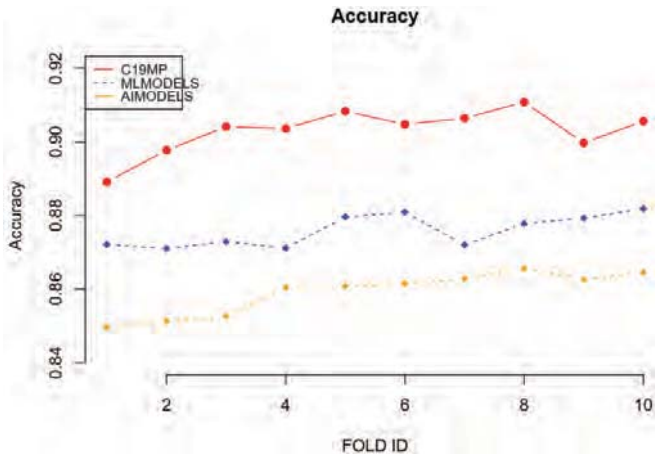

Figure 5. Accuracy obtained from tenfold cross validation

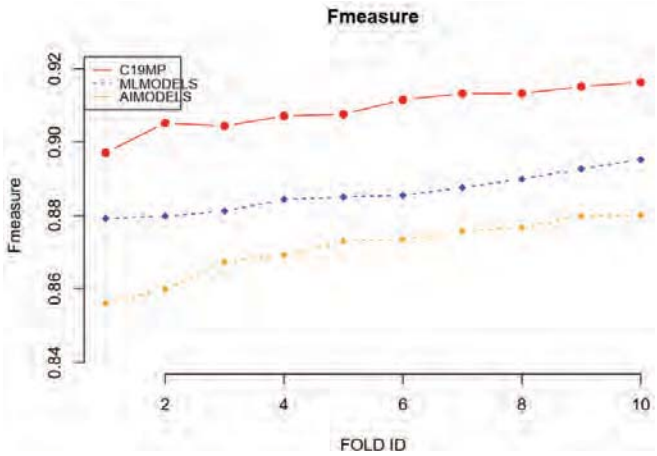

Figure 6. F-measure obtained from tenfold cross validation

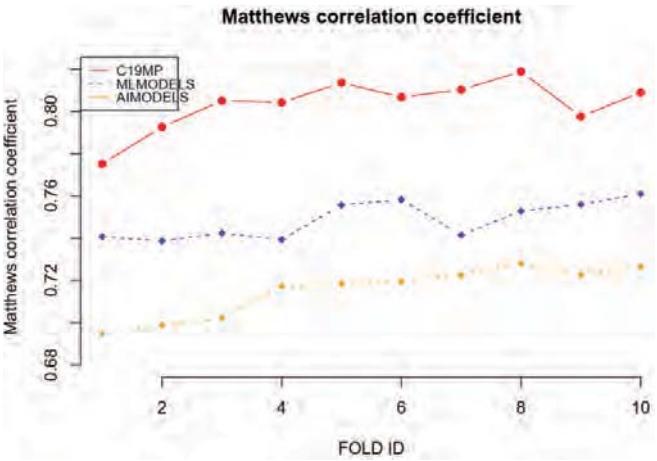

Figure 7. MCC obtained from tenfold cross validation

Figure 2 shows a graph depicting the comparison of Precision across 10 folds of cross validation observed from the suggested and contemporary models. The Precision for the ML-MODELS, AI-MODELS, and suggested C19MP, respectively, is 0.89961±0.004257, 0.88624±0.006422, and 0.9203±0.004796.

Figure 3 shows a graph depicting the comparison of Specificity over ten folds cross validation of C19MP, AI-MODELS, and ML-MODELS. In that order, the average specificity of the projected C19MP model, corresponding ML-MODELS, and AI-MODELS models is 0.89812±0.006397, 0.87287±0.005889 and 0.85659±0.008803.

In figure 4, the Sensitivity of the contribution C19MP, which indicates real positive rate, was compared to the sensitivity observed from counterpart models ML-MODELS and AI-MODELS. In that order, the average sensitivity of the ML-MODELS, AI-MODELS, and C19MP is 0.87811±0.005502,0.86118±0.004322, and 0.90675±0.008177.

Figure 5 shows a graph depicting the comparison of Accuracy observed from tenfold cross validation of C19MP, AI-MODELS, and ML-MODELS. The average accuracy of the contribution C19MP model, as well as its ML-MODELS and AI-MODELS counterparts are 0.903±0.005864, 0.87585±0.004175 and 0.85919±0.005471.

In figure 6, the F-measure obtained from tenfold cross validation of the proposed and contemporaneous models. ML-MODELS have an average F-measure of 0.88605±0.005087, while AI-MODELS have an average F-measure of 0.87115±0.007662. The contribution C19MP has an average F-measure of 0.90907±0.00561.

In figure 7, the Mathews Correlation Coefficient (MCC) observed from the contribution C19MP, counterpart models ML-MODELS and AI-MODELS were compared. The average MCC of the ML-MODELS and AI-MODELS obtained from tenfold cross validation is 0.74865±0.008393 and 0.71515±0.011289, respectively. This contribution's average MCC is 0.80326±0.011731.

VI. Conclusions

A novel statistical strategy for predicting the mortality scope of a patient who has tested positive for covid-19 has been proposed. Unlike current models, which solely examine demographic features, the proposed model reflects both demographic and pathology report features when performing supervised learning. A novel feature optimization metric based on the distribution diversity method t-test has been presented to reduce the process complexity of the learning phase. The tenfold cross validation performed on the recommended dataset demonstrated the relevance of C19MP's contribution. By comparing modern methodologies with the past, the suggested model C19MP has been scaled. Future research can incorporate cross-media features, which are a combination of demographic, picture, and signal formats, to increase the accuracy of the mortality scope prediction of COVID-19 positive patients.

References

[1] Sohrabi C, Alsafi Z, O'Neill N, Khan M, Kerwan A, Al-Jabir A, Losifidis C, Agha R. World health organization declares global emergency: a review of the 2019 novel coronavirus (COVID-19). Int J Surg 2020. doi:10.1016/j.ijsu.2020.02.034.

[2] Zhu N, Zhang D, Wang W, Li X, Yang B, Song J, et al. A novel coronavirus from patients with pneumonia in China, 2019. N Engl J Med 2020.

[3] Tan W., Zhao X., Ma X., Wang W., Niu P., Xu W., et al. A novel coronavirus genome identified in a cluster of pneumonia cases–Wuhan, China 2019– 2020China CDC Weekly2020; 2(4):61-62.

[4] Ivanov, D. Predicting the impacts of epidemic outbreaks on global supply chains: A simulation-based analysis on the coronavirus outbreak (COVID-19/SARS-CoV-2) case. Transp. Res. Part E Logist. Transp. Rev. 2020, 136, doi:10.1016/j.tre.2020.101922.

[5] Li, Yun, et al. "Individual-Level Fatality Prediction of COVID-19 Patients Using AI Methods." Frontiers in Public Health 8 (2020): 566.

[6] Ardakani AA, Kanafi AR, Acharya UR, Khadem N, Mohammadi A. Application of deep learning technique to manage COVID-19 in routine clinical practice using CT images: results of 10 convolutional neural networks. ComputBiol Med 2020;121:103795. 2020 https://doi.org/10.1016/j.compbiomed.2020.103795.

[7] Ozturk T, Talo M, Yildirim EA, BalogluUB, Yildirim O, Rajendra Acharya U. Automated detection of COVID-19 cases using deep neural networks with Xray images. ComputBiol Med 2020:103792. doi:10.1016/j.compbiomed.2020. 103792.

E-ISSN 2581 – 7957
P-ISSN 2277 – 3916

CVR Journal of Science and Technology, Volume 22, June 2022
DOI: 10.32377/cvrjst2206

Development of Smart Navigation System using GSM and RFID Technology in Indoor Surroundings

Gangepogu Sucharitha[1] and P. Srinivasa Rao[2]
[1]PG Scholar, CVR College of Engineering/ECE Department, Hyderabad, India.
Email: gangepogusucharitha@gmail.com
[2]Professor, CVR College of Engineering/ECE Department, Hyderabad, India.
Email: srinivasarao@cvr.ac.in

Abstract: **The primary goal of this work is to develop a smart navigation system using global system for mobile communication (GSM) and radio frequency identification (RFID) to assist the blind people to notice hindrances and navigate in the direction to target. Maximum of the blind individuals in the world use white sticks to travel from one place to another place. Due to their blindness, they are unable to be aware of their environment. The flexibility of the visually impaired persons is limited in number. The purpose of this development is to design a navigation system that will be able to direct a visually impaired person securely and comfortably in an indoor situation. This goal is to use an ultrasonic sensor to find out the range of hindrances. and a microcontroller to perform according to the receiving input. The arrangement includes a warning instruction through voice translation and a buzzer sound.**

It can be simply operated by a blind person by identification of hindrances by using the ultrasonic sensor device. Here GSM works as a mobile telephone which gives information about the emergency condition experienced by the blind. Project aims to provide accurate directions to the blind with help of RFID reader and tags. It is a flexible navigation system which gives information to a blind person with about the shortest routes and to authorize him to travel universally exclusive of accidents.

Index Terms: **GSM module, Rfid, microcontroller, ultrasonic sensor.**

I. Introduction

Contemporary world has come across different kinds of techniques. Visually weakened persons face limitations in independent flexibility and navigation. Flexibility means the prospect of generously moving, deprived of any additional person, at home-based and aware circumstances. Individuals with visual loss tackle huge restrictions in terms of suppleness.

Blindness is the visual impairment due to physiological or neurological aspects partly or completely. The foremost concept of this paper is to deliver an automated assistance to the blind to overcome visual hurdles and to provide efficient, simple, configurable automatic navigation system to them and to automate impaired perambulators. Ultrasonic sensor is the planned automatic assistance which senses the hindrances in his path by uninterruptedly conveying the ultrasonic signals. While a hindrance performs in its locality then the ultrasonic signals become echoed to the system directly. And formerly ultrasonic receiver observes these ultrasonic signals. This technique supports the microcontroller to get the information from ultrasonic signals. It alarms blind perambulators by voice communication. The benefit of our project is to provide voice-based message to a blind pedestrian to enable him through a busy street. Furthermore, this system is an auditory supervision system for the visually impaired walkers in which it converts ultrasonic waves to auditory signals.

India has a great deal of blind population. Out of 37 million, half of 15 million people who are blind are from India. Most of them are dependents and poor. This paper suggests a navigation system that comprises a white stick capable of sleuthing obstacles and delivering response. Blind people are efficient in hearing, and they hold strong sensibilities than ordinary people. Hence this innovative navigation system is designed for helping the blind people to circumnavigate everywhere securely and safely. There is no need to move the white stick around to perceive obstacles as they move an ordinary stick. The user can effortlessly walk with the help of white stick and continuously acquire information about hindrances around with the help of ultrasonic device. Good deal of research is being done on building a navigation system for the visually diminished people. Many researchers address this task in indoor as well as outdoor environment [1]. However, most of these methods have limitations and challenges (e.g., usability, coverage, accurateness, Interoperability) which are difficult to report with the present knowledge.

Electronic transportable devices are planned and developed to support the blind people to navigate securely and self-sufficiently. Various devices available for indicating directions are not affordable and tough to handle. The project described here offers a cost effective and dependable resolution to the above problem. The primary goal of our project is to propose a small and simple direction-finding device to support the blind people to get route instructions through voice message which varies on the real-time assistance deliver by the Rfid tags. It is used to find the location where the person is located on the earth planet.

Voice appreciation mechanism is to recognize and understand the system and translate audio signals into transcript or instructions.

The project uses controlled power supply to provide fixed 5V DC voltage. The different type of sensors is used in this project plan for different purposes. Ultrasonic sensor is used to perceive obstacles. An IR sensor is used to locate man-

Received on 22-09-2021, Revised on 19-03-2022, Accepted on 21-04-2022

CVR Journal of Science and Technology, Volume 22, June 2022
DOI: 10.32377/cvrjst2206

hole or a set of steps . A water level sensor is used to sense the water level. The output received from any of mentioned sensors gives information to Arduino nano controller. The controller activates voice sensor, which in turn activates the speaker and buzzer to alert the blind person.

The output will come out in the form of audio speech from speaker. RFID assists in finding the position of the blind person. GSM module acts as mobile telephone which can also be used for taking and receiving calls, transmitting, and getting SMS and MMS messages.

II. Lieterature Review

The author boyina anticipated that the project title was development of blind navigation system using GPS and voice recognition. This paper includes ARM7 micro controller, GPS receiver, Zigbee transceiver, LCD display, ultrasonic sensor, speech recognition HM 2007 IC, APR 9600 speech unit. Here the GPS is used to record the latitude, altitude, and longitude values continuously.

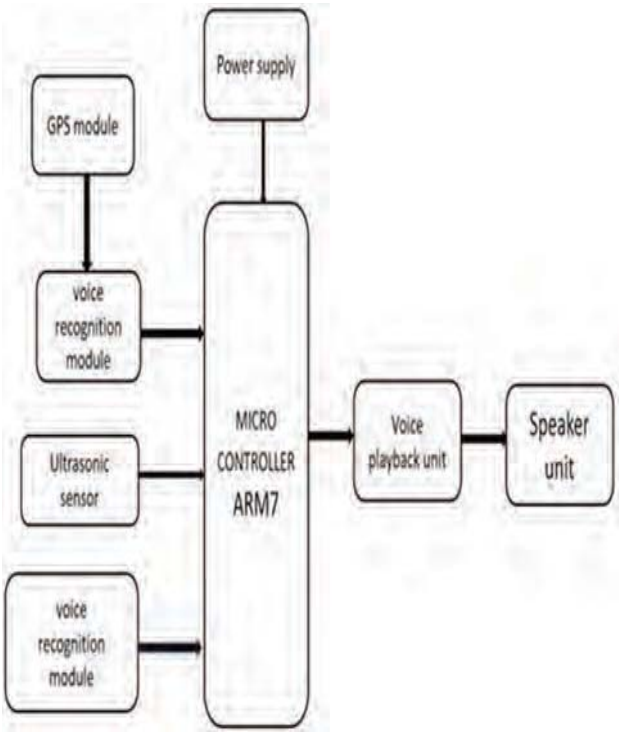

Figure 1. Block diagram of voice and GPS based blind navigation system

This GPS is interfaced with the ARM7 microcontroller after it will display the latitude, altitude, and longitude values on the liquid crystal display (LCD) unit. And the ARM microcontroller is programmed to the ultrasonic sensor. So that we can find out the distance between the obstacles and blind stick. Ultrasonic sensor sends ultrasonic waves continuously with the frequency of 39khz through the oscillator which is inbuilt itself in the sensor only. Then by using the signal conditioner module it will convert getting analog signal into the digital signal. And it is linked to ARM microcontroller. The sensor proposals a resonance pulse proportional to the distance [2].

The Author dhruv jain developed a project, Roshni. This is used for indoor navigation of the blind people. This project comprises of functional elements to determine the user's location in a large building, a complete internal map of that building and it can be used a mobile application. Through pressing buttons on a mobile phone, orientation, instructions concerning location, and direction-finding can be found from this project plan via voice instructions.

The navigation system using RFID technology was proposed by the author Punit Dharani. This delivers a technological explanation for the blind people to journey through public places by using RFID tags and reader.

The author Parth Mehta presented a novel interior navigation system for blind people. This paper demonstrates a structure in which uses magnetic compass and the IR sensor. which is a handheld device to determine the location and orientation of person in a fast and robust by using a voice with GPS module is inserted inside environment.

Koley developed a project with the title, A voice based outdoor Navigation system for blind. This system is made up of GPS module, voice module and ultrasonic sensor for hindrance detection. The GPS gives the current location of blind person, and it provides directions to reach respective remote destination. Nevertheless, this structure delivers text/audio direction, but it doesn't able to detect obstacles and doesn't give warning instructions.

In this proposed navigation system primarily concentrates on two things:

(i). Observing the direct surroundings of blind persons against obstacles and

(ii). Notice about the hindrances with the help of buzzer, vibration, and voice output system.

This navigation system is efficient and a cutting-edge instrument for both indoor and outdoor environment.

The Author projected on Ultrasonic sensor-based navigation System. In this system, the project mission is to perform functions given below:

Recognition of hindrances by using the ultrasonic sensors, Operation to get vibrational alert and voice output system by using vibrator motor and APR9600 voice module. The arrangement comprises mainly three ultrasonic sensors HC- SR04. These sensors will be perceiving the barriers in the pathway. Total project is developed by using ATMEGA16 microcontroller. This controller detects distance with the help of ultrasonic sensors by using delicate motor circuitry to generate vibrational alert. APR9600 voice module is interfaced to get an audio speech output. Therefore, the person will identify the direction of the hindrance and observe its distance. Aim of the system is to build a transportable, simple and ease, cost effective stick. This will help blind people to travel in unskilled location.

The project system guides or support the blind. This is done with the help of voice or audio commands. Research is on to design a blind navigation system with different technologies. Most of technologies have some limitations. These limitations include accurateness, interoperability, attention and usability. These are difficult to overcome with existing technologies.

E-ISSN 2581 – 7957
P-ISSN 2277 – 3916

DOI: 10.32377/cvrjst2206

III. Proposed System

The proposed block diagram of blind navigation system is shown in Figure 2.

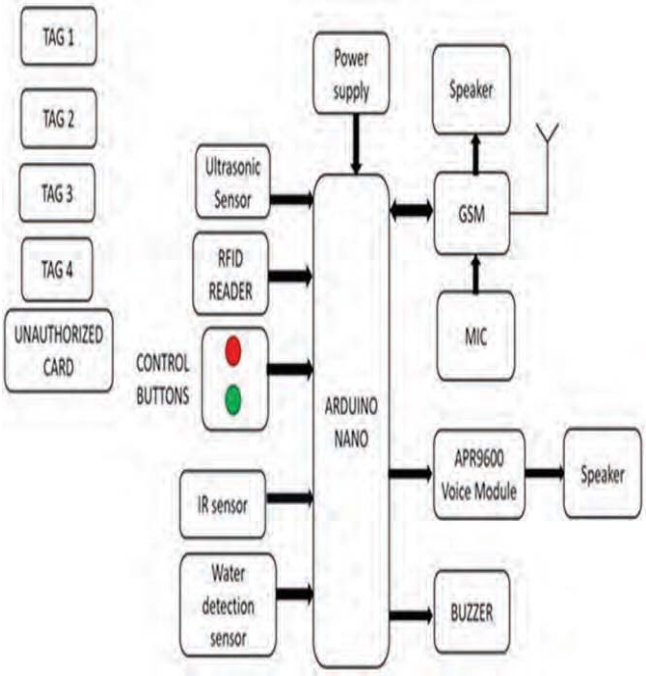

Figure 2. Block diagram of blind navigation system using GSM and RFID.

In the proposed project, it comprises many devices for the operation of the system these devices include Arduino nano microcontroller, infrared (IR) sensor, ultrasonic sensor, water level sensor, APR9600 voice module, speaker, power supply, RFID reader module, RFID tags and GSM module etc. Comprehensive explanation with circuit details of various blocks is presented as follows:

A. Arduino nano

The fig 3 shows Arduino nano microcontroller. It is a compatible, small, flexible, and bread board-friendly based on the ATmega328 microcontroller. It operates at low voltage 5v. This board use mini-USB cable for connection with a computer, to run code.

Figure 3. Arduino nano

B. Ultrasonic sensor

This sensor sends ultrasonic waves into the air then it notices and then reflect waves from object. Ultrasonic signals are resonances which can't be heard and commonly the frequencies above 20 khz.

Figure 4. Ultrasonic sensor

To observe the existence of an object, ultrasonic signals are replicated on objects. It is used to sense hindrances then it alerts the blind person through speaker with an audio device.

C. IR sensor

IR sensor stands for infrared sensor. Here the work of IR sensor having a LED and a photodiode. If there is any of objects like stairs, pit holes in the road path, then this sensor alerts blind person through an audio device.

D. GSM module

The Fig. 4 demonstrates GSM module. The full form of GSM is Global System for Mobilecommunication. It is acts as a mobile telephone which is used to send messages to any person connected to GSM unit when the blind person is in danger. Whenever the blind person is in trouble or in danger, he needs to press emergency switch then the SMS goes to family members or nearby police through GSM.

Figure 5. GSM module

E. APR9600 Speech IC unit

The Fig. 5 represents APR9600 speech IC. This IC unit sends true solo-chip voice recording, non-volatile storage, and repeat capability for 40 to 60 seconds. Now this is used to replicate the speech signals in the ordinary procedure.

E-ISSN 2581 – 7957
P-ISSN 2277 – 3916
CVR Journal of Science and Technology, Volume 22, June 2022
DOI: 10.32377/cvrjst2206

Figure 6. APR voice module

F. RFID

RFID is stands for radio frequency identification. RFID is like wireless communication technologies such as Bluetooth, Long range radio (LoRa), radio transmitters etc. Systems are made up of two apparatuses, tags, and readers. Tags comprise data, and readers sense the tag and process the data from the tags. The tags should be in range. It has a small amount of memory that stores a unique tag identifier (TID), which is constant, not changeable. The little bit of information left on tag can be read-only or writeable, depending on how the tag was designed.

It is a new technique to give the location of person. RFID reader is a module which reads the ID data stored in RFID tags. This ID data is different for each tag which cannot be copied.

IV. METHODOLOGY

A. Flowchart

Flowchart of the indoor blind navigation system is presented in the following figures 7&8.

B. Working

In this project primarily used elements are:

i). GSM module
ii). RFID reader and tags
iii). Ultrasonic sensor.

- Here the GSM module is acts as a mobile phone such as making and receiving phone calls, transmitting, and receiving messages.
- With the help of GSM and headset the blind person and customer care can communicate through each other.
- RFID is used to give the exact location of blind person through reader which is placed on the roadside. A blind person is available in voice mode through APR9600 voice module.
- The several sensors are interfaced with the Arduino nano microcontroller. They are:
  i). Ultrasonic sensor
  ii). IR sensor
  iii). Water level sensor.
- Ultrasonic sensor is used for finding obstacles such as rock, tree, any barriers in their footpath. And also, it will measure distance between obstacle and blind person.
- IR (infrared) sensor used for detecting the manholes or staircases (set of steps). And it will give output in voice feedback through speaker.
- Water level sensor is used for detecting water level or any mud or rainwater is there in their way.
- With this sensor can avoid accidents.
- Inputs are given to micro controller it reads it and gives output in the form of voice/audio through speaker.
- If the customer care receives message as an ID1, then the blind person is guided in the right direction through tags.
- If the person is in emergency or in trouble, he can press a secondary switch to alert the police or the family.
- If the blind takes a wrong direction, there will be a voice alert through the speaker unit.

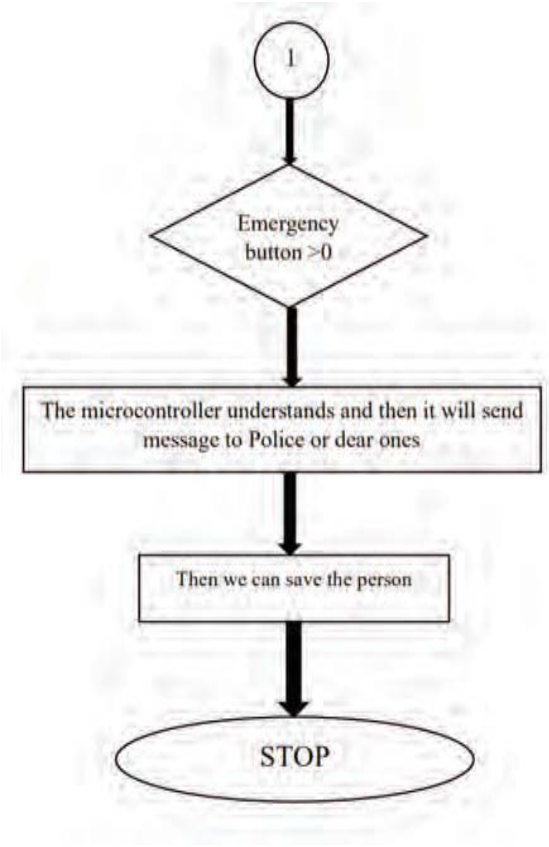

Figure 8. Flowchart (Part 2)

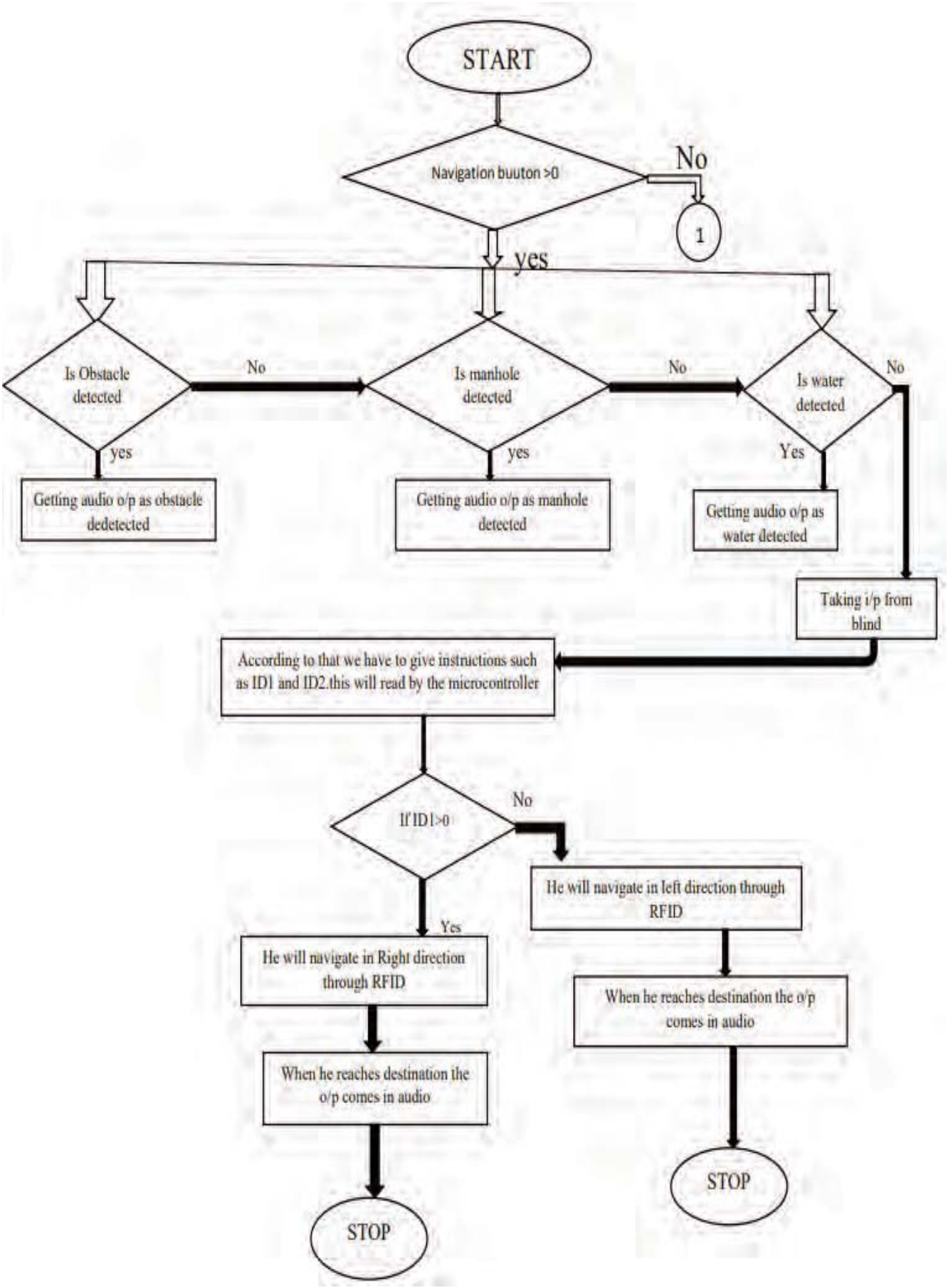

Figure 7. Flowchart (Part 1)

CVR Journal of Science and Technology, Volume 22, June 2022
DOI: 10.32377/cvrjst2206

V. Results And Discussions

The system designed by us can assist the blind as they can go anywhere with the assistance of IR, ultrasonic sensors and with RFID knowledge without the help of a human support.

Ultrasonic sensor with output 0 – 10V, threshold voltage is 5V. The sensor has 300 kHz sound frequency. Measurement range from 2 cm to 400 cm and threshold range is 10cm. Accuracy is ±0.15%.

IR sensor wavelength range from 2 to 14 µm. It will detect the signals in the range of 20cms. Detection range of RFID reader is 10-15cms.

This arrangement provides improved results in performance and increased the efficacy of visually weakened explorers at interior environments. It is cost effective. This structure is mobile. The executed project outcome is presented in the following image.

Figure. 9. Final output of project

VI. Conclusions

Our country India is having considerable amount of blind population. In the past the blind were dependent only on sticks or on guide dogs. The devices available to guide them were very expensive. We tried to develop a device that is cheaper and easy to be operate. We introduced this system which gives advanced resolutions to substitute the traditional techniques for directing the blind. The arrangement planned comprises of GSM, Rfid reader, several sensors, voice module. All these elements are interfaced to the Arduino nano controller. The blind person gets the navigation directions through Rfid reader and tags also navigate blind people using voice module.

This navigation system is available formally and is economically feasible. We can use this project as a device for the blind in different places such as commercial parks, hospital zones, municipal residences, government parks, small businesses and in university campuses.

VII. Future Scope

This work can be prolonged by including a GPS module. By using GPS module, we can connect this module to Arduino micro controller to get exact location of a blind person. When I add GPS module to the designed project it becomes more efficient, and it can be used for both indoor as well as outdoor navigation. Whenever person is in trouble or in emergency, it can track him within minutes. By using this we may get good effective results in terms of accuracy.

The RFID reader module can be kept inside the stick of the arrangement. And we can replace the Controlled power supply with a recharge-battery. The blind stick might be operated without a power source.

References

[1] Intelligent Navigation System for Blind People with Real Time Tracking – IJERT

[2] Dr Boyina.S.Rao "Blind Assistant Navigation System" in IEEE Transactions, March 2011.

[3] Ulrich and J. Borenstein, "The GuideCane — Applying Mobile Robot Technologies to Assist the Visually Impaired" in IEEE Transactions on Systems, Man, and Cybernetics, —Part A: Systems and Humans, Vol. 31, No. 2, March 2001, pp. 131-136.

[4] Harsha Gawari Somnath Koley, Ravi Mishra," Voice Operated Outdoor Navigation System For Visually Impaired Persons", International Journal of Engineering Trends and Technology- Volume3Issue2- 2012.

[5] A. M. Kassim, H. I. Jaafar, M. A. Azam, N. Abas and T. Yasuno, "Design and development of navigation system by using RFID technology," 2013 IEEE 3rd International Conference on System Engineering and Technology, 2013, pp. 258-262, doi: 10.1109/ICSEngT.2013.6650181.

[6] Abdel IlahNour Alshbatat Chaudhry M., Kamran M., Afzal S., "Speaking monuments — design and implementation of an RFID based blind friendly environment." Electrical Engineering, 2008. ICEE 2008.

[7] Punwilai, J. Noji, T. Kitamura, "The design of a voice navigation system for the blind in Negative Feelings Environment", Communications and Information Technology, ISCIT 2009.

[8] Kaminski, L. Kowalik, R. Lubniewski, Z. Stepnowski, "VOICE MAPS — portable, dedicated GIS for supporting the street navigation and self- dependent movement of the blind", Information Technology (ICIT), 2010.

[9] Marsh, A. May, M. Saarelainen, "Pharos: coupling GSM and GPS TALK technologies to provide orientation, navigation and location-based services for the blind", Information Technology Applications in Biomedicine, 2000.

[10] Chaitali K. LakdeB. B. Blasch, W. R. Wiener, and R. L. Welsh, Foundations of Orientation and Mobility, 2nd ed. New York: AFB Press, 1997.

[11] Smart walking stick - an electronic approach to assist visually disabled persons Mohammad Hazzaz Mahmud,Rana Saha, Sayemul Islam.

[12] Mohd Helmy Abd Wahab, Amirul A. Talib, Herdawatie A. Kadir, Ayob Johari, A. Noraziah, Roslina M. Sidek, Ariffi. "Smart cane: assistive cane for visually impaired people", IJCSI, Vol.8 Issue 4, July 2011.

[13] M. Bousbia-Salah, A. Larbi, and M. Bedda, "An approach for the measurement of distance travelled by blind and visually impaired people," in Proc. 10th IEEE International Conference on Electronics, Circuits and Systems, Sharjah, United Arab Emirates, pp. 1312-1315, 2003.

[14] Hashino, S.; Ghurchian, R.; A blind guidance system for street crossings based on ultrasonic sensors. Information and Automation (ICIA), 2010 IEEE International Conference on June 2010.
[15] Singh J, Bhardwaj P. 'Design and Development of Secure Navigation System for Visually Impaired People' International Journal of Computer Science Technology, 2013,5(4), pp.15.

E-ISSN 2581 – 7957
P-ISSN 2277 – 3916

CVR Journal of Science and Technology, Volume 22, June 2022
DOI: 10.32377/cvrjst2207

Video Inpainting using self-adaptive GMM with Improved Inpainting Technique

B. Janardhana Rao[1], K. Revathi[2], G. Harish Babu[3]
[1]Assoc. Professor, CVR College of Engineering/ECE Department, Hyderabad, India
Email: janarhdan.bitra@gmail.com
[2]Asst. Professor, CVR College of Engineering/IT Department, Hyderabad, India
Email: revathi.kandula@gmail.com
[3]Asst. Professor, CVR College of Engineering/ECE Department, Hyderabad, India
Email: harish.sidhu12@gmail.com

***Abstract*: Nowadays photography and videography have become part of life. There are many challenging tasks in videography, one of these is video inpainting. Repairing the damaged videos or removing and filling undesired objects in videos is defined as video inpainting. In this paper, an object-splitting video inpainting is proposed. The background subtraction is implemented by self-adaptive Gaussian Mixture Model (SAG). The moving foreground and static background are inpainted by using enhanced inpainting technique with improved patch priority calculation. The structure consistency patch matching is proposed to search for the similar patch in the source region to fill the target region. The video inpainting results are obtained for the own video. The proposed inpainting technique is implemented for state of art videos utilized in other related works. The experimental results show that the proposed technique attained impressible inpainted videos compared to related works.**

***Index Terms*: Video inpainting; SAG, background subtraction; patch priority; Structure consistency**

I. Introduction

Video inpainting plays a vital role in video processing applications such as video restoration, video stabilization, films post-processing. Video inpainting is used to reconstruct the damaged parts of old videos and to remove the unwanted objects in the video without identifying by human eye visually. Image inpainting is the process of repairing damaged images and restoring the images by removing undesired parts in the image. The traditional image inpainting techniques are Partial Differential Equation (PDE) based [1] and texture synthesis techniques [2, 3]. In PDE based inpainting techniques, the gradient vector is calculated around the unknown region and local structures adjacent to the lines perpendicular to gradient vectors are diffused to the target region. This is completely pixel-based method and failed to fill large target regions. These are well suited for images with more structure information. In texture synthesis algorithms, the texture patches in the source region diffuse to target region and neglects the structured content. Both these methods are combined and formed a new algorithm, exemplar based inpainting [4, 5]. These algorithms preserve both structure and texture information in the inpainted region.

The video inpainting is achieved with image inpainting by dividing the video into sequence of images called frames. Due to this, the temporal coherence between the frames is missing [6]. Bertalmio was proposed video inpainting using Partial Differential Equations (PDE) based image inpainting [7] by preserving the temporal coherence between the frames. But in this, the texture information is not retrieved properly and failed to fill the large portions of target region. Patwardhan [8] consider the motion vector along with image inpainting. This is achieved by taking the preprocessing in video frames by separating the moving foreground from the static background which is called background subtraction. This method has given reasonably good results but not works for videos having nearby moving objects and moving background. Chang [9] proposed the method to remove moving objects in both static and moving background. T. K. Shih [10] given an algorithm which suited for complex camera motions. N. C. tang proposed a new technique for patch searching and patch alignment to get the temporal coherence of the video. C. W. Lin [11] proposed method applicable for videos having dynamic background with a fixed camera or still background with moving camera. In these mosaics of frames are constructed from background-based camera motion. A. Koochari [12], separated the moving objects from the background and constructed the mosaics of moving objects, these are inpainted by using large patches.

The video inpainting problem is achieved in three ways [13]. (i) Patch matching method (ii) Object-background splitting (iii) Structure and texture classification.

In patch matching method, the patches searching to fill the hole in target region is achieved in the spatiotemporal domain. In [14, 15] the color components, spatial and temporal vectors are compared to attain spatiotemporal volume matching. In object-background splitting, background subtraction is used to separate static background from moving foreground. The inpainting will apply individually to both moving objects and static background [8, 16, 17] by maintaining the temporal coherence between the frames. Gaussian Mixture Model

Received on 16-03-2022, Revised on 02-04-2022, Accepted on 23-05-2022.

CVR Journal of Science and Technology, Volume 22, June 2022
DOI: 10.32377/cvrjst2207

(GMM) [18, 19] is used for background subtraction. In structure and texture classification, the video frames are divided into structure and structure regions, and these are inpainted using different inpainting techniques by maintaining region priorities. Recently, the novel video inpainting technique is implemented with hybridization of cuckoo search algorithm and multi verse optimization [21] for optimizing the patch matching and Recurrent Neural Network (RNN) for categorizing the patch as smooth or structured. This method produced the optimal video inpainting results compared to available methods. Another video inpainting technique [22] proposed by using enhanced priority computation method and optimal patch selected for inpainting the target region with Grey Wolf Optimization (GWO). This method outperformed the existing techniques of video inpainting in terms of metrics PSNR, SSIM and Edge similarity.

In this paper, an object-background splitting method is implemented. The GMM based background subtraction has its limitations to separate moving foreground and background. The GMM method failed to handle the sudden changes in illumination and irregular background motion. Due to its parametric modelling, it is time-consuming and complex hence didn't produce proper results in real time applications [20]. Proposed a new background subtraction technique, self-adaptive GMM (SAG) has adaptive learning rate and withstand for sudden illumination changes and adaptively select the number of Gaussians to model the pixels in the image. An improved inpainting technique with enhanced priority function is used to identify the priorities of the patches on the boundary of the target region. Structure consistent patch matching method is utilized to search for the best matching patch in the source region.

This paper is organized as, section II explains the proposed video inpainting algorithm, and in section III experimental results are discussed. Section IV is conclusion.

II. PROPOSED VIDEO INPAINTING ALGORITHM

The proposed architecture for video inpainting is shown in figure 1. The input video applied to the background subtraction or foreground detection method which divides the static background and foreground in each frame. In the moving foreground, the object which is removed is identified by tracking using a Kalman filtering technique. This produces the past, present and future steps of the moving object. This is target identification. After this, the target identified is removed by manual method, freehand tool in MATLAB. Then the enhanced inpainting technique is applied to background and foreground frames separately. Finally, all the frames are combined to form the in painted video.

A. Background Subtraction Method

To overcome the disadvantages in GMM, in this paper proposed an advanced background subtraction technique called self-adaptive GMM (SAG). This model uses a dynamic adaptive learning rate to take advantage of fast illumination changes. The flowchart for self-adaptive GMM is shown in figure 2 [20]. This flowchart contains two modules, the background learning module, and a foreground extraction module.

In the background learning module, spatiotemporal filter is used to remove the noise and smoothen the image this increases the robustness of the model. The global illumination changing factor (G) is obtained by using MofQ from the smoothened image. The global illumination changing factor is obtained by equation (1).

$$g = median_{i \epsilon I} \left(\frac{i_{p,i}}{i_{r,i}} \right) \quad (1)$$

The G value calculated for all pixels of i in the image I between the present image i_p and reference image i_r. The background is learned using SAG, the learning factor (g) calculated between the learned background and the present image, and it keeps on track the global illumination changes. The counter value (c_k) will increase if the parameters of Gaussian model changes. Then the Gaussian is reassigned and set the counter to 1.

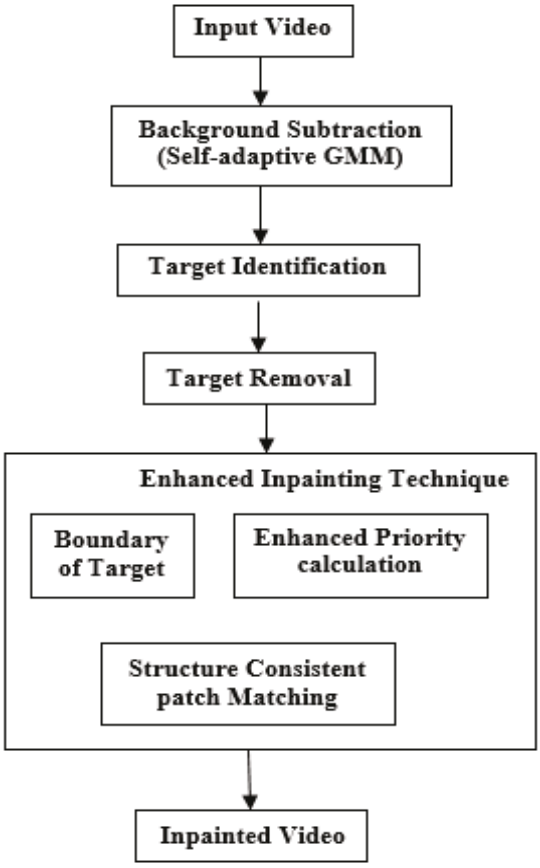

Figure 1. The architecture of proposed video inpainting.

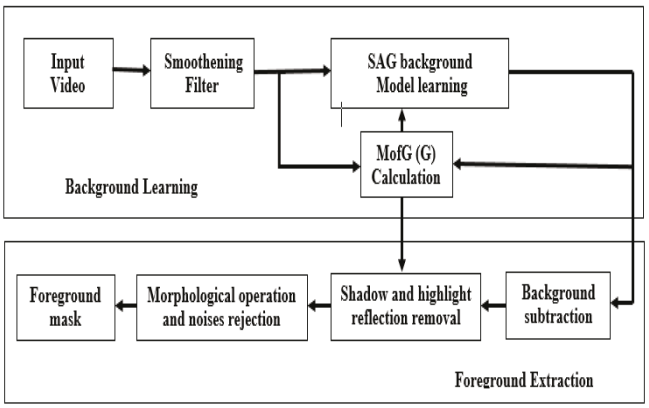

Figure 2. Flowchart of self-adaptive GMM.

CVR Journal of Science and Technology, Volume 22, June 2022
DOI: 10.32377/cvrjst2207

When the parameters of Gaussian changed, the new learning rate β_k is calculating from equation (2).

$$\omega_{k,t} = (1-\alpha)\omega_{k,t-1} + \alpha(M_{k,t} + C_T) \quad (2)$$

$$\beta_{k,t} = \alpha(l + c_k)/c_k \quad (3)$$

$$\mu_{k,t} = \mu_{k,t-1} + M_{k,t}(\beta_{k,t}/\omega_{k,t})\delta_{k,t} \quad (4)$$

$$\sigma^2_{k,t} = \sigma^2_{k,t-1} + M_{k,t}(\beta_{k,t}/\omega_{k,t})(\delta^T_{k,t}\delta_{k,t} - \delta^T_{k,t-1}) \quad (5)$$

$$c_k = c_k + 1 \quad (6)$$

where l is a constant, $\alpha = 1/T$ is a constant defined to limit the effects of old data and exponentially decreased envelope. The components that are not utilized in the data are represented by negative prior weight C_T. $M_{k,t}$ is taken as 1 for matched components and 0 for other components.

The foreground extraction in self-adaptive GMM is for dividing the foreground mask from the background. It identifies the shadows and highlights spatial, spectral, and temporal features in combination of three domains and with individual features. The distortion effect of highlight and shadow are divided into brightness and chromaticity distortion. The distortion of brightness (B_i) and chromaticity (C_i) are taken as

$$B_i = \frac{g\left(I_{R_i}\mu_{R_i}/\sigma^2_{R_i} + I_{G_i}\mu_{G_i}/\sigma^2_{G_i} + I_{B_i}\mu_{B_i}/\sigma^2_{B_i}\right)}{\left(\mu_{R_i}/\sigma_{R_i}\right)^2 + \left(\mu_{G_i}/\sigma_{G_i}\right)^2 + \left(\mu_{B_i}/\sigma_{B_i}\right)^2} \quad (7)$$

$$C_i = \sqrt{\left((gI_{R_i} - B_i\mu_{R_i})/\sigma_{R_i}\right)^2 + \left((gI_{G_i} - B_i\mu_{G_i})/\sigma_{G_i}\right)^2 + \left((gI_{B_i} - B_i\mu_{B_i})/\sigma_{B_i}\right)^2} \quad (8)$$

where, $I_i = \left[I_{R_i}, I_{G_i}, I_{B_i}\right]^T$ is the intensity of the i[th] pixel in RGB space, mean $E_i = \left[\mu_{R_i}, \mu_{G_i}, \mu_{B_i}\right]^T$ and standard deviation $\sigma_i = \left[\sigma_{R_i}, \sigma_{G_i}, \sigma_{B_i}\right]^T$

From the above information the foreground pixels are classified with the following condition,

$$\begin{cases} shadow; & if\ C_i < \gamma_1\ and\ \gamma_2 < B_i < 1 \\ highlight; & if\ C_i < \gamma_1\ and\ B_i < \gamma_3 \end{cases} \quad (9)$$

where, $\gamma_1, \gamma_2, \gamma_3$ are threshold values.

After separating the background from the moving foreground, enhanced inpainting technique is applied to inpaint the frames with enhanced priority calculation and patch matching method, which is discussed in the subsequent sections.

B. Enhanced Priority Calculation

In the existing exemplar-based inpainting method [5], the inpainting results are slightly defected due to the unusual calculation of confidence term. The confidence term reduced to a low value for less number of iterations, this is called dropping effect [23]. Due to this the priorities of the patches on the boundary of the target region also decreases drastically. This gives improper result of inpainting. To avoid this an enhanced priority calculation method is introduced with a modified confidence term. In the existing exemplar-based inpainting method, the priority of the patches on the target region is calculated by product of confidence term and data term. The modified priority function [23] is taken as equation (10).

$$prority(p) = x * R_c(p) + y * D(p) \quad (10)$$

where x and y are multiplication factors of confidence term and data term respectively, $x \geq 0$, $y \leq 1$,and $x + y = 1$. The modified data term to avoid dropping effect is shown in equation (11).

$$R_c(p) = (1-\beta)\, C(p) + \beta \quad (11)$$

where β is called the regularization term ranging the values over 0.1 to 0.7.

The confidence term $C(p)$ from existing exemplar inpainting method is given by expression (12).

$$C(P) = \frac{\sum_{t\in\psi_p\cap\Phi} C(t)}{|\psi_p|} \quad (12)$$

where, t denotes the coordinates of pixel p on both source region Φ and patch on the boundary of the target regionψ_p. The data term, $D(p)$ is defined by the equation (13).

$$D(p) = \frac{|\nabla I_P^{\perp}.n_p|}{255} \quad (13)$$

where n_p is the unit vector orthogonal to the boundary of the target region at pixel p and $\nabla I_P^{\perp}$ is the isophote vector. Isophote is a line used to combine similar pixel points.

C. Structure Consistent patch Matching Method

After obtaining the highest priority patch to fill on the boundary of the target region, it is to be filled with the similar matching patch in the source region. The similar matching patch is searched by equation (14).

$$\psi_{q^1} = arg\ \min_{\psi_q\in\Phi} d\left(\psi_p, \psi_{q^1}\right) \quad (14)$$

where, $\psi_{q^1}$is the best matching patch in the source region.

In the traditional exemplar-based inpainting method, Sum of Squared Difference (SSD) is used for finding $d\left(\psi_p, \psi_{q^1}\right)$. The SSD method calculates only the difference between the intensity values and avoids the structural variations between the two patches. Considering the structure consistency between the source region and target region along with content obtained in SSD calculation improves the quality of the in painted image.

The structure consistency is achieved by utilizing the spatial distribution through standard deviation [25] of patch differences as given by equation (15).

$$d\left(\psi_p, \psi_{q^1}\right) = d_{SSD}\left(\psi_p, \psi_{q^1}\right) * \left\{\left[d_{STD}(\psi_p - \psi_{q^1})\right]^{\alpha} + 1\right\} \quad (15)$$

with

$$d_{STD}\left(\psi_p - \psi_{q^1}\right) = \sqrt{\frac{1}{n}\sum\nolimits_t \left[\psi_p(t)N_p(t) - \psi_{q^1}(t)N_{q^1}(t) - (\overline{\psi_p} - \overline{\psi_{q^1}})\right]^2} \quad (16)$$

where $n = \sum_t N_p(t)$; α is a constant adjust, the weight of d_{STD} over the final quality. $\overline{\psi_p}$ and $\overline{\psi_{q^1}}$ are mean values. The value of α set to 0.8. From this, it is observed that if d_{STD} is

CVR Journal of Science and Technology, Volume 22, June 2022
DOI: 10.32377/cvrjst2207

small then the two patches are similar in structure. The structure variations are consistent in both patches if d_{STD} is zero. Under different illumination conditions if the patches have a same structure, then d_{STD} becomes zero, this gives errors in results. To avoid this 1 is added in the equation. In this structure consistent patch matching method due to standard deviation, attain best matching patches considering structure distributions also.

III. Experimental Results

The experimental results are implemented in MATLAB. In enhanced inpainting, the priority of the patches on the boundary of the target is calculated taking the regularization term $\beta = 0.7$, the multiplication factors of confidence term and data terms are $x = 0.8$ and $y = 0.2$ respectively [24]. These values result the best inpainting. The inpainting is applied to my own video. Some of these inpainted frame results are shown in figure 3.

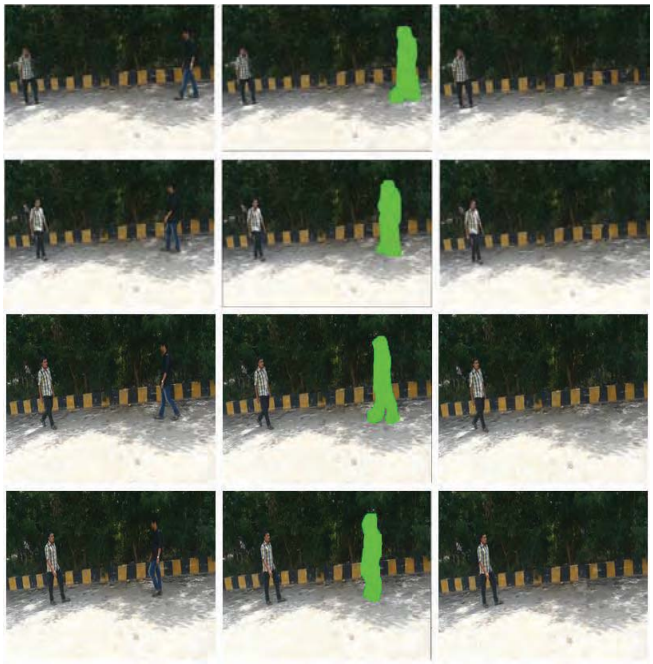

(a) (b) (c)

Figure 3. Own video inpainted Results: a) Input frame b) Object to be removed c) Inpainted frame.

The proposed inpainting is compared to the state of art existing techniques taken their input videos [26]. Applied to the input of table tennis and produces the results as shown in figure 4.

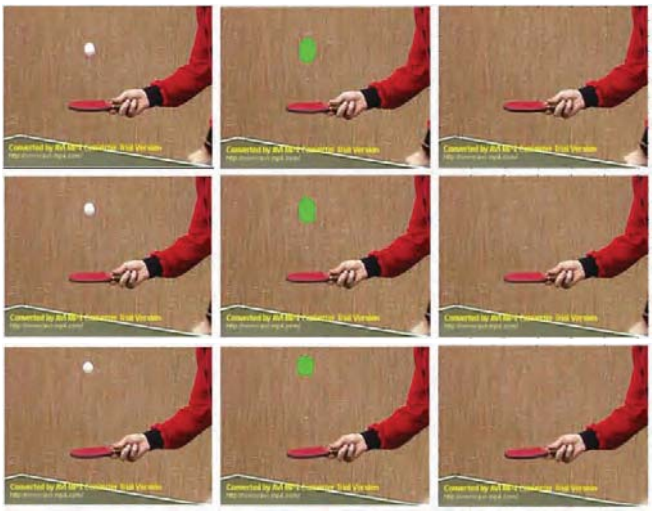

(a) (b) (c)

Figure 4. Table tennis inpainted results: a) Input frame b) Object to be removed c) Inpainted frame

The proposed technique is also compared, [27] for videos of walking man and throwing ball. The inpainted results for some frames are shown in figure 5 and 6.

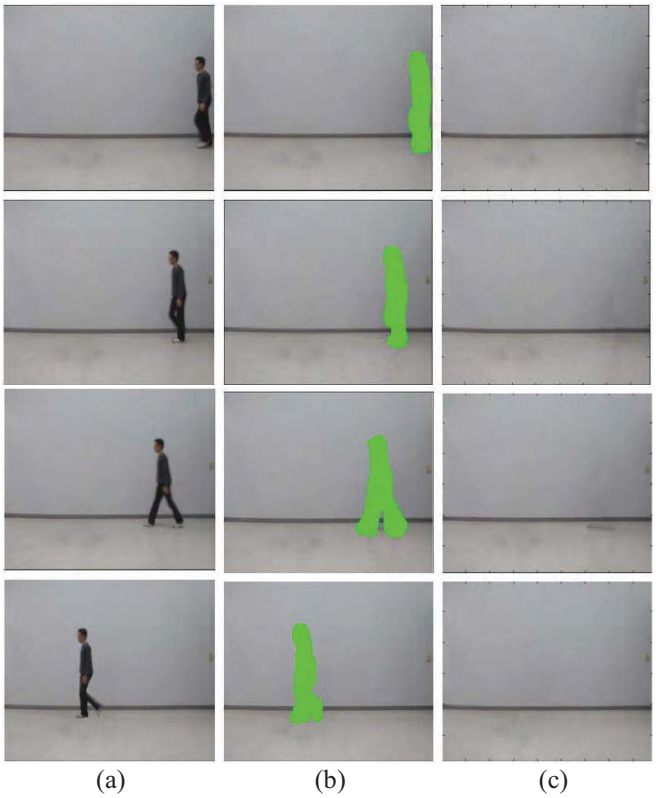

(a) (b) (c)

Figure 5. Walking man inpainted results: a) Input frame b) Object to be removed c) Inpainted frame

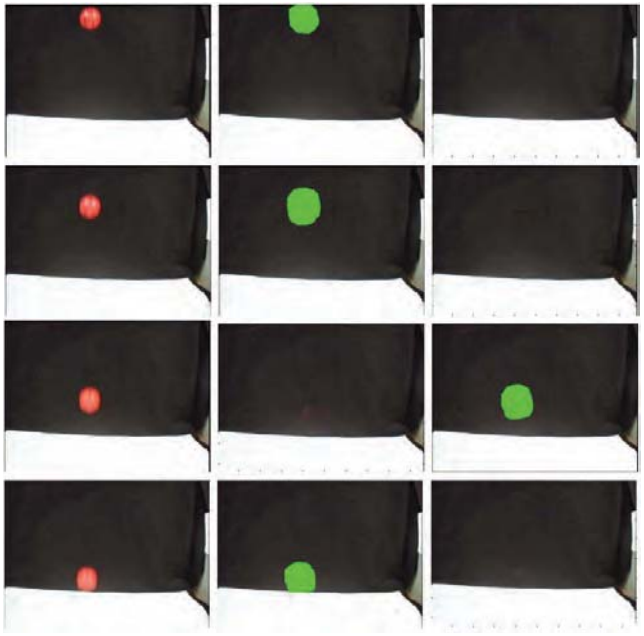

(a) (b) (c)

Figure 6. Throwing ball inpainted Results: a) Input frame b) Object to be removed c) Inpainted frame

IV. CONCLUSIONS

This paper proposed a new video inpainting technique using self-adaptive GMM (SAG) background subtraction method. The background subtraction method separated the moving foreground and static background any sudden illumination changes in the video. The separated static background and moving foreground are inpainted with improved priority calculation technique and structure consistent patch matching method. The patch priorities on the boundary of the target region have been calculated with multiplication factors of confidence term and data term as $x = 0.8$ and $y = 0.2$ for regularization term $\beta = 0.7$. The experiment results are shown that the proposed method produced the results quite better compared to existing techniques.

REFERENCES

[1] M. Bertalmio, G. Sapiro, V. Caselles, C. Bellester, Image inpainting, in: Proc. ACM SIGGRAPH, New Orleans, Lousiana, 2000, pp. 417-424.

[2] A .A . Efros , T.K. Leung , Texture synthesis by non-parametric sampling, in: IEEE Conf. on Computer Vision, vol. 2, Sept. 1999, pp. 1033–1038 .

[3] L. Liang , C. Liu , Y.Q. Xu , B. Guo , H.Y. Shum , Real-time texture synthesis by patch-based sampling, ACM Trans. Graph. 20 (3) (Jul. 2001) 127–150 .

[4] A. Criminisi , P. Perez , K. Toyama , Object removal by exemplar-based inpainting, in: IEEE Conf. on Computer Vision and Pattern Recognition, vol. 2, Jun. 2003, pp. 721–728 .

[5] A. Criminisi , P. Perez , K. Toyama , Region filling and object removal by exemplar-based image inpainting, IEEE Trans. Image Process. 13 (9) (Sept. 2004) 1200–1212 .

[6] M. V. Venkatesh, S. S. Cheung, J. Zhao, "Efficient Object Based Video Inpainting", *Journal of Pattern Recognition Letters*, vol. 30, no. 2, pp. 168-179, 2009.

[7] M. Bertalmio, A. L. Bertozzi, G. Sapiro, "Navier-Strokes, Fluid Dynamics, and Image and Video Inpainting", In Proc. IEEE Computer Society Conf. Computer Vision and Pattern Recognition, vol. 1, pp. 355- 362, 2001.

[8] K. A. Patwardhan, G. Sapiro, M. Bertalmio, "Video Inpainting under Constrained Camera Motion", In Proc. IEEE Trans. Image Processing, vol. 16, no. 2, pp. 545-553, 2007.

[9] R. C. Chang, N. C. Tang, C. C. Chao, "Application of Inpainting Technology to Video Restoration", In Proc. 1st IEEE Int. Conf. Ubi-Media Computating, pp. 359-364, 2008.

[10] T. K. Shih, N. C. Tang, J. N. Hwang, "Exemplar-Based Video Inpainting Without Ghost Shadow Artifacts by Maintaining Temporal Continuity", In Proc. IEEE Trans. Circuits and Systems for Video, vol. 13, no. 3, pp. 347-360, 2009.

[11] C. W. Lin, N. C. Cheng, "Video Background Inpainting Using Dynamic Texture Synthesis", In Proc. IEEE Int. Symposium on Circuits and Systems, pp. 1559-1562, 2010.

[12] A. Koochari, M. Soryani, "Exemplar-Based Video Inpainting with Large Patches", Journal of Zhejiang University, vol. 11, no. 4, pp. 270-277, 2010.

[13] Kuo, Tien-Ying, Po-Chyi Su, and Yun-Ping Kuan. "SIFT-guided multi-resolution video inpainting with innovative scheduling mechanism and irregular patch matching." *Information Sciences* 373 (2016): 95-109.

[14] Y. Wexler , E. Shechtman , M. Irani , Space-time video completion, in: IEEE Conf. on Computer Vision and Pattern Recognition, vol. 1, Jul. 2004, pp. 120–127 .

[15] Y. Wexler , E. Shechtman , M. Irani , Space-time completion of video, IEEE Trans. Pattern Anal. Mach. Intell. 29 (3) (Mar. 2007) 463–476 .

[16] J. Jia , Y.W. Tai , T.P. Wu , C.K. Tang , Video repairing under variable illumination using cyclic motions, IEEE Trans. Pattern Anal. Mach. Intell. 28 (5) (May 2006) 832–839 .

[17] J. Jia , T.P. Wu , Y.W. Tai , C.K. Tang , Video repairing: inference of foreground and background under severe occlusion, in: IEEE Conf. on Computer Vision and Pattern Recognition, vol. 1, Jul. 2004, pp. 364–371.

[18] W.H. Press , S.A. Teukolsky , W.T. Vetterling , B.P. Flannery ,in: Numerical Recipes: The Art of Scientific Computing, Third Edition, Cambridge University Press, 2007, pp. 842–848 .

[19] C.H. Yeh , C.Y. Lin , K. Muchtar , L.W. Kang ,Real-time background modeling based on a multi-level texture description, Inf. Sci. 269 (June 2014) 106–127 .

[20] Goyal, Kalpana, and Jyoti Singhai. "Review of background subtraction methods using Gaussian mixture model for video surveillance systems." *Artificial Intelligence Review* 50.2 (2018): 241-259.

[21] B Janardhana Rao, Y Chakrapani, S Srinivas Kumar, Hybridized Cuckoo Search with Multi-Verse Optimization-Based Patch Matching and Deep Learning Concept for Enhancing Video Inpainting, *The Computer Journal*, 2021; bxab067, https://doi.org/10.1093/comjnl/bxab067.

[22] B Janardhana Rao, Y Chakrapani, S Srinivas Kumar, An Enhanced Video Inpainting Technique with Grey Wolf Optimization for Object Removal Application, Journal of Mobile Multimedia (2022), Vol. 18, Issue 3, pp. 561-582.

[23] J. Wang, K. Lu, D. Pan, N He, B. Bao, Robust object removal with an exemplar-based image inpainting approach, Neurocomputing 123 (2014) 150-155.

[24] Janardhana Rao, B., Y. Chakrapani, and S. Srinivas Kumar. "Image Inpainting Method with Improved Patch Priority and Patch Selection." *IETE Journal of Education* 59.1 (2018): 26-34.

[25] H. Wang et al., Exemplar-based image inpainting using structure consistent patch matching, Neurocomputing (2017), http://dx.doi.org/10.1016/j.neucom.2016.08.149.

[26] Hung, Kuo-Lung, and Shih-Che Lai. "Exemplar-based video inpainting approach using temporal relationship of consecutive frames." *Awareness Science and Technology (iCAST), 2017 IEEE 8th International Conference on*. IEEE, 2017.

[27] Dusane, Meenal R., and G. S. Sable. "Video Inpainting for Moving Object Removal Using Patch Sparsity." *International journal of computer engineering & technology* (2013): 2277-9655.

E-ISSN 2581 – 7957
P-ISSN 2277 – 3916

CVR Journal of Science and Technology, Volume 22, June 2022
DOI: 10.32377/cvrjst2208

Grid Connected PV System using Incremental Conductance MPPT Technique

G. Sree Lakshmi[1] and G. Divya[2]
[1]Professor, CVR College of Engineering/EEE Department., Hyderabad, India
Email: sreelakshmisampath@gmail.com
[2]Asst. Professor, CVR College of Engineering/EEE Department, Hyderabad, India
Email: divya.gongidi@cvr.ac.in

Abstract: **Solar system is an Eco-friendly system which helps in production of abundant energy with PV arrays. PV System comes under the category of distributed energy. This system helps the existing system to meet the power demand at some point of time. In this paper PV Standalone System is used and is interfaced with Power Grid which is a three-phase system. Observation on Pertub and Observe (P&O) MPPT technique and Incremental Conductance MPPT technique has been done to know the best MPPT technique for tracking maximum power from the PV System. In both the techniques boost converter is used to provide Duty Cycle for switching pulses generation. Inverter is used with 2-level configuration for DC to AC Power Conversion along with pulse width modulation technique. For synchronizing PV to Grid, Phase Lock Loop (PLL) technique is implemented. Active and Reactive Power is Supplied to the load depending on demand by the Control Circuit through PV System. P&O method and Incremental Conductance method is simulated in MATLAB and results of both the methods are used for analysis.**

Index Terms: **P&O, MPPT, PLL, PV**

I. Introduction

The Renewable energy like Solar, Wind, Tidal, Biomass has the capability to generate the power for supplying it to local areas. The combination of above systems is also taking the advantage to compensate the continuous availability of the renewable resources throughout the day. Specially the Solar Power is ever green resource among renewable resources which can be obtained almost consistently thorough out the day. Even the PV System maintenance [1] is also very less compared to other systems. If PV System can be connected to Grid when maximum power is generated and with minimizing phase unbalance, reactive power, power quality issues [9], then the power system becomes more efficient and dependency on the other non-renewable resources also reduces.

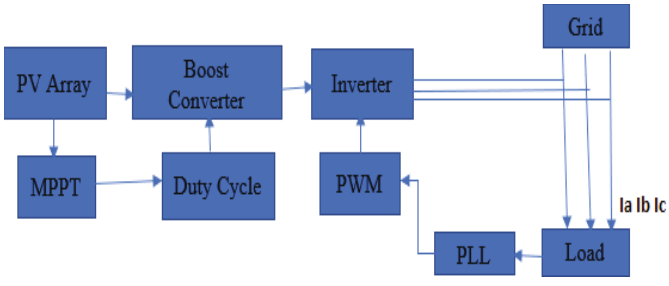

Figure 1. Block diagram of Grid Connected PV system

II. Types of MPPT Techniques

A. Perturb and Observe

Perturb & Observe algorithm is mostly used in the PV maximum power tracking and to adjust Duty Cycle. P&O is a continuous process of observation and perturbation till maximum power point is obtained. In this algorithm comparison of the power and voltages at a time (t) with the sample taken at a time (t-1) and estimation is made to understand the time to approach MPPT. A small voltage perturbation changes the power of the solar panel if the power alteration is positive, voltage perturbation is continued in the same track. But if power is negative, it indicates that maximum time is needed to reach MPP and the perturbation is decreased to reach the MPP. So whole PV System is checked. Fig 2. Shows the flow chart of P&O technique.

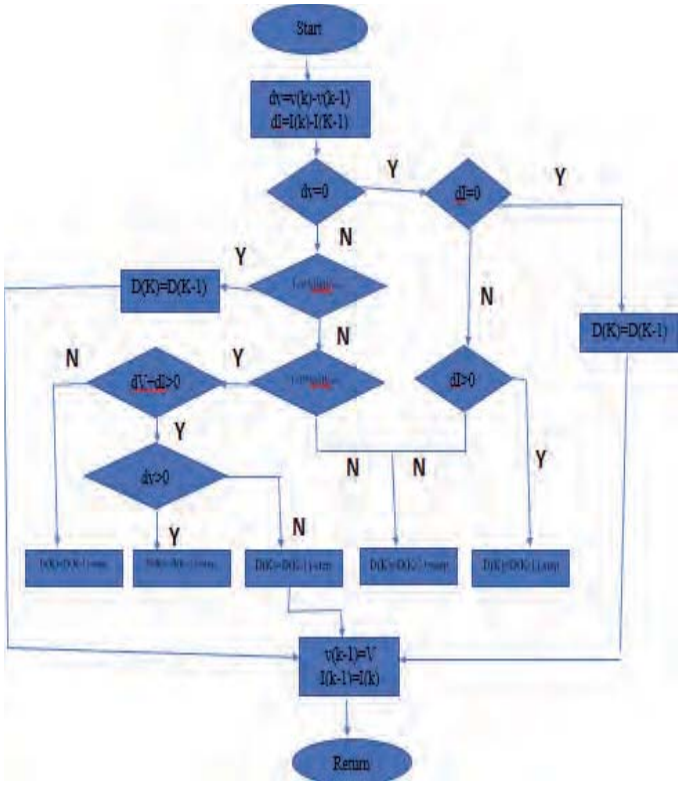

Figure 2. Flow chart of Perturb and Observe MPPT Technique

B. Incremental Conductance MPPT

The incremental conductance algorithm detects the slope of the P–V curve, and the MPP is tracked by searching the

Received on 03-02-2022, Revised on 20-04-2022, Accepted on 15-05-2022.

CVR Journal of Science and Technology, Volume 22, June 2022
DOI: 10.32377/cvrjst2208

peak of the P–V curve. This algorithm uses the instantaneous conductance I/V and the incremental conductance dI/dV for MPPT [2]. Fig 3. Shows the flow chart of IC MPPT.

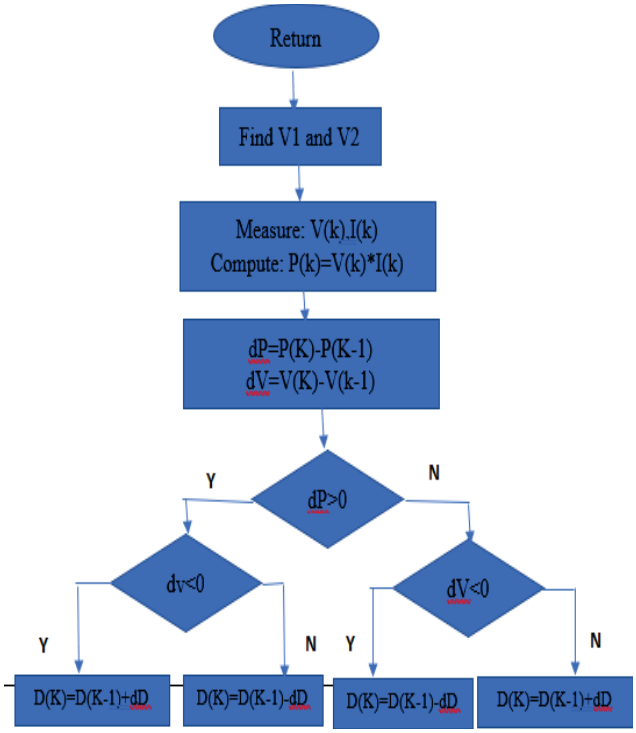

Figure 3. Flow chart of Incremental Conductance MPPT Technique

In incremental conductance method the terminal voltage control is done depending on the maximum voltage which in turn depends on the incremental conductance of PV. For the change in output conductance if dI/dV is negative then the voltage is decreased and if dI/dV is positive then voltage is increased to track the maximum power at every instant. Power=Voltage*Current. By differentiating power with respect to voltage.

$$\frac{dP}{dV} = \frac{V * I}{dV} \quad (1)$$

$$\frac{dP}{dV} = I + V\left(\frac{dI}{dV}\right) \quad (2)$$

For maximum power point is reached the slope. Thus, the condition would be.

For maximum power point is reached the slope.

$$I + V\left(\frac{dI}{dV}\right) = 0 \quad (3)$$

C. Fractional Open Circuit Voltage

This method will consider a linear dependency on array open circuit voltage which will give maximum power at various irradiation and temperatures. Compared to all other MPPT methods, it is the simple one. The drawback of this method is for sampling array voltage the PV array will get disconnected with load at regular intervals. Because of this, there are power losses. If sampling period is too long the losses also increases. After tracking MPP there will not be any change in MPP even if there is change in irradiation between two sampling periods [10].

D. Fractional Short Current

There is a linear relation always with short circuit current when MPP is considered. It is expressed as

$$I_{mpp} \sim KI_{sc} \quad (4)$$

here K is the constant of proportionality. The K value will be different for different PV modules 0.72 to 0.92 variation will be there. This is just an assumption so actual MPP will not be tracked. Efficiency is around 90% and even tracking speed is also fast. It is the cheapest and easy method to implement as it requires only one current sensor, only periodic measurement of I_{sc} is enough to track MPP [11].

III. Basic PV System and MPPT

A. PV System

It has solar cells which are connected in series and parallel to get the required voltage and currents [8][2]. The basic terminology and the constants used in the PV system are given in the equations which are represented from equation 5 to equation 12. Fig 4. Shows the single diode circuit used for the analysis.

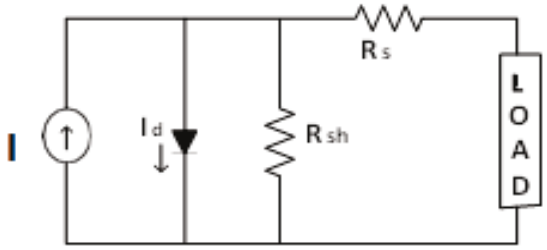

Figure 4. Single diode Circuit

I_{ph} = Photo Current (5)
I_d = Module saturation cells number (6)
N_p, N_s = Series and Parallel cell number (7)
T= Temperature in (Kelvin) (8)
K= Boltzmen Constant($1.381*10^{-23}$) (9)
A= Ideality Factor (10)
Q= charge of e^-($1.602*10^{-19}$) (11)
R_s= Series Resistance in Ω (12)

B. MPPT

Maximum Power Point: In Perturb and Observe (P &O) MPPT Power and Voltage values are used for perturbation. Perturb and Observe Control algorithm is designed in such a way that change in voltage measures the maximum power in forward direction, if power decreases for voltage change or back direction for maximum power. Fig 5. Shows the PV curve for MPPT.

dp /dv>0 then +ve slope which is left side of curve
dp /dv<0 then -ve slope which is right side of curve
dp /dv=0 then maximum power point MPP

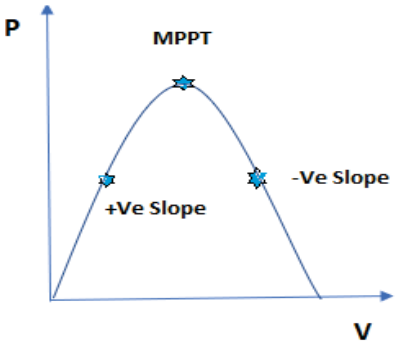

Figure 5. P-V Curve for MPPT

IV. Boost Converter

As DC voltage is needed to step up the AC voltage, Boost Converter is

Case 1: ON state of Switch, current flows will be through Inductor (L), Switch.

Case 2: OFF state of Switch, current flows will be through Inductor, Diode, Capacitor, Load. Here energy storage of Inductor flows through the circuit in mode2 operation. The circuit diagram of Boost Converter shown in Fig. 6.

Output of Boost Converter Voltage is

$$\frac{dI}{dV} = I \quad (13)$$

$$\frac{dP}{dV} = 0 \quad (14)$$

$$V_{out} = V_{in}/1 - D \quad (15)$$

From above equation the Duty cycle is extracted and is given to IGBT switch which is used through PWM generator. Fig 6. shows the boost converter used in the circuit.

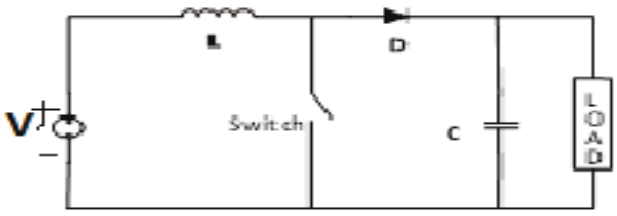

Figure 6. Boost Converter

V. PWM Inverter and Control Circuit

First stage is done by Boosting the DC voltage whereas this is second stage where 2- level inverter is used to convert 3 phase AC supply. Two Level Voltage Source Inverter (VSI) will convert fixed DC voltage to 3-Phase AC voltage. These types of inverters are employed in machines and converter control. The VSI inverter consists of three legs which has two IGBT switches on each leg and have DC Source and Load. Fig 7. Shows the Voltage Source Inverter.

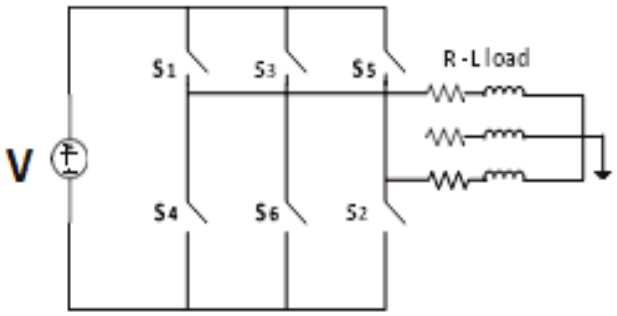

Figure 7. Voltage Source Inverter (VSI)

A. Pulse Width Modulation (PWM)

In this paper, for switching purpose the pulses of IGBT are driven by PulseWidth Modulation (PWM) Technique. In PWM Triangular Carrier Wave (fc) is compared with Sinusoidal Reference wave (fr) of desired frequency. Depending on the condition between fr & fc provides switching instant pulses to IGBT. VSI is equipped with DC link of capacitance bank which is used for grid synchronization purpose.

B. Controller Circuit

Interfacing the voltage source inverter with the grid, phase angle information is needed. For getting accurate results of phase angle, Phase Lock Loop (PLL) technique has been used. This PLL helps in load sharing between standalone PV and grid. It estimates the phase and frequency values [5]. Interfacing phase angle parameter is necessary for active and reactive power flow control [6]. The power flow is controlled by Current Control Scheme. Fig 8. Shows the PLL controller circuit.

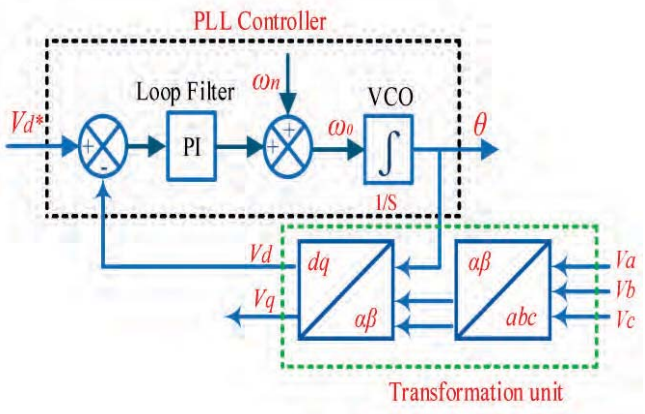

Figure 8. Phase Lock Loop

In PLL, Three-phase AC voltage (Va Vb Vc) are transformed to 2-phase stationary frame (Vds Vqs) using equation and again two-phase voltage are transformed to rotating frame of d, q axis (Vdr,Vqr). To transform from rotating frame to synchronous frame PI Controller and Integrator are used to estimate angular frequency and phase angle. The below equations are used for calculations.

E-ISSN 2581 – 7957
P-ISSN 2277 – 3916

CVR Journal of Science and Technology, Volume 22, June 2022
DOI: 10.32377/cvrjst2208

$$\begin{bmatrix} V_\alpha \\ V_\beta \\ V_0 \end{bmatrix} = \frac{2}{3}\begin{bmatrix} 1 & \frac{-1}{2} & \frac{1}{2} \\ 0 & \frac{\sqrt{3}}{2} & \frac{-\sqrt{3}}{2} \\ \frac{1}{\sqrt{2}} & \frac{1}{\sqrt{2}} & \frac{1}{\sqrt{2}} \end{bmatrix}\begin{bmatrix} V_a \\ V_b \\ V_c \end{bmatrix} \quad (16)$$

$$\begin{bmatrix} V_{dr} \\ V_{qr} \end{bmatrix} = \begin{bmatrix} Cos\theta & Sin\theta \\ -Sin\theta & Cos\theta \end{bmatrix}\begin{bmatrix} V_\alpha \\ V_\beta \\ V_0 \end{bmatrix} \quad (17)$$

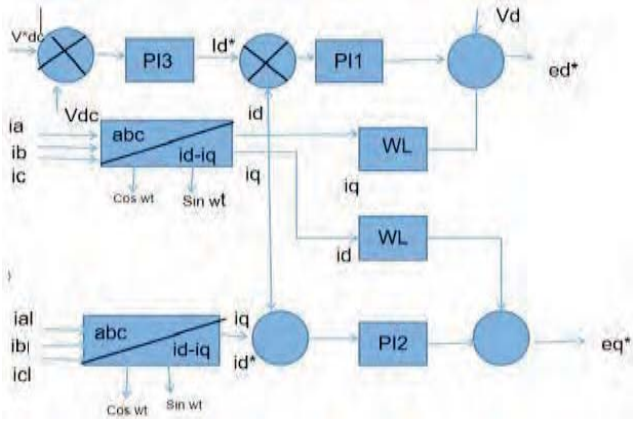

Figure 9. Three-phase to two-phase Transformation block diagram

VI. Standalone PV System Connected to the Grid

Standalone PV System consists of PV array, MPPT, Boost converter, Inverter, PWM, 3-phase load. Voltage (V) and currents (I) are grasped from PV array using MPPT for adjusting the duty cycle to provide gate pulses to IGBT switch of Boost converter. This process helps in boosting up the DC voltage. DC voltage obtained is supplied to dc link (capacitor). DC link acts as a source to the inverter (2- level) converting DC to AC voltages. For conversion process in inverter switching pulses to IGBT switches are given by Pulse Width Modulation (PWM) technique. Three phase voltage and currents from inverter are provided to 3-phase loads.

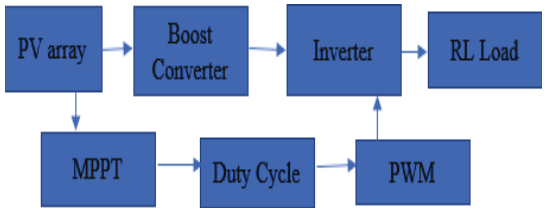

Figure 10. Standalone PV

The Standalone PV system simulation study is done using data provided to the system for the block diagram.

A. Values used in PV System

Array Irradiance—1000
Array Temperature—$25^0{}_C$
Maximum Power (Pump)-- 83.2W
Maximum Im Voltage (Vmp)-- 10.3V
Maximum Current (Imp)-- 8.07A

B. PV System Connected to Grid

Grid connected; standalone system has grid which is connectedto load as shown in Fig. 11 For interfacing both PLL technique is used to maintain at same phase angle and frequency at inverter and grid side [7]. According to the load standalone PV the grid PV supplies necessary voltage and current.

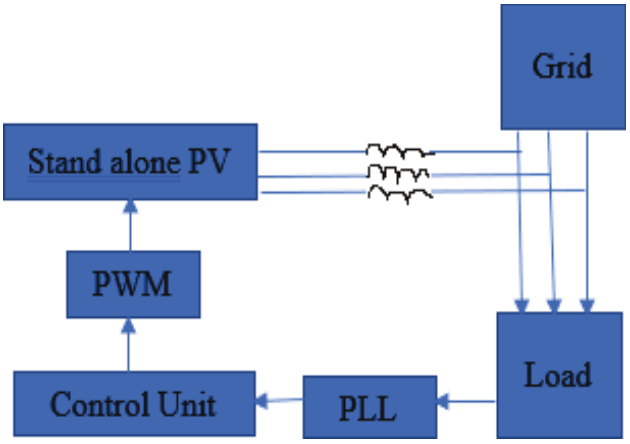

Figure 11. Grid side PV

For sharing the load among PV system and grid a dq current control scheme is used. In this control reference signals are estimated according to the load demand md and mq are estimated voltages given by equation value of voltage of 440 volts V_{dr} is calculated to 359 volts whereas V_{qr} is calculated to zero by using the above phase lock loop equations. To find the angular frequency of V_{qr}, it is calculated by $2\pi f$ where f is 50 hz which gives ω value as 314 rad/sec as shown in Fig 12. Unit vector of phase values are estimated by harmonic oscillator.

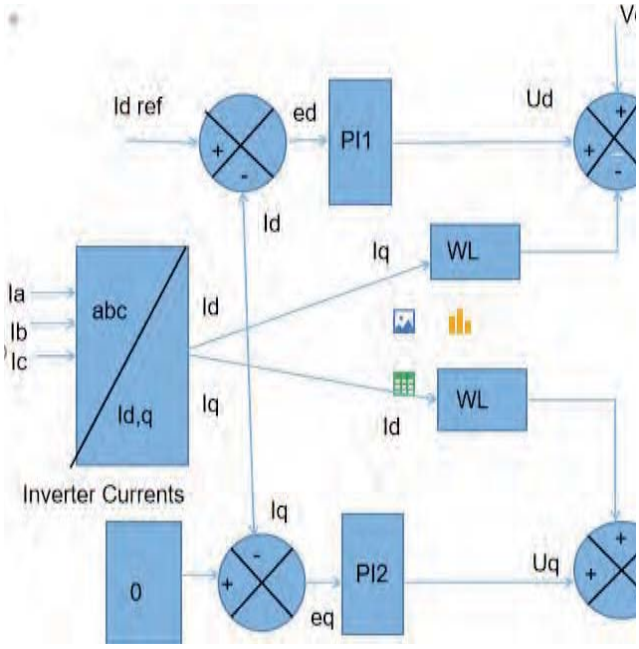

Figure 12. dq Current Control diagram

The phase lock voltages is shown in the Fig. 13 is in phase according to the simulation results obtained when d-q current control scheme is applied.

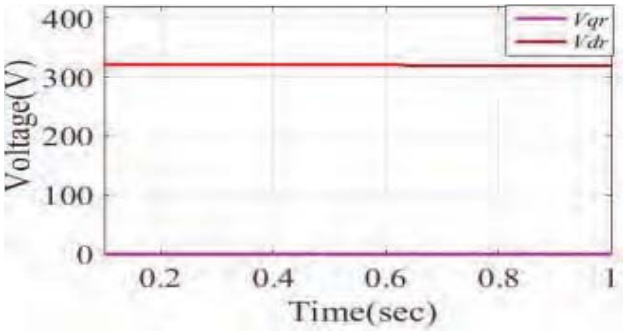

Figure 13. Phase Lock, voltages

TABLE I.
SIMULATION PARAMETERS

Parameters	Values
Grid Voltage	400V
Grid Frequency	50Hz
Load	R=4.6Ω, L=0.0146H
Inverter Capacitor	60e-6
PLL PI Control	P=50, I=100
Control PI	P=0.1, I=0.2

VII. SIMULATION RESULTS OF P&O TECHNIQUE

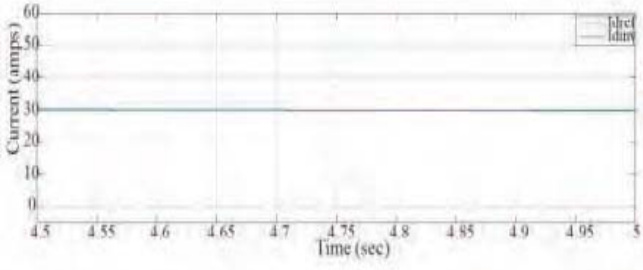

Figure 14. Idinv and Idref Currents

Fig 14. Shows the dq- currents of the circuit which are in inphase with eath other using dq control circuit used in the analysis.

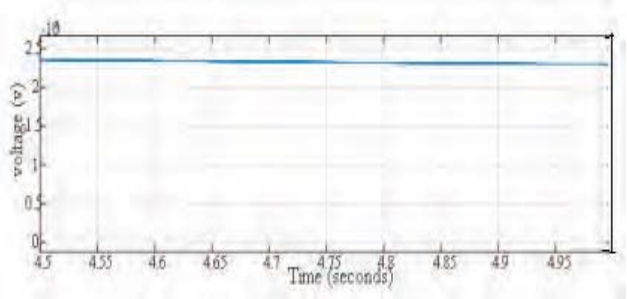

Figure 15. DC voltage (VDC)

Output of DC voltage waveform in the Fig 15. from the results obtained shows that the voltage is constant without any variations which is near to the ideal case.

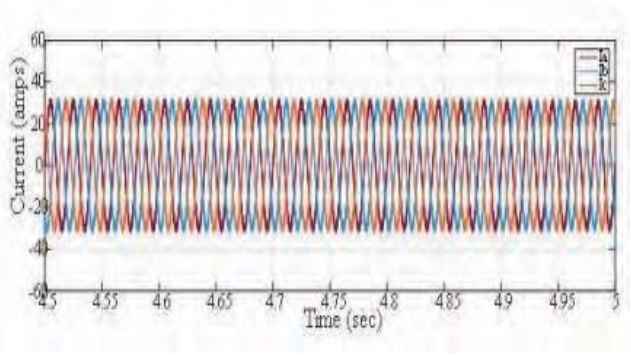

Figure 16. Inverter Current

Simulation results which is shown in Fig 16. is the current output of three phase Inverter. The output obtained from P&O technique is obtained as expected.

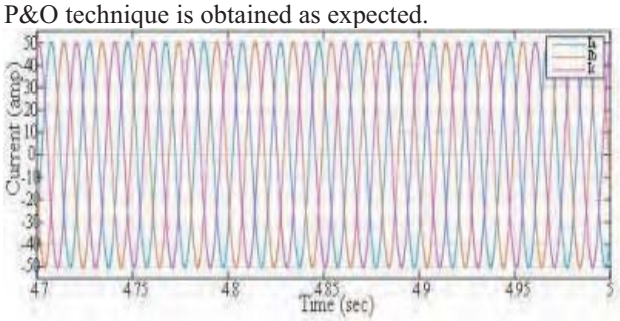

Figure 17. Load Current

The load currents of P&O results are obtained from simulation is obtained for all the three phases as expected in Fig 17.

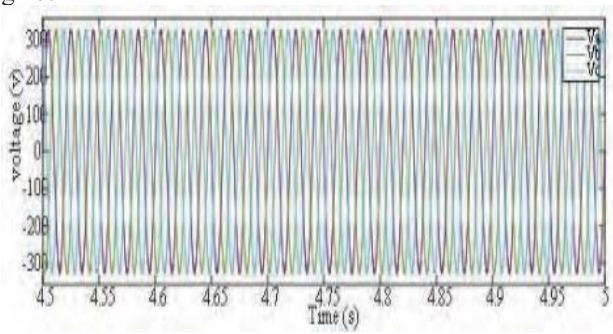

Figure 18. Grid Voltage

The PV output is connected to Grid using Phase lock method in P&O technique. The grid voltage waveform using P&O method is shown in Fig 18.

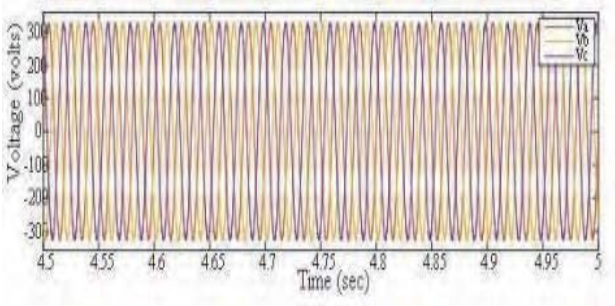

Figure 19. Inverter output Voltage

The inverter output voltage is shown in the Fig 19.

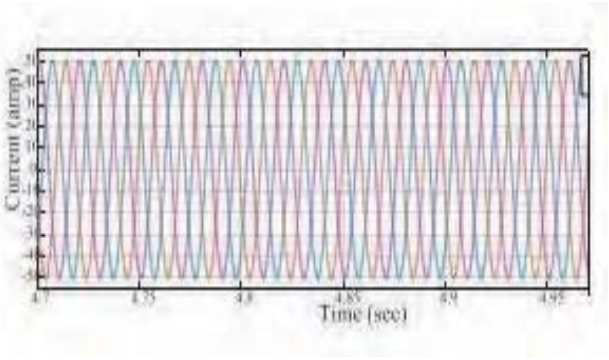

Figure 20. Inverter output currents

Fig 20. shows the three pahse inverter output currents using P&O method.

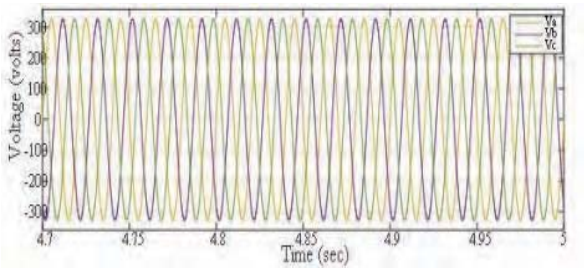

Figure 21. Load Voltage

The PV output is connected to Grid using Phase lock method in P&O technique. The Load voltage at all the three phases is also as expected which is shown in Fig 21.

VIII. Simulation Results of Incremental Conductance Technique

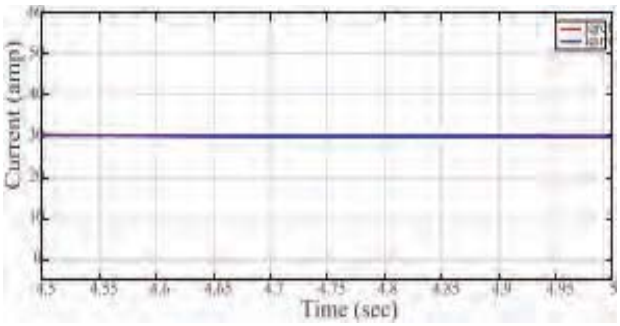

Figure 22. Idinv and Idref Currents

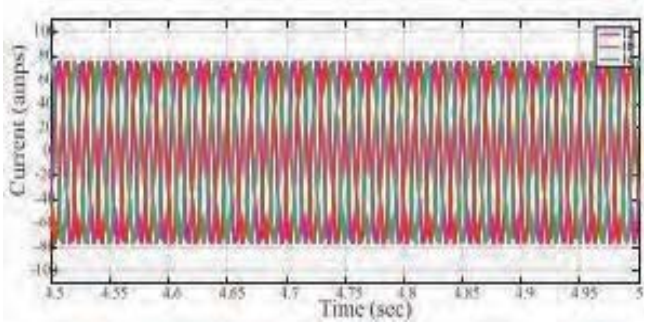

Figure 23. Grid Currents

The dq- currents are as shown in the Fig 22. for incremental Conductance method. The grid current waveforms of Incremental Conductance is shown in Fig 23. to observe the variations obtained with repecet to reference current. Grid voltage is also simulated for all the three phases for analysis in Fig. 24.

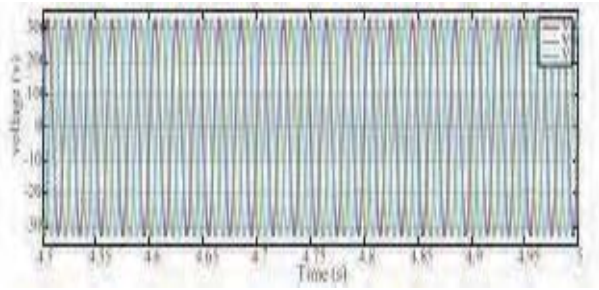

Figure 24. Grid Voltage

Fig 25. shows the simulation results obtained for the three phase inverter voltage in case of Incremental Conductance method.

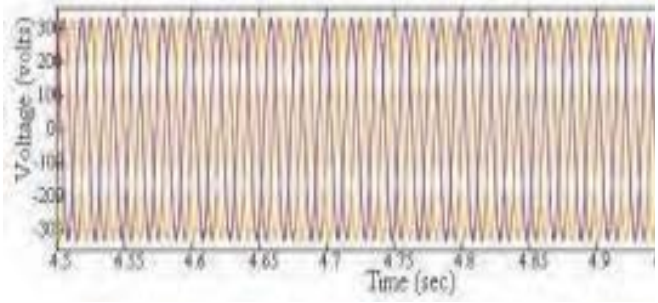

Figure 25. Inverter Voltage

Load voltage of the circuit for 3 phases is shown in Fig 26. for analysing the best method.

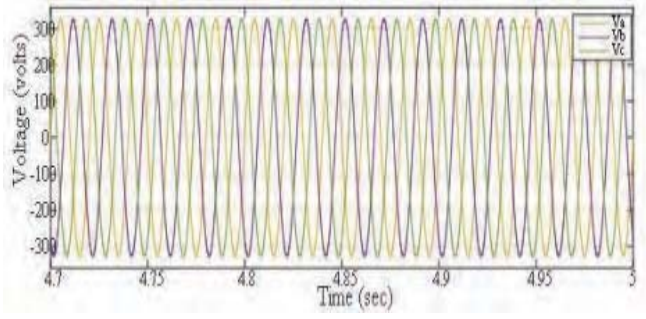

Figure 26. Load Voltage

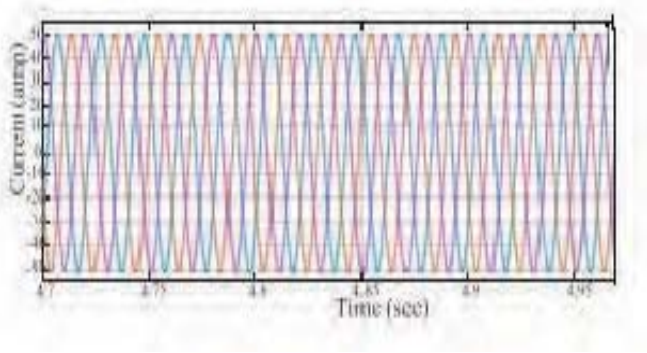

Figure 27. Load Current

The waveform obtained in Fig 27. is for load current of all the three phases for the Incremental Conductance method.

The voltage and currents of Inverter, load and Grid is simulated for both Incremental Conductance method and perturb and observation method for the same parameters. The main disadvantage of the P&O method is tracking the peak power under fast varying atmospheric condition, this can be overcome by using IC method. The IC method can identify when the MPPT has reached the MPP, whereas in P&O method the MPPT oscillates around MPP. The IC method also track the changes in irradiance with higher accuracy. From the results obtained for both the methods shown above and from the analysis it is observed that the Incremental Conductance method gives good tracking efficiency, high response with well controlled for the extracted power. The comparison between P&O and IC MPPT has done using the same conditions. When the atmospheric conditions are constant or changed slowly, the IC method is found to be accurate and the P&O method oscillates close to the MPP. The comparison between the two algorithms for various parameters are given in Table II.

TABLE II.
COMPARISION BETWEEN P&O AND IC MPPT ALGORITHMS

Parameter	P&O MPPT	IC MPPT
Output Current	0.073A	0.087
Output Voltage	36 V	45V
Output Power	2.6 W	3.8 W
Time Response	0.0175 sec	0.1 sec
Accuracy	Less	Accurate

IX. CONCLUSIONS

The P&O and the Incremental Conductance MPPT algorithms are used for the analysis and the simulation results of both the methods are presented. Both P&O and Incremental Conductance MPPT comparison is done with respect to Inverter current, Inverter voltage, Grid voltage, Grid Current, Load voltage and Load current. It is clear from the simulation waveforms that incremental conductance method has better performance than P&O method. These algorithms improve the steady state and the dynamic behaviour of the PV system and improves the efficiency of the DC-DC converter system. From the results obtained Incremental Conductance is showing better output in all terms. Incremental conductance is faster, and output obtained is more precise. In P&O technique the control logic is generating reference voltages and given to inverter to supply active power to the load. The P&O system is applicable for load variations under balanced condition.

REFERENCES

[1] M. Arun Bhaskar, B. Vidya, R. Madhumitha, S. Priyadharcini, K.Tayanti and G. R. Malarkodi, “A simple PV array modeling using matlab,” Int conf. Emerging trends in elec. And comp. tech., IEEE, pp. 122–126, 2011.

[2] B. Subudhi and R. Pradhan, “A comparative study on maximum power point tracking technique for photovoltaic power systems,” IEEE Trans. Sustainable energy, vol. 4,No. 1, pp. 89–98, Jan 2013.

[3] Amit Anand, A.k. Akella, “Modelling and analysis of single diode photovoltaic module using matlab/simulink,” IEEE Trans. Research and Appl., Vol. 6, Issue 3, PP. 2934, March 2016.

[4] Se-Kyo Chung, “A phase tracking system for three-phase utility interface inverters,” IEEE Trans. Power Electronics, Vol. 15, No. 3, PP. 431-438, 2000

[5] Vikram Kaura, Vladimir Blasko, “Operation of a phase locked loop system under distorted utilitiy conditions”, IEEE Trans. Industry Appl., Vol. 33, Issue. 1, PP. 58-63, Jan/Feb. 1997.

[6] Yash P. Bhatt and Mihir C .Shah,”Design, analysis and simulation of synchronous reference frame based phase lock loop for grig connected inverter”, 1st IEEE Int. conf. Power Electronics, pp. 1-5, 2016

[7] S. Kouro, M. Malinowski, K. Gopakumar, J. Pou, L. G. Franquelo, B.Wu,J. Rodriguez, M. A. Perez, and J. I. Leon,“Recent advances and industrial applications of multilevel converters,” IEEE Trans. Ind. Electron., vol. 57,no. 8, pp. 2553–2580, Aug. 2010.

[8] R.Krishan, Y.R.Sood and B.U.Kumar,”The simulation and design for analysis of photovoltaic systembased on matlab”, in proc.ICEETS, PP. 647-671, April 2013.

[9] J. Sreedevi, AshwinN, M.Naini Raju,”A study on grid connected pv system”, IEEE, 2016.

[10] Ahmad, Jawad “A fractional open circuit voltage based maximum power point tracker for photovoltaic arrays”,IEEE 2010 2nd International Conference on Software Technology and Engineering (ICSTE 2010)

[11] Sher, Hadeed Ahmed; Murtaza, Ali Faisal; Noman, Abdullah; Addoweesh, Khaled E.; Al-Haddad, Kamal; Chiaberge, Marcello (2015),”A New Sensorless Hybrid MPPT Algorithm Based on Fractional Short-Circuit Current Measurement and

[12] P&O MPPT”,IEEE Transactions on Sustainable Energy, (), 1–9. doi:10.1109/TSTE.2015.2438781

E-ISSN 2581 – 7957
P-ISSN 2277 – 3916

CVR Journal of Science and Technology, Volume 22, June 2022
DOI:10.32377/cvrjst2209

Test Bench Solar Power Measurement

Banothu Suresh[1] and M. Lakshmi Swarupa[2]
[1]PG Scholar, CVR College of Engineering/EEE Department, Hyderabad, India
Email: sureshbanoth523@gmail.com
[2]Professor, CVR College of Engineering/EEE Department, Hyderabad, India
Email: swarupamalladi@gmail.com

Abstract : **Solar energy is increasingly being used in residential, commercial, and industrial settings. Solar energy is a kind of renewable energy derived from the sun's heat. India will have 34,627 MW of solar power built by 2020. An experimental system for measuring solar panel power was established in this research. This current has been used to monitor voltage and light intensity. The sun has a declination angle of +23.5 degrees and a declination angle of -23.5 degrees with respect to the earth. An incandescent bulb light is used to mimic the sun, with the angles carefully adjusted. This diagram shows the variance in solar power output at the load side, as well as the power and load resistance.**

An incandescent light bulb is used to create light intensity for the solar panel. Using a voltage regulator, the light intensity was varied. Voltmeter and ammeter measurements are used to calculate the power. Solar energy is used to mimic the properties of solar panels' output power. To move from east to west, the model of the sun was turned into an incandescent bulb light and set on the circular iron track. With the aid of a D.C speed regulator, you may adjust the bulb's position and light intensity. The solar panel is positioned such that it may easily move to various orientations. Calculate the power with the use of a voltmeter and an ammeter. Resistance is compared to power, which is the only source of energy. The important intention of this paper is to ascertain that the most electricity output occurs when a resistor bank is used as a load.

Index terms: **Solar panel, light intensity, resistor, voltage, current, power, incandescent bulb light.**

I. Introduction

Solar power is an alternative source which is available from the sun. Electrical power is generated from solar panel output D.C terminals. Solar energy is renewable energy. Most of the power systems generate power from resources such as coal, water etc.

Solar energy produced from sun rays is an inexhaustible source of convenient energy. Solar energy is electromagnetic energy. The sun rays falling on the earth's surface create angles. The photovoltaic effect principle is used to produce electricity. Solar energy depends on the sun. There is a need for monitoring and measurement of solar energy. For thousands of years, the sun has generated energy. For thousands of years, the sun has been a source of energy [1]. The sun's beams that reach the earth's surface are known as solar energy. Solar energy is unique source of energy, and it can be exploited into useful form by different ways such as:

1. Photosynthesis converts sunlight directly into fuel.
2. Photovoltaic panels convert sunlight directly into energy (PV).
3. By direct conversion into electricity through thermal electric power systems. In this system, the solar radiation is converted into heat energy which is further converted into mechanical energy and then into electrical energy.

• Solar power generation is increasing day by day. Solar energy is a renewable source of energy that is generated by the sun as shown in figure 1.

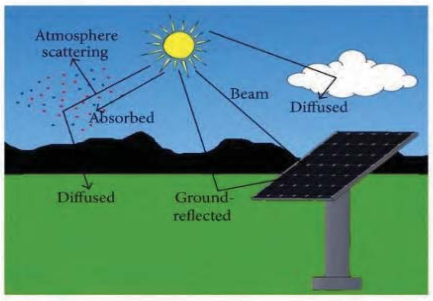

Figure 1. Sun rays on the earth surface

• Atmospheric scattering is a natural phenomenon that can be described as the result of the interaction between sunlight and particles in the atmosphere.

• Diffuse radiation is solar radiation that reaches the earth's surface after being dispersed by molecules in the atmosphere from the direct sun beam.

• Beam radiation is solar energy that has not been dispersed and is directed in the same direction as the relative geometric location between the sun and the earth.

• Solar radiation near to the earth surface can be measured by following instruments: Pyrheliometer, Radiometer, photometer, Ground radio meter, Microwave radiometer, Multifilter rotating shadow band radiometer, Narrow field of view zenith radiometer etc.

II. Basics of Solar System

A. Solar Power

Sun-oriented power is the conversion of energy from daylight into electricity, either directly using photovoltaics (PV), indirectly via focused sun-based force, or a combination of the two. Sun-powered global positioning frameworks and concentrated sun-based force frameworks employ focal points or reflections to focus a large amount of sunshine onto a small pillar. Photovoltaic cells use the photovoltaic effect to convert light into an electric current. Solar energy is an extremely significant source of energy for

Received on 13-08-2021, Revised on 03-10-2021, Accepted on 02-01-2022

CVR Journal of Science and Technology, Volume 22, June 2022
DOI:10.32377/cvrjst2209

the planet and its people. There is no life if the sun isn't shining. Solar energy is the source of all biomass on the planet's surface, as well as fossil fuels. Winds are created by solar energy, which evaporates water and causes rain, waves, and ocean thermal power [2].

B. Solar Energy

Energy is the capacity of an item to do some measure of work. Energy is accessible in positive systems like motor electricity, predicted energy. Sunlight primarily based power is the electricity of the solar. Consistently the earth gets the strength at once from the solar. Utilizing some logical strategies, sunlight-primarily based strength can be modified over in a few beneficial kind of electricity.

For example, we are able to alternate over into other structures like warmth electricity, dynamic energy, capacity energy and so forth Sun based power arrives at the earth as waves which in sunlight. One meter square area of the ecosystem 1.4 KW/m^2 intensity created. The sun-oriented energy diminished because of gas particles, water fumes, dust particles and appearance in air. The force of sun powered energy arriving at the earth is around 1 KW/m^2.Hence this energy is used to warm water and produce the power. Sunlight based energy is changed over into electrical energy by utilizing photovoltaic cells which are made by utilizing silicon.

C. Solar Constant

The heat is created by many types of fusion reactions, resulting in a vast sphere of very hot gases. Its diameter is 1.39×10^6 kilometers, whereas the earth's is 1.27×10^4 kilometers. Although the sun is huge, it only subtends an angle of 32 minutes at the earth's surface, therefore the average distance between them is 1.5×10^8 km. This is due to the fact that it is also located at a considerable distance. As a result, the earth's beam radiation from the sun is almost parallel. The sun's brightness ranges from its core to its periphery. For engineering calculations, however, it is common to assume that the brightness of the solar disc is homogeneous throughout. The energy emitted by the sun seems to be nearly comparable to that emitted by a black surface at 5262 degrees K when seen from Earth.

III. PRINCIPLE OF CONVERSION OF SOLAR RADIATION HEAT

The greenhouse effect is the basic method for heat conversion. Exotic plants may be grown in cold areas by making greater use of the available sunshine. Solar thermal generating is the most efficient technique to convert the energy in sunshine into heat. It includes the sun as a source of heat that is distributed to the ground. This heat is captured, concentrated with the help of solar collectors [3].

Components used in Solar Power Measurement:

A. Two Channel Relay Module

Figure 2. Two channel relay

Two channel transfer module is the module configuration to control two transfers in a basic manner and adaptable. It is viable with Arduino, the hand-off module associated with the assistance of jumpers as shown in figure 2. By utilizing transfer mounted on module two Arduino computerized input/yield pins, it is feasible to control motors, inductive burdens, and other devices. This two-channel hand-off module is utilized in homegrown tasks and in the space of mechanical technology papers.

Optocouplers are installed on the IN1 and IN2 lines of the module to guarantee galvanic protection between the transfer load and the control board that drives it. Associations Capacity of pins TTL advanced information for IN1 TTL computerized input IN2 Ground +5V Force (+5V) GND NO1 Keep the communication open on a regular basis. Normal contact (COM1) NC1 Normally closed contact 1 NO2 Normally open contact Normal contact (COM2) NC2 normally closes contact 2; Pin Capacity +5V power supply.

B. Incandescent Bulb Light

Energy conservation is changing into an addition of a priority. One objective is to utilise more energy-efficient lighting in reception areas, schools, companies, and public areas. This article will define essential concepts that should be used when discussing light weighting as well as different types of light bulbs.

- Watt (abbreviated W) is a unit that measures the rate at which energy (or power) is used in an electrical circuit, such as in the case of a light bulb as shown in figure 3.

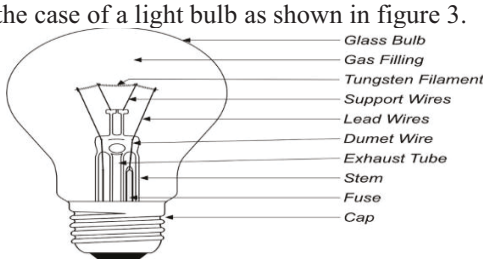

Figure 3. Incandescent bulb light

- Lumens square measures the unit of the number of sunshine (energy) as seen by the human eye that's given off by the sunshine bulb.
- One lumen covering a sector of one square metre is defined as one lux. To put it another way, a lux (light intensity) measurement informs you how many lumens are necessary for the realm to be light.

The incandescent lightweight bulb has had identical style for over a hundred years since Edison fictionalized it.

C. Dataset Description

Arduino mega microcontroller is associate degree open supply, computer onerous product and programming organization, activities, and a customer-specific facility that designs and manufactures single-board microcontroller units for use in sophisticated devices and intuitive goods that can detect and control things in the real world. The comes things sent as ASCII text file instrumentality and programming, which area unit approved below the wildebeest lesser overall population license (LGPL) or the wildebeest overall population license (GPL), allowing for the grouping of Arduino sheets and the distribution of Arduino code to anybody.

Arduino board plans use a partner degree variety of central processor and regulators. The sheet area unit comes with a set of cutting-edge and basic data/output (I/O) sticks that may be connected to a variety of augmentation boards (shields) and circuits. On versions that are unit to boot, the sheets include progressive exchange connectors, including Universal Serial Bus (USB), which is used for stacking applications from PCs. The region unit of the microcontroller was altered in a routine manner utilizing features from the programming languages C and C++. In addition to employing standard compiler instrument chains, the Arduino comes with a partner degree integrated development environment (IDE) for dealing with language papers.

The Arduino began in 2003 as a programme for understudies at an association design institute in Ivrea, Italy, with the goal of providing the most cost-effective and straightforward techniques for kids and experts to choose contraptions that interact with their current condition employing sensors and actuators as shown in figure 4 and 5. conventional examples of such contraptions papered for novice experts to join essential robots, indoor controllers, and development identifiers. The name Arduino is derived from a tavern in Ivrea, Italy, where a number of the ventures' pioneers congregated. Arduino of Ivrea, the margrave of Ivrea's promenade and ruler of a European kingdom from 1002 to 1014, was the inspiration for the bar's name.

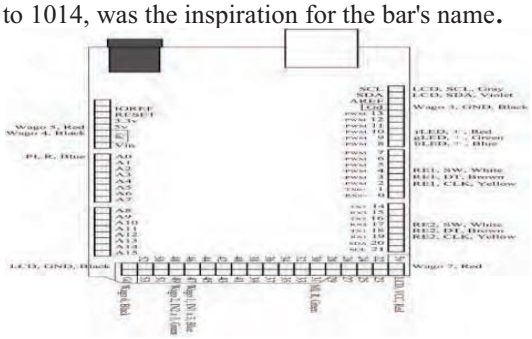

Figure 4. Arduino mega 2560 pin configuration

Figure 5. Arduino Mega 2560 layout

Arduino is basically a microcontroller which controls the relay functions. Arduino MEGA 2560 is used in this paper.

D. Power

The Arduino Mega area is often powered via a USB connection or an outside power supply. The power offer is mechanically selected. An associate degree AC-to-DC adapter(wall-mole) or battery will return external(non-USB) force. Connecting a pair of 1mm focus positive fittings to the board's force jack is a common way to associate the connection. Leads from a battery are often placed in the force connector's Ground and Vin pin connectors. The board will run on a six-to-twenty-volt external power supply. When supplied with less than 7V, however, the 5V pin may give less than 5 volts, making the board unsafe. If you use more than 12V, the voltage controller will overheat and cause damage to the board. There are seven to12 volts. The Mega 2560 is not constant as each single goes before the board.

The power pins are as per the following:

- VIN: While the Arduino board is using an external power supply, the data voltage to the Arduino board (rather than five volts from the USB association or different directed force source). This pin may be used to deliver voltage or to obtain voltage from a force jack.
- 5V: The controlled power allows the microcontroller and other board components to be handled in the same way they are used to. This might come from VIN through an on-board regulator or a purchase of a USB or other directed 5v supply.
- 3V3: The on-board controller has produced a 3.3 potential unit offer. 50 mA is the maximum current draw.
- GND: Ground pins.

It comprises 54 advanced info/yield pins, where 14 are PWM pins,16 pins are Analog inputs,6 equipment sequential ports. It controls the wheels forward and backward movements by using switches. It's also used for irradiation measurement using sensor LDR and used for relay operation.

E. Electrical device (Transformer)

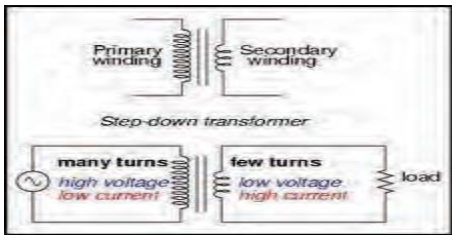

Figure 6. Transformer

- Transformer is a constant frequency device as shown in figure 6.
- Transformer is a constant power device.
- A transformer is a device that converts electromagnetic energy (Internal process).
- A complete transformer is not a device for energy conversion.
- It is a coupled circuit.
- Transformer is a constant flux device.

CVR Journal of Science and Technology, Volume 22, June 2022
DOI:10.32377/cvrjst2209

- More number of turns on the transformer side is called high voltage winding and lesser number of turns on the transformer side is called low voltage winding.
- Supply connected to the transformer called primary, load connected to the transformer so called secondary.
- A step-down transformer is used for converting high voltage to low voltage. Generally, 230 volts,50HZ A.C transformers are used [4].

F. Push Buttons

Press button is a switch which associates its terminal if it is squeezed. As the catch is delivered the terminal gets detached. Hence it is utilized to take contributions from users. This information can be high or low voltage that depends on that one terminal is associated with which source as shown in figure 7.

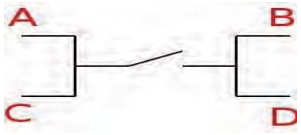

Figure 7. Schematic Diagram of Push Button

G. Light dependent resistor (LDR)

It is basically a photoconductivity device. A photoresistor, also known as a light dependent resistor LDR, is a passive component that reduces resistance in relation to the received luminance on the sensitive surface of the component. It works on the principle of voltage division. It has three terminals VCC (5 volts), Ground and voltage divider point(V) as shown in figure 8.

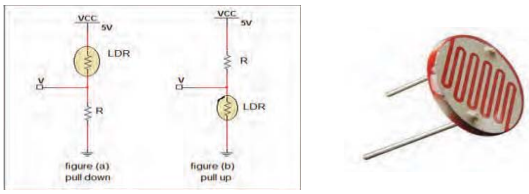

Figure 8. Light dependent resistor (LDR)

H. Solar Panel

A solar panel consists of a collection of solar cells. A solar battery is a collection of solar cells that are electrically linked on support structure. An electrical phenomenon module is a pre-assembled, solar-cell-connected assembly [5]. The solar battery will be utilized as part of a larger electrical grid system to generate and distribute power in commercial and residential settings as shown in figure 9 - 13.

Figure 9. Solar panel

A sun-oriented cell is a specific semiconductor gadget diode that changes over apparent light into direct current. Photovoltaic cells are an indispensable piece of sun based electric energy frameworks, which are turning into an inexorably significant option as wellsprings of utility force as shown in figure 10.

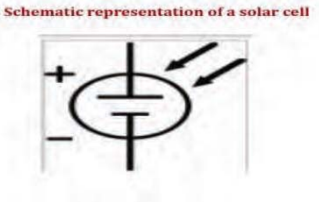

Figure 10. Simple representation of solar cell

I. Four Wheels

These wheels are rubber tires which have a rough surface to move the upper wooden board with the help of motor rotation. Four wheels, in this two Wheels Run by D.C motor which are supported to rotate another two wheels.

IV. Hardware Setup Operation and Measurement of Power

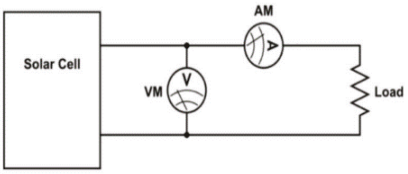

Figure 11: Solar panel connected to resistive load

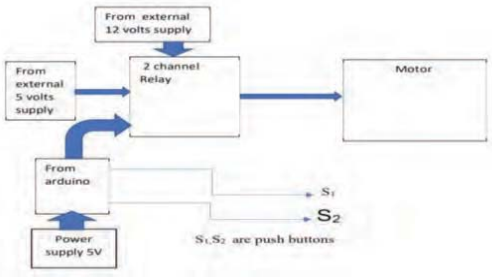

Figure 12. Block diagram for connection of Arduino, relay, motor, push buttons

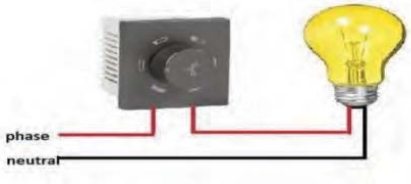

Figure 13. Incandescent bulb light intensity changed with the help of D.C speed regulator

Irradiance, a radiometric amount, measured in watts per square measure (W/m^2). The hardware setup is shown in figures 14 -20.

Figure 14. Four wheels D.C motor

Figure 15. Solar panel and incandescent bulb setup

Figure 16. D.C regulator, load connection

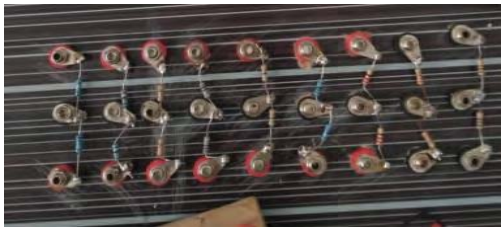

Figure 17. Resistive load as per requirement

Figure 18. Two channel relay with Arduino snapshot

Figure 19. Hardware setup snapshot RPS, bulb at 90°

Figure 20. Snapshot of solar power measurement.

V. PROCEDURE

- Connect the power connector to Arduino from CPU for 5V.
- A 5V D.C supply given to relay input.
- A 12V D.C supply taken from D C regulated power supply for motor input.
- A 230V A.C supply given to the Incandescent bulb through voltage regulator for varying light intensity.
- Connect required connection from Arduino,2 Channel Relay, Switches motors and main A.C supply.
- Dump the program into the Arduino.
- Switch ON all power supply.
- Set the solar panel at 0°.
- Place LDR at the solar panel for light intensity measurement.
- Move the incandescent bulb at various degrees from 15° to 90°.
- Connect the load across Solar output terminals.
- Measure the voltage and current by placing ammeter in series and voltmeter in parallel to the load and power is calculated from readings.
- Set the solar panel at 23.5°, -23.5° and move the incandescent bulb (high intensity only) at 90° and measure voltage, current and calculate the power.
- The graph shows the relationship between Resistance (R) and Power (P) [6 - 10].

VI. EXPERIMENTAL RESULTS

A. Solar Panel at 0^0 Degree

(a). Incandescent bulb at 15° high light intensity

TABLE I.
INCANDESCENT BULB AT 15 DEGREES HIGH LIGHT INTENSITY CLASSIFICATION PERFORMANCE

Resistance (ohms)	Voltage(volts)	Current(mA)	Power(mW)
10	0.04	1.95	0.078
20	0.059	1.95	0.115
47	0.101	1.94	0.195
75	0.165	1.94	0.32
220	0.43	1.92	0.82
330	0.629	1.91	1.20
470	0.951	1.89	1.79
660	1.21	1.88	2.28

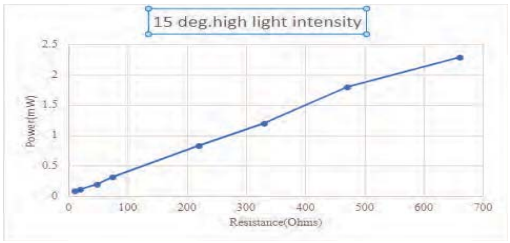

Figure 21(a). R versus P incandescent bulb at 15° high light intensity.

(b). Incandescent bulb at 15° less light intensity

TABLE II.
INCANDESCENT BULB AT 15 DEGREES LESS LIGHT INTENSITY CLASSIFICATION PERFORMANCE

Resistance (Ohms)	Voltage (Volts)	Current(mA)	Power(mW)
10	0.033	1.67	0.052
20	0.049	1.64	0.08
47	0.084	1.63	0.13
75	0.13	1.63	0.22
220	0.35	1.62	0.58
330	0.53	1.61	0.85
470	0.80	1.6	1.28
660	1.05	1.61	1.67

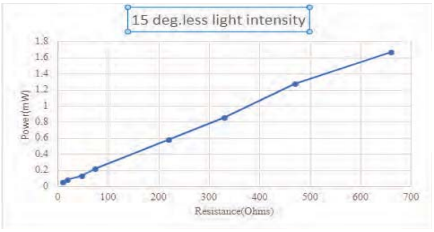

Figure 21(b). R versus P incandescent bulb at 15° less light intensity

(c) Incandescent bulb at 30° degrees less light intensity

TABLE III.
INCANDESCENT BULB AT 30 DEGREES LESS LIGHT INTENSITY CLASSIFICATION PERFORMANCE

Resistance (Ohms)	Voltage (Volts)	Current(mA)	Power(mW)
10	0.05	2.34	0.127
20	0.071	2.34	0.166
47	0.121	2.34	0.463
75	0.198	2.34	0.463
220	0.521	2.33	1.21
330	0.765	2.32	1.77
470	1.144	2.27	2.59
660	1.492	2.28	3.4

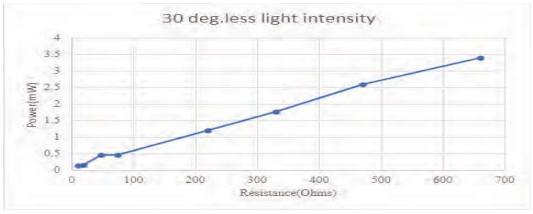

Figure 21 (c). R versus P incandescent bulb at 30° less light intensity

(d) Incandescent bulb at 30° degrees high light intensity

TABLE IV.
INCANDESCENT BULB AT 30 DEGREES HIGH LIGHT INTENSITY CLASSIFICATION PERFORMANCE

Resistance(ohms)	Voltage(volts)	Current(mA)	Power(mW)
10	0.111	4.42	0.49
20	0.135	4.41	0.595
47	0.23	4.4	1.012
75	0.370	4.39	1.624
220	0.967	4.34	4.19
330	1.42	4.31	6.12
470	2.2	4.25	9.46
660	2.73	4.20	11.47

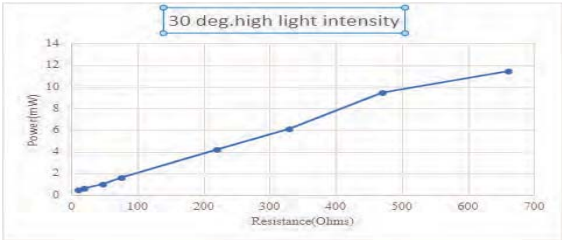

Figure 21 (d): R versus P incandescent bulb at 30° high light intensity

(e) Incandescent bulb at 45° less light intensity

TABLE V.
INCANDESCENT BULB AT 45 DEGREES LESS LIGHT INTENSITY CLASSIFICATION PERFORMANCE

Resistance(ohms)	Voltage(volts)	Current(mA)	Power(mA)
10	0.097	4.2	0.407
20	0.127	4.18	0.53
47	0.216	4.15	0.896
75	0.339	4.02	1.362
220	0.905	3.98	3.6
330	1.28	3.87	4.96
470	1.878	3.73	7.0
660	2.4	3.74	9.0

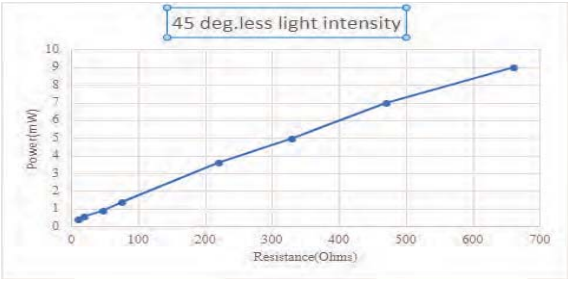

Figure 21(e). R versus P incandescent bulb at 45° less light intensity

(f) Incandescent bulb at 45° high light intensity

TABLE VI.
INCANDESCENT BULB AT 45 DEGREES HIGH LIGHT INTENSITY CLASSIFICATION PERFORMANCE

Resistance(ohms)	Voltage(volts)	Current(mA)	Power(mW)
10	0.37	10.23	3.06
20	0.308	10.19	3.13
47	0.521	9.14	4.76
75	0.84	9.15	7.68
220	2.19	9.85	21.57
330	3.21	9.75	31.29
470	4.8	9.58	45.9
660	5.96	9.19	50.17

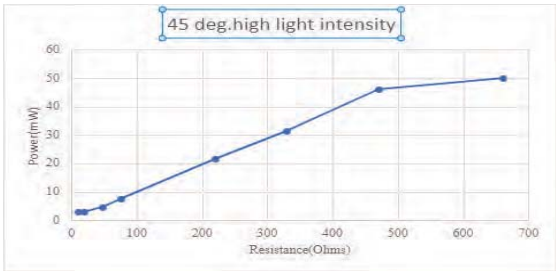

Figure 21 (f). R versus P incandescent bulb at 45° high light intensity

(g) Incandescent bulb at 60° degrees less light intensity

TABLE VII.
INCANDESCENT BULB AT 60 DEGREES LESS LIGHT INTENSITY CLASSIFICATION PERFORMANCE

Resistance (Ohms)	Voltage (Volts)	Current(mA)	Power(mW)
10	0.13	6.25	0.81
20	0.191	6.31	1.205
47	0.328	6.21	2.04
75	0.516	6.09	3.14
220	1.329	5.91	7.8
330	1.89	5.74	10.84
470	2.94	5.64	16.58
660	3.58	5.52	19.76

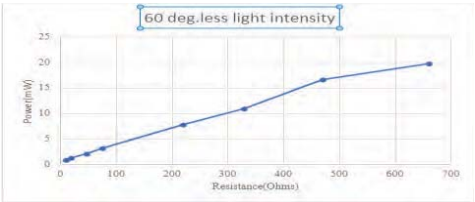

Figure 21 (g). R versus P incandescent bulb at 60° less light intensity

(h) Incandescent bulb at 60° degrees high light intensity

TABLE VIII.
INCANDESCENT BULB AT 60 DEGREES HIGH LIGHT INTENSITY CLASSIFICATION PERFORMANCE

Resistance (Ohms)	Voltage (Volts)	Current(mA)	Power(mW)
10	0.414	17.84	17.385
20	0.54	17.6	9.504
47	0.356	17.45	23.66
75	1.5	17.28	25.937
220	3.74	16.73	62.57
330	5.37	16.33	87.69
470	7.84	15.52	121.67
660	8.27	12.78	105.69

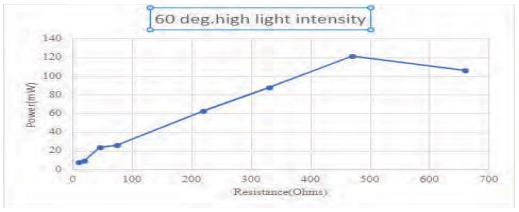

Figure 21 (h). R versus P incandescent bulb at 60° high light intensity

(i) Incandescent bulb at 75° degrees less light intensity

TABLE IX.
INCANDESCENT BULB AT 75 DEGREES LESS LIGHT INTENSITY CLASSIFICATION PERFORMANCE

Resistance (Ohms)	Voltage (Volts)	Current(mA)	Power(mW)
10	0.18	8.76	1.57
20	0.268	8.75	2.34
47	0.512	8.65	4.42
75	0.742	8.58	6.36
220	1.874	8.32	15.59
330	2.634	8.05	21.2
470	4.08	7.64	31.17
660	5.06	7.54	38.15

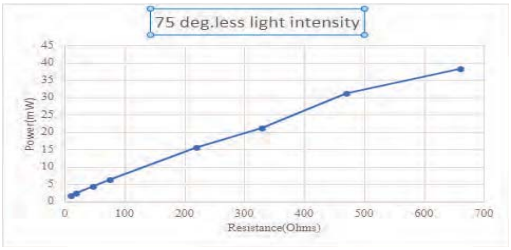

Figure 21 (i). R versus P incandescent bulb at 75° less light intensity

(j) Incandescent bulb at 75° degrees high light intensity

TABLE X.
INCANDESCENT BULB AT 75 DEGREES HIGH LIGHT INTENSITY CLASSIFICATION PERFORMANCE

Resistance (Ohms)	Voltage (Volts)	Current(mA)	Power(mW)
10	0.334	27.1	9.05
20	0.59	26.9	15.87
47	1.19	26.2	31.23
75	1.95	25.2	49.14
220	5.19	24.3	126.11
330	7.53	23.6	177.7
470	8.44	16.6	140
660	8.65	13.37	115.65

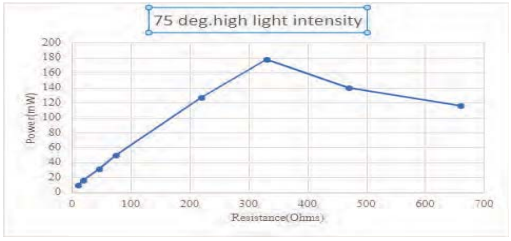

Figure 21 (j). R versus P incandescent bulb at 75° high light intensity

(k) Incandescent bulb at 90° less light intensity

CVR Journal of Science and Technology, Volume 22, June 2022
DOI:10.32377/cvrjst2209

TABLE XI.
INCANDESCENT BULB AT 90 DEGREES LESS LIGHT INTENSITY CLASSIFICATION PERFORMANCE

Resistance (Ohms)	Voltage (Volts)	Current(mA)	Power(mW)
10	0.198	16.8	3.32
20	0.362	17	6.15
47	1.03	16.8	17.43
75	1.27	16.9	21.59
220	3.64	17.2	62.69
330	5.4	17	91.93
470	7.26	14.8	107.44
660	7.84	12.3	96.43

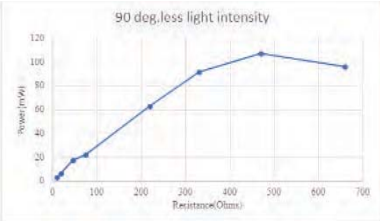

Figure 21 (k). R versus P incandescent bulb at 90° less light intensity

(l) Incandescent bulb at 90° high light intensity

TABLE XII.
INCANDESCENT BULB AT 90 DEGREES HIGH LIGHT INTENSITY CLASSIFICATION PERFORMANCE

Resistance (Ohms)	Voltage (Volts)	Current(mA)	Power(mW)
10	0.66	30.2	19.9
20	0.674	29.9	19.3
47	1.414	29.4	41.5
75	2.18	28.8	62.9
220	6.05	28.3	171.21
330	7.83	24.5	191.83
470	8.41	17.1	143.6
660	8.61	13.5	116.23

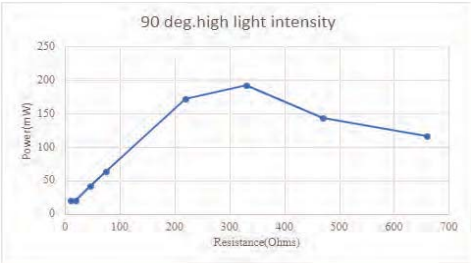

Figure 21 (l). R versus P incandescent bulb at 90° high light intensity

B. Solar panel at -23.5° and bulb at 90° high light intensity

TABLE XIII.
SOLAR PANEL AT -23.5^0 AND BULB AT 90^0 HIGH LIGHT INTENSITY CLASSIFICATION PERFORMANCE

Resistance (Ohms)	Voltage (Volts)	Current(mA)	Power(mW)
10	0.243	19.6	4.76
20	0.426	19.5	8.307
47	0.974	19.3	18.79
75	1.62	19.1	30.94
220	4.02	18.8	75.57
330	5.93	18.2	107.9
470	7.59	15.13	114.83
660	7.99	12.32	98.43

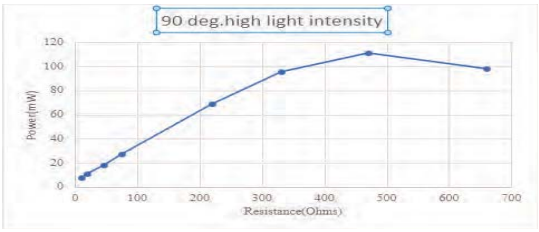

Figure 22. Solar panel at -23.5° R versus P incandescent bulb at 90° high light intensity

C. Solar panel at +23.5° and incandescent bulb at 90° high light intensity.

TABLE XIV.
SOLAR PANEL AT -23.5^0 AND BULB AT 90 HIGH LIGHT INTENSITY CLASSIFICATION PERFORMANCE

Resistance (Ohms)	Voltage (Volts)	Current(mA)	Power(mW)
10	0.417	18.55	7.735
20	0.572	18.4	10.524
47	0.978	18.11	17.711
75	1.54	17.74	27.319
220	3.928	17.45	68.54
330	5.62	17.05	95.82
470	7.5	14.84	111.3
660	7.99	12.27	98.03

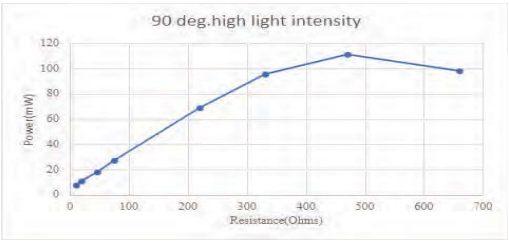

Figure 23. Solar panel at 23.5° R versus P incandescent bulb at 90° high light intensity.

Hence from all the results it is observed that the maximum power output comes from Solar panel at 0° and incandescent bulb light (high light intensity) at 90°.In this case the graph shows maximum power output at 330 ohms resistance.

VII. CONCLUSIONS

The solar panel parameters like voltage, current have been measured. At high light intensity, solar panels produce more power compared to less light intensity. The solar panel output characteristics are drawn between output power and load resistance. The future scope of this project is by changing the brightness of the light with degree of rotation per day of the year and time of the day. This paper can be extended as single axis, dual axis, no tracking. For future development, it is recommended that the framework be built with greater precision sensors and that it be able to retain information received from the estimates in order to ensure accurate monitoring and evaluation. Furthermore, the framework may be modified to use a DC supply from a battery, with a charging circuit added to allow the battery to be charged, making the framework more adaptable.

REFERENCES

[1] https://www.leafyfuels.org/what-is-solarenergyvaluable facts-to-know/ Fetched: 7/21/2021.
[2] https://www.intechopen.com/books/innovation-in-energy-systems-new-technologies-for changing-paradigms/energy-return-on-investment-analysis-of-a-solar-photovoltaic-system Fetched: 12/16/2019
[3] http://www.aliet.ac.in/adv/eee/EEE%20Conference%20%2020 19%20book%20.pdf Fetched: 6/25/2021
[4] http://dspace.daffodilvarsity.edu.bd:8080/bitstream/handle/123 456789/2272/P13069%20%2838%25%29.pdf?sequence=1&is Allowed=y Fetched: 2/23/2021
[5] https://www.slideshare.net/AnkitKaul1/maximum-solar-absorption-using-dual-axis-solar panel-report Fetched: 5/28/2020
[6] https://www.pluginindia.com/what-is-a-solar-cell-and-how-does-it-work.html Fetched: 7/21/2021
[7] http://etd.astu.edu.et/bitstream/handle/123456789/783/Bacha%2CRoman%2CTaddele%20%282%29.pdf?sequence=1&isAllowed=y Fetched: 6/30/2021
[8] Design and implementation of a solar energy measurement and monitoring system Agbetuyi Ayoade Felix, Orovwode Hope, Olowoleni Joseph, Nwangwu Chukwu Buka The authors are from the department of Electrical and Information Engineering, Covenant University, Canaan Land, Ota, Ogun State, Nigeria. IEEE PES/IAS Power Africa (Postgraduate Forum) 2018, IEEE PES/IAS Power Africa (Postgraduate Forum), IEEE PES/IAS Power Africa.
[9] Estimation of Solar Irradiance on Solar Fields: An Analytical Approach and Experimental Results Samer Yassin Alsadi, Member of IEEE and Yasser Fathi Nassar.
[10] Effects of the Solar Module Installing Angles on the Output Power Chang Ying-Pin 1 Shen Chung-Huang 2 (Dept. of Electrical Engineering, Nan Kai Institute of Technology, 568 Chung Cheng Rd., Tsaotun, Nantou, Taiwan 542).

E-ISSN 2581 – 7957
P-ISSN 2277 – 3916

CVR Journal of Science and Technology, Volume 22, June 2022
DOI: 10.32377/cvrjst2210

Maximizing Power Yield from Mismatched Environment in Grid-Connected PV System by Fuzzy Logic Control

M. Krishnaprasad[1] and Vijay Raviprabhakaran[2]
[1]PG Scholar, CVR College of Engineering/EEE Department, Hyderabad, India
Email: krishna703.kp@gmail.com
[2]Assoc. Professor, CVR College of Engineering/EEE Department, Hyderabad, India
Email: vijai.mtp@gmail.com

Abstract: **Solar power generation is one of the suggested methods of generating renewable energy due to its vast availability. Various concerns of the grid-connected photovoltaic (PV) system occur due to fluctuation in voltage and low efficiency. A fuzzy logic-based Buck-Boost converter (FLBBC) is proposed in this paper to produce constant voltage and increase the efficiency, when the PV arrays are exposed to different irradiance. The proposed FLBBC is operated either in buck or boost mode based on the output voltage of the PV subarray. The maximum power point (MPP) trackers are employed in each subarray. This ensures that both the subarrays are operated at their respective MPPT. A fuzzy logic controller is used for generating the necessary sinusoidal duty ratios for the switches of FLBBC. The different magnitudes of power are extracted from the two subarrays and delivered to the grid. When two different magnitudes of power are supplied to the grid it is needed to maintain the grid current sinusoidal and in phase with the grid voltage. The proposed FLBBC has been validated by comprehensive simulation in MATLAB. Furthermore, FLBBC can be employed in solar farms to maximize power yield and increase efficiency.**

Index Terms: **Grid connected photovoltaic system, Fuzzy logic based Buck Boost converter, Maximum power point tracker, Different irradiance, Fuzzy logic controller.**

I. Introduction

A photovoltaic (PV) system's primary goal is to guarantee the optimal performance of individual PV modules in a PV array when the modules are subjected to mismatched atmospheric conditions caused by differences in insolation level and operating temperature. The PV array's power output is considerably reduced when there is a discrepancy in module operating conditions. The issues related to mismatched operating conditions (MOC) become considerable when the number of series linked modules in a PV array is large. The required magnitude of input dc voltage of the inverter of a grid linked transformerless system is achieved by employing several series linked modules. As a result, during MOC, the power output of a grid linked transformerless (GLT) PV system, such as single-phase grid linked transformerless (SPGLT) inverter-based systems derived from H-bridge [1] and neutral node clamp (NNC) inverter-based systems [2] is significantly affected.

Various techniques have been described in the literature to solve the problem of MOC in a PV system. An in-depth examination of such approaches has been given in [3]. The power extraction during MOC can be enhanced by choosing suitable interconnections between PV modules [4] or by utilizing fuzzy logic controller algorithms to track the maximum power point (MPP) of the PV array [5]. Although, for low-power SPGLT PV systems, these approaches are ineffective. Similarly, reconfiguring PV modules in a PV array by altering the electrical connection of PV modules [6] is not effective for the SPGLT PV system because of the significant increase in component count and increase in operational complexity. During MOC, to get the most power out of each PV module. It has been attempted to control each PV module in a PV array using either a power electronic equalization or a dc-to-dc converter [7]. Power electronic equalization schemes need a large component count, increasing the system's cost and complexity of the operation. The technique described in [8] employs a Generation Governor Circuit (GGC) to run each PV module at its MPP, the difference in power between each module being processed only by the GGC. To improve power yield during MOC, the scheme proposed in [9] uses shunt current compensation of each module as well as series voltage compensation of each PV string in a PV array. Dedicated dc to dc converters is incorporated with each PV module in the systems based on module integrated converters [10]. However, the efficiency of the above-mentioned schemes is low due to the huge number of converter stages involved, and the component count in these schemes is high, thus they suffer from the same constraints as the power electronic equalization-based system. Instead of guaranteeing MPP functioning of every module, [11] link a specific number of modules in series to form a string, which is then made to work under MPP. Even yet, the total component count and control complexity do not decrease significantly.

Simplifying the control setup and reducing the component count schemes [12] combine all PV modules into two subarrays, and then each of the subarrays is made to operate at its respective MPP. However, both methods' overall efficiency is reported below. Power extraction during MOC is enhanced by adding a buck and boost stage to the SPGLT PV inverter. Furthermore, the demand for series linked PV modules in a PV array has decreased because of the presence of the intermediate boost stage. The switches of the dc-to-dc converter stage and the inverter stage work at high frequency in the schemes given in [13], resulting in a significant

Received on 26-07-2021, Revised on 06-11-2021, Accepted on 25-02-2022.

CVR Journal of Science and Technology, Volume 22, June 2022
DOI: 10.32377/cvrjst2210

reduction in the size of the passive element count and therefore increasing the operational efficiency of these schemes. Optimization techniques were also applied to optimal PV placement [14-16]

In this paper, an effort has been made to partition the PV modules into two serially linked sub-arrays, with each sub-array being controlled by a fuzzy logic-based buck and boost-based inverter to ensure optimum power evacuation from the sub-arrays during MOC. In comparison to the systems suggested in [17], this technique of separating an input PV array into two sub-arrays decreases the number of series linked modules in a sub-array by almost half. The suggested inverter's topological structure and control technique ensure that the magnitude of leakage current associated with PV arrays stays within the permitted range. Furthermore, as compared to the methods given in [18], the voltage stress across the active devices is reduced by approximately half. As a result, a very high-frequency operation is possible without increasing switching loss. The size of the passive components is also reduced because of the high-frequency operation. As a result, the suggested scheme's operational efficiency is high.

II. Incremental Conductance method VS Fuzzy Logic Control

In the method of incremental conductance, when the light intensity on the PV array fluctuates, the output voltage may smoothly follow the fluctuations, preventing the power output oscillation from repeating at a steady state. The voltage swings are minor. It can change the logic style to decrease oscillation. The voltage fluctuation is modest compared to the P & O technique, making the technology ideal for quickly changing environmental conditions. This method is more sophisticated and performing A/D conversion will take a long time, causing problems managing the processor and placing a significant demand on hardware, particularly the precision of the sensor. Adjusting the step and threshold in the incremental conductance technique might be tricky. The tracking speed is determined by the size of the step; when the step size is big and the system responds quickly, the solar system may not function at its true maximum PowerPoint, and the fluctuation around the maximum power point will cause. The smaller the threshold, the closer the ultimate functioning point is to the maximum power point in principle, but in practice, if the threshold is set too low, the system will not attain a steady-state and will eventually fluctuate within a given range.

Fuzzy Logic Controllers are excellent at modeling nonlinear systems. It performs the needed procedures using linguistic variables. It's a simple and practical approach to establishing a nonlinear system's properties throughout implementation and design. Fuzzification, fuzzy inference, and defuzzification are the three primary components of the Fuzzy Logic Controller.

III. Fuzzy Logic Based Buck-Boost Converter

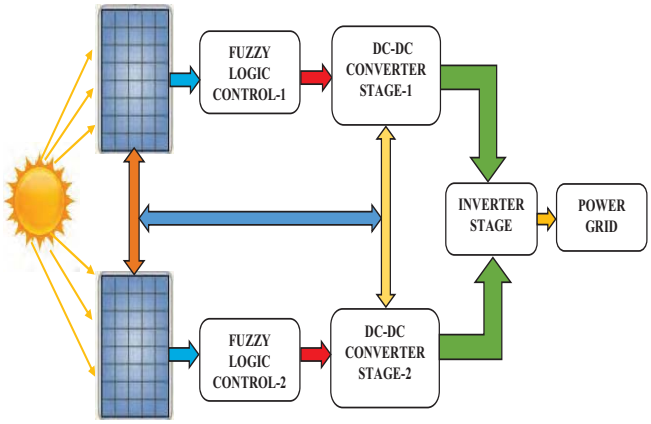

Figure 1. Block diagram of proposed FLBBC

The block diagram and circuit diagram of the proposed FLBBC are illustrated in fig.1 & fig.2. FLBBC is made up of two stages: a dc-dc converter stage and an inverter stage. The dc-to-dc converter stage contains two dc to dc converter sections $CHOP_1$ and $CHOP_2$ deals with the two sub-arrays PV_1 and PV_2 of the solar PV array. Fuzzy logic control-1 is employed to give gating pulses for the switches of dc-dc converter-1 and fuzzy logic control-2 is employed to give gating pulses for the switches of dc-dc converter-2.

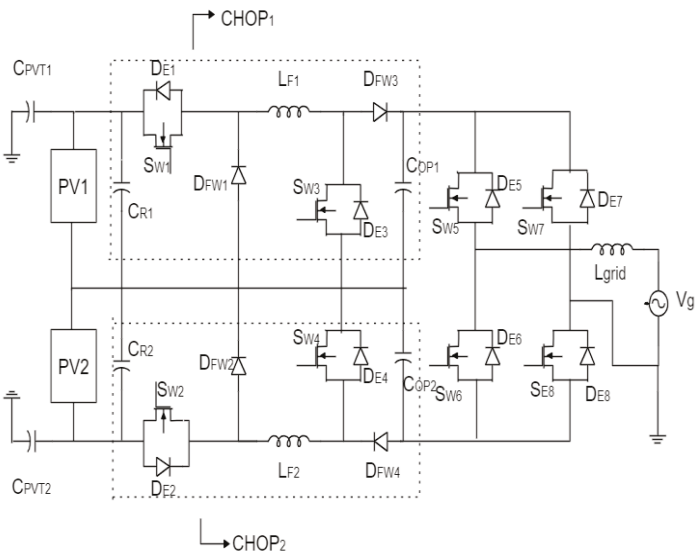

Figure 2. Circuit diagram of proposed FLBBC

The dc to dc converter section $CHOP_1$ is consisting of the switching device, S_{W1} along with its anti-parallel diode, D_{E1}, S_{W3} along with its anti-parallel diode, D_{E3}, the freewheeling diodes, D_{FW1}, D_{FW3} and the filter inductor L_{F1}, and capacitors, C_{R1}, and C_{OP1}. Similarly, the dc to dc converter section $CHOP_2$ is consisting of the switching device, S_{W2} along

E-ISSN 2581 – 7957
P-ISSN 2277 – 3916
CVR Journal of Science and Technology, Volume 22, June 2022
DOI: 10.32377/cvrjst2210

with its anti-parallel body diode, D_{E2}, S_{W4} along with its anti-parallel body diode, D_{E4}, the freewheeling diodes, D_{FW2}, D_{FW4} and the filter inductor L_{F2}, and capacitors, C_{R2}, and C_{OP2}. The inverter section is consisting of the switching devices, S_{W5}, S_{W6}, S_{W7}, S_{W8}, and their corresponding diodes, D_{E5}, D_{E6}, D_{E7} and D_{E8} respectively. The inverter section is combined with the grid through the filter inductor, L_{grid}. The stray capacitance of the PV array to the ground is modeled by the two capacitors, C_{PVT1} and C_{PVT2}.

$CHOP_1$ operates in buck mode when $V_{PV1} \geq V_{COP1}$, while $CHOP_2$ operates in buck mode when $V_{PV2} \geq V_{COP2}$. Here V_{PV1}, V_{PV2} are the MPP voltages of PV_1 & PV_2 and V_{COP1}, V_{COP2} are the output voltages of $CHOP_1$ and $CHOP_2$ respectively. During buck mode duty ratios of the switches, S_{W1} and S_{W1} are varied sinusoidally to ensure sinusoidal grid current (I_g) while S_{W3} and S_{W4} are kept off. $CHOP_1$ operates in boost mode when $V_{PV1} \leq V_{COP1}$, while $CHOP_2$ operates in boost mode when $V_{PV2} \leq V_{COP2}$. During boost mode duty ratios of the switches, S_{W3} and S_{W4} are varied sinusoidally to ensure sinusoidal I_{grid} while S_{W1} and S_{W1} are kept on throughout this mode. The sinusoidal switching pulses of the switches $CHOP_1$ and $CHOP_2$ are synchronized with the grid voltage (V_{grid}), to accomplish unity power factor operation. The switches, S_{W5} and S_{W8} are kept on and switches S_{W6} and S_{W7} are kept off permanently during the entire positive half cycle. While during the entire negative half cycle, the switches, S_{W6} and S_{W7} are kept on and switches, S_{W5} and S_{W8} are kept off permanently.

IV. FLBBC Control Strategy

A. Control Strategy

Gate triggering pulses for the switching devices are generated to operate both the subarrays at their respective MPP and to ensure the flow of sinusoidal grid current in phase with the grid voltage. Two MPP tracking algorithms are used to generate two separate reference voltages V_{mppt1} and V_{mppt2} for the two subarrays. These reference voltages V_{mppt1} and V_{mppt2} are compared with the sensed subarray voltages V_{pv1} and V_{pv2} and the errors generated are processed through two separate fuzzy logic controllers. The detailed flow diagram is shown in fig.3. The reference current of inductor L_1 is I_{L1ref} and inductor L_2 is I_{L2ref}. The sensed inductor currents I_{L1} and I_{L2} are compared with their corresponding references I_{L1ref} and I_{L2ref}. The errors obtained are processed through the two separate fuzzy logic controllers to generate the required sinusoidal duty ratios for the switches S_1 and S2 during buck mode. Similarly, the two separate fuzzy logic controllers are engaged to process the generated errors and generate the required sinusoidal duty ratios for switches S_3 and S_4 during boost mode. Pulse width modulation (PWM) generator is used to generate gating signals for the switches of inverter S_5, S_6, S_7, S_8.

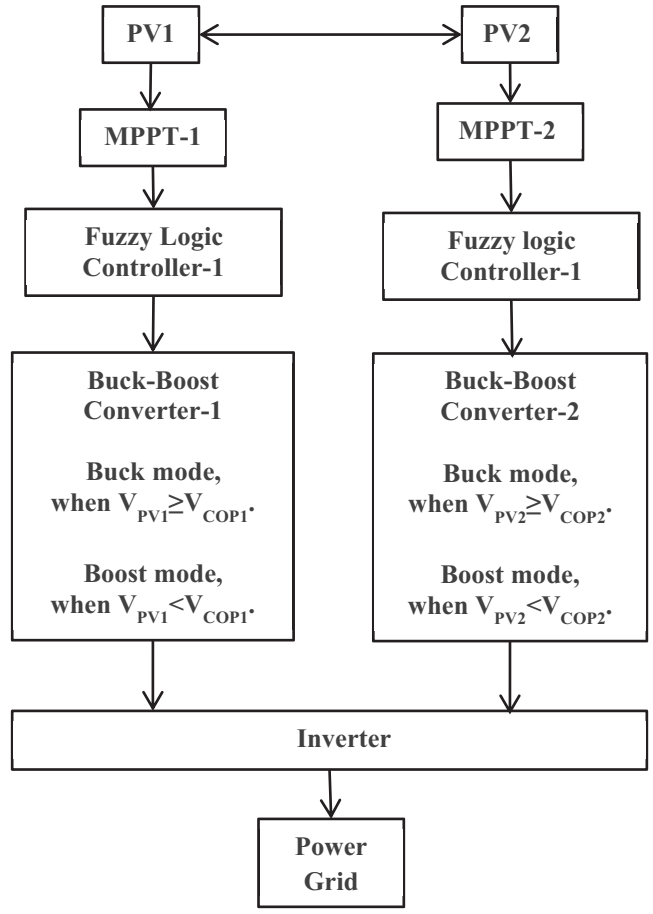

Figure 3. Control flow of the fuzzy logic-based buck-boost converter

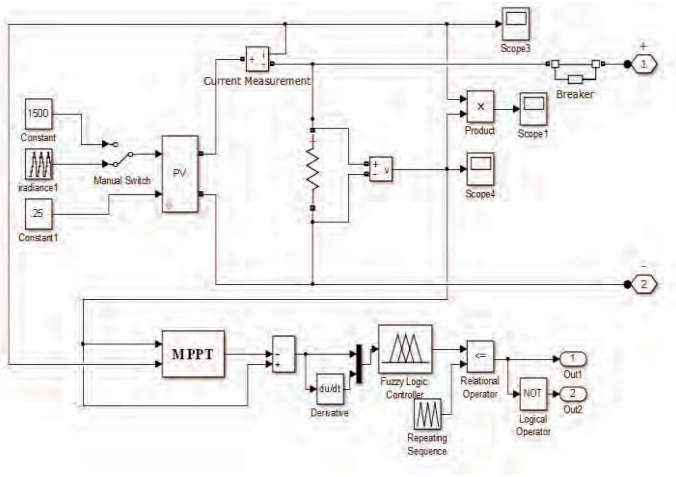

Figure 4. Control configuration of the buck-boost inverter

Using the photovoltaic effect, a photovoltaic cell turns sunlight into an electric current. When PV cells are linked in

CVR Journal of Science and Technology, Volume 22, June 2022
DOI: 10.32377/cvrjst2210

series, the voltage is increased. When PV cells are linked in series, the current is increased. Two PV arrays are connected in series and each PV array is employed with a separate MPPT and fuzzy logic controller. The proposed FLBBC operates in buck mode when the sensed voltage of PV1 is greater than the capacitor voltage COP1 and the sensed voltage of PV2 is greater than the capacitor voltage COP2. FLBBC operates in boost mode when the sensed voltage of PV1 is less than the capacitor voltage COP1 and the sensed voltage of PV2 is less than the capacitor voltage COP2. To provide voltage or current feedback control, switching regulators employ a duty cycle. The duty cycle is the ratio of the turn-on time (TON) to the turn-off time (TOFF), and it provides a straightforward connection between the input and output voltages. The duty cycle of a switching regulator is determined by the topology of the switching regulator. The duty cycle of a step-down (buck) converter is D, where D = output voltage/input voltage. The duty cycle of a step-up (boost) converter is D = 1 – (input voltage/output voltage). The detailed control configuration is shown in Fig.4.

B. Fuzzy Controller Design

Fuzzy control is a technique that permits nonlinear controllers to be built using heuristic information derived from expert knowledge. The input signals are processed by the fuzzification block, which assigns them a fuzzy value.

The set of rules is based on process knowledge and provides for a linguistic description of the variables to be managed. The inference mechanism oversees determining how the rules and their membership functions should be interpreted. The defuzzification block converts the fuzzy information from the inference mechanism into non-fuzzy information that can be used to manage the operation.

V. Results & Discussion

To validate the effectiveness of the proposed FLBBC comprehensive simulation studies are performed on MATLAB and shown in fig.5. The simulation study's major goal is to examine the FLBBC performance while both PV subarrays are experiencing a large difference in irradiance. The several parameters that are used for the simulation studies are listed in Table I. The MPP parameters of each sub-array at standard test state (STS) are as follows: Vpv1 = Vpv2 = 116 V, Ipv1= Ipv2 = 5.7A and Ppv1 =Ppv2 = 661W. The fluctuation in irradiance level concerning time for the two sub-arrays that are used to illustrate the efficacy of the proposed inverter is tabulated in Table II. The variation in the insolation level of PV_1 is indicated in Table II while the insolation level of PV_2 is maintained at 0.8 kW/m^2.

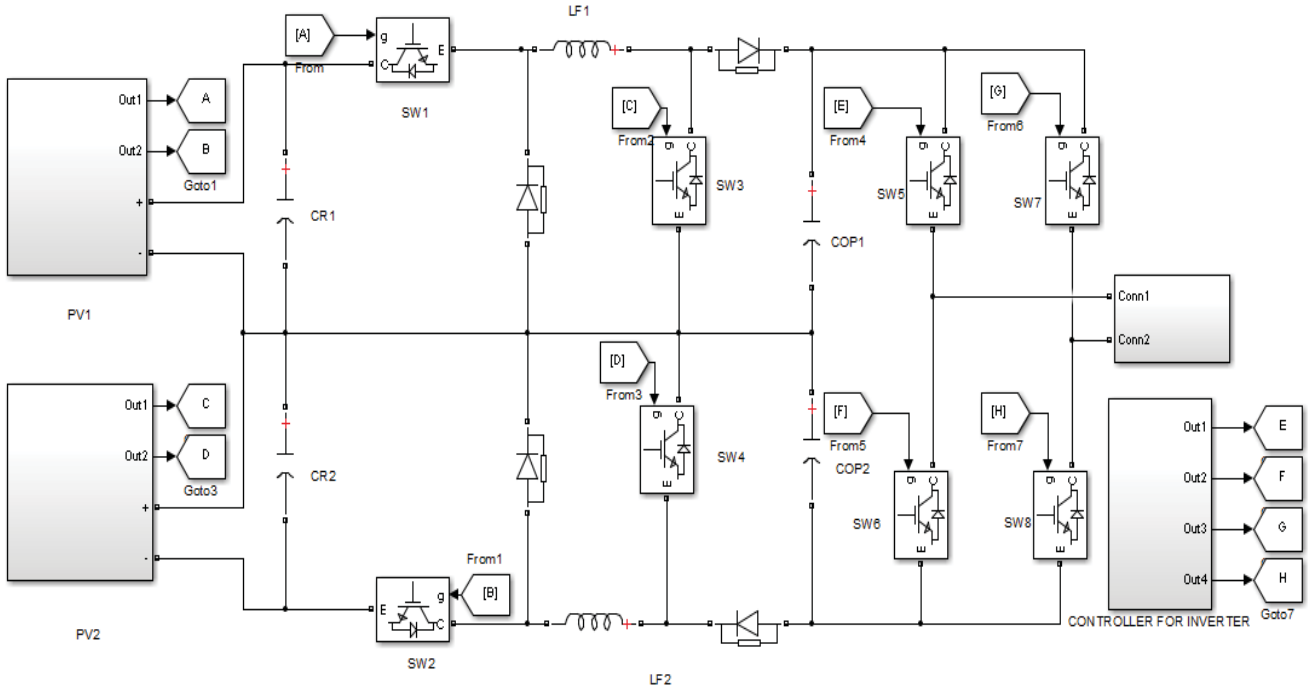

Figure 5. Simulation diagram of proposed buck-boost inverter

TABLE I.
APPLIED VARIATIONS ON INSOLATION AND TEMPERATURE OF TWO SUB ARRAYS

Time in second	0-1	01-2	22-3	33-4	44-5	55-6	66-7	77-8
Irradiance on PV_1 (kW/m^2)	0.5	0.6	0.7	0.8	0.9	1.0	1.0	1.0
Irradiance on PV_2 (kW/m^2)	0.8	0.8	0.8	0.8	0.8	0.8	0.8	0.8
Temperature in PV_1 ($^\circ C$)	25	225	225	225	225	225	225	325
Temperature in PV_2 ($^\circ C$)	225	225	225	225	225	225	225	225

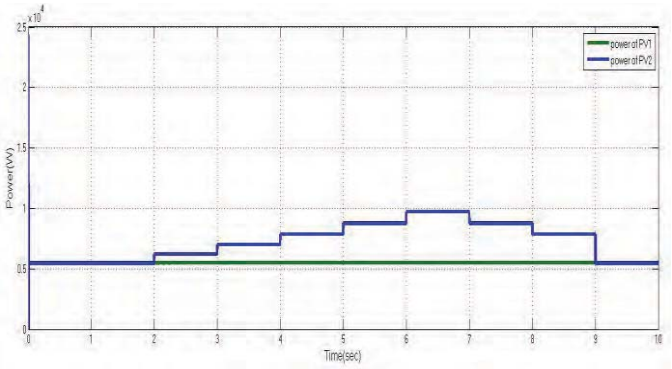

Figure 6. Variation in P_{pv1} and P_{pv2} during the entire range of operation

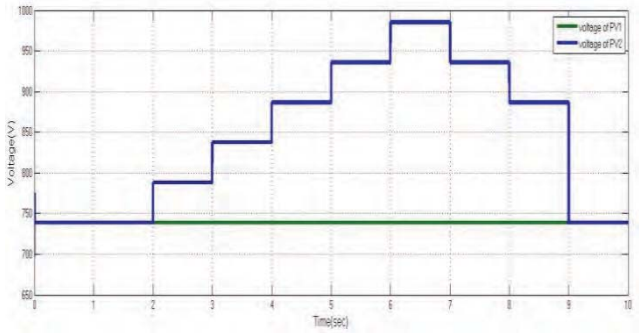

Figure 7. Variation in V_{pv1} and V_{pv2} during the entire range of operation

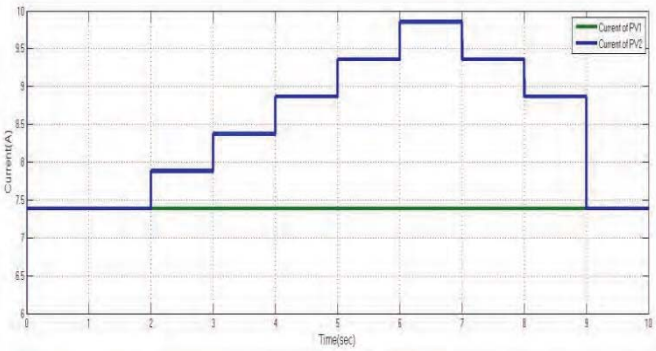

Figure 8. Variation in I_{pv1} and I_{pv2} during the entire range of operation

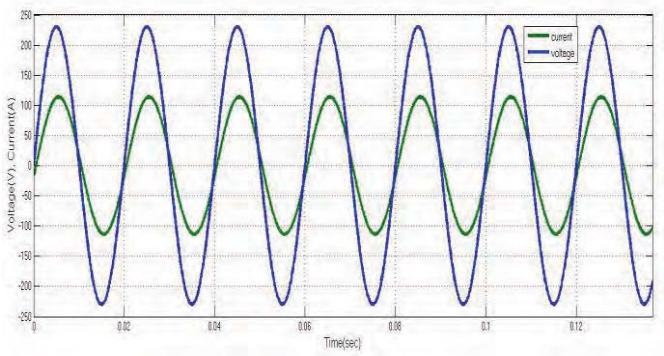

Figure 9. Grid current in phase with the grid voltage

The pulse width modulation generator is used to generate gate triggering pulses for these switches. A single-phase voltage source is used as the power grid connected to the output terminals of the inverter. A filter inductor is connected between the inverter and the power grid. Each PV array is connected to the ground by using stray capacitance.

Figures 6–9 show the change in P_{pv1}, P_{pv2}, V_{pv1}, V_{pv2}, I_{pv1}, I_{pv2} throughout the range of variation in the irradiance levels indicated in Table II. These waveforms indicate that the proposed inverter can extract maximum power from two sub-arrays operating under MOC. Two different magnitudes of power are drawn from the two sub-arrays. When different magnitudes of power are supplied to the grid it is needed to maintain the grid current is sinusoidal and in phase with the grid voltage. This can be achieved by providing the proper gate triggering pulses for the switching devices of the proposed FLBBC. The reference voltages are compared with the sensed voltages across the capacitors C_{OP1} and C_{OP2}. If the sensed voltage is greater than the reference voltage the FLBBC operates in buck mode and sensed voltage is less than the reference voltage the FLBBC operates in boost mode. The voltage across the output capacitors is maintained constant. From Fig.10. It can be concluded that when two different magnitudes of power are supplied to the grid the grid current is sinusoidal and in phase with the grid voltage. This can be achieved by using the proposed FLBBC.

The simulation diagram of the proposed FLBBC is connected as per the circuit diagram and shown in fig.6. The PV array is designed using the equivalent circuit of a photovoltaic cell. The irradiance of the PV1 is varied concerning time and the irradiance of the PV2 is kept constant at 0.8kW/m2. The temperatures on both PV panels are kept constant at 25◦C. The insulated gate bipolar transistor (IGBT) is used as a switching device because of its high voltage capability. Each self-commutated switch is connected to its anti-parallel diode. A freewheeling diode connected between the two self-commutated switches in both buck-boost converters. A filter inductor is also connected between the self-commutated switches. Two output capacitors are connected between the dc-dc converter stage and the inverter stage to provide a constant input voltage to the inverter. The inverter section consists of four self-commutated switches.

TABLE II.
COMPARISON OF VARIOUS TRANSFORMERLESS SCHEMES

Schemes	N_{PVA}	N_{PVO}	V_{IN}	E_{MOC}
H-bridge based [1]	1	1	$>V_m$	High
NNC based [2]	1	1	$>2V_m$	Highest
TSGI based [12]	2	2	$<V_m$	Low
BBBBI based [18]	1	1	$<V_m$	Low
Proposed FLBBC	2	2	$<V_m$	Lowest

A comparison of several aspects of the proposed scheme with previous transformerless methods such as the H-Bridge-based scheme, the NNC-based scheme, transformerless single-phase grid-connected inverter (TSGI) scheme, and boost in boost, buck in buck inverter (BBBBI) scheme are tabulated in Table III. N_{PVA} is referred to as the required number of PV arrays/subarrays, N_{PVO} is referred to as the number of PV arrays operated together, V_{IP} is referred to as the input voltage requirement, E_{MOC} is referred to as the chance of being impacted by MOC. The fuzzy logic controller gives the required gate triggering pulses to the switches of the buck-boost converter depending on the MOC. Based on the objective comparison in Table III, the proposed FLBBC is the most successful method in dealing with MOC.

Advantages of FLBBC over previous transformerless schemes

- Maximum power extraction from two different PV panels, regardless of their environmental conditions.
- Because it is a buck-boost inverter, it can handle a broad range of PV panel voltages.
- The inverter's neutral point clamped-based construction eliminates the problem of leakage current.
- There is no shoot-through fault in the inverter.
- For the operation FLBBC, it is not necessary to sense grid current.

VI. CONCLUSIONS

In this paper, a fuzzy logic-based buck-boost converter is proposed to deal with the mismatched operating conditions on the PV arrays. The number of serially linked PV modules is less, so the effect of shading on the PV modules is minimized. The proposed FLBBC ensure that the two serially linked PV arrays are controlled together and operate at their respective MPPT. As a result, it was well suited for PV subarrays with mismatched operating conditions. The suggested inverter's topological structure and control technique ensure that the amount of leakage current associated with PV arrays stays within the permitted limit. Power from both PV arrays is delivered to the grid simultaneously while maintaining the grid current is sinusoidal and in phase with the grid voltage. This is achieved by employing separate FLBBC for both PV arrays. A fuzzy logic controller is used to generate the required gate triggering pulses for the switches of the buck-boost converter. By using the proposed FLBBC, the operating efficiency of the system is increased. The effectiveness of the proposed FLBBC is validated by comprehensive simulation studies. By using the proposed FLBBC, two serially connected PV arrays are controlled simultaneously at their respective MPPT. Furthermore, this FLBBC is designed to operate several PV arrays controlled together at their respective MPPT. The environmental mismatch conditions are high in solar farms because of their large space. Due to this, the power output from solar farms is greatly reduced. Furthermore, FLBBC can be employed in solar farms to maximize power yield and increase efficiency.

REFERENCES

[1] Araújo, Samuel Vasconcelos, Peter Zacharias, and Regine Mallwitz. "Highly efficient single-phase transformer less inverters for grid-connected photovoltaic systems." *IEEE Transactions on Industrial Electronics* 57.9 (2009): 3118-3128.

[2] Xiao, Huafeng, and Shaojun Xie. "Transformer less split-inductor neutral point clamped three-level PV grid-connected inverter." *IEEE transactions on power electronics* 27.4 (2011): 1799-1808.

[3] Bidram, Ali, Ali Davoudi, and Robert S. Balog. "Control and circuit techniques to mitigate partial shading effects in photovoltaic arrays." *IEEE Journal of Photovoltaics* 2.4 (2012): 532- 546.

[4] Kaushika, Narendra D., and Nalin K. Gautam. "Energy yield simulations of interconnected solar PV arrays." *IEEE Transactions on Energy Conversion* 18.1 (2003): 127-134.

[5] Patel, Hiren, and Vivek Agarwal. "Maximum power point tracking scheme for PV systems operating under partially shaded conditions." *IEEE transactions on industrial electronics* 55.4 (2008): 1689-1698.

[6] Velasco-Quesada, Guillermo, et al. "Electrical PV array reconfiguration strategy for energy extraction improvement in grid-connected PV systems." *IEEE Transactions on Industrial Electronics* 56.11 (2009): 4319-4331.

[7] Villa LF, Ho TP, Crebier JC, Raison B. A power electronics equalizer application for partially shaded photovoltaic modules. IEEE Transactions on Industrial Electronics. 60.3 (2012):1179-90.

[8] Shimizu, Toshihisa, Osamu Hashimoto, and Gunji Kimura. "A novel high-performance utility-interactive photovoltaic inverter system." *IEEE transactions on power electronics* 18.2 (2003): 704-711.

[9] Sharma, Pooja, and Vivek Agarwal. "Maximum power extraction from a partially shaded PV array using shunt-series compensation." *IEEE journal of photovoltaics* 4.4 (2014): 1128- 1137.

[10] Olalla, Carlos, et al. "Performance of power-limited differential power processing architectures in mismatched PV systems." *IEEE Transactions on Power Electronics* 30.2 (2014): 618-631.

[11] Elserougi AA, Diab MS, Massoud AM, Abdel-Khalik AS, Ahmed S. A switched PV approach for extracted maximum power enhancement of PV arrays during partial shading. *IEEE Transactions on Sustainable Energy*. 6.3 (2015):767-72.

[12] Debnath D, Chatterjee K. Maximising power yield in a transformerless single-phase grid connected inverter servicing two separate photovoltaic panels. *IET Renewable Power Generation*. 10.8 (2016):1087-95.

[13] Abbaszadeh, M. A., Monfared, M., & Heydari-doostabad, H., "High Buck in Buck and High Boost in Boost Dual-Mode Inverter,". *IEEE Transactions on Industrial Electronics*, 68.6 (2020): 4838-4847.

[14] R.Vijay and J. Durga Devi. “Optimal placement and sizing of wind-PV integrated power generation by ant colony optimization technique,” International Journal of Recent Trends in Engineering & Research 3.5(2017): 2455-1457.
[15] Raviprabakaran, Vijay, and Ravichandran Coimbatore Subramanian. "Enhanced ant colony optimization to solve the optimal power flow with ecological emission." International Journal of System Assurance Engineering and Management 9.1 (2018): 58-65.
[16] Vijay, Raviprabakaran. "Quorum sensing driven bacterial swarm optimization to solve practical dynamic power ecological emission economic dispatch." International Journal of Computational Methods 15.03 (2018): 1850089.
[17] Sedaghati, F., & Pourjafar, S. Analysis and implementation of a boost DC–DC converter with high voltage gain and continuous input current. *IET Power Electronics*, 13.4 (2020):798-807.
[18] Wu W, Ji J, Blaabjerg F. Aalborg inverter-a new type of “buck in buck, boost in boost” grid-tied inverter. IEEE Transactions on power electronics. 30.9 (2014):4784-93.

E-ISSN 2581 – 7957
P-ISSN 2277 – 3916

CVR Journal of Science and Technology, Volume 22, June 2022
DOI: 10.32377/cvrjst2211

Diagnosis of Acute Lymphoblastic Leukemia using Microscopic Blood Cell Images

Narendra B Mustare [1] and C. Pramod Kumar[2]
[1]Professor, CVR College of Engineering/EIE Department, Hyderabad, India
Email: narendra@cvr.ac.in, drnamust@gmail.com
[2] Asst. Professor, CVR College of Engineering/EIE Department, Hyderabad, India
Email: pramod.kumar@cvr.ac.in

Abstract: **Acute Lymphoblastic Leukemia (ALL) is a kind of blood illness attributable to the surprising ascent in the development of unhealthy WBCs in the spongy tissues of the bone, prompting blood malignant growth. It may be seen in children and aged people too.**

The study of microscopic images proves a substantial role in the evaluation of leukemia and its effective detection. The existing techniques are of traditional type and somewhat depend on human intervention, which is laborious. So, an automated leukemia diagnostic system is very much needed that reduces manual intrusion and provides more precise medical information.

This paper describes an automated system developed, based on image processing techniques for the detection of acute lymphoblastic leukemia in blood cells. Here a system is proposed to detect ALL by examining microscopic blood cell images obtained from a standard dataset. In our research work, two image processing techniques are suggested for the detection of the illness. The first technique depends on the conventional feature extraction procedure where the features like region, edge, quantity of nuclei etc., are separated. Data is then sent to the classifier to be categorized. Prior to feature filtration, the images are processed by an adaptive k-means segmentation algorithm to separate the nucleus. The input image is fed to DNN in the other technique.

The overall appraisal of the presentation of classifiers like SVM ANN is performed with features obtained from the first technique. The first technique furnishes a detection efficacy of 89.37% with SVM and 92.16% with ANN. The CNN-dependent feature extraction technique offers a detection efficacy of 93.36%.

***Index Terms*: Microscopic Blood Cell Images, acute Lymphoblastic Leukemia (ALL), SVM, ANN, CNN, automated leukemia detection**

I. Introduction

Medical imaging has become one of the foremost necessary visual images and interpretation strategies in biology and medicine over the past decade. Now, it has witnessed incredible progress of new, powerful instruments for processing and analyzing medical images. This has directed to a huge growth in the application of digital image processing tools [1] for resolving medical issues. The foremost difficult facet of medical imaging lies within the development of integrated systems for the utilization of the clinical sector. Model development, execution, and authentication of modern medical systems need strong partnership between doctors and engineers. The main objective of image processing is to collect data, detection of diseases, diagnose diseases, manage medical care, observation, and analysis [2].

Presently, the identification of blood illness is beyond visual survey of microscopic blood cell images. The detection of blood disorders may be useful for the classification of a variety of diseases connected to blood**.** One of the most feared human syndromes is cancer. Leukemia is a type of blood cancer, and if it is detected late, it'll lead to death. The images of normal blood cell and Leukemia blood cell is shown below in Figure 1

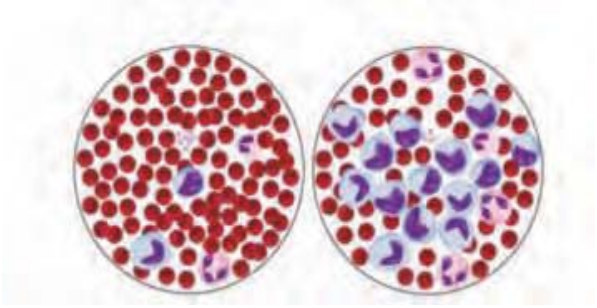

Figure 1. (a) Normal blood (b) Leukemia

White blood cells (WBCs) are one of the cells that help the body to fight infections. Having the generic term as leukocytes, the WBCs are classified based on their appearance into neutrophils, basophils, eosinophils, lymphocytes, and monocytes. The structure of different types of WBC is shown in Figure 2.

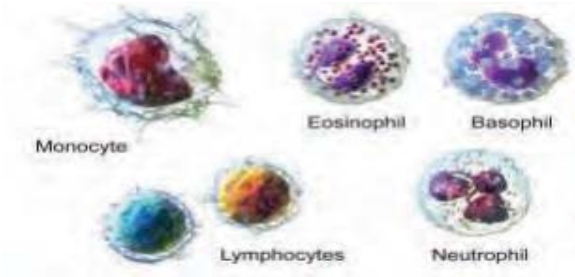

Figure 2. Composition of White Blood Cell

Received on 18-10-2021, Revised on 28-10-2022, Accepted on 26-11-2022.

CVR Journal of Science and Technology, Volume 22, June 2022
DOI: 10.32377/cvrjst2211

Leukemia occurs when a lot of abnormal lymphocytes are produced by bone marrow due to which, the balance of the blood system will be disrupted. Leukemia can be termed as a group of haematological malignancies that are demonstrated by the tumorous proliferation or increased life span of immature white blood cells in the bone marrow [3]. The extreme production of these cells named as lymphoblasts or leukemic cells progressively dislocates healthy cells in the bone marrow and even extend to vital organs such as the liver, lymph nodes, spleen, and nervous system causing complications in fighting infections, transporting oxygen [4,5].

Clinically, leukemia is classified based on the speediness of the disease progression to acute and chronic forms. Whereas the acute kind of leukemia develops quickly and therefore the number of leukemic cells rises rapidly, chronic leukemia develops slowly over time [6]. In keeping with the sort of affected cells from that the malignancy develops, acute leukemia is again divided into two classes: acute lymphoblastic leukemia and acute myeloid leukemia [7]. In our research work, we are considering Acute lymphoblastic leukemia (ALL), which is the second most common type of blood disorder leading to leukemia in adults above fifty years and the most common type of childhood malignancy for the age less than five years, accounting for around one-third of all paediatric cancers [8].

The quantity of lymphoblasts could be a strong sign of acute lymphoblastic leukemia. For this, the blood sample is taken and scrutinized by haematologists. Microscopic images are inspected visually by haematologists and so, the method is time intense and laborious [9], [10], [11]. The method is vulnerable to errors because of human physical capability and necessitates human professionals. Moreover, it is difficult to get steady results from microscopic visual inspection. The recently used diagnostic methods rely on analyzing immune phenotyping, fluorescence in situ hybridization (FISH), cytogenetic analysis dan cytochemistry [12], [13].

The immediate and quick classification of the leukemia considerably aids in delivering the proper medication for it [14]. An automatic microscopic imaging system is greatly needed which can carry away related limitations in the visual microscopic inspection.

The system developed here is based on microscopic images to acknowledge the type of leukemia. With this system, more images can be screened, decrease evaluating time, eliminate the effect of subjective factors, and enhance the precision of the diagnosis process at the same time [15].

The execution is completed in MATLAB by utilizing an image processing toolbox. The input database is taken from public benchmark datasets: ALLIDB2. It is publicly open to download the dataset available online [10]. They provide high-quality images

In our work, we considered 108 samples of images taken from healthy and infected patients as shown in Figure 3, taken with a sophisticated optical microscope together with a high-resolution camera. The images are in a digital photographic structure having a resolution of 5.04MP pixels.

In this paper, two techniques are suggested for the detection of the illness. The first technique depends on the conventional feature extraction procedure where the features like region, edge, quantity of nuclei etc, are separated. Next, the data is given to the classifier for categorization. Here, the images are exposed to segmentation by adaptive k-means for separating the nucleus prior to feature extraction.

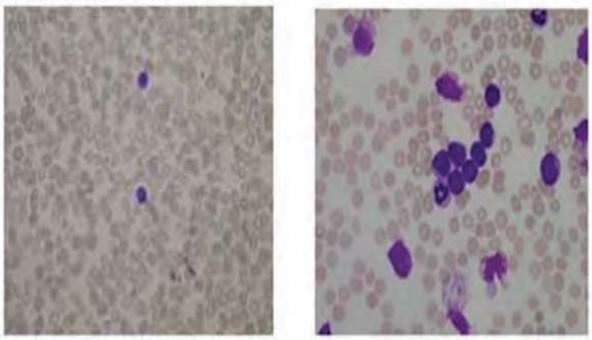

Figure 3. (a) Healthy Sample (b) Infected Sample

In the other technique, the image from the dataset is exposed to CNN- based DNN. The overall appraisal of the presentation of classifiers like SVM ANN is performed with features obtained from the first techniques. The first technique furnishes a detection efficacy of 89.37% with SVM and 92.16% with ANN. The CNN-dependent feature extraction technique offers a detection efficacy of 93.36%.

II. Literature Review

In this section, the work demonstrated by different experts on several techniques for the diagnosis of leukemia using microscopic blood cells is discussed. Normally, the study of Leukocyte cell images has been done under three headings:

A. Image Segmentation
B. Feature Extraction
C. Detection and Classification

A. Image Segmentation

[16] used a color-based division technique in the L * a * b color region instead of a Fuzzy C-Means clustering to divide WBCs into 4 classes. This region is utilized since it is a two-dimensional color region.

Analysis [17] uses the Otsu thresholding technique to get an effective segmentation. The author employed an arithmetic algorithm to competently eliminate all the blood components excluding WBCs.

In [18], a comparison of three strategies is made: K-Means clustering, Fuzzy C-Means, and K-Means modification. The same technique was utilized in HSI color space. It is noticed that each has a unique performance.

In [19] segmentation with the K-Means technique is used in greyscale color space and this divided blood into 4 groups.

In [20], the nucleus lymphocytes were obtained using the L * a * b * color space and the K-Means Clustering approach, tracked by thresholding technique developed by Otsu. They got a digital image with a structural filter to remove the undesired area and get the best nucleus images feasible for classification. The same methodology is utilized by the researcher in [21].

Color segmentation in the HSI color space was employed in [22] after a pre-processing procedure that used a contrast improvement methodology to enable segmentation findings.

To improve the quality of segmentation, [23] applied thresholding within the HSI color space on the value S, along with a median filtering technique and a region-expanding method.

[24] suggested a color segmentation technique in the HSI color space with a white blood cell discriminating area. The idea is to create a discriminating region for the scatter plot of pixels that are related to white blood cells. White blood cells can be identified by evaluating if a pixel falls inside the Discriminating zone.

Active Contour and Watershed Transformation were two approaches used in [25] for segmentation. They discovered that watershed transformation provides a promising result for nucleus segmentation, as it can segment more regions and has a lower computational cost than the Active Contour Technique.

The threshold value utilized in [26] was calculated using the Zack Algorithm. Their research shows that the Zack Algorithm is effective when the Y- Component histograms formed from leucocytes and red blood cells show obvious dips between high and weak peaks.

A dual threshold technique for segmenting White Blood Cells was proposed by [27]. Two threshold values were generated from the search method and implemented in many color spaces -grayscale and HSV.The step for image analysis and image processing of A LL is explained in [28]. Image segmentation methods such a s thresholding, clustering, region expanding, and others have been employed in the literature.

B. Feature Extraction

[16] used a variety of parameters to classify lymphoblasts. Hausdorff dimension, signature contour, shape features that incorporate area, perimeter, and form factor are examples of fractal dimension features. A color characteristic that is the normal value of color, as well as texture features like homogeneity and entropy are utilized to improve recognition accuracy.

To obtain the most effective feature extraction for leukemia identification, researchers [17] proposed a Fisher's Discrimination Ratio (FDR) technique followed by extensive analysis. They discovered the three most distinguishing features: nucleus diameter, nucleus prominence, and the nucleus axis.

[25] uses the LDP operator to abstract features from the segmented nucleus, based on [19]. The LDP operator provided a histogram, which revealed the features.

Basophilic intensity texture features were established in the LAB color space, according to [26]. They also talked about a new way to visualize the cytoplasmic profile. It assesses the cytoplasm's prognoses utilizing the WT-segmented periphery region around the cell. The green component is segmented using thresholding, and the pixels in this zone are counted.

C. Detection and Classification

Only a few studies have focused on specific classification strategies.

[17] employed k-nearest neighbor classification with Euclidean Distance in their analysis. The physical similarities between normal lymphocyte cells and lymphoblast cells resulted in some misinterpretation.

In [20], a sequential neural network classifier with two stages was utilized, the first of which was used to distinguish between normal and abnormal cells, while the second stage was used to distinguish between ALL and AML. However, due to a lack of input picture databases, they only explored step one, which involves distinguishing between normal and lymphoblast cells. The next study [21] accomplished advancement using HSV and FCM to identify cancerous and non-cancerous cells.

They used two algorithms for training, the Lavenberg-Marquardt algorithm (LM) and Bayesian Regulation, based on research [22]. They related two methods for classification of white blood cells, the Multilayer Perceptron as in [23], but they used two algorithms for training, the Levenberg-Marquardt algorithm, and Bayesian Regulation. The ARTMAP Simplified Fuzzy Neural Network is the second classification method. The results show that when compared to other approaches that employed 100 training epochs and six hidden nodes, the MLP with trainer BR algorithm produces the highest accuracy of 95.7 percent.

[23] also discussed three methods for categorizing white blood cells, with MLP achieving the highest level of accuracy when compared to SVM and CNN. The diagnosis of leukemia using image processing with a focus on segmentation and preprocessing to improve segmentation results. The accuracy of lymphoblast classification depends on the results of cell nucleus segmentation. Furthermore, the lymphoblast detection accuracy is determined by the classification technique used.

The processes of recognizing leukemia are divided into three phases, according to the literature survey: segmentation, feature extraction, and classification. During the segmentation phase, the results often exhibited a relative maximum degree of accuracy of more than 90%. Segmentation techniques such as the K-Means approach and Fuzzy C-Means are widely employed. The texture, color, and geometrical properties are utilized during the feature extraction process. Using SVM and MLP algorithms, the accuracy grades in the classification phase are quite high.

III. PROJECTED METHODOLOGY

The blood smear image is exposed to various steps in the projected method. To start with, the image is exposed to division in segmentation process. Later, the image improvement activity is executed. Next features are separated from the image. Ultimately, the feature elements

CVR Journal of Science and Technology, Volume 22, June 2022
DOI: 10.32377/cvrjst2211

are arranged by a classifier. The goal of the suggested method is to foster a mechanized and exact technique to analyze whether or not the blood image is impacted by leukemia. It incorporates the identification and characterization of leucocytes. Additionally, find the best strategy which classifies the leucocytes amongst the current strategies. The projected approach conjointly points in examining the exhibition of SVM, ANN, and CNN

Based on the literature, we have added the following steps to our methodology as shown in Figure 4.

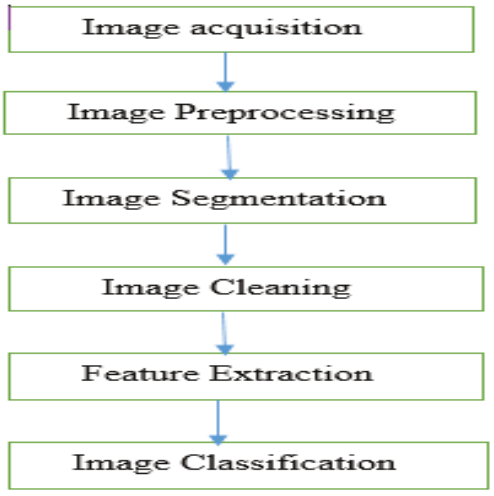

Figure 4. Steps involved in Proposed System

1.Image Acquisition

Image slides of blood samples obtained from normal and abnormal patients are included in the input, which are appropriately differentiated by an expert professional. This will be the source for evaluating the execution's outcomes. Microscopic images from the clinic are fed into the system via the higher-end camera. As a result, most of the images have a 5.04MP pixel resolution with various modifications.

2.Image Prepossessing

During image acquisition and too much staining, the images are going to be disturbed by noise. The noise could also be because of brightness or darkness that makes the region of interest (ROI) looks like a blurry image region. The background is going to be removed as our ROI is going to be white blood cells. Throughout this pre-process, image augmentation is going to be done since the contrast augmentation method is skilled to increase the medical image quality [29].

3.Segmentation

Image segmentation is a technique by which an image is divided into totally unique components. It assists with making over the overall type of the enhanced images into a more expressive and clearer image for a framework to additionally investigate. In this manner, the pictures are sectioned alluding to a bunch of consistency measures. A few division strategies have bases like threshold, edge-based, and so on [30]. K-means is one of the easiest algorithms skilled for resolving every kind of clustered issue. moreover, division by k-mean clustering has a few inadequacies. A couple of arbitrary spots are chosen as centroids in k-means technique. We ought to indicate the number of clusters. Adaptive k-mean clustering is used to provide an incredibly further developed division result. The K-Means approach is a multipurpose technique that can be used in a variety of situations. In the arranging step, the position of the k-centroids is very vital since different positions will contribute to different outcomes. The standard K-Means strategy utilizes the erratically picked k-centroids that end up in the ill-advised division. This might prompt temperamental outcomes in image division.

Despite using the standard arbitrarily chosen on k-centroids, this adaptable methodology handles the local's least and most noteworthy characteristics reliant upon the RGB coloring space during the sorting. The further created sorting out strategy yields a two-element bunch with the least and most prominent RGB regards from the whole pixel region. We register the best and least pixel regards for each band of an isolated image inside the ROI. This technique is a cycle-based grouping that yields an ideal worth of starting k-centroids by diminishing the genuine capacity.

The below-mentioned objective function can be used to get the underlying k-centroids:

$$\alpha = \sum_{i=1}^{c} \sum_{i=1}^{n} \delta(\mu_{min}, \mu_{max}) \quad (1)$$

Where α is the Euclidean distance among minimum and maximum RGB values, n is the quantity of image pixels and c is the quantity of bunches.

4. Image Cleaning

It is expected to clean up the image to further develop results. It is accomplished using the area opening methodology, which can wipe out all of the things with a smaller size than the organizing component, which has a round structure, and its size value can be assumed to represent the typical size of items in the image. As a result, the region was opened followed by morphological enlargement. This may fill the unfilled region inside the cell structure and get an unmistakable segregated image. The quantity of the nucleus is determined by marking the associated items.

5. Feature Extraction

This is the most typical method of removing characteristics as descriptors from observable images, as recommended by specialists, and it is also the most appropriate stage for classification. Shape descriptors and the amount of nucleus in the image is utilized for this purpose. Shape descriptors are a group of statistics that can be used to characterize a certain shape. The essential shape descriptors like area, major and minor turn, the edge is utilized.

6. Classification

Classification is a method of assigning a known class to an unknown vector. In this research, feature vectors are used

CVR Journal of Science and Technology, Volume 22, June 2022
DOI: 10.32377/cvrjst2211

to classify whether an individual is infected or not. The most often used classifiers include K-Nearest Neighbor, Decision Trees, and SVM. Each classifier will figure out how to build a required bunch of yields with defended class using a strategy in which there are a number of information sources. A SVM classifier is used in the leukemia conclusion system, and it sorts the images into one of two categories: impacted or not impacted. A double-layer feed-forward network and CNN network are used in addition to SVM. We're curious to see which strategy provides the best results.

A. Support Vector Machine (SVM)

In this classifier, the total input data is parted into 2 sets that are prepared and tested. Preparing data is the learning worldview that will prepare the vectors and update the boundaries. Then again, the test information is used to verify the classifier and approve the classifier execution along these lines. Presently, SVM classifies every lymph cell as intestinal sickness impacted or unaffected relying upon the element

vector got in the component extraction stage. The system is rehashed for each image to prepare and designate the class and produce meriting yield. SVM incorporates numerous characterization strategies like straight, quadratic, spiral, and so on. In a computerized structure, the image tests are isolated into normal and abnormal. For instance, the samples are normal once the WBCs are not experiencing leukemia and abnormal once the WBCs are impacted by leukemia. This likewise assists us with assessing the exactness.

B. Artificial Neural Network (ANN)

A neural network is a tool that makes use of the biological anxious system to trigger and is designed input processing. An ANN is constructed using a number of neurons that are mutually connected. The same neurons act as processing elements and as an integrated unit. ANN is a smart system that learns from images. Learning is the technique of instilling know-how into a neural community to better put together to execute categorization obligations. There are forms of training methods for neural networks: supervised and unsupervised. In this paper, a double-layer feed-forward network is used which gives more accuracy than SVM.

C. CNN Based Recognition System

Figure 5 shows the basic framework of CNN. It is a type of neural network that has been proven to be very effective in identifying and classifying images. Each neuron picks up information, generates dots, and then tracks it indirectly. However, the complete network shows one distinctive function, ranging from unprocessed images to processed images on the other side.

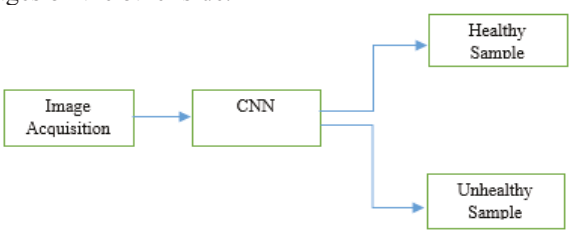

Figure 5. Basic structure of CNN

But these have a loss function in the final layer, however, each technique that we developed here is still adequate. The CNN design creates a certain impression that the information sources are images, which grants us scrambling properties into the design. As a result, the forward function becomes more efficient, and the number of parameters in the network decreases. The CNN network outperforms other categorization algorithms when it comes to grouping.

CNN has a lot of convolutional and pooling layers. The tangled yield is obtained as an actuation map at the point when we give an information image to the principal convolution layer. The convolution layer's filters remove the image's legitimate attributes from the image. Each filter will produce a distinct character to aid in the accurate prediction of elegance. In case we are intrigued to keep up with the size of the picture, we should utilize zero cushioning since it helps to diminish the assortment of attributes. To limit the quantity of characters, pooling layers are utilized. Numerous convolutions and pooling layers are incorporated preceding making the forecasts.

Many unique and advanced characters are extracted in CNN compared to SVM and ANN. The input is flattened and routed in CNN to convert the output into the wide range of categories that the network anticipates. The output layer is then used to create the output, which is then compared against the output layer to determine the error. A single forward and backward flow is termed one training cycle.

The implementation of the submitted work is evaluated by utilizing CNN to have a look at which of these three can provide the best outcomes. A CNN is a form of deep, feed-forward ANN that uses convolutional neural networks with the divergence of a multilayer model designed to minimize pre-processing. In this study, a 2- layered CNN is used. Generally, CNN will work efficiently with a huge quantity of images. But in our study, we have used 120 images and we got an accuracy of about 92.86%. if the quantity of images is increased, then definitely we will get accuracy more than this value.

IV. Experimental Results

In this proposed work, the input database is taken from a standard public benchmark dataset ALL_IDB1. It is publicly open to download the dataset available online [31]. They provide high-quality images. we have used sixty images for training and forty-five images for testing. The proposed technique is assessed with the other existing models and noticed that the submitted technique is more précised and accurate. The microscopic color image of an infected blood cell which acts as an input to our model shown in Figure 6.

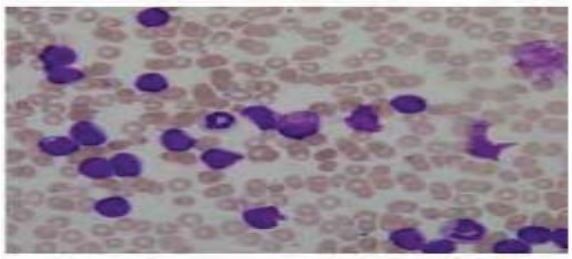

Figure 6. Input Image

CVR Journal of Science and Technology, Volume 22, June 2022
DOI: 10.32377/cvrjst2211

The input image is then subjected to a segmentation process by means of an adaptive k-means algorithm. Thus, in this stage, the nuclei are separated from the image. The output image obtained from the segmentation process is depicted in Figure 7.

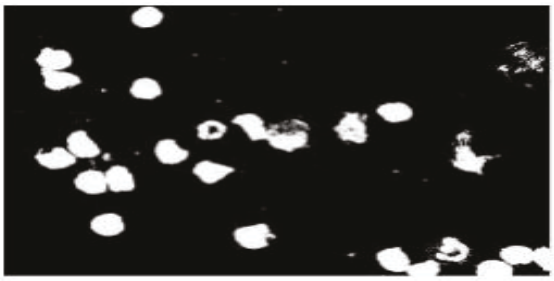

Figure 7. Image after segmentation

Next, image cleaning is carried out. In this stage, we perform two processes: area opening and structural expansion. In this stage, the small objects are filtered out from the focal point of an image. Figure 8 shows the image after the area opening

Figure 8. Image After area opening

The structural expansion uses the elements for expanding the shapes contained in the input image. Here, the pixels are added to the boundaries of objects in the image. The number of pixels added depends on the size and shape of the structuring element that is employed to process the image. The outcome of structural expansion is shown in Figure 9.

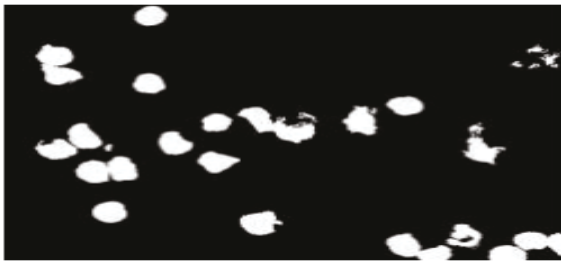

Figure 9. Image After structural expansion

After image cleanup, the feature extraction process is carried out. The basic form descriptors such as area, major and minor axis, the boundary, etc., are applied. Aside from that, the quantity of nuclei in the image sample is counted. The existence of leukemia in the sample will be evaluated in the classification step, and the sample will then be classed as healthy and unhealthy. The classification is accomplished utilizing SVM, ANN, and CNN. The performance of all the three is evaluated based on the parameters like accuracy, error, sensitivity, precision, and specificity. Usually, an image region is said to be positive or negative, depending on the data type. Moreover, a decision for the detected result will be either true or false. So, the prediction will be one of four possible types: true positive (TP), true negative (TN), false positive (FP), and false negative (FN).

Accuracy: It gives the ability of the performance of the whole classifier. It is defined as

$$\text{Accuracy} = \frac{\text{Number of correct predictions}}{\text{Total number of predictions}} \quad (2)$$

Accuracy can also be defined in terms of positive and negative for binary classification as given below:

$$\text{Accuracy} = \frac{TP+TN}{TP+TN+FP+FN} \quad (3)$$

Precision: It is described as the ratio of the quantity of true positive observations to the total quantity positive observations

$$\text{Precision} = \frac{TP}{TP+FP} \quad (4)$$

Similarly, we can write the equation for

$$\textbf{Sensitivity} = \frac{TP}{TP+FN} \quad (5)$$

$$\textbf{Specificity} = \frac{TN}{TN+FP} \quad (6)$$

$$\textbf{Error} = \frac{FP+FN}{T} \quad (7)$$

Where T= TP+TN+FP+FN

The Table which describes the comparison between SVM, ANN, and CNN are illustrated below in table 4.1.

TABLE I.
COMPARISON BETWEEN SVM, ANN AND CNN

Rates	SVM	ANN	CNN
Accuracy	0.89	0.92	0.93
Specificity	1.00	1.00	1.00
Sensitivity	0.72	0.83	0.88
Precision	1.00	1.00	1.00
Error	0.10	0.05	0.04

Depiction of measure of performance parameters of SVM, ANN and CNN in 3D Clustered Column is shown below in Figure 10.

CVR Journal of Science and Technology, Volume 22, June 2022
DOI: 10.32377/cvrjst2211

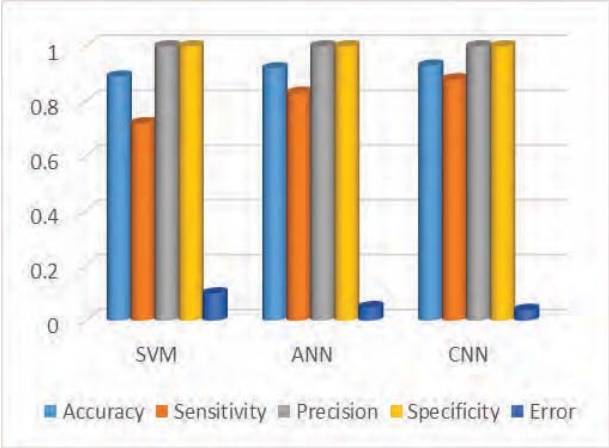

Figure 10. 3D Clustered Column

We can easily observe that CNN yields the best prediction results since it has the highest accuracy, sensitivity, and less error amongst the three approaches.

V. Conclusions

A technique for diagnosing acute lymphoblastic leukemia based on microscopic blood cell images is devised in this study. The diseased area is segmented using adaptive K-means clustering, which is a unique technique. The diagnosis is accomplished by using two techniques. The first uses SVM and ANN, whereas the second uses a DCNN. The finding of leukemia in blood image sample requires more precision.

Along with other parameters, the features like boundaries, region, and the quantity of nuclei recovered from the images will contribute to the accuracy of the projected methodology. As a result, our approach will be able to diagnose and classify input samples with greater precision.

Since it evades the common practice of first segmenting the cells and then the nucleus from an image, the projected methodology will be a watershed moment in leukemia diagnosis. Adaptive K-means clustering is used to separate the nucleus at the initial stage of this work. For flexibility and speed of prototyping image processing options, the proposed methodology is implemented in the MATLAB environment. Along with classifying leukemia into infected and non-infected, this proposed approach investigates classification using SVM, ANN, and CNN and concludes that CNN is a better classifier than the other two for the present research.

It's worth mentioning here that we recorded an efficiency of 89.37% with SVM, 92.16% with ANN and 93.36%. with CNN-based diagnosing technique. Hence, it is observed that CNN based diagnosis technique of Leukemia using microscopic blood cell images is superior because it provides the highest accuracy and sensitivity.

References

[1] C.R., Valencio, M.N., Tronco, A.C.B., Domingos, C.R.B., "Knowledge Extraction Using Visualization of Hemoglobin Parameters to Identify Thalassemia", Proceedings of the 17th IEE Symposium on Computer Based Medical Systems, 2004, pp. 1-6

[2] R., Adollah, M.Y., Mashor, N.F.M, Nasir, H., Rosline, H., Mahsin, H., Adilah, "Blood Cell Image Segmentation: A Review", Biomed 2008, Proceedings 21, 2008, pp. 141-144.

[3] American Dental Association [ADA] (2012). The ADA Practical Guide to Patients with Medical Conditions, ed. Patton L. L. (New York, NY: Wiley;). [Google Scholar]

[4] Katz A. J., Chia V. M., Schoonen W. M. (2015). Acute lymphoblastic leukemia: an assessment of international incidence, survival, and disease burden. Cancer Causes Control 26 1627–1642. 10.1007/s10552-015-0657-6 [PubMed] [CrossRef] [Google Scholar]

[5] Daniels R., Nicoll L. H. (2012). Contemporary Medical Surgical Nursing, 2nd Edn New York, NY: Cengage Learning. [Google Scholar]

[6] Serfontein W. (2011). "Cancer Diagnosed: What Now?" 2nd Edn Bloomington: Xlibris. [Google Scholar]

[7] Manisha P. (2012). "Leukemia: a review article". Int. J. Adv. Res. Pharm. Bio Sci. 2 397–407. [Google Scholar]

[8] Rose M. (2013). "Oncology in Primary Care", 1st Edn Philadelphia: Lippincott Williams & Wilkins. [Google Scholar]

[9] N., Ritter, J., Cooper, "Segmentation and Border Identification of Cells in Images of Peripheral Blood Smear Slides", 30th Australasian Computer Science Conference, Conference in Research and Practice in Information Technology, Vol. 62, 2007, pp. 161-169.

[10] D.M.U., Sabino, L.D.F., Costa, L.D.F., E.G., Rizzatti, M.A., Zago, "A Texture Approach to Leukocyte Recognition", Real Time Imaging, Vol. 10, 2004, pp. 205-206. [5] M.C., Colunga, O.S., Siordia, S.J., Maybank, "Leukocyte Recognition Using EMAlgorithm", MICAI 2009, LNAI 5845, Springer Verlag Berlin Heidelberg, 2009, pp. 545-555.

[11] M.C., Colunga, O.S., Siordia, S.J., Maybank, "Leukocyte Recognition Using EMAlgorithm", MICAI 2009, LNAI 5845, Springer Verlag Berlin Heidelberg, 2009, pp. 545-555

[12] S., Mohapatra, D., Patra, S., Satpathi, "Image Analysis of Blood Microscopic Images for Leukemia Detection", International Conference on Industrial Electronics, Control and Robotics, IEEE, 2010, pp. 215-219.

[13] A., Khashman, E., Esam Al-Zgoul, "Image Segmentation of Blood Cells in Leukemia Patients", Recent Advances in Computer Engineering and Applications, ISBN: 978- 960-474-151-9, 2009, pp. 104-109.

[14] K. Capell, "Meeting Leukemia's Diagnostic Challenge", Business Week, The McGraw Hill Companies, London. http://www.businessweek.com/magazine/content/05_36/b3949007_mz001.htm [27 January 2012]

[15] W., Shitong, W., Min, "A new Detection Algorithm (NDA) Based on Fuzzy Cellular Neural Networks for White Blood Cell Detection", IEEE Transactions on Information Technology in Biomedicine, Vol. 10, No. 1, January 2006, pp. 5-10.

[16] M. Subrajeet, P. Dipti, Satpathi, and Sanghamitra, "Image Analysis of Blood Microscopic Images for Acute Leukemia Detection." IEEE International Conference on Industrial Electronics, Control and Robotics. 2010.

[17] Madhloom, T. Hayan, Kareem, A. Sameem, Ariffin, Hany, "A Robust Feature Extraction and Selection Method for the Recognition of Lymphocyte Versus Acute Lymphoblastic Leukemia." International Conference on Advanced Computer Science Applications and Technologies, ACSAT. 2012.

[18] N.H. Harun, Nasir, A.S. Abdul, Mashor, M.Y. Mashor, R. Hassan, "Unsupervised Segmentation Technique for Acute Leukemia Cells Using Clustering Algorithms." International Journal of Computer, Electrical, Automation, Control and Information Engineering Vol:9, No:1, 2015.

[19] D. Goutam, S. Sailaja, "Classification of Acute Myelogenous Leukemia in Blood Microscopic Images Using Supervised Classifier." International Conference on Engineering and Technology. Maret.2015. [5] V. Ivan, K. Ki-Ryong, L. Suk-Hwan, M. Kwang-Seok, "Acute Lymphoid Leukemia Classification Using Two-Step Neural Network Classifier." IEEE Xplore, Frontiers of Computer Vision (FCV) 28-30 January 2015.

[20] M. Amin, S. Kermani, A. Talebi, et al. "Recognition of Acute Lymphoblastic Leukemia Cells in Microscopic Images Using K-Means Clustering and Support Vector Machine Classifier." Journal of Medical Signals and Sensors, 5(1), pp 49-58, Jan-Mar 2015.

[21] A. Nasir, M. Mashor, R. Hassan. "Classification of Acute Leukemia Cells using Multilayer Perceptron and Simplified Fuzzy ARTMAP Neural Network." 356 The International Arab Journal of Information Technology, Vol: 10, No: 4, July. 2013.

[22] E. Francis, M. Mashor, R. Hassan, et al. "Screening of Bone Marrow Slide Images for Leukemia using Multilayer Perceptron (MLP)." IEEE Symposium on Industrial Electronics and Applications (ISIEA2011). September. 25-28. 2011, Langkawi, Malaysia.

[23] M. Su, C. Cheng, P. Wang. "A Neural-Network-Based Approach to White Blood Cell Classification." The Scientific World Journal Volume 2014, Article ID 796371. 2014.

[24] E. Alférez, A. Merino, and L. Mújica, "Digital Blood Image Processing and Fuzzy Clustering for Detection and Classification of Atypical Lymphoid B Cells." Jornades de recerca euetib, 2013.

[25] M. Amin, S. Nasser., S. Kermani, A. Talebi, "Enhanced Recognition of Acute Lymphoblastic Leukemia Cells in Microscopic Images based on Feature Reduction using Principal Component Analysis". Frontiers in Biomedical Technologies, Volume 2, Issue 3, November 2015.

[26] L. Putzu, G. Caocci, C.Di Ruberto, "Leucocyte Classification for Leukemia Detection Using Image Processing Techniques", Journal Artificial Intelligence in Medicine Vol 62, pp 179 – 191, 2014. [13] Yan Li, Rui Zhu, Lei Mi, Yihui Cao, Di Yao, "Segmentation of White Blood Cell from Acute Lymphoblastic Leukemia Images Using Dual- Threshold Method". Journal of Computational and Mathematical Methods in Medicine. Volume 21 April 2016.

[27] R.G Bagasjvara, Ika Candradewi, SriHartati, AgusHarjo ko "Automated Detection and Classification Techniques of Acute Leukemia using Image Processing: A Review", 2016 2nd International Conference on Science and Technology-Computer (ICST), Yogyakarta, Indonesia

[28] N., H., A., Halim, M., Y., Mashor, R., Hassan, "Automatic Blasts Counting for Acute Leukemia Based on Blood Samples", International Journal of Research and Reviews in Computer Science, Vol. 2, No. 4, August 2011, pp. 971-976

[29] S. Jayaraman, S. Esakkirajan,T.Veerakumar, "Digital", http://www.mhhe.com/jayaraman/ dip.

[30] Farah H. A. Jabar, Rosline Hassan, "Image Segmentation Using an Adaptive Clustering Technique for the Detection of Acute Leukemia Blood Cells Images" 2013 International Conference on Advanced Computer Science Applications and Technologies'

[31] R. Donida Labati, V. Piuri, F. Scotti, "ALL-IDB: the acute lymphoblastic leukemia image database for image processing", in *Proc. of the 2011 IEEE Int. Conf. on Image*

E-ISSN 2581 – 7957
P-ISSN 2277 – 3916

CVR Journal of Science and Technology, Volume 22, June 2022
DOI: 10.32377/cvrjst2212

Predicting Diabetic Retinopathy using Deep Learning

P. Prathyusha[1] and A. Mallareddy[2]
[1]PG Scholar, CVR College of Engineering/IT Department, Hyderabad, India
Email: prathyu54parakala@gmail.com
[2]Assoc. Professor, CVR College of Engineering/IT Department, Hyderabad, India
Email: dramallareddy@gmail.com

Abstract: **Research works done so far are majorly focused on the risk factors which include diabetic retinopathy (DR); however, it is still unclear up to what extent the risk factors are associated with diabetic retinopathy. We use early prevention procedures considering diabetic retinopathy during the most high-risk group with better detected DR-related risk factors. Machine learning, a recent advancement during state-of-the-art technology, plays a critical and crucial role during image processing applications such as biomedical, satellite image processing & Artificial Intelligence applications includes object identification & recognition, among others. The goal of this study is to look towards a deep-learning system to predict the probability of diabetic retinopathy developing within two years among people with diabetes. Using colour fundus pictures, deep-learning algorithms predict the development regarding diabetic retinopathy and the diabetic systems were independent which were more informative to the existing risk variables. The proposed works aims to develop and validate the deep learning system towards the prediction of progression regarding diabetic retinopathy of diabetic individuals to receive tele-retinal diabetic retinopathy screening during a primary care environment.**

Index Terms: **Diabetic Retinopathy, Deep learning, Color fundus photographs, Screening.**

I. Introduction

There may exist billions of people who suffer from vision impairment, and certain issues may yet exist unsolved. Diabetic retinopathy is also often known as diabetic eye disease which develops when diabetes damages the retina. It's a systematic condition that affects up to 80% of the diabetic patient's eye who have been considered as 20 or above years. Inspite of these alarming statistics, research suggests that not less than 90% of the new case might exist and can be avoided if the eyes were treated, monitored properly and by keenly observing the changes. This is the sample images of the different stages of diabetic retinopathy in Figure 1. Diabetic retinopathy was more likely observed towards developing those who had diabetes considering a long time. Previous research has primarily concentrated on reducing one key risk factor like glucose levels; there are some more studies that investigate other risk factors that consider Diabetic Retinopathy [1]. Diabetes mellitus causes diabetic retinopathy, a micro vascular condition. It determines through a patient's history regarding their diabetes problems [2].

Diabetic retinopathy is a highly specific vascular consequence regarding both type 1 and type 2 diabetes provides a clear correlation between prevalence and diabetes duration.

Diabetic Retinopathy (DR), on other hand, can be frequently undiscovered until it has progressed towards point where it is endangering one's eyesight. Due to low adherence and access towards retina screening visits, current state regarding DR screening during real world, based on assessments regarding color fundus photographs (CFPs) through a retina specialist otherwise a trained grader, leaves a large proportion regarding the patients who have not been diagnosed and thus receiving medical help too late [3,4]. Given the pandemic magnitude regarding diabetes community, in-person expert exams exist unfeasible and unsustainable [5, 7]. Regardless, early detection & prevention regarding DR progression exist critical towards reducing rising threat regarding Diabetic retinopathy.

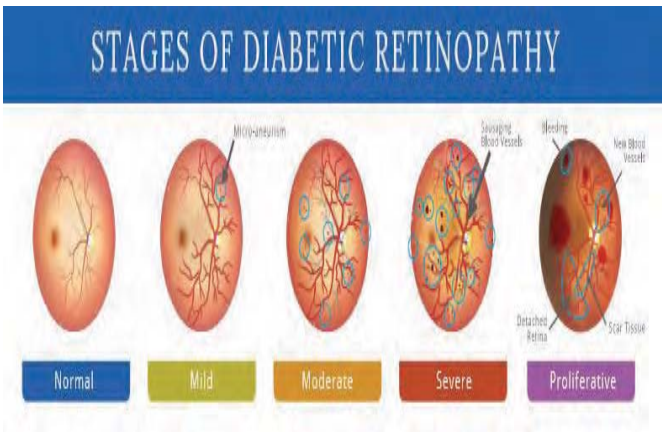

Figure 1. Sample images of the retina

Diabetes is caused when pancreas fails to produce enough insulin or otherwise the body is unable to process it. Vision loss can be avoided if they are detected early.

There exist two forms of diabetic retinopathy: non-proliferative & proliferative. Non proliferative stage is the first stage of diabetic retinopathy detection. Patients with diabetes should consult a doctor and proper clinical tests should be done to discover the disease in the early stage and to stop vision loss or eye related problems. Treatment

Received on 16-09-2021, Revised on 13-11-2021, Accepted on 09-02-2022.

CVR Journal of Science and Technology, Volume 22, June 2022
DOI: 10.32377/cvrjst2212

regarding the vision-threatening retinopathy prevents 98 percent of the visual loss caused through diabetic retinopathy.

With the advancements in numerous technologies such as Internet of Things, big data, cloud computing, artificial intelligence, and DL. Deep learning has become increasingly important during the categorization approaches. The various stages of diabetic retinopathy can be classified in table 1.

Retinal examination can be identified during several phases: such as observing color change in the image. Traditional classification strategy and DL processes are the two machine learning procedures considering solving diabetic retinopathy, because it is built on convolutional neural networks, we gain superior accuracy, classification results, & prediction regarding human retina features.

TABLE I.
STAGES REGARDING DIABETIC RETINOPATHY

S.NO	DESCRIPTION	STAGE OF DR
1	Small areas of balloon – in the retina's tiny blood vessels called micro aneurysms may leak fluid into the retina	Mild NPR
2	Blood vessels that nourish retina may swell and damaged, so it is not able to transport blood	Moderate NPDR
3	Many more blood vessels are blocked, for the supply of blood to the blood vessels.	Sever NPDR
4	Advance stage, growth factors secrete by the retina trigger the proliferation of new blood vessels, which grow along the surface of the retina	PDR

There can be repeatedly no symptoms during the early stages of diabetic retinopathy. Changes in the vision can be observed as, difficulty of reading, seeing distant things, and other signs people may or may not notice. These modifications may appear and disappear.

Causes: When you have immoderate sugar within the blood, tiny blood vessels that nourish your retina gets closed, cutting off your retina's blood supply. As a result, these eyes make a conscious attempt to produce new blood vessel. These blood vessels, on the other hand, do not form properly and are prone to leaking.

II. RESEARCH MATERIAL

A. Motivation Towards This Paper

Several factors influence the annual screening by considering the global population affected through diabetes. Among them lower risk groups can exist and safely screened less frequently than with high risk groups.

B. Dataset

As we know that dataset is a collection of different and useful information about various things, persons etc. considering an example of a patient's statistics or data, it stores their information about the age, gender, state, religion, language etc. But basically, DR Dataset contains data in the form of images.

Some of the existing datasets are STARE, DRIVE, Messidor-2, Messidor, CHASE-DB 1, FAZ (Foveal Avascular Zone), ARIA, DR2, DR1, DRiDB.
Some of the accessibility regarding to the diabetic dataset is given in table 2.

Some of the private datasets:

1. *HUPM dataset:* It contains about 250 fundus images among them 200 images were labeled as diabetic retinopathy and 50 were labeled as normal images. This dataset abides used during works [3].

2. *SNDRSP dataset:* Singapore National DR Screening Program collected a count regarding 1, 97,085 fundus images. This dataset is used during [4] for research related towards eye diseases.

3. *JMU dataset:* This dataset contains 9939 digital fundus images. These images were recorded through a RGB camera regarding 45o FOV. This dataset is one of the private datasets used in [5].

Some of the public datasets:

1. *Kaggle dataset:* It is a well-known dataset for the use of retinal images to find the diabetic retinopathy. It mainly contains 88,702 retinal images in which 35,126 images are used for training and 53,576 for testing. Gulshan et al. [6] it uses the dataset to identify the diabetic retinopathy.

2. *DIARETDB1dataset:* It is also one of the datasets considered for diabetic retinopathy identification. There can be 89 retinal pictures in the total dataset. Among them five pictures were classified like normal &84 image were likely to classify as diabetic retinopathy. Bui et al. [7] used dataset used to detect cotton wool of diabetic retinopathy study.

3. *Messidor-2:* It contains fundus images which were captured using a camera at 45 degrees FOV. It contains about 1784 digital fundus

TABLE II.
ACCESSIBILITY OF DIABETIC RETINOPATHY DATASETS

S.NO	NAME OF DATASET	STATUS	
		AVAILABLE	NOT-AVAILABLE
1	Kaggle	YES	
2	E-Ophtha	YES	
3	ROC	YES	
4	DIABETD B1		
5	DIABETD B0	YES	
6	STARE	YES	
7	DRIVE	YES	
8	Messidor -2	YES	
9	Messidor	YES	
10	CHASE_D B1	YES	
11	FAZ	YES	
12	ARIA	YES	
13	DR2	YES	
14	DR1	YES	
15	DRiDB	YES	
16	HUMP, Cadiz, Spain		YES
17	KMCM, India		YES
18	LECHCR India		YES
19	SNDRSP		YES
20	JMU		YES
21	CLEAPTRA		YES
22	Moorfields Eye Hospital		YES
23	TMUMH		YES

A. Procedure

The basic procedure or the flow of the system is shown in the Figure 2 shows the flow of the model.

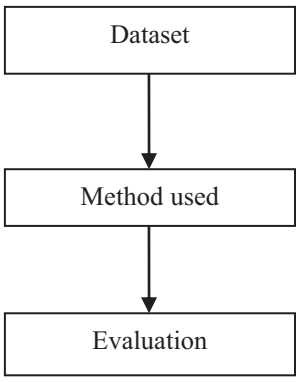

Figure 2. Basic components of the system

B. Performance regarding DL approaches:

Deep learning gives high performance in the areas of image processing and to find out diabetic retinopathy using the images of fundus camera. The performance regarding the traditional and Deep learning approaches can be shown in the table 3.

TABLE III.
PERFORMANCE REGARDING TRADITIONAL & DL APPROACHES

TECHNIQUE	RESEARCH STUDY	DATASET	ACCURACY
Deep learning	CNN	DIARTDB1	98.50%
Traditional	Morphological operations	DIARTDB1	97.75%
Deep learning	ANN	DIARTDB1	96
Traditional	Random forest Classifier	DIARTDB1	93.58%
Deep learning	Random forest Classifier	DIARTDB1	98%
Traditional	Fuzzy Technique	DIARTDB1	93%

III. RELATED WORKS

A) IDF diabetes atlas: global estimates considering prevalence regarding diabetes considering 2015 & 2040.

To develop present estimates regarding the diabetes of national, regional, & global impact considering from 2015 to 2040. A systematic literature analysis was carried out towards discovering the statistics sources on diabetes prevalence since research conducted between 1990 and 2015. Estimates considering the countries lacking data a can be modeled using extrapolation from similar countries among accessible data, utilizing an analytic hierarchy procedure for choosing most applicable research or method by considering each country. Smoothed age-specific estimates were generated using logistic regression models were applied for UN population estimates. Diabetes prevalence, diabetes-related fatalities, and diabetes-related health spending are more towards climb around world, among significant social, economic, & health-system.

Diabetes prevalence during adults aged 20–79 years were estimated 8.8% during 2015 and is expected to rise 10.4% through 2040. Diabetes' high incidence during the adults has significant social, economic, and developmental consequences. Governments are under increasing pressure towards establishing policies to reduce the risk factors among the type 2 diabetes and gestational diabetes. To guarantee all persons living with diabetes have proper access to the treatment. IDF continues to act like an advocate considering persons having diabetes through educating not only individuals but also governments keep their efforts done in the direction of the prevention and managing condition.

B) Screening intervals considering diabetic retinopathy & implications considering care.

To examine the lower-risk population that could exist and can be evaluated by sight-threatening diabetic retinopathy (DR) are less frequently screened than once a year. Patients with no signs of diabetic retinopathy in neither of the eyes are considered at low risk within 2 years

CVR Journal of Science and Technology, Volume 22, June 2022
DOI: 10.32377/cvrjst2212

irrespective of the methods used. Figure 3 shows the variation of DR in the left and right images.

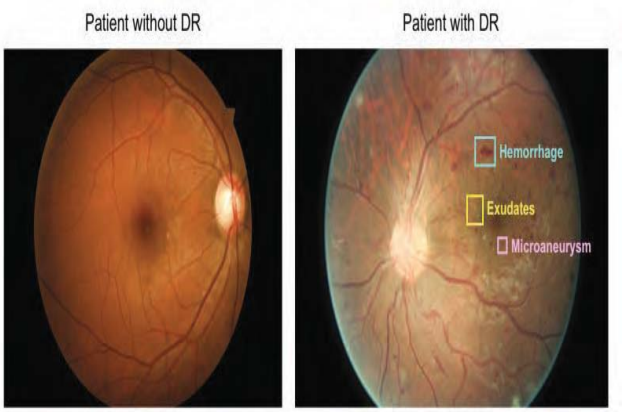

Figure 3. Example regarding fovea-centered color fundus photographs (CFPs) regarding a patient without DR (left) & a patient among signs regarding DR (right)

The goal of the study abides towards how well these central retinal fields predicted DR progression when compared towards peripheral retinal fields (F3, F4, F5, F6, & F7). The peripheral retinal fields (F3, F4, F5, F6, & F7) were discovered to be the most useful predictors as they include in the portions of the retina away from both the fovea and the optic nerve. Our result is supported by performance comparisons of models trained exclusively on central fields (F1 & F2) against models trained on all seven retinal fields.

C) Diabetic retinopathy and diabetic macular edoema disease severity measures proposed for international clinical use.

To improve the communication and treatment coordination among diabetic physicians we create a global agreement on clinical disease severity categorization techniques for diabetic retinopathy and diabetic macular edoema. Clinical diabetic retinopathy disease severity scales were developed.

A group of 31 people representing comprehensive ophthalmology, retina subspecialties, endocrinology, and epidemiology from 16 different countries. The group accepted the first clinical categorization system based on publications like the Early Treatment Diabetic Retinopathy Study and the Wisconsin Epidemiologic Study on Diabetic Retinopathy. By e-mail, each participant evaluated it and the responses were categorized using a custom Delphi system. Separate systems for diabetic retinopathy and macular edoema were developed at a subsequent meeting. Members of the group then reevaluated them, and a modified Delphi procedure was used to determine degrees of the agreement once more. Several classification schemes have been agreed upon. Three levels of low risk, a fourth level of severe non-proliferative retinopathy and a fifth level of proliferative retinopathy make up a five-stage disease severity classification for diabetic retinopathy. There are two forms of diabetic macular edoema: apparently present and apparently lacking. Macular edoema can be classified as a function of its distance from the central macula if the screener's abilities and equipment allow them to make an informed decision.

There appears to be a definite requirement because diabetic retinopathy and diabetic macular edoema are classified using evidence-based clinical categorization systems that are worldwide comparable. Diabetic retinopathy and macular edoema are to be appropriately classified using the recommended clinical categorization systems. These technologies exist expected to exist beneficial during increasing both diabetes screening & communication & discussion among those who care considering these patients.

D) Two-year incidence of retinal intervention within individuals with modest otherwise non-diabetic retinopathy who were screened by telemedicine.

Importance: Most diabetic patients have little or nil retinopathy on initial inspection. Following these people long-term, outcome could help us to learn more about how it provides check out.

Objective: Finding how many people with mild retinopathy or no signs of retinopathy will need retinal action to improve within two years of their initial retinal examination.

Designs, settings, & participant: Patients who had low or otherwise no retinopathy on fundus photographs after being examined for diabetic retinopathy through a telemedicine programme at Kaiser Permanente Southern California was included within this retrospective cohort research.

Exposure: Retinal treatments were conducted within two years of screening.

Main outcome & measures: during 2012, patients with minimal or no retinopathy on first screening images had their medical records CPT code for intravitreal injections, retinal lasers, and pars plana vitrectomy have been reviewed. When patients were recognized as having received these procedures within two years regarding their retinal evaluation, their medical records were manually evaluated for further description.

Fundus photographs of regular checkup has taken for 1, 16,134 patients were taken and their (mean [SD] age, 58 [12.8] years; 54,582 [47.0 percent] female; 46,453 [40.0 percent] male). Out of these people 79,445, including 69,634 people show no signs of retinopathy and 9,811 people show some or little signs of retinopathy within two years of checkup.

The discovery to put forward for the patient with mild or no signs of the baseline retinopathy are unlikely to receive retinal therapies within two years after undergoing a retinal examination. Because most people are not likely to have vision-loss conditions if they have necessary treatment. It indicates that the recommended checkup intervals for the risk-free individuals to be reasonable if it does not result in a worse condition within the subsequent years.

IV. Proposed Method

Now a day's machine learning, deep learning has become an emerging hot research topic for image processing [12] and highly efficient [13]. We mainly focus on convolution neural networks for the process of image classification. CNN mainly consists of an input layer, hidden layer, and an output layer. Here the hidden layer plays a prominent role as the hidden layers increase the complexity of the system or

CVR Journal of Science and Technology, Volume 22, June 2022
DOI: 10.32377/cvrjst2212

model also increases. It has some components like convolution layer, activation layer pooling layer or sub-sampling layer, fully connected layer and finally the loss layer. The main basic flow of any model is shown below (Figure 4).

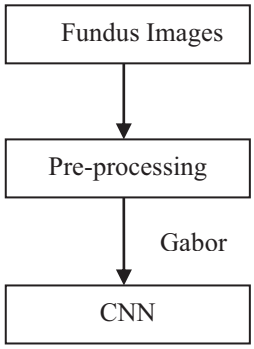

Figure 4. Proposed method

V. Risk Factors of Diabetic Retinopathy

Long-term diabetes is the key risk variable assessed during a pooled analysis of the population-based research throughout world [8]. High hemoglobin A1C (HbA1C) levels and high blood pressure were also found towards the existing risk factors during this study [9]. According to UKPDS, incidence regarding diabetic retinopathy is closely linked towards the length ofT2D and a lower HbA1c level to reduce the chance in developing DR during these patients [10]. During clinical practice, it has been noted that certain individuals among long-term managed HbA1c levels still have a risk regarding diabetic retinopathy during T2D [11]. Most relevant risk factor is identified through every piece of empirical research diabetes duration. High fasting glucose, high postprandial glucose and high HbA1C are the symptoms of poor glycemic control. All three provides information on distinct aspects of diabetes and should be considered.

VI. Stastical Analysis

To compare prognostication using a deep-learning system so that utilising risk variables, we can develop a set to train univariable and multivariable logistic regression models then to tested them on validation sets. We looked at the calibration to make sure that the deep-learning algorithm wasn't overconfident on the development set. Each dataset contained its own set of risk variables, and each experiment includes the patients who had risk factor statistics. Within the internal validation sample, glycated haemoglobin, self-reported diabetic control, years with diabetes, and insulin were the risk factors. Diabetes control was assessed as poor, fair, moderate, outstanding, or otherwise exceptional.

Performance evaluation metrics: evaluation metrics also plays a vital role during classification. Identification regarding the stage of diabetic retinopathy using a fundus camera should exist pre-processing like median filtering, average filtering & also adjustment regarding contrast during image [14].

The outcome regarding the statistics used during the medical treatment was mainly of two types. One becomes class among the disease and the second one becomes towards class without disease. So, the correctness regarding the disease exists correctly estimated through specificity, sensitivity measures respectively.

VII. Discussion

We have developed a deep-learning algorithm for predicting the onset of diabetic retinopathy within two years which we tested using datasets that included an internal validation set of images from predominantly Hispanic patients in the United States, as well as an external validation set of images from Thailand. Deep-learning system performed well on both datasets and during isolation & risk.

Deep learning accepts color fundus pictures towards predict advancement on Early Treatment Diabetic Retinopathy Study scale through two or more levels.

VIII. Conclusions

The determination of clinical relevance will be accepted by the patient-level examination preferably within prospective settings. Findings show that a deep-learning system may be built to improving diabetic risk categorization.

Here, we developed a systematic DL process considering detecting phases regarding retinopathy during diabetic patients. A clear view regarding the collection of datasets is also included. Choosing a performance metrics plays a vital role during outcome. Designing such system will give more information and identification to different stages of diabetic retinopathy. Although there exist various approaches towards detect, but DL models gives us more accuracy and providing future directions to the researchers. It mainly focuses on betterment of the patient life with minimum cost.

IX. Future Direction and Challenges

We can also apply feature optimization algorithms to this work. So, in the next paper we are planning to apply genetic algorithm or Gabor feature algorithm to optimize image statistics to get better prediction accuracy [15].

It is necessary to build an effective DL – based procedure which should have consumed less time and less expensive. Performance regarding the present model (deep learning) exists improved through using a cascade regarding dynamic sized frameworks. As a result, cost regarding training considering individual models to reduce and they will be able to work independently.

References

[1] Cheung N, Mitchell P, Wong TY. Diabetic retinopathy. Lancet 2010; 376: 124–36.
[2] Solomon SD, Chew E, Duh EJ, et al. Diabetic retinopathy: a position statement through American Diabetes Association. Diabetes Care 2017; 40: 412–18.
[3] Q. Abbas, I. Fondon, A. Sarmiento, S. Jiménez, & P. Alemany, ‘‘Automatic recognition regarding severity level considering diagnosis regarding diabetic retinopathy using deep visual features,’’ Med. Biol. Eng. Comput., vol. 55, no. 11, pp. 1959–1974, Nov. 2017.

[4] J. Kaur & D. Mittal, ‘‘A generalized process considering detection regarding vascular structure during pathological retinal images,” Biocybernetics Biomed, Eng., vol. 37, no. 1, pp. 184-200,2017.
[5] Sonali, S. Sahu, A. K. Singh, S. P. Ghrera, & M. Elhoseny, ‘‘A process considering de-noising & contrast enhancement regarding retinal fundus image using CLAHE,’’ Opt. Laser Technol., vol. 110, pp. 87–98, Feb. 2019.
[6] V. Gulshan, L. Peng, M. Coram, M. C. Stumpe, D. Wu, A. Narayanaswamy, S. Venugopalan, K. Widner, T. Madams, J. Cuadros, R.Kim, R. Raman, P.C. Nelson, J.L. Mega, & D. R. Webster, “Development & validation regarding a DL algorithm considering detection regarding diabetic retinopathy during retinal fundus photographs,” JAMA, vol. 316, no.22,pp. 2402-2410, Dec. 2016.
[7] T. Bui, N. Maneerat, & U. Watchareeruetai, ‘‘Detection regarding cotton wool considering diabetic retinopathy analysis using neural network, during Proc. IEEE 10th Int. Workshop Comput. Intell. Appl. (IWCIA), Nov. 2017, pp. 203-206.
[8] M. D. Abràmoff, Y. Lou, A. Erginay, W. Clarida, R. Amelon, J. C. Folk, & M. Niemeijer, “Improved automated detection regarding diabetic retinopathy on a publicly available dataset through integration regarding deep learning,’’ Investigative Opthalmol. Vis. Sci., vol. 57, no. 13, pp. 5200-5206, oct.2016.
[9] Wilkinson CP, Ferris FL 3rd, Klein RE, et al. Proposed international clinical diabetic retinopathy & diabetic macular edema disease severity scales. Ophthalmology 2003; vol. 110, pp. 1677- 82.
[10] Mehlsen J, Erlandsen M, Poulsen PL, Bek T. Individualized optimization regarding screening interval considering diabetic retinopathy: a new model. Acta Opthalmol. 2012; 90(2):109 – 114.
[11] Bearse MA Jr, Adams AJ, Han Y, et al. A multifocal electroretinogram model predicting development regarding diabetic retinopathy. Prog Retina Eye Res 2006; 25: 425–48.
[12] Bakator M, Radosav D. Deep learning and medical diagnosis: a review of literature Multimodal Techno Interact 2018;2(3):47
[13] Guo Y, Liu Y, Oerlemans A, Lao S, Wu S, Lew MS. Deep learning for visual understanding: a review. Neurocomputing 2016;187:27–48.
[14] Zhang W, et al. Automated identification and grading system of diabetic retinopathy using deep neural network.Knowledge Base Systems 2.19: 175:12-25.
[15] Raghava, M., B. Rambabu, and V. Dattatreya. "Hooke and Jeeves Pattern Search Method and Global Optimal Solution." CVR Journal of Science and Technology 17.1 (2019): 67-72.

E-ISSN 2581 – 7957
P-ISSN 2277 – 3916

CVR Journal of Science and Technology, Volume 22, June 2022
DOI: 10.32377/cvrjst2213

Design and Analysis of Injection Mold for Plastic Rivet with Buttress Thread Profile: DFM Approach

Neeraj Kumar Jha[1], Vidyanand Kumar[2]
[1]Assoc. Professor, CVR College of Engineering/ Mechanical Engg. Department, Hyderabad, India
Email : neerajjha.me@gmail.com
[2]Asst. Professor, CVR College of Engineering/ Mechanical Engg. Department, Hyderabad, India
Email: vidyanandk75@gmail.com

Abstract: **Manufacturing is the process of transforming raw materials to useful product. Due to this transformation the finished product used to be costlier than the raw materials. Generally, the entire process is planned to maximize profit. Different attributes help to achieve this goal. The fulfilment of customer needs or use of the product is unalterable, but many other aspects can be adjusted in the focus of ultimate profit. Selection of material, process selection and design of the part are few among such attributes. Injection molding is one of the widely used processes to process polymers, especially thermoplastics to any required shape. This paper aims to make rivets with Polypropylene (PP) using the injection molding process. The paper proposes a new design for plastic rivets with modified buttress profile. Simultaneously this work checks the suitability of making such rivets by injection molding process. It was found after the software simulation that such new product can be easily molded without any considerable defects. The software implemented in this works are, UG Nx 12.0 for solid modeling of the parts, Autodesk Moldflow Adviser 2019 for flow analysis and UG Nx 12.0 Design simulation for stress analysis.**

Index Terms: **Injection molding, Buttress Threads, Rivet, Polypropylene, Plastic Mold, Tool, Inserts.**

I. Introduction

Design for manufacturing (DFM) is a tool that is used during product development phase with the aim of ease of design and manufacturing of the component [1]. It is prudent to use DFM principles while designing a new product for the assurity that not just the need of the product is fulfilled but the design and manufacturing processes of the product is also done in the most efficient way [2]. Implementation of DFM principles ensures, standardization, quality improvement of product, reduction of number of parts and steps in manufacturing as well as manufacturing cost reduction. Similar and improved manufacturing philosophies that evolved from DFM are Design for Assembly (DFA), Design for Manufacturing and Assembly (DFMA), Design for Excellence (DFX) etc. All these terms collectively aim at design and manufacturing excellence without compromising with the profit. In general, there are no set rules for implementation of DFM. It depends on the manufacturing process or the set of operations to be followed for a product, in order to fulfill its aim of decreasing number of processes and steps to gain maximum profit. As minimum number of parts and optimized assembly sequence are considered as healthy DFA practices, in the same way the best process selection, the best material selection, adequate tolerance selection and the least process sequence can be considered as pillars of DFM. A suitable process selection is an unavoidable step in the production process. Many activities in process planning are influenced by the selection of manufacturing process selected for the manufacturing of a part [3]. Though a part can be prepared by various manufacturing processes, a good designer takes decision based on parameters like estimated time, cost involved, skill involved, expected quality etc.. Correct selection of material is very important for operational aspect of a product. Additionally, it influences the manufacturing operation selection also. Different materials are treated differently, utilizing adequate manufacturing processes. Time and energy consumed in the processing, affects the cost of production. Adequate tolerance selection is another important factor in DFM implementation. Close tolerance dimensions keep the cost of production on the higher side, which is not needed unless it is required. Thus, open tolerances should be given as maximum as possible for the parts to control the cost of manufacturing. Contribution of least process sequence can never be avoided in DFM as well as in product process planning. It is evident that more processes involve more inventory and resources, thus making the entire processes costlier. Many revolutionary changes are made worldwide in the consumer product industries. The outcomes were phenomenal and resulted in cost saving, time saving, sustainable product development etc. Automobile industries are the most benefited sector from the implementation of DFM principles. Advancement in material technology and manufacturing processes has added extra dimensions in the implementation of DFM principles. Evolution of different grades of plastic and their processing methods have made exceptional changes in the field of design and manufacturing. A plastic material, due to its unique properties is becoming the most suitable material for many engineering applications. One of the best properties of plastic is its moldability, which makes it more suitable to come to a usable shape [4]. Usually, reusable grade of plastic i.e., thermoplastics are processed by injection molding process. Nearly 70% of total plastic products are made by this process [5]. The process utilizes a metal mold with shaped cavity in it. Hot plastic in semi solid phase is injected to the shaped cavity. The mold is opened, and the part is ejected from the cavity after cooling and solidification of the shot volume. The process is simple to adapt and opted for mass production of small to big size plastic parts with simple to complex profiles. The process is simple and can be automated also but, if the process parameters are not controlled properly the defects will be

Received on 08-04-2022, Revised on 18-04-2022, Accepted on 25-05-2022.

unavoidable. Recent advances in analysis and simulation techniques are useful for designers to take care of defects [6]. Utilizing these techniques one can easily estimate defects without wasting time and money. Autodesk Moldflow Advisor is one such simulation software which replicates the actual injection molding process. It utilizes actual process parameters viz. injection pressure, mold and injection temperature, material properties etc. to give output like cycle time, cooling time, defects visualization and molding quality corresponding to a part model [7, 15].

This paper attempts to redesign plastic rivets and see its feasibility to be manufactured by the injection molding process. Rivets are mechanical members which are used to create semi-permanent joint between sheets or plates. Metallic rivets were much in use till there were limited welding processes available for joining thick metal plates. Development of welding technology limited the use of rivets but the place of rivets in engineering applications is unavoidable. After revolution of plastic as engineering materials, plastic sheets were being made by the calendaring process and rivets were used for joining them. In various consumer products, especially in automobiles plastic rivets can be seen joining plastic parts together. Advantage of using rivets is that they hold the joining parts permanently but if there is need of detaching the parts, rivets are broken, and the joined parts remains unharmed. Parts of metallic rivets are formed by joining. Plastic rivets implement snap fits for their joining. In later portion of this paper product design of plastic rivet is explained, further with help of a sample mold its simulation for injection molding process is done. Its operation and stress analysis are also performed. There is crucial need of such innovative approaches in order to simplify the production process.

II. Product Design

A. Product Modifications

The existing plastic rivets are made in two parts which interlock with each other after they are inserted through the hole made in the parts to be joined. Snap fits are widely used for interlocking across the various existing models. In this research work, buttress profile was used for the interlocking instead of snap fits. The purpose is of utilizing high load carrying capacity of the profile to prevent opening or the rivet. The terms buttress profile here must not be wrongly considered as buttress threads. Only the cross-section is being used here but not the helical profile. Buttress profiles are asymmetric profiles used in buttress threads, preferably used when there is need of bearing high load in one direction only. Fig. 1 shows a standard buttress profile which is as per 45° DIN 2781 standards, while Fig. 2 and Fig. 3 (All dimensions are in mm) indicates the part drawing with modified buttress profile which is used for this work. The first part with internal buttress profile is termed as body while its counterpart with external buttress profile is termed as core. The overall dimension of the rivet is taken from standard dimension of a snap head rivet with body diameter 10mm. The snap head profile is in the same standard proportion.

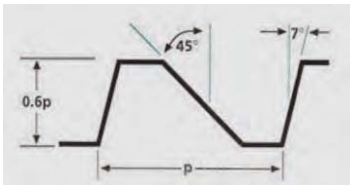

Figure 1. Buttress profile (p: pitch)

The pitch value (p) is considered 1.5 from standards. The internal diameter of rivet body and the external diameter of rivet core are taken as empirically compatible dimension.

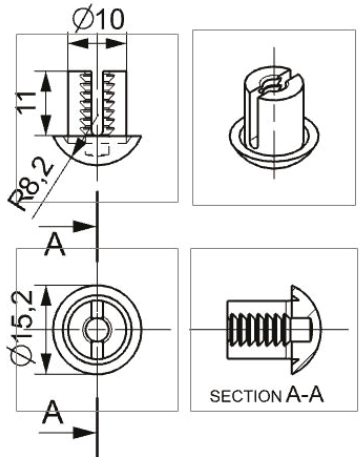

Figure 2. Snap head rivet body drafting

Apart from the modified buttress profile, few other design features can also be visualized. The body is profiled by two slotted recesses on it. This allows proper insertion of core in the body while applying them against a joint

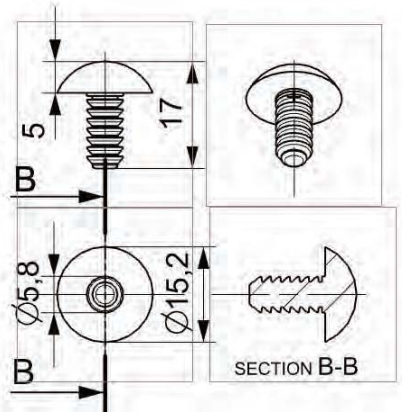

Figure 3. Snap head rivet insert drafting

B. Embodiment Design

For any product the process parameters lead a crucial part in determining its feature details and ultimate form. Thus, a product's final form can be decided after many critical decisions are taken. The embodiment design is primary and important phase of product design. At this phase important decisions like material selection, process selection, component size etc. are taken. The part is modified accordingly and further process planning for corresponding

CVR Journal of Science and Technology, Volume 22, June 2022
DOI: 10.32377/cvrjst2213

to a part is done [8]. The material for the part was decided as Polypropylene (PP) for instance, due to its usually low range of processing temperature and adequately high range of strength. Other suitable materials can be HDPE as well as PVC for this application. Other advantages of using these materials can be reusability, good surface finish and relatively low density. It is evident that these grades of plastics can be conveniently processed by injection molding process. Other important properties for the point of view of process parameters are shown in Table 1.

TABLE I.
MATERIAL SPECIFICATION , POLYPROPYLENE (PP)

Density	946 kg/m³
Melting Point	160 °C
Formula	$(C_3H_6)_n$
Type	Thermoplastic
Flexural Strength	40 N/mm²
Shrinkage	1-2.5% mm/mm
Tensile Strength	32 N/mm²
Injection Temperature	32-36 °C
Heat Deflection Temperature	100 °C
Specific Gravity	0.91

In the phase of embodiment design the designers conventionally choose material and processes based on their experience or it is done based on the experience of the manufacturing engineer. Once it was decided that the part will be made from PP using injection molding process, the part should be made suitable for injection molding process. Thus, as per DFM principles adequate fillets, draft etc. should be given. The plane of symmetry is considered as parting line. On all the faces, which are in the direction of ejection the adequate drafts are to be given. As the part is mostly curved body thus, no drafts are needed. Fillet is an important concern for proper filling of the mold. On all necessary surfaces adequate fillets were given. This can be observed from the drawings as well as from the solid model shown in Fig. 4. In the figure the left side image shows core and body engaged in fully lock position. In the right-side image, body is kept 50% translucent for better visibility. Empty space under snap head was an attempt to reduce material accumulation so that shrinkage cavities can be avoided. This gap additionally acts as compression member for tight fitting of rivet. This can be ignored in the manufacturing phase.

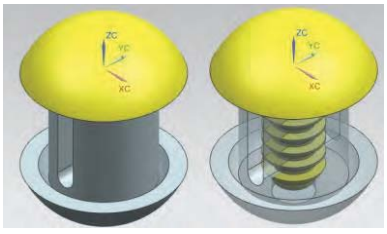

Figure 4. Solid model: snap head rivet

The thick mass analysis is shown in Fig. 5. Minimum wall thickness is considered as 5mm. Green color is indicating more than 5mm thick wall where less than 5mm thick wall is indicated by red color. Thick mass regions may attract shrinkage cavities which can be taken care by design as well as process parameters. Its solution as per design is making weight reduction pocket, as it is made under snap head of the body. Shrink cavities can be taken care by high injection pressure as well as by packing pressure. For specific component profiles, proper cooling can also help to overcome shrink cavities.

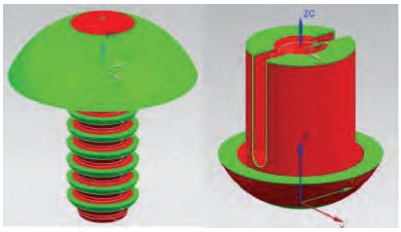

Figure 5. Thick mass analysis

The proposed design is capable to join variable thickness of sheets. It is observable that gap between head of body and the insert is 10mm but, it can accommodate sheets with total thickness 1.5mm to 15mm. The gap between each step is 1.5mm. The gap between heads can be made 15mm when few steps are effectively in contact. This functionality is unavailable in most of the existing plastic rivets. To accommodate length, extra part can be sliced. Snap head also can be rubbed off if there is need of flat surface. By considering all the aspects of design as per ease of manufacturing the part without defect, there are few changes made in the body design. It is indicated in Fig. 6. The gap under snap head is filled and a through hole is provided to prevent mass accumulation. The same will help in positioning the insert to achieve internal buttress profile.

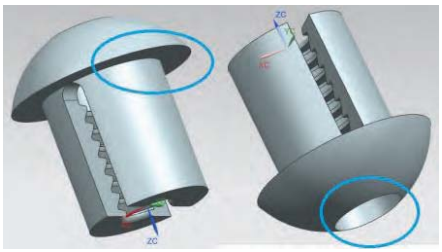

Figure 6. Final design changes in rivet body

III. VALIDATION

The designed component must be validated to check if it is meeting the design and manufacturing expectation. Stress calculation supported by design simulation UG Nx 12.0 results was done for validation. Similarly, its manufacturability was predicted by Mold flow adviser.

A. Stress Analysis

A rivet fails mainly in three situations, viz., shearing, tensile failure and crushing. While installing metallic rivets against metallic plates, rivets get work hardened and their strength and hardness increases. This hardened rivet when pulled along rivet plate, it causes elongation of hole in the plate in which rivets are installed. Such failure of riveted joints is termed as crushing or bearing failure. Unlike metals, plastic shows least or negligible chances of work hardening. Thus, crushing failure of plastic rivets is not

CVR Journal of Science and Technology, Volume 22, June 2022
DOI: 10.32377/cvrjst2213

being given much importance in this work. Shearing of the plastic rivets is also not so frequent unlike metal rivets. Reason behind this phenomenon can be existence of plastic rivet in two pieces. Metal rivets used to be in one part. Thus, along a plane they may get sheared much easily than compared to plastic rivets. By ignoring chance of failure of plastic rivets by shearing failure also this work is focusing only on tensile failure of the plastic rivet which is much in agreement with the design modification of the proposed part. Further two aspects were checked. One is checking of the maximum load this rivet can take, and at that load whether the teeth are deflecting to get detached. The maximum stress occurs at least cross-sectional area. There are two places where smaller cross-sectional area is possible. One is body and another is smallest diameter of core as shown in Fig. 7.

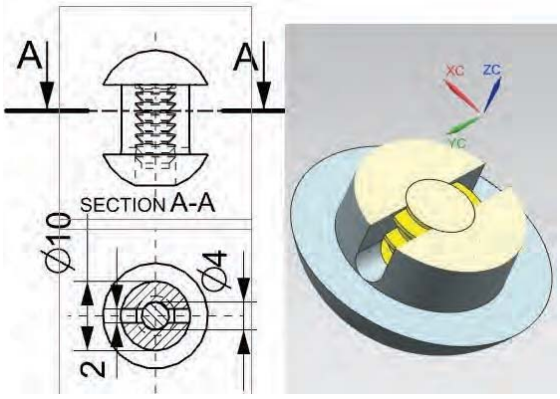

Figure 7. Cross sectional areas to be considered for tensile strength

By visual inspection smaller area can be observed but the same is calculated in (1) and (2). From these calculations it is predictable that, more stress is going to develop on core. Ultimate load that can be applied on this area also is calculated in (3). This is the maximum amount of load which the designed rivet can take before breaking. Displacement analysis of buttress profile is done on UG Nx 12.0 design simulation software. The same is shown in Fig. 8. Ten node tetrahedral elements were created with 2mm size elements for meshing. Left portion of figure indicates the constrained face and the faces on which load is being applied. It is evident that the load will come from the similar faces of rivet body. Right side image in Fig. 8 represents the deformation result. The load applied for the analysis is 200N. This load range is empirically taken, assuming half of the ultimate load. It is observable that small deformation has occurred, but the profile is maintained. Thus it can be assumed that due to deformation the teeth will not disengage.

Cross section area of Body = $[\pi(10^2-4^2)/4] - 2(3\times2)$
$= 53.97mm^2$ (1)

Cross section area of Core = $\pi(4^2)/4 = 12.56mm^2$ (2)

Maximum tensile force can be applied on core
= (Tensile strength of PP) X (CS area of core)
= 32 X 12.56 = 402 N (3)

This work is focusing only on the tensile failure. Failure of rivets by combined effect of stresses as well as analyzing the efficiency of plastic rivets is beyond the scope of this work.

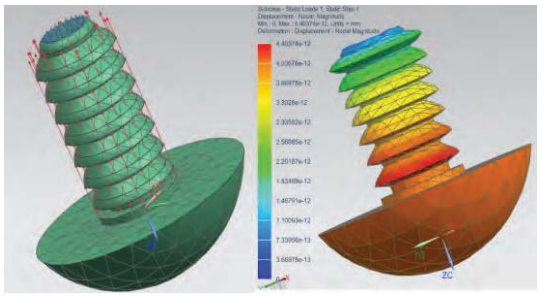

Figure 8. Constrained face and faces with applied load along with the displacement results

The displacement result is quite in agreement with the design expectations. Further the manufacturability of the part should be analyzed.

B. Process Simulation

To check the compatibility of the part to be made by injection molding processes, this work utilized Autodesk Moldflow Adviser 2019 software. This is widely used software in industries for the purpose of injection molding processes simulation. It is efficient and cost-effective tool for process simulation during component development. Thus, it helps in reducing product development time and cost. Before running the simulation on the designed model, few input parameters related to the process are provided. For this purpose, this research work has taken parameters from an injection molding machine. For reference these parameters are indicated in Table II.

TABLE II.
MACHINE SPECIFICATION
(TEXPLASST 1HD, MP LAB, CVRCE)

Shot Capacity	2 – 45 gms / shot
Plunger Diameter	25 mm
Stroke Length	450mm
Clamping Capacity	6.0 Tons
Injection Pressure	80 kg/cm^2
Heating Capacity	1.5 kw
Total Installed Power	3.7 kw
Total Shut Height	100 - 450mm

The process simulation helps in predicting defects and other process related issues. This work was aimed at checking if the proposed design is manufacturable or not. From the standard calculations the gate and runner diameters were calculated [9]. In single impression, core as well as body of the rivet were planned. Edge feeding was finalized along plane of symmetry. The expected shot volume for the part cavity including flow path elements is estimated from the software as 15.3gm, which is well within the shot capacity of the machine. After entering the needed input parameters, the flow analysis simulation was conducted and various useful outputs were obtained. Confidence of fill is indication of how conveniently the planned cavity can get filled under given process parameters. There is high

probability of filling which is shown in Fig. 9. It is observable that sudden sections changes, as per modified buttress profiles are also not an obstacle in proper filling of the mold. This can be considered as outcome of DFM related modification and the design changes made accordingly [14].

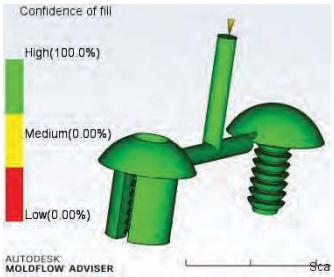

Figure 9. Confidence of fill result

Similarly, another important prediction is shown in Fig. 10, which displays expected time which the part will take to solidify. Time to reach ejection temperature is sum of fill time and solidification time. It helps in estimation of cycle time. In the figure, mostly the part is blue i.e. in 8 seconds majority of the part is solidifying. Some thick mass regions of core are taking time in solidification. Usually, 60% of the cycle time is cooling time. A designer always aims at decreasing this time to as least as possible [10, 16]. It is significant to mention that cooling channels were not planned here.

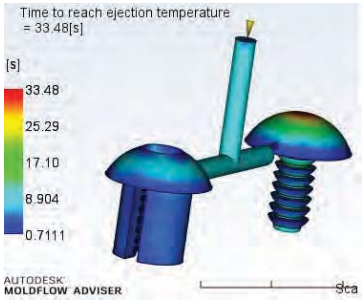

Figure 10. Time to reach ejection temperature result

As stress will be involved in rivet while in application, it is important to check weld lines. These can be considered as structural deficiency which comes into existence due to merging of flow fronts [11]. In Fig. 11 the weld line results are displayed. Due to empty space provided in the rivet body, slight weld line of small angle is appearing in snap head. It is not a problem in this case due to its small quantity in low stress region.

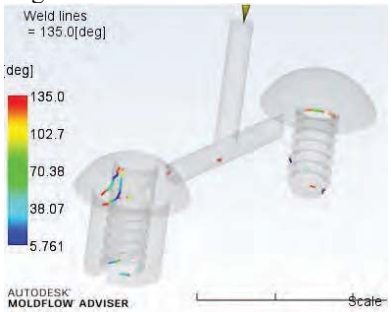

Figure 11. Weld line result

As expected from embodiment design of part, there is minute sink mark in thick mass region of the part, as indicated in Fig. 12 as sink mark results. Maximum possible mass reduction in terms of design were done. Thus, this sink mark can be possibly handled in actual process by applying packing pressure [12].

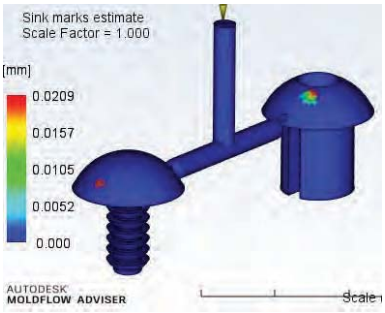

Figure 12. Sink mark result

Another important result is shown in Fig. 13. This is cooling quality result. It indicates the region where heat will remain for the longer time during solidification. Portions of the parts, which are appearing in green will solidify earlier and the portions indicated in red will be the last to solidify. This result further helps in planning of cooling channels for maintaining temperature of the metallic mold used in the injection molding process [13].

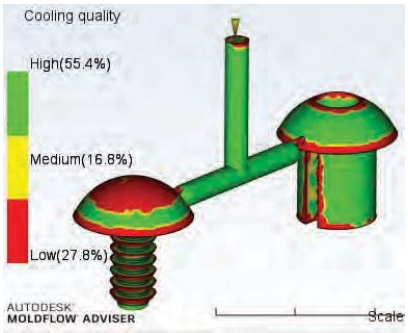

Figure 13. Cooling quality prediction

IV. The Mold

Based on the simulation results, a mold was modelled for making the samples of the designed rivets with buttress profile and the same is shown in Fig. 14. The mold is planned according to the machine specification of which is considered for the flow analysis. The machine is with vertical injection and horizontal clamping facility. In the mold, cavity was planned accordingly. Dimensions of the mold were taken as per die design parameter handbook [9]. In the figure, one half of the mold is made translucent so that flow channels, mold cavity and placement of insert can be seen. For better understanding rivet core and body is placed in their respective mold cavities and rivet body is made further translucent to see the insert placed in the cavity. This insert is to be placed in the mold before injection so that internal buttress profile of the rivet body can be obtained. Machining of the mold cavity can be done by end milling. The insert is to be obtained by turning for ease of manufacturing. This is plan of a model mold. Thus, cooling channels are not installed and the same is not

considered in the analysis. After filling the plastic material will solidify around insert. Thus, after ejection the insert will be removed manually from the rivet body. The same insert will be placed in the mold before next filling. In actual die which will be made for the production purpose, ejection of insert can be mechanized. As the mold is split in two halves, there is provision of four guide bush and pillars to prevent mismatch of both the halves while closing and filling.

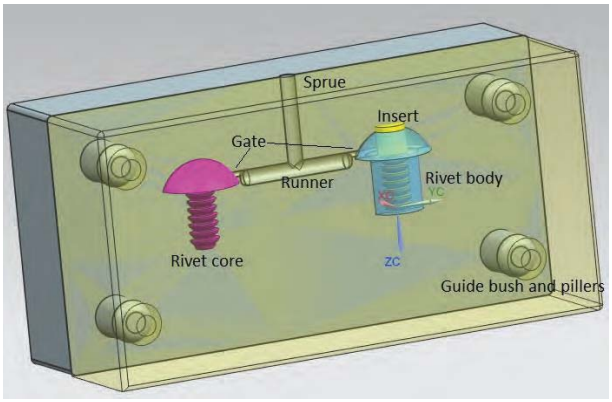

Figure 14. The designed mold

V. Conclusions

In this research work an attempt was made to modify the design of existing plastic rivets and check its manufacturability. Adequate load analysis and mold flow analysis was performed which resulted in assurity that the design modifications are not only making the product capable to sustain loads, but the design changes are making the product manufacturable also. This work gives clear methodologies for a new product development to the young researchers. Designing a mold for this component for industrial purpose can be further part of research. Planning optimum flow path for a multi cavity mold can also be taken as future scope of work. Current innovations in material and manufacturing technologies are making the manufacturing of designed parts simpler and more cost effective. Thus, comparing the manufacturing of a part by different manufacturing process also can be added in further analysis. For example, the parts taken in this work can also be manufactured by 3D printing technology. Usually design of a part is finalized by considering a manufacturing process, but a successful design not just contributes to manufacturing but to overall profit of the entire production process. There are no set rules for implementation of DFM principles. It all depends on the designer to take profitable decisions in process planning.

References

[1] Boothroyd, G., Dewhurst, P., Knight, W. (1994). Product Design for Manufacture and Assembly. New York: Marcel Dekker Inc.

[2] Barbosa, G.F, J. Carvalho, Design for Manufacturing and Assembly methodology applied to aircrafts design and manufacturing, IFAC Proceedings Volumes, V- 46, Issue 7, 2013, pp.116-121, https://doi.org/10.3182/20130522-3-BR-4036.00044.

[3] Darshak Desai, Bhavikkumar Nileshbhai Prajapati, "Competitive advantage through six sigma at plastic injection molded parts manufacturing unit: a case study", International Journal of Lean Six Sigma, https://doi.org/10.1108/IJLSS-06-2016-0022

[4] Farotti, E.; Natalini, M. (2018). Injection molding. Influence of process parameters on mechanical properties of polypropylene polymer. A first study.. Procedia Structural Integrity, 8, 256–264. doi:10.1016/j.prostr.2017.12.027

[5] Naol Dessalegn Dejene, Sololo Kebede Nemomsa, "Design for Manufacturing and Assembly- Review," World Academics Journal of Engineering Sciences, Vol.7, Issue.3, pp.60-67, 2020.

[6] Ming-Tsan Chuang , Yung-Kuang Yang & Yun-Hsiang Hsiao (2009) Modeling and Optimization of Injection Molding Process Parameters for Thin-Shell Plastic Parts, Polymer-Plastics Technology and Engineering, 48:7, 745-753, DOI: 10.1080/03602550902824630

[7] Sateesh, N.; Devakar Reddy, S.; Praveen Kumar, G.; Subbiah, Ram (2019). Optimization of injection moulding process in manufacturing the flip cover of water meter. Materials Today: Proceedings,S2214785319337721,doi:10.1016/j.matpr.2019.11.089.

[8] Proceedings of DETC'04 ASME 2004 Design Engineering Technical Conferences and Computers and Information in Engineering Conference September 28-October 2, 2004, Salt Lake City, Utah, USA.

[9] Technical committee, *Technical Directory on Design and Tooling for Plastics*, Central Institute of Plastic Engineering & Technology. pp. 43-64, 1970.

[10] SÃ¡nchez, R.; Martinez, A.; Mercado, D.; Carbonel, A.; Aisa, J. (2021). Rapid heating injection moulding: An experimental surface temperature study. Polymer Testing, 93, 106928–. doi:10.1016/j.polymertesting.2020.106928

[11] Mehdi Moayyedian, Kazem Abhary, Romeo Marian, Improved Gate System for Scrap Reduction in Injection Molding Processes, Procedia Manufacturing, Volume 2, 2015, Pages 246-250, ISSN 2351-9789, https://doi.org/10.1016/j.promfg.2015.07.043.

[12] Neeraj Kumar Jha, G. Bharath Reddy, Vidyanand Kumar, "*Design and Process Analysis of Single Cavity Injection Molding Die for Plastic Wing Nut*", CVRJST, Vol. - 20, 2021.

[13] Rashid, O.; Low, K.W.Q.; Pittman, J.F.T. (2020). Mold cooling in thermoplastics injection molding: Effectiveness and energy efficiency. Journal of Cleaner Production, 264(), 121375–. doi:10.1016/j.jclepro.2020.121375

[14] Neeraj Jha, G. Avinash, V. Siddharth, "Design and structural analysis of plastic chain link with polypropylene and polyoxymethylene material", November 2020, Materials Today: Proceedings 38(1)

[15] Huang, Yu-Chen; Tu, Jui-Che; Kuo, Kuo-Pin (2017). Establishing sustainable design and development for plastic mold under product service system. Advances in Mechanical Engineering, 9(7), 168781401770969–. doi:10.1177/1687814017709699

[16] Singh, Gurjeet; Verma, Ajay (2017). A Brief Review on injection moulding manufacturing process. Materials Today: Proceedings, 4(2), 1423–1433. doi:10.1016/j.matpr.2017.01.164

E-ISSN 2581 – 7957
P-ISSN 2277 – 3916

CVR Journal of Science and Technology, Volume 22, June 2022
DOI: 10.32377/cvrjst2214

The Phase Transformation of Low Carbon Steel using Controlled Cooling Systems

Dr.Manjeet Kharub
Assoc. Professor, CVR College of Engineering/Mechanical Engg. Department, Hyderabad, India
Email: manjeetkharub@gmail.com

Abstract: **Automobile manufacturers face mounting pressure to develop new materials that improve their vehicles' fuel economy, pollution emissions, and crash safety. These objectives appear ambiguous when they must be met while reducing the weight of a vehicle. This requires using materials with a high strength-to-weight ratio and high formability. The objectives of the work presented in this paper were to control the cooling of steel with lean chemistry to generate a multi-functional multi/dual-phase steel. The calculations were performed using JMat-Pro and Thermo-Calc. The CCT, TTT, equilibrium diagram, and phase fraction diagram of the steel is under investigation. It was found that inter-critical annealing can be achieved with a variety of strength-ductility combinations in steels with proper cooling pathways. Therefore, by modifying the heat treatment parameters, the examined steel's alloy chemistry enabled the achievement of a wide variety of strengths and ductility combinations.**

Index Terms: **dual-phase (DP) steels, heat treatment, annealing, phase transformation, control cooling**

I. Introduction

Engineers and scientists have developed a new class of steels specifically for vehicles [1]. Compared to traditional mild steel, these steels are designed to meet stringent safety and emissions regulations and the requirements of today's vehicles at a modest rate [2]. These steels are approximately six times more resistant to corrosion than those used earlier. They are known as Advanced High-Strength Steels (AHSS) and are more sophisticated, complex materials [3]. These steels also provide a higher strength-to-weight ratio without sacrificing durability, ductility, or formability with a carefully chosen chemical composition. They exhibit a better strength-to-elongation ratio than conventional steels due to their dual/multiphase crystallites caused by conventional cooling or controlled cooling of steels with high chemistry (high alloy content) [4]. Because processing of chemistry-rich steels is expensive, the objective of cost-effectiveness was never met using these steels. Various processing techniques have been described in the relevant literature, the majority of which employ standard cooling methods from the heat treatment processes [5]. Few authors have reported on manufacturing these steels using controlled cooling ideas but have instead used steels with rich chemistry to achieve the necessary attributes. Also, the cost-efficiency target is not attained with significant alloy content in these steels. Therefore, the primary goal of this study was to develop multi-functional steels with dual/multiphase microstructures generated by controlled cooling of low carbon steel. Microstructures with many phases were created in low normalized carbon steel (0.11C, 1.8Mn, and 0.325 Si) by adjusting inter-critical annealing settings in an annealing simulator. Thus, this paper makes an effort to employ steels with low carbon content and treat them utilizing controlled cooling techniques. Dual-phase microstructures were obtained by inter-critical annealing followed by quick cooling to ambient temperature, while multiphase microstructures were obtained by maintaining the bainitic and martensitic temperature ranges, respectively The present research work is an effort to address the following:

- To study the formation and stabilization of the austenite phase during inter-critical (isothermal) annealing of normalized steel under fast heating rates (up-quenching).
- To establish the process routes for the annealing cycle to produce the required multi/dual phase microstructures. The overall objective of the present work consisted of several sub-problems/ issues.

II. Literature Review

This section contains brief background knowledge based on the literature on the different methods used by past scholars to manufacture third-generation dual-phase steels and enhance their qualities.

Seong et al. [6] investigated the influence of retained austenite and the quantity of soluble carbon in TRIP (Transformation Induced Plasticity) steels on their mechanical characteristics. Two cold-rolled strips, CS1 (C-.077, Si-1.00, Mn-1.50, P-0.0084, and Sol. Al-0.036) and CS2 (C-0.079, Si-1.51, Mn-1.50, P-0.0095, and Sol. Al-0.033), each having a thickness of 1.3 mm, were heat treated. The heat treatment procedure included 50 seconds of austenitizing at 830 °C, fast cooling to the bainitic transition temperature of 360–460 °C, and 5 minutes of isothermal holding (austempering). In CS1 steel specimens, it was noticed that the retained austenite concentration dropped when the austempering temperature was increased. This occurred because increasing the austempering temperature resulted in cementite precipitation, which resulted in a quicker drop in the carbon content of residual austenite, facilitating the nucleation of new bainitic ferrite plates. The silicon-rich CS15 sample inhibited carbide production during bainite transformation, enriching the residual austenite with carbon. The authors found that increasing the austempering temperature reduced the amount of retained austenite and carbon. Additionally, the quantity of kept austenite was related to its carbon content, and elongation increased as retained austenite, and carbon content rose.

Hulka [7] examined the influence of niobium addition on the characteristics of Multi-Phase (MP/TRIP) steels. When MP steel was manufactured, the initial heat treatment was

Received on 18-03-2022, Revised on 07-05-2022, Accepted on 31-05-2022.

performed at a slightly higher temperature in the two-phase zone (50% ferrite and 50% austenite by wt). Quenching was enacted to prevent the production of significant ferrite—the final transition isothermally in the bainite zone (second heat treatment). Carbon spread into the remaining austenite islands during bainite production, eventually enriching them to a level of more than 1% carbon. It was observed that austenite containing a large amount of carbon was also stable at room temperature. Additionally, austenite may be stabilized at room temperature with the addition of niobium to multiphase steels.

According to Fang et al. [8], the addition of niobium alters the microstructure and mechanical properties of the material. It shortens the annealing time, resulting in increased retained austenite at room temperature due to carbon enrichment of austenite; the formation of NbC precipitates, which inhibit grain growth, results in fine-grained austenite. Additionally, Nb retards austenite recrystallization during hot strip rolling. So, by preparing additional nuclei for the austenite to ferrite transition, the grain size of the hot band was reduced. Thus, the parameters discussed above enhanced both strength (as a result of grain refining and NbC precipitation) and length (due to stability of austenite at room temperature and also by nucleation of ferrite at austenite-ferrite inter-phase during cooling).

After solidification, the slabs were hot-rolled and forged to produce rods with a 24x24mm section. The specimens were heated in three different ways. In routes I and II, the steel was heated to 910 °C (+ area) and held there for 30 minutes. In route I, the specimen was chilled to room temperature, then reheated to 750 °C and quenched with water. In route II, the specimen was quenched with water at both 910 °C and 750 °C. Method III entails austenitizing steel at 910 °C and then air cooling to 750 °C for 45 seconds to complete the partial transformation, followed by water quenching. The steel that had been heat-treated according to route I has a ferrite structure with an uneven martensite envelope at grain boundaries. In route II, austenite nucleation occurs mostly on the borders of martensite laths generated following initial quenching from a temperature of 910 °C. The predominating martensite component is found mainly as thin fibres at grain boundaries.

Additionally, tiny grains of recrystallized ferrite may be seen in the vicinity of martensite, particularly near the border zone of big grains of the alpha phase. Martensite was discovered on the grain boundaries of the alpha phase along route III. After 45 seconds of air cooling, the optimal martensite percentage of 20% occurs. The heat treatment parameters utilized resulted in the formation of DP-type steels with equivalent ferrite and martensite percentages. The optimal martensite fraction was found between 21% and 24%, and the phase grain size was between 7m and 10m. The varied shape of martensite has an effect on the steel's diverse mechanical characteristics and deformability.

The route II steel had the optimal strength and ductility. This steel had a yield point of about 520 MPa, a tensile strength of approximately 800 MPa, a total elongation of 20%, and uniform elongation of around 16%. Ahmad et al. (2007) investigated the influence of thermomechanical processing on the hardenability and tensile fracture characteristics of dual-phase (DP) steels. Thermo-mechanical processing with varied rolling reductions (0-50%) was used to quench low alloy hot rolled steel (0.09 C, 1.2 Mn, 0.78 Cr, 0.26 Si, 0.15 Ni, 0.2 Cu, 0.04 Mo, and balance Fe, percent wt) in the intercritical temperature range of 725–830 °C. The steel as received had a microstructure composed of ferrite and pearlite phases, as determined by the metallographic investigation. Inter-critical samples were heated for 20 minutes in an argon atmosphere to a temperature range of 725–830 °C and then quenched in a brine solution. Due to the rapid cooling rate, the austenite phase changed nearly entirely into martensite. The volume percent of austenite was determined using the point-counting technique. At a temperature of 790 °C, about 50% of austenite was created; at this temperature, samples were rolled, and cross-section reductions of 0–50% (0, 20, 30, and 50% reductions in the lateral and longitudinal directions) were attained. All specimens were quenched in an ice-cold brine solution, which provided a cooling rate of about 500 °C /s. Following grinding and polishing, specimens were etched with 5% picral solution, followed by 2% nital solution, and then submerged in a boiling alkaline chromate solution (8g CrO3 + 40g NaOH + 72 ml H2O). It was discovered that while rolling at a temperature of 790 °C for a thickness reduction of 0 to 50%, about 6% of ferrite increased in rolled specimens but not in un-rolled specimens, indicating that rolling in the inter-critical area lowered hardenability.

The increased rolling reduction resulted in increased strain, resulting in more fibrous martensite particles. Rolling extended and thinned the martensite fibres in the longitudinal direction, and they did not lengthen in the transverse direction, but widened in the direction corresponding to the rolling plane. Thus, the aspect ratio of the martensite fibres was greater in the longitudinal direction than in the transverse direction, which had a significant effect on the tensile characteristics. Total elongation was also considerably impacted by 50% rolling in the transverse and longitudinal directions, resulting in total elongation of 13% and 18%, respectively. Hot rolling at the inter-critical area boosted the steel's strength without sacrificing its ductility significantly. Additionally, rolling enhanced the aspect ratio of the martensite in the longitudinal direction more than in the transverse direction, resulting in the development of tensile characteristics.

Zhao et al. [2021] developed a novel approach for processing DP steel in which a sample of 0.17C-0.74Mn steel was treated in five phases to generate ultrafine-grained DP steel. After 30 minutes of soaking, the sample was quenched in an ice-brine solution, resulting in a completely martensite microstructure that was tempered in the second stage. In the third phase, the sample was cold rolled to an extent of 80 percent. In the fourth phase, the sample was annealed to 550 °C and soaked for 75 minutes before being quenched in water to create an ultrafine aggregate of ferrite and carbide. In step five, a system was quickly heated at a rate of 300 °C/s to a temperature between Ac1 and Ac2 and then soaked for 5–10 seconds to decrease ferrite grain development and enhance carbide dissolution and austenite production. On water quenching, an ultrafine structure with

CVR Journal of Science and Technology, Volume 22, June 2022
DOI: 10.32377/cvrjst2214

a martensite volume percentage of about 0.42 was formed with a uniform distribution of 2 um martensite islands.

For manufacturing TRIP steel, the authors advocated using nitrogen as an austenite stabilizer to enhance mechanical qualities; however, 200 ppm N2 was recommended for traditional steelmaking due to nitrogen's limited solubility. A significant degree of retained austenite stabilization occurs due to the high nitrogen concentration. The authors concluded that steels with desirable qualities would have a high proportion of austenite and high strength elements such as martensite, bainite, and ultrafine-grained ferrite.

III. Experimental Procedure

The following information outline the experimental approach used in this study work:

A. Analytical characterization of the material that was received

A sheet of normalized steel, 1.0 mm thick, with the chemical composition described in Table 1 was used as a starting point.

TABLE I.
CHEMICAL COMPOSITION OF THE AS-RECEIVED STEEL

element	C	Mn	Si	S	P	Al	N	Fe
%wt.	0.11	1.8	0.325	0.006	0.016	0.052	0.0056	Rest

Standard metallographic processes such as mounting, planar grinding, rough polishing, final polishing, etching, etc. were used to prepare specimens of the as-received steel for microstructural investigation. The specimens were etched using Nital, a solution of HNO3 (3 percent) in ethanol. For varying levels of detail, images were captured using an optical microscope.

B. Software to Conduct Research on Phase Transformation

For heat-treated steel, annealing parameters needed to be determined once microstructure analysis was completed on the raw material. As a result, the focus of this stage of the study was on the specifics of the steel's annealing temperature range (the lower and higher critical temperatures), soaking times, cooling rates, and other cooling parameters. JMat-Pro and Thermo-Calc were used to do these calculations. The steel under investigation's CCT (continuous cooling transformation), TTT (time-temperature transformation), equilibrium diagram, and phase fraction diagram were all calculated using the software programmes.

C. Heat Treatment and Microstructural Analysis

Thermo-Calc and JMat-Pro software were used to compute process parameters for annealing tests. There were two kinds of samples used in the annealing process. Samples for the muffle furnace were produced as normal dog-bone specimens with 35-mm gauge length, whereas samples for the annealing simulator were created as 10-by-10-by-1-mm^3 samples. After heating in the muffle furnace and quenching with water, the quantity of austenite formed in the specified steel was determined by conducting annealing tests.

Different cooling methods were used in annealing simulator tests. Simulated alternative cooling paths were created by varying the concentrations and pressures of hydrogen and nitrogen gases fed into the simulator. Samples were annealed in the temperature range of Ac1–Ac3 for 3 minutes at various inter-critical temperatures and then cooled. This study employed the holding times described by Thomas et al. [10]. Water quenching was used as the cooling technique for muffle furnace samples, and samples were cooled following the CCT diagram for annealing simulator treatment. The resulting microstructures were distinct for each of the three cooling procedures (A, B, and C in Fig. 1).

There were martensite/ferrite microstructures in samples of type A that were immediately cooled (at a rate greater than critical cooling rate) to room temperature. Microstructures of type B samples were obtained by quickly cooling and holding them in the bainitic zone for one minute. To temper, the martensite, samples of type C were immediately cooled to a temperature between M_S and M_F and maintained there for one minute. Even before the samples were loaded, the heating chamber of the annealing simulator was pre-charged with a combination of hydrogen and nitrogen gases to guard against sample oxidation in a reducing atmosphere.

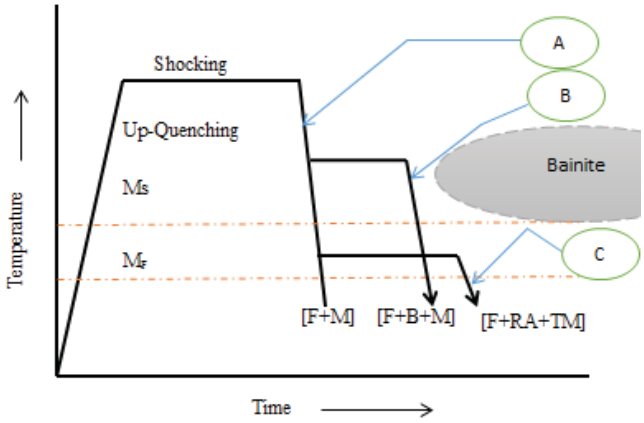

Figure 1. Schematic of different heat treatment routes

IV. Results and Discussion

A. Microstructure of Material as received

With an average grain size of 15 micrometres, the microstructure of the obtained steel is composed of pro-eutectoid ferrite (88%) and pearlite (12%). See Fig. 2 for further information.

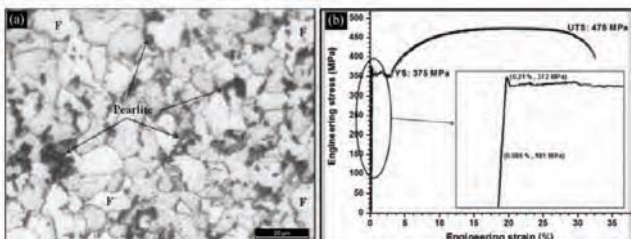

Figure 2. optical micrograph and tensile curve for the received steel

B. Process Parameter Predictions Using Software

The as-received normalized steel's equilibrium phase diagram and phase fraction diagram were constructed using Thermo-Calc software (See Fig. 3), which anticipated the Ac_1 and Ac_3 temperatures to be 684 °C and 834 °C, respectively. Using JMat-Pro, a CCT diagram for each annealing temperature was created. As indicated below, JMat-Pro predictions were used to calculate the proportion of austenite available for transformation into various products.

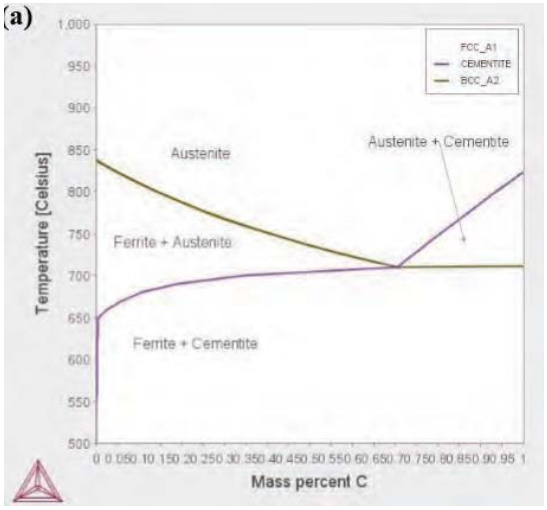

Figure 3. Thermo-Calc result window for equilibrium phase diagram for Steel chemistry

C. Annealing Simulation for Microstructure Tailoring

Following this, the specimens were isothermal annealed in the annealing simulator for 3 minutes at each of the inter-critical annealing temperatures (ICATs) of 700-750-800 °C and 850 °C. Then regulated cooling (via various cooling paths) as per CCT diagrams. A, B, and C cooling curves were derived from the annealing chamber thermocouple data logs and overlaid on the CCT diagrams as illustrated in Fig. 4.

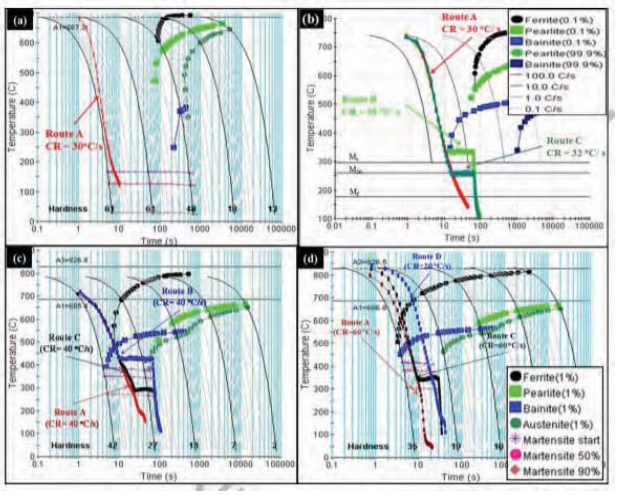

Figure 4. CCT diagrams with cooling curves superimposed for annealing temperature of (a) 700 ^{0}C (b) 750 ^{0}C (c) 800 0C (d) 850 ^{0}C

D. Simulation At 700 ^{0}C

For route A, the specimen was heated to 700°C, immersed for 3 minutes, and then cooled to room temperature at a rate of 30°C/s. The annealed specimen had ferrite and fine martensite laths. Heating and chilling created a necklace-like structure with recrystallized ferrite at the grain boundaries.

The optical micrograph revealed martensite and grain boundary ferrite. There was some remaining pearlite. Pearlite in the received steel recrystallized to ferrite during heating and soaking and phase transformed to austenite. The ferrite phase remained constant as austenite converted to martensite: ferrite (both original and recrystallized), martensite, and residual pearlite microstructure. Insufficient annealing temperature and duration reduced martensite. During inter-critical annealing of DP steel, ferrite recrystallization and austenite transformation compete and overlap. In the current study, coupling of these two processes happened at 700°C annealings. However, ferrite recrystallization was dominating, and austenite production was minor. The absence of austenite and hence martensite development prevented the creation of a suitable dual-phase structure following 700°C annealing. The other two procedures (B and C) were not used because austenite was found in tiny fractions at this annealing temperature.

E. Simulation At 750 ^{0}C

During annealing at 750°C, the cooling rates were 20–40°C/s. Route A was the same as 700°C. After 3 minutes of soaking at 750°C, the specimen was cooled at 35°C/s up to 350°C for route B. After 1 minute, the specimen was cooled to room temperature at a rate of 20°C/s. After 3 minutes of soaking at 750°C, the specimen was cooled at 32°C/s up to 250°C for route C. (martensitic region, identified). After 1 minute, the specimens were cooled to room temperature at a rate of 20°C/s. These three methods acquired the optical micrographs. Optical examination revealed ferrite and martensite phases with a 15% martensite volume percentage. There is evidence of partial austenite production and ferrite recrystallization-grain boundary recrystallization at 750°C. Austenite converted into fine-grained martensite upon further cooling along route A. Annulling at 750°C with cooling route A produced DP microstructure with ferrite and martensite phases.

A carbon redistribution occurred during the initial cooling (at 35 °C/s) up to 350 °C and subsequent holding in the bainitic zone for this approach. Some parts of austenite became carbon-rich, while others became carbon-deficient. Low carbon austenite became bainite (during holding at bainite region). Some carbon-rich austenite produced carbides during additional cooling (second cooling at 20 °C/s), while the rest formed martensite. A multiphase microstructure for cooling method C was expected, including ferrite, martensite, tempered martensite, bainite, and carbides. During the initial fast cooling (at 32 °C/s) along route C, austenite largely changed to martensite; on holding in the martensitic zone, this martensite received tempering and became tempered martensite. Carbon is predicted to permeate into untransformed austenite, stabilizing it. However, after a second cooling at 20 °C/s,

part of the untransformed austenite converted into martensite, including carbides. During the soaking time, a highly saturated carbon solution was transformed into ferrite (route B).

F. Simulation At 800 ^{0}C

By Routes A, B, and C: Cooling rates of 20–40 °C /s were reached at an annealing temperature of 800 °C. For route A, a cooling rate of 40 °C /s was used. After three minutes of specified soaking at 800 °C, the specimen was cooled to about 400 °C (bainitic area) at a rate of 40 °C/s. After 1 minute, specimens were cooled to room temperature at a rate of 20 °C /s. After three minutes of soaking at 800 °C, the specimen was cooled to 280 °C (martensitic area) at a rate of 40 °C/s. After 1 minute, the specimen was cooled to room temperature at a rate of 20 °C /s. A dual-phase microstructure with a 20% martensite volume fraction was achieved by procedure A. Although the CCT diagram indicated the production of bainite, this phase combination was not detected in the steel specimen because of the lack of holding. A multiphase microstructure composed of ferrite, bainite, martensite, and traces of carbides was identified for route B. A multiphase microstructure including ferrite, conventional martensite, tempered martensite, and traces of bainite and carbides was reported for route C.

G. Simulation At 850 ^{0}C

By Routes A, C, and D: Cooling rates of 20–70 °C /s were reached at an annealing temperature of 850 °C. Three distinct specimens were annealed using three distinct cooling techniques (A, C, and D, respectively). Cooling pathway B (which was previously employed to induce bainite production) was omitted. This occurred because the bainitic zone in the CCT diagram migrated to the left at this inter-critical annealing temperature (ICAT = 850 °C). Additionally, the temperature range for bainitic transition was rather narrow. Thus, route B at 850 °C required an extremely rapid initial cooling rate prior to reaching isothermal holding in the bainite area. With such rapid cooling rates (and a short bainitic transformation range), it was challenging to manage regulated cooling while maintaining the proper transformation temperature range. Thus, in lieu of route B, a new (slow) cooling route D was established, consisting of continuous cooling at a rate of 20 °C /s. A cooling rate of 60 °C /s was used for route A. After three minutes of soaking at 850 °C, the specimen was cooled to 350 °C (martensitic area) at a rate of 60 °C/s. After 1 minute, the specimen was cooled to room temperature at a rate of 31 °C /s. After 3 minutes of soaking at 850 °C, the specimen was cooled to room temperature at a rate of 20 °C /s.

A dual-phase microstructure incorporating ferrite and martensite (37%) phases were discovered for route A. During cooling, the ferrite phase is comprised of both original ferrite and newly produced ferrite. The CCT diagram for 850 °C demonstrates that all cooling paths travel through the ferrite area, culminating in the transition of austenite to ferrite. This ferrite is referred to in this study as newly created ferrite to distinguish it from the ferrite that was in the steel prior to annealing. A multiphase microstructure incorporating ferrite (both original and freshly generated), martensite, tempered martensite, and a trace of bainite was expected for cooling route C. Following the initial cooling and subsequent retention in the martensitic zone, some carbon from newly created martensite seeped into untransformed austenite (leading in the development of tempered martensite) and enriched some parts of austenite. A piece of untransformed austenite (austenite with a low carbon content) converted into a bainite phase mixture. The untransformed austenite (austenite with a high carbon content) remained stable and converted to martensite during the second cooling [11, 12].

Carbides did not develop at this annealing temperature because to the rapid cooling rate (> 30 °C /s) used for the second cooling step after holding in the martensitic zone. The microstructure of route D consisted of ferrite (both original and newly produced), martensite, and bainite. Austenite first converted into ferrite, then into bainite, and lastly into martensite as it cooled.

V. CONCLUSIONS

Using inter-critical annealing process, a broad range of strength's combinations has been achieved. It is concluded that when hard phases like martensite, bainite, and others were present in the microstructure, they boosted UTS but decreased ductility and YS. Compared to route A, the presence of bainite may lower the UTS and raise the YS through route B. Route A provided the most strength, but at the sacrifice of ductility. Route C offered the optimum balance of strength and ductility. Annealing results achieved from annealing tests are much more accurate than those predicted by software. The differences are due to the fact that software projections are based on the premise of equilibrium heating, which is seldom seen during industrial heating. Additionally, cooling rates obtained by water quenching are much greater than those obtained under simulated circumstances. In samples annealed at 700, 750, and 800 °C, approach A resulted in significantly greater UTS and ductility than procedures B and C. This was ascribed to carbide production during pathways B and C. Due to the presence of carbides, ductility was reduced. Strength reduced due to these pathways (B and C) not resulting in the development of martensite fractions as route A did. The natural stress-strain curves (of the steel containing the DP structure at different annealing temperatures) acquired from actual tensile measurements were very consistent with the true stress-strain curves predicted by micromechanical modelling. As a result, it is stated that micromechanical modelling may be used to predict material behaviour without substantial experimental examination.

The greatest volume proportion of martensite obtained in this investigation was 37% at 850 °C through route A. Annealing tests may be expanded to higher temperature ranges in order to obtain a larger austenite content and hence a higher martensite proportion in order to analyze the change in mechanical characteristics. The research considered the influence of non-equilibrium heating, but only in a qualitative sense. Future research might involve

determining the precise influence of heating rates on the microstructure by monitoring the heating rate throughout the austenitization process. The TRIP effect was not found to a substantial level in this investigation. Additional research may be undertaken with substantially longer holding durations to determine the TRIP impact.

REFERENCES

[1] Lesch, C., Kwiaton, N., & Klose, F. B. (2017). Advanced high strength steels (AHSS) for automotive applications− tailored properties by smart microstructural adjustments. Steel research international, 88(10), 1700210.

[2] Horvath, C. D. (2021). Advanced steels for lightweight automotive structures. In Materials, design and manufacturing for lightweight vehicles (pp. 39-95). Woodhead Publishing.

[3] Nanda, T., Singh, V., Singh, V., Chakraborty, A., & Sharma, S. (2019). Third generation of advanced high-strength steels: Processing routes and properties. Proceedings of the Institution of Mechanical Engineers, Part L: Journal of Materials: Design and Applications, 233(2), 209-238.

[4] Liu, Qinglong, Jeffrey Venezuela, Mingxing Zhang, Qingjun Zhou, and Andrej Atrens. "Hydrogen trapping in some advanced high strength steels." Corrosion Science 111 (2016): 770-785.

[5] Liu, L., He, B., & Huang, M. (2018). The role of transformation-induced plasticity in the development of advanced high strength steels. Advanced Engineering Materials, 20(6), 1701083.

[6] Seong, BS; Shin, E.J.; Han, Y.S.; Lee, C.H.; Kim, Y.J.; Kim, S.J. (2004) Effect of retained austenite and solute carbon on the mechanical properties in TRIP steels. Physica B, 350:

[7] Hulka, K. (2005) The Role of Niobium in Multiphase Steel, presented at METAL 2005, Germany 20-22 May, 2005.

[8] Fang, F., Lan, M. F., Lu, X., Zhang, Y. X., Wang, Y., Yuan, G. and Wang, G. D. (2017). The impact of niobium on the microstructure, texture and magnetic properties of strip-cast grain oriented silicon steel. Journal of Magnetism and Magnetic Materials, 442, 1-7.

[9] Zhao, J., Ma, L., Zayed, M. E., Elsheikh, A. H., Li, W., Yan, Q., & Wang, J. (2021). Industrial reheating furnaces: A review of energy efficiency assessments, waste heat recovery potentials, heating process characteristics and perspectives for steel industry. Process Safety and Environmental Protection, 147, 1209-1228.

[10] Thomas, G.A.; Speer, J.G.; Matlock, D.K. (2011) Quenched and Partitioned Microstructure Produced via Gleeble Simulations of Hot-Strip Mill Cooling Practices, Metallurgical and Materials Transactions A, 42A: 3652–3659.

[11] Kumar, G. N., & Reddy, G. B. (2017). Experimental Analysis on Nano-Based Phase Change Material for Cooling Applications in Tropical Buildings. *CVR Journal of Science and Technology*, *13*, 101-106.

[12] Rao, T. M., Srikar, N., Reddy, G. S., & Praveen, B. (2015). Ductility of Reinforced Concrete Beams. *CVR journal of Science and Technology*, *9*, 7-12.

E-ISSN 2581 – 7957
P-ISSN 2277 – 3916

CVR Journal of Science and Technology, Volume 22, June 2022
DOI: 10.32377/cvrjst2215

Wing design for Jet model Dassault FALCON 7X

Jarugu Tirumala Sri Vidyananda Sagar[1] and Vignesvar Krish Subramani[2]

[1,2]PG Scholar, IPSA, ECOLE, D'INGENIURS, DE L'AIR ET DE L'ESPACE, Department, Paris, France
Email: jtsv.sagar@gmail.com
Email: tirumalasatya@gmail.com

Abstract: **Present-day wing design is more challenging in aerodynamics and there is a need for flights that consume less fuel and the necessity of self-healing for dynamic damages due to bird strikes, turbulence, etc., and aerodynamically improve the performance. Wings should be strong, stiff, durable, and lightweight to withstand aerodynamic forces. A comparative study of the use of variable geometry wings on one of the most famous business jet models, the Dassault Falcon 7X, is presented in this paper to address this problem. Here, the computational program STAR CCM+ CFD solver is used to conduct a comparative aerodynamic study of variable geometry wing advantage in the design of one of the most famous business jet modules Dassault FALCON 7X. The Falcon 7X is chosen in this work because of its structural features such as wings fitted with winglets, windshields, typical landing weight, etc., CFD study is done using self-healing material which can be auto repair under stimulus when the damage or fracture occurs in the time-of-service operation either aging or accidentally.**

Index Terms: **Swept wing, FALCON 7X, Super healing materials, CFD study.**

I. Introduction

In aeronautical engineering, variable geometry wing is a futuristic concept of wing design that helps the aircraft to morph its wing geometry while in-flight according to its different phases of flight which can enormously reduce the fuel consumption and can aerodynamically improve the performance of the aircraft. During World War II, German research came into light the concepts of the variable-sweep wing and they developed transonic flight and the Messerschmitt Me P.1101 made with a single-seat, single-jet fighter. This became the foreseen for the second generation of jet fighters for the third reach. X-plane Bell X-5[1] is a world-famous plane built based on the Me.P.1101 prototype designed after World War II with seized sheets.

There are four forces acting upon the flight during its fly, they are weight, lift, drag and thrust. The aircraft is pulled back down the earth due to weight as a force of gravity. Throughout the flight, the weight will slowly decrease as fuel is burned to power the engine. To explain the creation of lift, which is a key for the flying of an aircraft, Newton's laws of motion and Bernoulli's principle are used. The air flows smoothly around the wing making it deflect downward and causing the wing to lift. The drag limits the forward speed of an aircraft. Parasite and induced drag are the two types, parasitic drag directly proportional to the square of the speed of aircraft. For example, an aircraft traveling 120 knots will experience 4 times as much parasite drag as the same plane going 60 knots at the same altitude. In another way, the induced drag is higher at lower speeds and decreases as speed increases. This is because induced drag is worst when the airplane is flying at a high angle of attack like when we are flying slowly. The thrust and lift must be greater than the drag for an aircraft to fly. Further, there is a possibility of wing damage or ripped from the aircraft, damage may occur through the bird's strikes, or damage may occur through the severe turbulence or mechanical failure in the aircraft. The repairing of such damage is more difficult. Therefore, the design of the wing's platform, camber, aspect ratio, and the wing area is important in designing aircraft [2].

An angle of sweep is defined as the angle at which a wing is translated backward (or occasionally forward) relative to the root chord of it. An aircraft's sweep angle[3] assists when flying at supersonic or transonic speeds, resulting in the delaying of shock wave formation that results from the compression of air at high speeds.

Dassault Aviation introduced the Falcon 7x in 2001 as a new addition to the Falcon family of business jets. There is only one tri-engine business jet in service today that is as technologically advanced as the Falcon 7x. Compared with other business jets in its class, this new aviation technology consumes up to 30% less fuel, dramatically lowering operating costs and allowing multiple flights without refueling. With a Mach maximum operating speed (MMO) of 0.90, the Falcon 7X can cover 11,019 km. With a 7X, nearly 90% of its maximum takeoff weight can be landed. The landing weight of the 7X would result in an approach speed of only 104 knots (193 km/h). Upon landing and stopping, it takes just 2,070 feet (630 m). Due to this, it can reach airports that other planes cannot, such as airports with high temperatures, steep approaches, and noise restrictions. Falcon 7X's unique structural features are a longer fuselage than Falcon 900EX, winglets designed differently, and a windshield with a different structure than Falcon 900EX.

II. Wing

To withstand the aerodynamic[4] forces the wing should be strong, stiffness durable, and lightweight. Materials that are used in the early period and at the current moment are fabric material, metal alloys, and composite materials which are modern materials that are suitable for the aircraft parts but the damage that occurred through the above consequences are very severe and the repairing the damage is very difficult. The figures of the Swept wings and Dassault Falcon 7X are shown in Figure 1. and Figure 2.

Received on 06-09-2021, Revised on 21-02-2022, Accepted on 30-11-2021.

E-ISSN 2581 – 7957
P-ISSN 2277 – 3916

CVR Journal of Science and Technology, Volume 22, June 2022
DOI: 10.32377/cvrjst2215

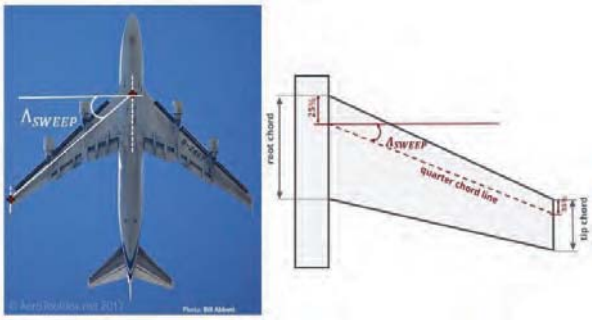

Figure 1. Swept wings

The problem of the self-healing [5-6] composite is the best source for the aircraft wing which will withstand aerodynamic forces. A pair of swept-back wing assemblies equipped with winglets are fitted to the FALCON 7X. An attachment of the type of piano is installed on each wing's lower section at the fuselage center. To attach the main landing gear to the wing, hinges are used.

Figure 2. Dassault Falcon 7X [7]

A.Fixed structure

Winglets, trailing edge, leading-edge, wing box (primary structure).

B.Movables elements

Three anti-iced slats (slat outboard, slat middle, and inboard slat), one spoiler (primary flight control system), one aileron (primary flight control system), two flaps (inboard and outboard flap), two airbrakes (airbrake inboard and airbrake outboard), and one main landing gear door.

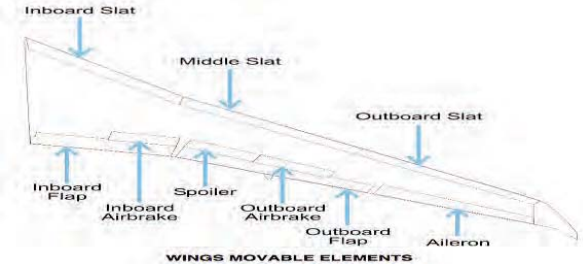

Figure 3. Falcon 7x wing

The Falcon 7x wing is shown in Figure 3. There are three major components of the wing box. They are spars, ribs, and skin panels. Wing boxes are the primary structural components of the wing, acting as both a structured box and as drag and lift resisting box. Furthermore, ground loads are applied from the main landing gear and jacking points. It is the fuselage that bears the load of the wings. There are three separate compartments in the fuel tank on the wing box. This structure is attached to the box front spar and is in front of it. Fixed trailing edge structures are attached to the wing box aft spar behind the trailing edge structures.

Figure 4. Swept wing spanwise flow

An airplane with a straight wing normally has airflow that runs parallel to the chord line of the aircraft. In contrast, only a small amount of air flows along the chord line of a swept wing. Another portion flows across the chord. This part is also known as spanwise flow. According to this, the airflow only accelerates in parallel to the chord line. Therefore, reducing airflow parallel to the chord line results in a reduction in lift caused by the wing. If the airspeed is high, this is not a problem since lift can be created by a small angle of attack. The issue occurs at slow speeds since lift is dependent on a high angle of attack. Although swept-wing aircraft are sometimes forced to fly at high angles of attack, even near the stalling point, most swept-wing aircraft ensure they do not do this by using advanced flap mechanisms, such as fowler flaps, and leading-edge slats.

Air has time to react at lower speeds, and spanwise pressure is practically applied to the wingtip. When the leading edge is pushed towards the wingtip, the leading edge is not the only thing pushing the airflow, the spanwise moving air beside it also pushes the airflow, so eventually, the airflow is moving toward the wingtip and not over it.

Consequently, sweeping the wings will disrupt the stall pattern. As spanwise flow approaches the wingtip, this creates a thickening of the boundary layer, resulting in a decrease in the wingtip's effective airspeed and stalling before the wing root. In this scenario, the airplane loses aileron control as soon as a stall occurs. For this reason, flow fences have been placed on the wings so that the spanwise flow is prevented from becoming too large.

III. SELF-HEALING COMPOSITES – MATERIAL STUDY

In recent developments, composite materials are used in place of metal alloys to provide lightweight and improved mechanical properties. To extend the lifetime of structures self-healing composite materials are enormously developed and used for different applications. There are two types called intrinsic healing and extrinsic healing based on the healing agent. Self-healing composite materials such as polymer matrix composite, ceramic composite (CMCs), metal matrix composite (MMCs), and cementitious

CVR Journal of Science and Technology, Volume 22, June 2022
DOI: 10.32377/cvrjst2215

composites are extensively used in various structures. This type of material is also advisable in the aerospace industry to repair the damage that may have occurred during the flight and increase the lifetime of the components including anti-corrosion and barrier coating. The approaches for this are:

1. The dispersed catalyst is combined with an encapsulated liquid agent
2. The catalyst and healing agent embedded in different capsule
3. The functionality of the matrix and healing agent both directly reacts with each other
4. The catalyst or the healing agent placed in the matrix as a separate phase under external stimulus.

Self- healing efficiency of composites are shown in table I.

TABLE I.
SELF-HEALING EFFICIENCY OF SOME COMPOSITES COMPARISON

Material	Healing approach	Loading condition	Property of interest	Efficiency
Epoxy - carbon fibres	Microcapsules	Width-tapered double - cantilever beam	Fracture toughness	80
Epoxy E-glass fibres	Epoxy E-glass fibres	Double-cantilever beam	Fracture toughness	60
Mendomer 401-carbon fibres	Reversible DA reaction	Three-point bending	Strain energy	94
2MEP4F polymer	Reversible DA reaction	Compact tension	Fracture toughness	83
Epoxy-SMA wires	Microcapsules and SMA wires	Tapered double-cantilever beam	Fracture toughness	77
Epoxy vinyl ester	Microcapsules	Tapered double cantilever beam	Fracture toughness	30
Epoxy-PCL phase	Mel table phase	Single-edge notched beam	Peak fracture load	>100
PDMS	Microcapsule	Tear test	Tear strength	>100

A.Self- Healing Aircraft wing

Materials that are used in the early period and at the current moment are fabric material, metal alloys, and composite materials which are modern materials that are suitable for the aircraft parts, but the damage occurred through the reasons mentioned consequences are very severe and the repairing the damage is very difficult. To overcome this problem, the self-healing composite is the best source for the aircraft wing which will withstand aerodynamic [8-10] forces. For instance, cut the branch in the tree, automatically the tree repairs it, and the new branch will grow. In the same way, anyone cuts the finger, it will bleed, and a scab is formed, and it will protect the damaged region as soon as the wound will be repaired automatically. The same approach will use in the self-healing composite materials. In manufactured composites, liquid fills the microcapsules. When the composite materials are used to manufacture aircraft wings, the liquid leaks from cracks resulting from microcapsule ruptures caused by the damage to the composite materials. The immediate reaction will take place and the chemicals harden the materials and fill the cracks and gluing also take place similarly. This process is known as polymerization and catalysis. Because of polymerization reactions in small molecules, the wound is sealed and known as monomers and used to join in a long chain called a polymer. The monomers released from the microcapsules contain reactive chemical groups called epoxides. These groups are three-membered ring structures, they will continuously react until the polymer is created. This process is known as curing, forming the high crossed structure that is like the undamaged composite. This healing can recover up to 100 percent of the material's mechanical strength repairing the damage causes the color change. The microcapsule could be designed to leak color when ruptured, signaling the area of repair. In general, when an aircraft wing is repaired might cause panic on board of flight. Testing of the healing agent is very important because the agent must be stable enough to last the aircraft's lifetime.

IV. CFD STUDY

The wing was first designed using the computational program CATIA. The design of the wing did not take into consideration devices and details such as flaps, wingtips, or the type of surfaces. The design of the wing followed the dimensions and tolerances of a real swept wing of our jet in question, Falcon 7x. This paper introduced the conceptualization of variable wing geometry with a range of 15 degrees to 40 degrees as the maximum sweep angle. The following Figure 4 and Figure 5. represents the Swept wing spanwise flow and design of the swept wings, being the first graph the corresponding to sweep angle of 32.5º(actual wing), the second one to 15º, and the wing of the right part to 40º.

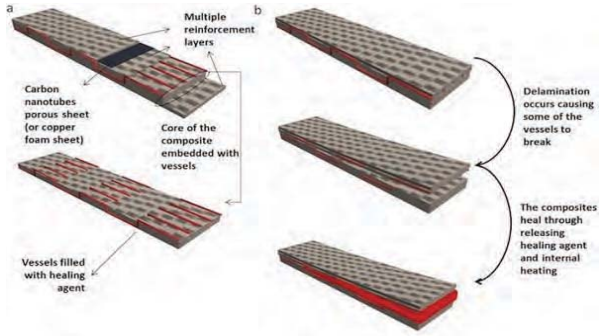

Figure 5. Self-healing process

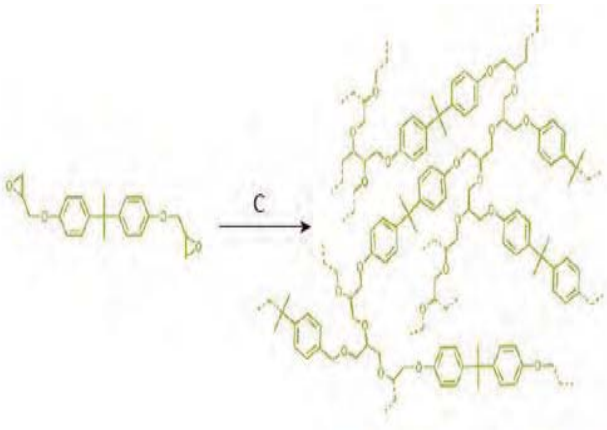

Figure 6. Colour change process

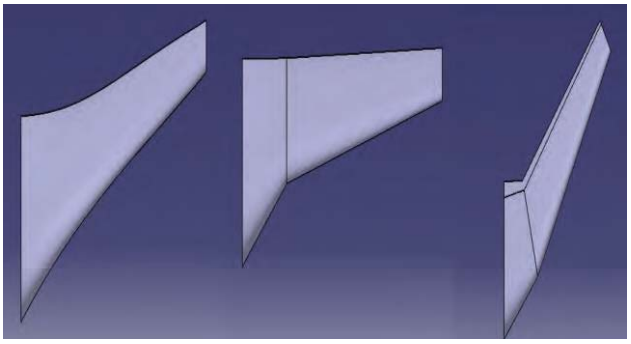

Figure 7. Swept wing designs by CATIA

The wind tunnel will be 60m x 25m x 25m in size as shown in Figure 6. The Figure 7. Shows Swept wing designs by CATIA. The wing is positioned inside the domain as a resemblance to a real wind tunnel testing. The meshing procedure was initiated after the domain was created and the wing imported in Star CCM+. The Figure 8. shows the Domain view in Star CCM+. Mesh continua parameters are shown in table II. The surface and volumetric mesh parameters were optimized in a way that would save simulation time and yield better residual convergence since a better mesh would save simulation time and yield better results. CFD analysis was implemented using assumptions for our fluid medium that were derived from the type of research. Our study is concerned with the transonic flow, which assumes that the air is a steady, compressible gas. Because our fluid the domain is a turbulent one. Choose the K-Omega's turbulent model to simulate airflow turbulent phenomena in a real environment. Consider the inlet region as a "Velocity inlet" of 0.8 Mach representing the cruise speed of the aircraft [11]. The outlet region is "Pressure outlet". The top, bottom, left and right regions of the domain region are "Symmetry plane" to simulate the atmospheric flow around the wing. The figures from Figure 9. to Figure 11. Shows the Generated volumetric mesh at different angles.

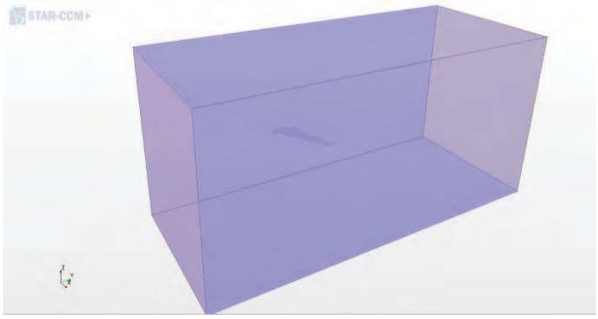

Figure 8. Domain view in Star CCM+

TABLE II.
MESH PARAMETERS

Mesh type	Polyhedral Mesher Surface Re mesher
Base size	5.0 m
Surface Size (Relative Minimum Size)	0.5
Surface Size (Relative Target Size)	50
Tet/Poly Density	0.5
Volumetric Controls – Block	Relative Size – 5%

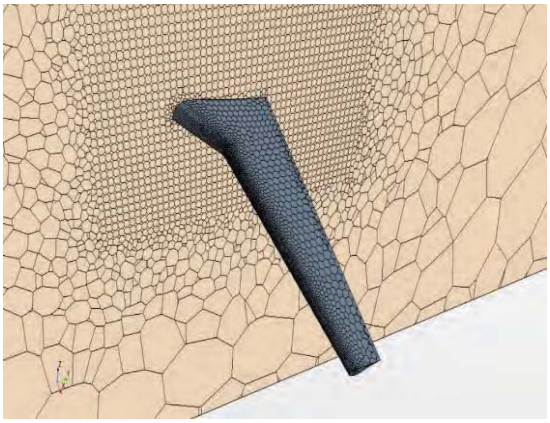

Figure 9. Generated volumetric mesh (sweep angle 15º)

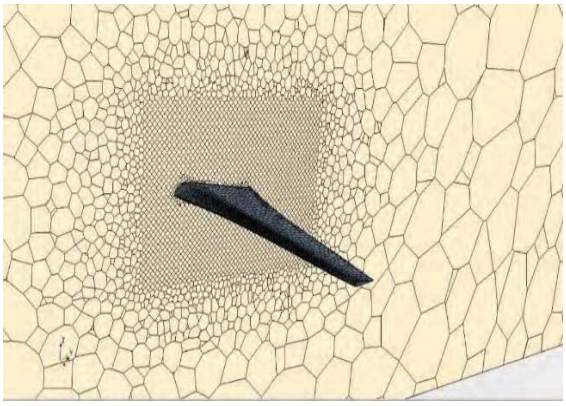

Figure 10. Generated volumetric mesh (sweep angle 32,5º)

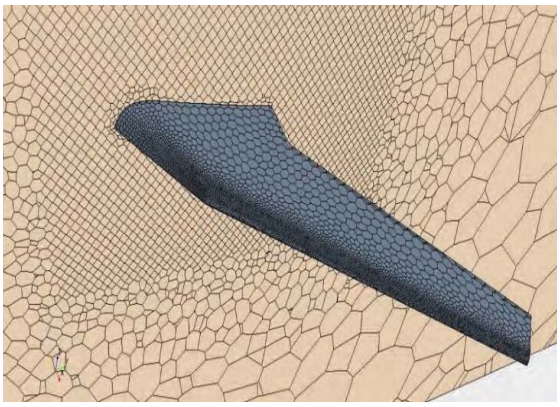

Figure 11. Generated volumetric mesh (sweep angle 40º)

A.Models chosen

- All y+ Wall Treatment
- Exact Wall Distance
- Fluid Film
- Coupled Energy
- Coupled Flow
- Gas
- Gradients
- K-Omega Turbulence
- Reynolds-Averaged Navier-Stokes
- SST (Menter) K-Omega

- Ideal Gas
- Steady
- Three Dimensional
- Turbulent

The boundary conditions of Wing are shown below in table III.

TABLE III.
BOUNDARY CONDITIONS

Boundary	Type
Top,Bottom, Left,Right	Symmetry plane
Outlet	Pressure outlet
Inlet	Velocity inlet

B. Initial conditions

Consider the cruise phase of the Falcon 7x to understand the transonic aerodynamics [8-10] of the aircraft. At a cruise altitude of 41000 ft and with a Mach number 0.8, the air standard properties at the cruise phase are the following. Table IV sows the Air standard properties at cruise altitude.

TABLE IV.
AIR STANDARD PROPERTIES

Cruise altitude	41000 ft
Cruise Mach	0.8 (274.399 m/sec)
Temperature	216.649 K
Pressure	17874.5 N/m^2
Speed of Sound	295.0728

V. RESULTS AND DISCUSSION

The Analysis is carried out in terms of pressure coefficient, lift coefficient, drag coefficient.

A. Pressure Contours

The airflow does not remain supersonic forever due to its speed exceeding Mach 1 and reversing back to capillary flow. At Mach numbers that are slightly above the critical value, shock waves begin to form on the wing.

Subsonic flight's pressure waves converge at this point, and they begin to affect the wing significantly. Essentially, this means that when pressure waves converge, the air in front of wings gets compressed. These can be visually observed on the pressure contour graphs, where the leading edge of the wing is where the pressure is greatest, then the bottom. Pressure waves are produced by the air as it passes along the wing at the speed of sound. The pressure waves cannot move forward in the supersonic flow of air, which means they are stationary. As a result, massive pressure is created. These large pressure changes also result in large forces and moments being transmitted to the wing as well. The plots above show that all three types of swept wings had negative lift coefficients. It is related to the previously discussed phenomena which happen at transonic and supersonic speeds. Figure 12. Shows the formation of shock waves. Different Pressure coefficients at different angles are shown in Figure 13 to Figure 15. Different Lift coefficients at different angles are shown in Figure 16 to Figure 18.

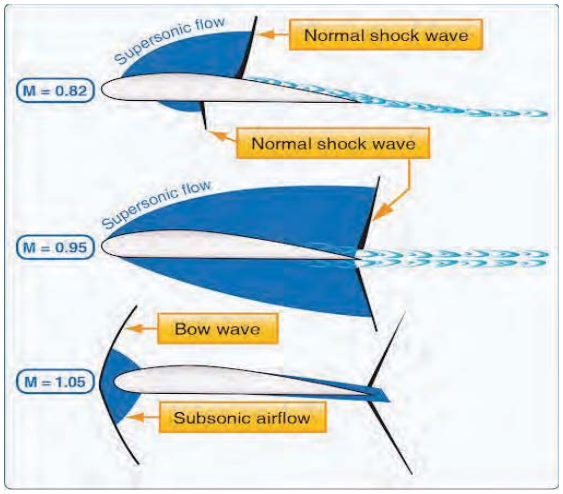

Figure 12. Formation of shock waves

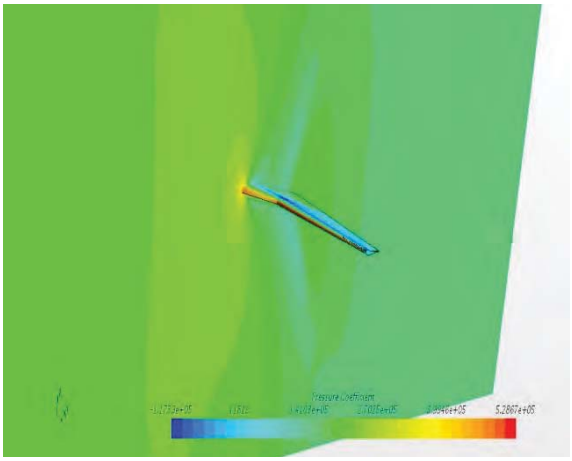

Figure 13. Pressure coefficient (sweep angle 15º)

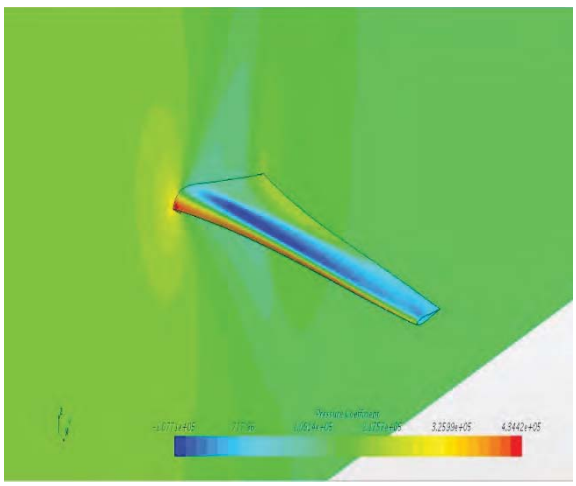

Figure 14. Pressure coefficient (sweep angle 32.5º)

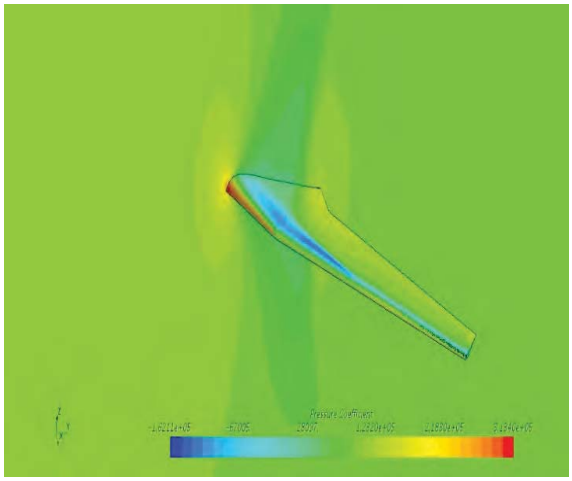

Figure 15. Pressure coefficient (sweep angle 40º)

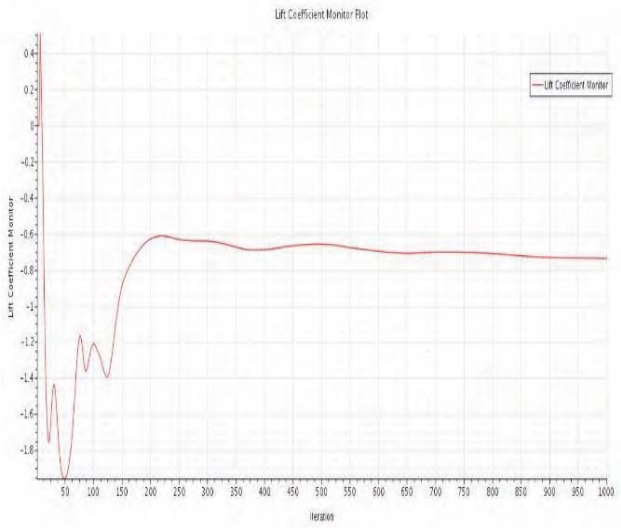

Figure 16. Lift coefficient (sweep angle 15º)

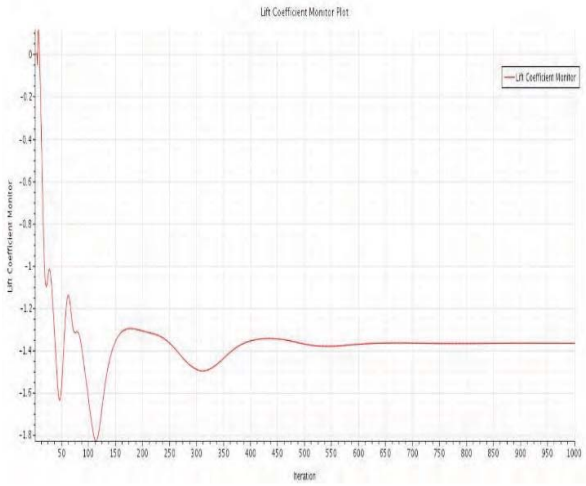

Figure 17. Lift coefficient (sweep angle 32.5º)

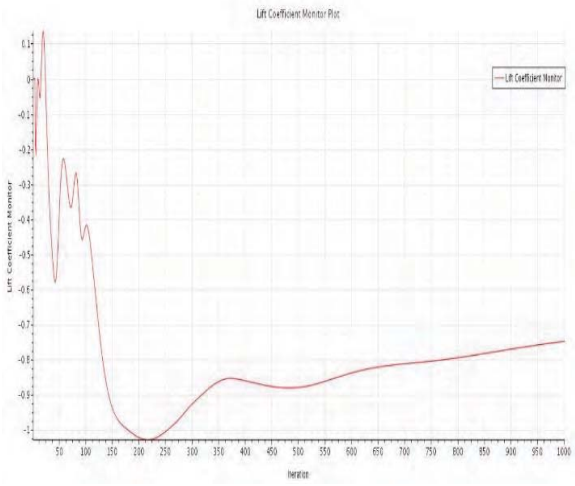

Figure 18. Lift coefficient (sweep angle 40º)

It is related to the previously discussed phenomena which happen at transonic and supersonic speeds. Upon reaching its critical Mach number, air passing over the wing surfaces forms a shock, which results in flow separation. As a result, the trailed edge of the wing experiences a high-pressure field, which negatively influences the lift coefficient.

For the sweep angle 15º, the lift coefficient has a value of 0.76 while for the actual wing it changes to 1.37. For the 40º swept wing, it does not show a proper convergence as for the previous ones, and the reasons why will be analyzed further through the residuals of the simulations. For this last wing, the lift tends to have a close value of 0.75 similar to the 15º swept wing. This drop-in lift can be explained by the theory of swept wings [12].

According to the graphs of the drag coefficient obtained, the drag coefficient value tends to decrease as the sweep angle increases, so they are inversely proportional. For example, for the 10º swept wing its corresponding drag coefficient value is equal to 2.3, and it is much bigger than the obtained one for the actual wing 32.5º which is about 1.64. For the last case, it was obtained a value of 0.37 represents a dramatic drop compared to the previous two cases.

The swept-wing thickness ratio and the airfoil thickness ratio are crucial factors in determining transonic drag levels. When the sweep angle is increased for a wing of a given thickness ratio, the drag level at higher speeds is also decreased significantly. It is essential to note that an aircraft designed to penetrate the low-supersonic speed range should have thin wings with swept tails. The advantage of this type of wing over a straight wing is that a swept-wing offers improved cruising Mach numbers while enabling robust aspect ratios to make maximum lift-drag values possible. There is a complex series of trade-off studies that must be carried out to arrive at the optimal sweep angle, aspect ratio, airfoil thickness ratio, and wing weight for adequate wing strength and stiffness.

E-ISSN 2581 – 7957
P-ISSN 2277 – 3916

CVR Journal of Science and Technology, Volume 22, June 2022
DOI: 10.32377/cvrjst2215

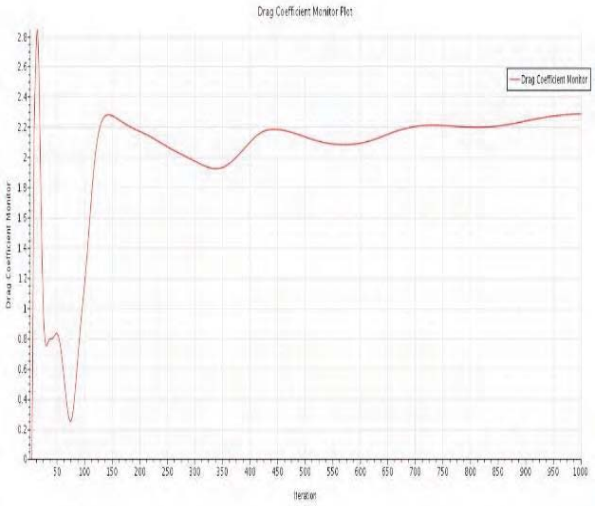

Figure 19. Drag coefficient (sweep angle 15º)

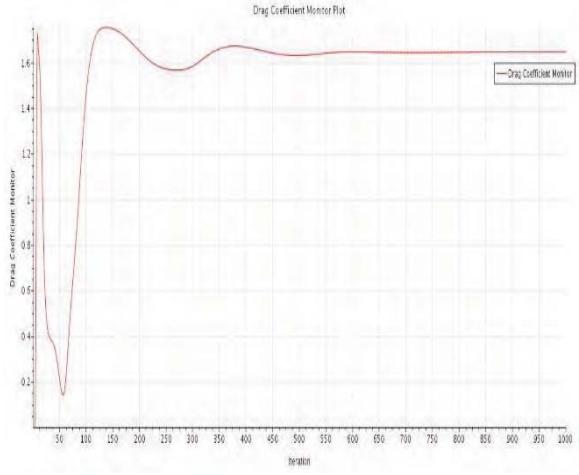

Figure 20. Drag coefficient (sweep angle 32.5º)

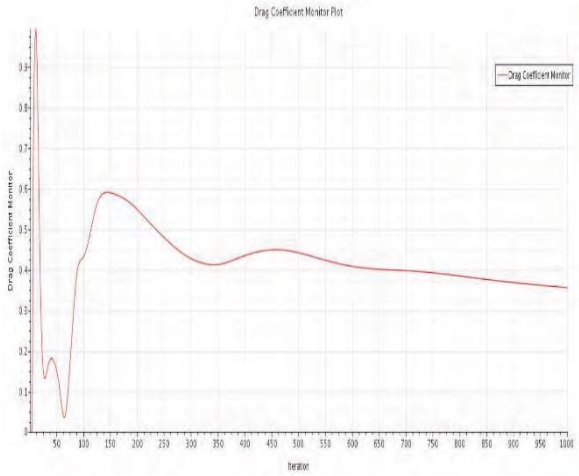

Figure 21. Drag coefficient (sweep angle 40º)

The figures from Figure 19. to Figure 21. Shows the drag coefficients at different angles.

A. Span Wise Pressure Distribution

The below plots illustrate pressure contours on three parts of the wingspan with an offset of 7m between each pressure contour plane. The Pressure coefficients along with wingspan at different angles are shown in Figure22 to Figure 24. The Residual graphs at different angles are shown from Figure 25. to Figure 27.

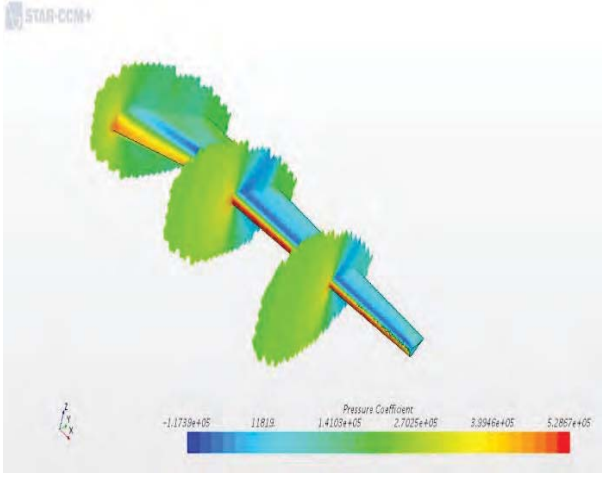

Figure 22. Pressure Coefficient along the wingspan (sweep angle 15º)

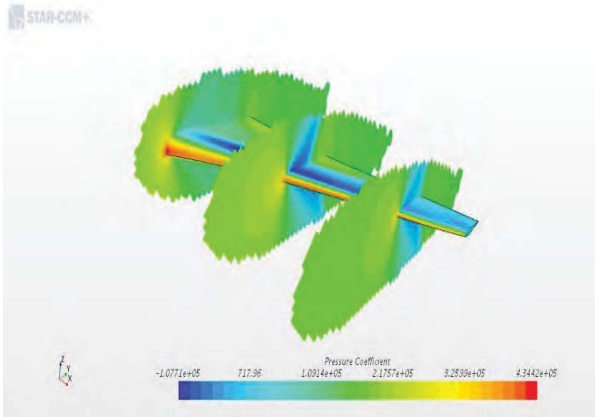

Figure 23. Pressure Coefficient along the wingspan (sweep angle 32,5º)

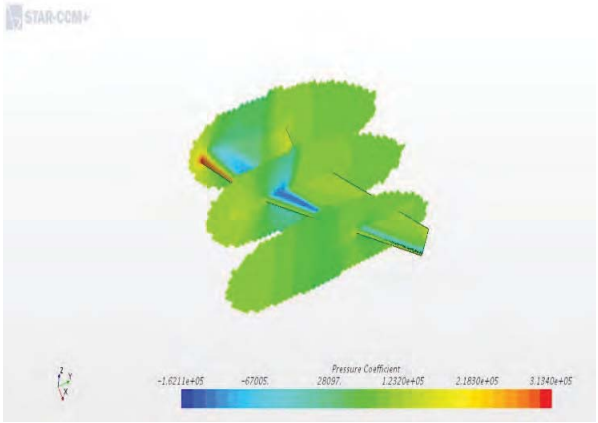

Figure 24. Pressure Coefficient along the wingspan (sweep angle 40º)

CVR Journal of Science and Technology, Volume 22, June 2022
DOI: 10.32377/cvrjst2215

The contours images clearly show that as the sweep angle increases, the pressure coefficient decreases at the leading edge of the wings. This again confirms the fact that at transonic speeds, the increasing sweep angle decreases the form drag as the airflow passes comparatively easier than that of the less swept wings (15º here).

B. Residuals Graphs

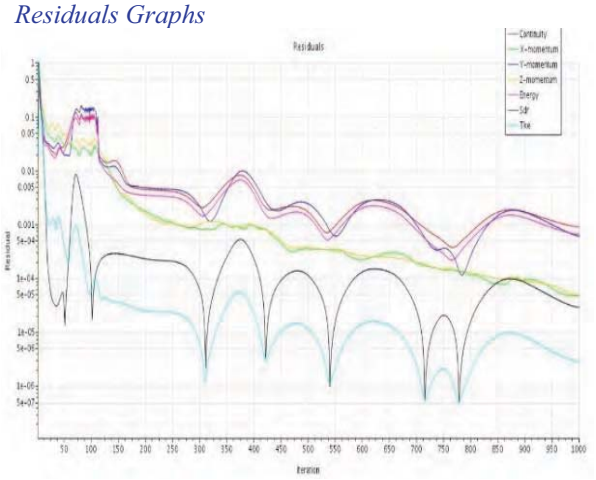

Figure 25. Residuals (sweep angle 15º)

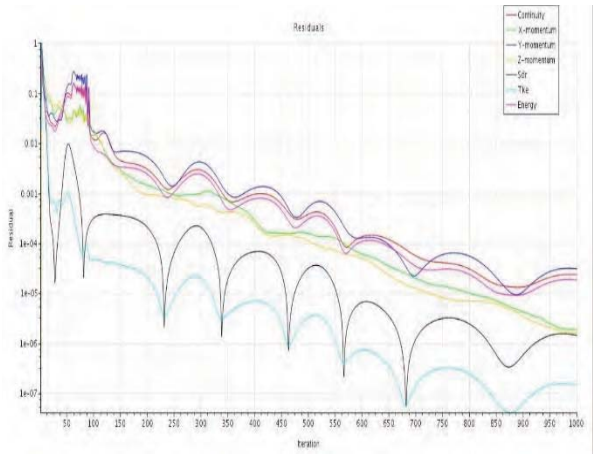

Figure 26. Residuals (sweep angle 32.5º)

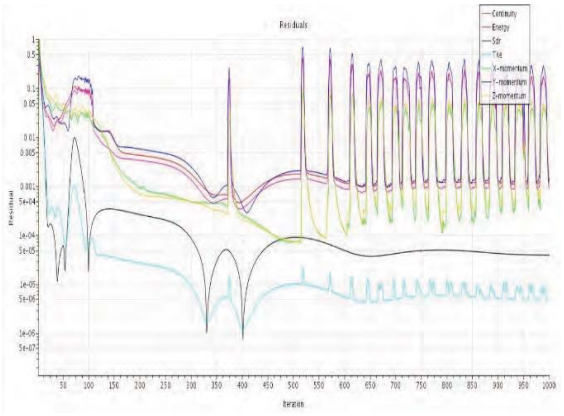

Figure 27. Residuals (sweep angle 40º)

An analysis of the drag and lift coefficients revealed that the convergence rates between the three cases were different. For the sweep angle 40º, the drag and lift coefficient tend to converge, but the behavior is not the same as in the other wings. Observed from the residual graph of a 40º swept wing, there are some unwanted perturbations after 500 iterations.

Those perturbations are due to the existence of a vortex shedding of the flow. This vortex shedding phenomenon happens when the attached flow over a body gets separated and therefore altering its dynamics. A wing's leading-edge vortices [13-15] have an important impact on its pressure distribution and, therefore, its aerodynamic performance, stability characteristics, and structural design loads.

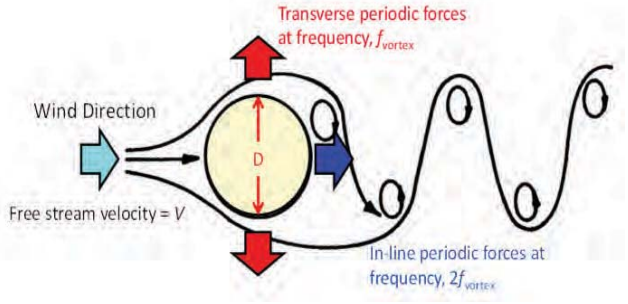

Figure 28. Vortex shedding phenomenon

Figure 28. shows the Vortex shedding phenomenon waveform. A very high negative pressure develops due to the expansion of the flow around the leading-edge pressure gradient. The boundary layer can easily separate due to this. A wing that is breaking up along its leading edge creates a region of concentrated vorticity in the lower surface of the boundary layer. As the vorticity opens, the upper side of the wing produces an intense side wash that travels towards the leading edge. A minimum of pressure results under these vortices, increasing lift in the form of a vortex on the upper surface of the wing. This could increase lift, generate forces and moments for flight control, and reduce drag by reducing the vortex effects. There are several ways to control the flow, including the control of flow separation, shear layer separation, and vortex formation. These phenomena are also dependent on the wing sweep angle, as well as their relative importance.

C. Boundry Layer

For that reason, as the sweep angle increases, the vortex starts to appear on the wing. As a result, sweeping wings with 40o swept are more likely to exhibit those kinds of perturbations than wings with 32.5º or 15º swept. Figure 29. to Figure 30. Shows Y+ distance or Boundary layer at different sweep angles. This line represents the distance between boundary layer walls, and the value gets larger at the trailing edge of the wing. Consequently, there is flow separation on the upper surface of the wing due to the supersonic flow. The supersonic flow is caused by the air traveling on the wing having an increase in velocity near the sound speed on both its upper and lower surfaces.

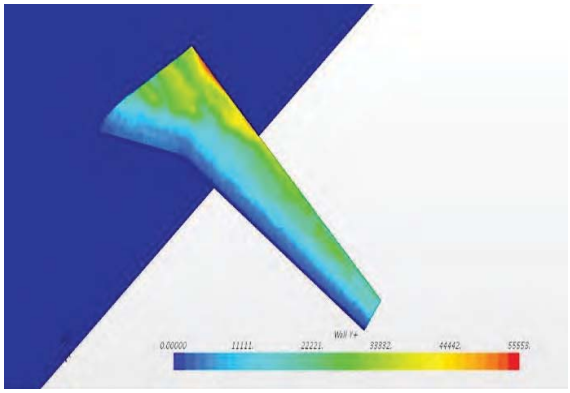

Figure 29. Y+ distance or Boundary layer (Sweep angle 15º)

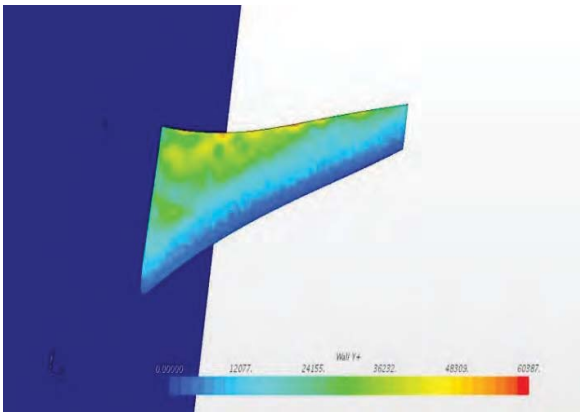

Figure 30. Y+ distance or Boundary layer (Sweep angle 32,5º)

This again confirms the presence of flow separation at the trailing edge of the 15-degree sweep angle wing which will lead to an unstable moment on the wing because of the stalling region formed by the flow separation regions. The stalling region reduces as it sweeps angle increases from 15 degrees to 40 degrees. Therefore, high-speed fighter jets like F-14 Tomcat and Mikoyan MiG-27 uses high swept wings for supersonic maneuvers and low swept wings for subsonic flight phases like takeoff, landing, and cruise.

VI. Conclusions

The CSV files exported from the STAR CCM+ CFD solver show that the Drag coefficients are significantly lower for the maximum swept wing at transonic speeds, but the Lift coefficients are better for the minimum swept wing. As a result, the undertaken concept of wing design will prove to be efficient for subsonic flight phases such as takeoff, landing, and climbing if we can employ a low sweep configuration. At transonic speeds, the maximum swept-wing configuration will improve its aerodynamic performance to a greater extent. To reduce the acceleration, the amount of air flowing parallel to the chord line must be reduced, by delaying the critical Mach number. This allows the aircraft to fly at higher Mach numbers before facing waves of drag. Therefore, sweeping the wing-back delays the supersonic flow from occurring over the wing by lessening the amount of acceleration over the wing. It is however important to consider the fact that a swept-wing always has more drag at slower speeds since low-speed drag is determined by the aspect ratio and by the span compared to chord, which in this case is shorter from tip to tip than a swept wing. Many airlines and commercial aircraft manufacturers hesitate to choose the morphing wings or the simple variable wings concept for its complex mechanical system which can lead to further increase in the MTOW (Maximum Take-off Weight) causing more demanding engine requirements and more fuel consumption. The recent research in the aerospace field under the fields of Flapping wings, Morphing airfoils, control surfaces, etc., which are highly futuristic and encourage aspiring students and engineers in exploring the underlying possibilities for a top-notch efficient future commercial aircraft

References

[1] PEI DAI et.al., “Modeling and Nonlinear Model Predictive Control of a Variable-Sweep-Wing Morphing Waverider”, IEEE Access, Vol.9, April 22, 2021.
[2] Dietrich Kuchemann, “The Aerodynamic Design Of Aircraft”, American Institute of Aeronautics and Astronautics, AIAA education series, 2012.
[3] LIANG GAO et.al., “Flight Dynamics Modeling and Control of a Novel Catapult Launched Tandem-Wing Micro Aerial Vehicle with Variable Sweep”, IEEE Access, Vol.6, August 20, 2018.
[4] Mark Drela, “Flight Vehicle Aerodynamics”, Massachusetts Institute of Technology, February 2014.
[5] R.DAS et.al., “Self-Healing composites for Aerospace applications”, Advanced Composite Materials for Aerospace Engineering, Processing, Properties and Applications, Pages 333-364, 24 June 2016.
[6] Duncan Wass, Tim Harrison, “Self-healing aircraft wings: a dream or a possibility?”, Science in School, The European journal for science teachers, Issue. 37, September 6, 2016.
[7] Fred George, “Business and Commercial Aviation”, Pilot report, Dassault Falcon 7x, August,2006.
[8] Nirmit Prabhakar, “Design and Dynamic Analysis of a Variable-Sweep, Variable-Span Morphing UAV”, Master thesis, EMBRY RIDDLE, Aeronautical University, December,2014.
[9] John J. Bertin, Russell M.Cummings, “Aerodynamics for Engineers”, Pearson Education Limited, Fifth Edition, 2009.
[10] Vos, Roelof, Farokhi, Saeed, “Introduction to Transonic Aerodynamics”, Springer Netherlands, Vol.110, 2015.
[11] Ajoy Kumar Kundu, “Aircraft Design” Cambridge Aerospace Series, Cambridge University Press, 2010.
[12] Charles J. Donlan and Joseph Weil Langley, “Characteristics Of Swept Wings At High Speeds”, Langley Aeronautical Laboratory National Advisory Committee for Aeronautics. Langley Aeronautical Lab, January 30, 1952.
[13] John K. Northrop, “The Development of All–Wing Aircraft”, Cambridge University Press, Vol.51, Issue 438, July 28, 2016.
[14] R. KULFAN, “Wing geometry effects on leading-edge vortices”, Aerospace research central, August 17, 2012.
[15] I Gursul, E Vardaki, P Margaris, Z Wang, “Control of wing vortices”, Department of Mechanical Engineering, University of Bath, Springer, pp.137-151, Berlin, Germany, 2007.

E-ISSN 2581 – 7957
P-ISSN 2277 – 3916
CVR Journal of Science and Technology, Volume 22, June 2022
DOI: 10.32377/cvrjst2216

Design and Structural Analysis of Leaf Spring using ANSYS Workbench

C. Sai Kiran[1], P. Ravi Kumar[2], V. Rahul[3], B. Appala Naidu[4]
[1]Asst. Professor, CVR College of Engineering/Mechanical Engg. Department, Hyderabad, India
Email: csaikiran001@gmail.com
[2]Asst. Professor, CVR College of Engineering/Mechanical Engg. Department, Hyderabad, India
Email: ravikumar.patibandla@gmail.com
[3]Asst. Professor, CVR College of Engineering/Mechanical Engg. Department, Hyderabad, India
Email: vudarahul@gmail.com
[4]Assoc. Professor, CVR College of Engineering/Mechanical Engg. Department, Hyderabad, India
Email: bnaidua@gmail.com

Abstract: **In this paper, a leaf spring was designed and analyzed which is useful for damping the vertical vibrations caused during driving a vehicle on an irregular road. Leaf spring is an essential component of any heavy vehicle, which is connected the frame of the vehicle at each end. The purpose of this work is to model a leaf spring which will supports the weight of the chassis and to improve the ride quality by reducing the disturbances caused by a bump road. Leaf spring is designed in CREO software. Analysis of leaf spring was performed by using ANSYS software and the results of von-mises stress and total deformation helps to predict the leaf spring failure when an external load acts on it.**

Index Terms: **Leaf spring, damping, ANSYS, von-mises stress.**

I. INTRODUCTION

Whenever any heavy vehicle is frequently crossing a bump on the road, passengers feel discomfort. Therefore, leaf spring is a critical part of a suspension system used to support the entire weight and damp shock impulse. Without leaf springs, the vehicle will have a bouncing ride. Leaf spring absorbs sudden shocks generated by the uneven road surfaces and makes the ride comfortable.

Sunil and jeevan [1] have created a leaf spring design for carrying loads of a vehicle. The leaf spring is modelled and static analysis is performed by varying the material in ANSYS Mechanical APDL software. After modelling the leaf spring, boundary conditions are applied. It's observed from the results that the maximum stress is developed at the inner side of the eye sections.

Raavendra and abdul [2] have developed a new design for leaf spring by using CATIA software and analysed in ANSYS Workbench software. In the results, total deformation, strain and stress induced in the leaf spring is observed.

Ramanareddy et al. [3] has modelled a leaf spring by using CATIA V5 R20 and structural analysis are performed on leaf spring by considering different materials for spring by using ANSYS software. Structural analysis was performed to validate the strength of the leaf spring by determining the stress and deformation.

Harinath and venugopal [4] have designed a leaf spring of TATA-407 vehicle. The leaf spring is modelled and analysis in ANSYS software, the results of deformation and von-mises stress were observed.

Pulkit and ajay [5] have reviewed ten papers of the leaf springs and compared the results among the papers between the conventional and composite leaf spring by viewing the results of stress and deflection.

Manash et al. [6] has modelled and analyzed the leaf spring using ANSYS software. Structural analysis is performed to know the deformations and stress induced.

Amitkumar [7] has designed a 3D model of leaf spring by using CREO software. Static structural analysis is performed in ansys. The results of natural frequency, total deformation and equivalent stress were observed.

Ajahar et al. [8] has modelled a leaf spring using CATIA V5 R20 software. Structural analysis of leaf spring is performed by using ANSYS software. Comparison of weight reduction%, stress and deformation is performed.

Sai and bhaskara [9] have modelled and analyzed in ANSYS 15.0 software. Total deformation and equivalent stress values are observed.

Ganesh and pawan [10] have designed and analysed the leaf spring in ANSYS software. In the analysis the results for orientation of the fiber, stress and deflections are observed.

Waghmare and patil [11] have created a leaf spring model by using Pro-E software. In structural analysis, the von-mises stresses and distribution plots are observed.

Lydia and siva [12] have designed a 3D model of a leaf spring by using CATIA software. Structural analysis is performed by using ANSYS software. Total deformation and equivalent stress is observed.

Dev and jain [13] have designed and analyzed the leaf spring by using ANSYS software. By considering different loading conditions, structural analysis is performed and the results of total deformation, equivalent stress and safety factor are observed.

Raja and manas [14] have modelled a leaf spring with different thickness of plates by using Solid works software. Structural analysis is performed to determine the maximum stresses, total deformation and maximum strain values.

Pankaj et al. [15] has modelled a leaf spring in AutoCAD 2012 software. The analysis of the leaf spring is performed in ANSYS 9.0 software. Von-mises stress and displacement results were observed.

Received on 06-11-2021, Revised on 10-03-2022, Accepted on 12-04-2022

CVR Journal of Science and Technology, Volume 22, June 2022
DOI: 10.32377/cvrjst2216

A. Different Types of Leaf Spring

Leaf spring is attached to the frame of the vehicle. A leaf spring consists of series of flat plates, the length of the top leaf gradually reduced and slightly bent. Leaf springs provide ride comfort and stability to the vehicle on uneven road surfaces by minimising the road shocks.

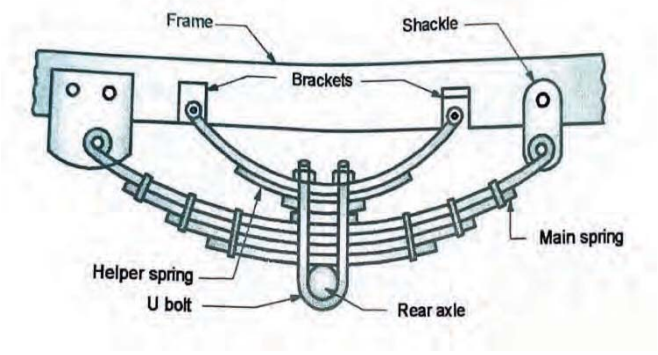

Figure 1. Leaf spring and its Parts

Leaf spring is represented in Fig. 1. The main parts of a leaf spring are main spring, helper spring, U-bolt and center clip. Some of the important types of leaf springs are given below:

1. Transverse leaf spring: In this, the two leaf springs are combined facing away from each other to create an oval shape. These leaf springs are in parabolic shape and appear on both front and rear axles.
2. Elliptical leaf spring: These leaf springs are in parabolic shape and appear on both front and rear axles.

B. Working Principle of a Leaf Spring

Whenever a vehicle hits a bump on the road, load will be applied on the eye of the leaf spring. Leaf spring works on the principle of bending as shown in Fig.2.

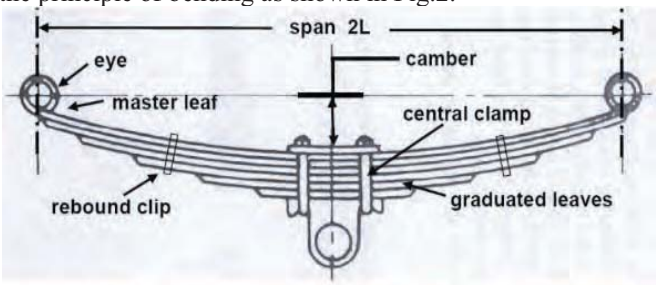

Figure 2. Working Principle of a Leaf spring

When the load is applied on the eye of the leaf spring, bending of the plates occurs. By the nature of the structure, it opposes the bending. This result in a reaction force of the leaf spring, which will oppose the load applied on eye of the leaf spring. Due to the stiffness property of the leaf spring the bended leaves will bounce back and absorbs the shock loads acted on it.

C. Leaf Spring Material

Leaf springs are generally made of materials which are very strong and which are suitable for withstanding heavier impact loads on it. Structural steel, Aluminum alloy and E-glass Epoxy are the materials selected for leaf spring.

TABLE I.
MATERIAL PROPERTIES OF LEAF SPRING

S. No	Properties	Structural Steel	Aluminum Alloy	E-glass Epoxy
1.	Density (Kg/m^3)	7,800	3,630	1900
2.	Young's Modulus (GPa)	210	77.9	300
3.	Yield Strength (MPa)	360	279	415
4.	Tensile Strength (MPa)	610	344	490
5.	Poisson's Ratio	0.3	0.327	0.22

II. MODELLING AND FINITE ELEMENT ANALYSIS

A. Leaf Spring Model

The important parts of a leaf spring are upper mount, piston rod, cylinder and lower mount. All the different parts of the leaf spring are modeled separately in CREO software and all the individual parts of the leaf spring are assembled in the CREO software as shown in Fig. 3

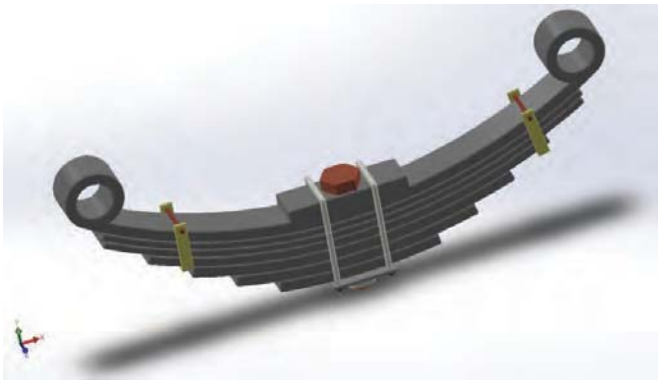

Figure 3. Assembled Model of Leaf Spring in CREO

B. Elememt Type

The element type selected for leaf spring is SOLID 186. It is a 20-node higher order solid element which has three degrees of freedom per node. The three degrees of freedom are nodal x, y and z translations.

It exhibits quadratic displacement behavior and have spatial orientation. SOLID 186 support large strain capabilities, plasticity, large deflection, hyper elasticity, stress stiffening and creep. SOLID 186 have capability for simulating deformations of incompressible elastoplastic materials and incompressible hyper-elastic materials.

C. Meshing

In meshing, the created 3D model is divided into the certain number of divisions or elements for accurate analysis result. By applying meshing on the model, we can determine the effectiveness and efficiency of any analysis. An automated mesh is generated on the created model which is shown in Fig. 4.

CVR Journal of Science and Technology, Volume 22, June 2022
DOI: 10.32377/cvrjst2216

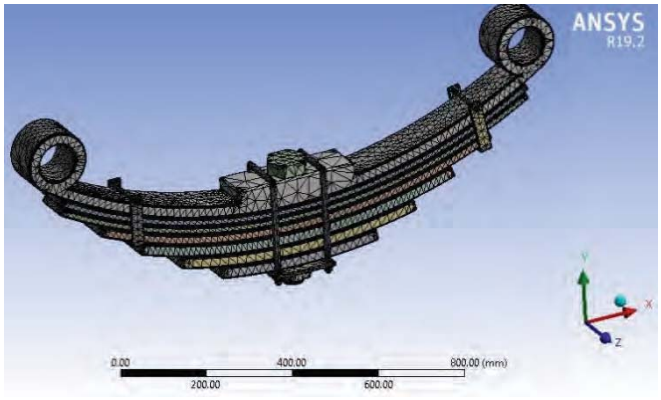

Figure 4. Meshing of Leaf Spring

In the automatic mesh, the mesh applied was a fine mesh to achieve precise and accurate results. Instead of using a fine mesh on all the components of the model, coarse mesh was applied on larger area and fine mesh was applied only on the area of higher stress concentration.

D. Applying Loads

On leaf spring, a remote displacement is assigned at two sides of eye locations. A force of vehicle weight of 20322 N is considered and applied on the center of leaf spring span as shown in Fig. 5.

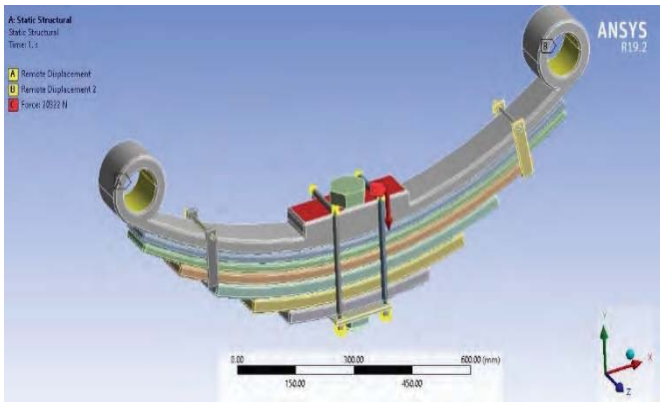

Figure 5. Loads on the Lower Mount of Leaf spring

III. Results and Discussions

After assigning two remote displacement supports on the eye locations and applying the static load of 20322 N on the center of the leaf spring, structural analysis is performed on the leaf spring for three different materials in ANSYS Workbench software to determine the total deformation and von-mises stress. The following results were observed in the analysis.

A. Total Deformation of Leaf spring

After performing structural analysis on structural steel material by applying the external load on leaf spring, a maximum total deformation of 0.30573 mm and the minimum total deformation of 0.029272 mm are observed from the Fig. 6.

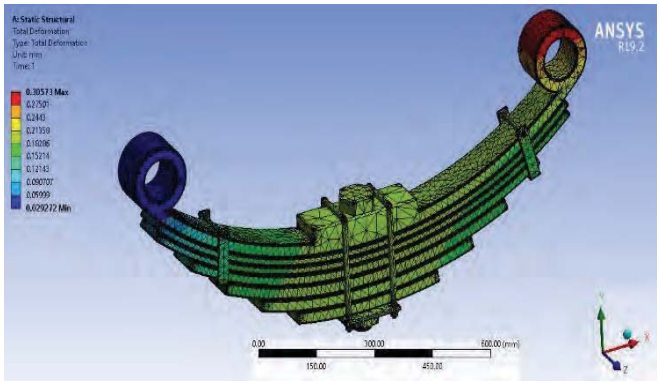

Figure 6. Total Deformation of Structural Steel Material

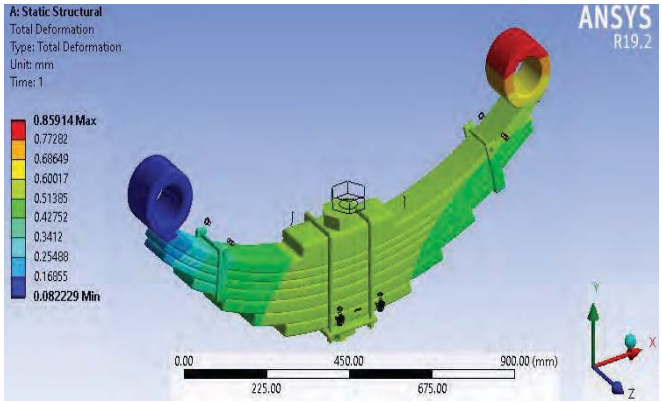

Figure 7. Total Deformation of Aluminum Alloy Material

After performing structural analysis on aluminum alloy material by applying the load on leaf spring, a maximum total deformation of 0.859 mm and the minimum total deformation of 0.0822 mm are observed from the Fig. 7.

After performing structural analysis on E-glass epoxy material by applying the load on leaf spring, a maximum total deformation of 0.76766 mm and the minimum total deformation of 0.07354 mm are observed from the Fig. 8.

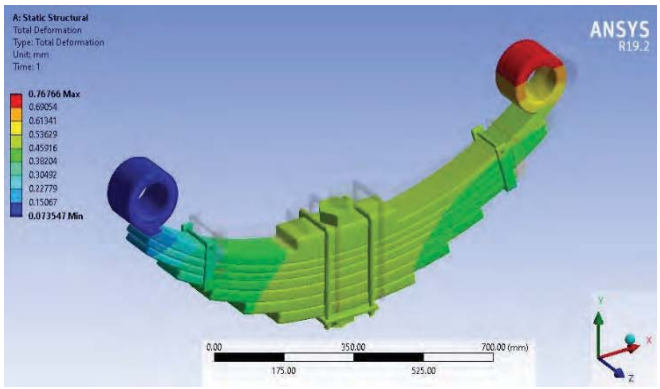

Figure 8. Total Deformation of E-glass Epoxy Material

B. Von-Mises Stress of Leaf spring

After performing structural analysis on structural steel material by applying the load on leaf spring, maximum von-mises stress of 85.306 MPa and minimum von-mises stress of 0.000058 Pa are observed from the Fig. 9.

E-ISSN 2581 –7957
P-ISSN 2277 – 3916

CVR Journal of Science and Technology, Volume 22, June 2022
DOI: 10.32377/cvrjst2216

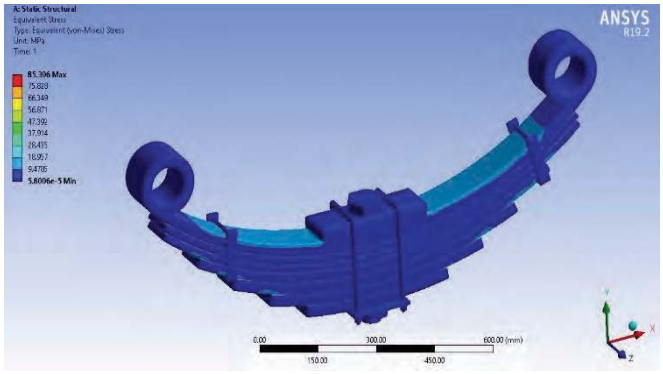

Figure 9. Von-Mises Stress of Structural Steel Material

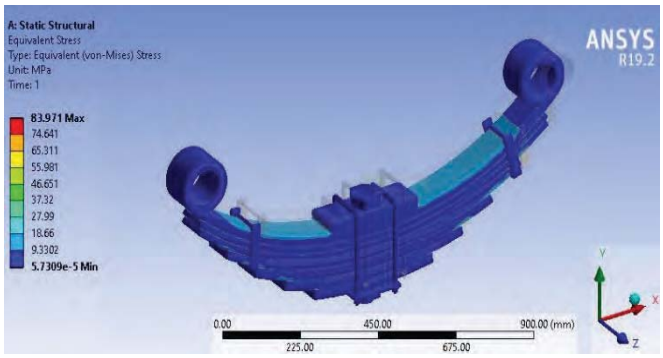

Figure 10. Von-Mises Stress of Aluminum Alloy Material

After performing structural analysis on aluminum alloy material by applying the load on leaf spring, maximum von-mises stress of 83.971 MPa and minimum von-mises stress of 0.000057 Pa are observed from the Fig. 10.

After performing structural analysis by applying the load on leaf spring for aluminum alloy material, maximum von-mises stress of 88.677 MPa and minimum von-mises stress of 0.000048 Pa is observed from the Fig. 11.

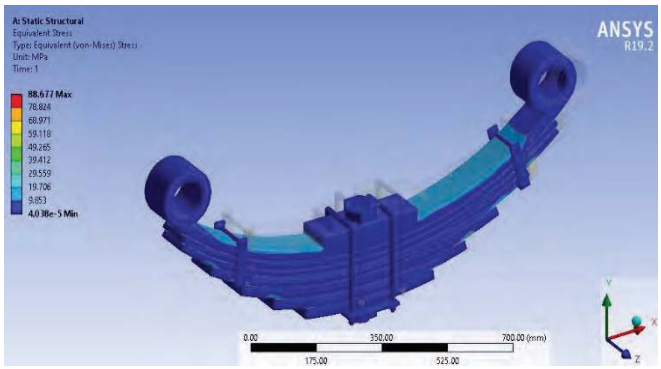

Figure 11. Von-mises Stress of E-glass Epoxy Material

After performing structural analysis by applying the load on leaf spring, the graph of total deformation for three different materials is observed from the Fig. 12.

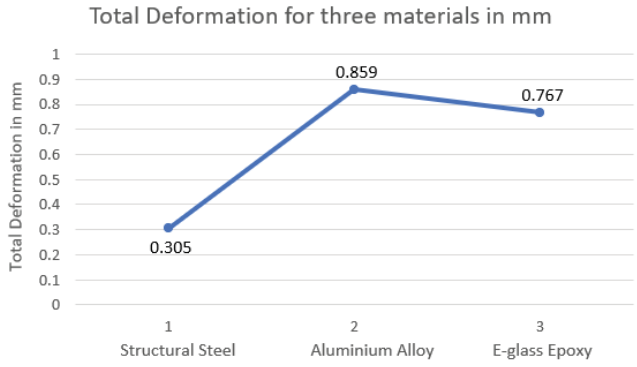

Figure 12. Total Deformation Graph for Different Materials

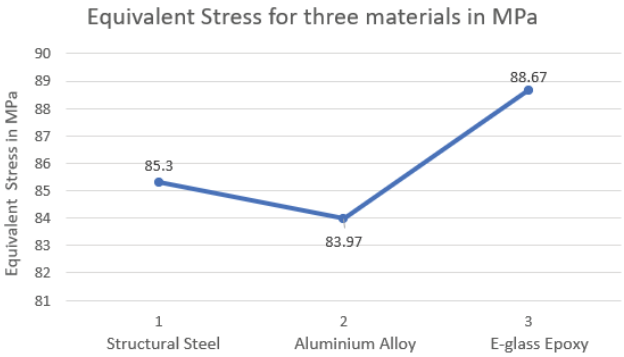

Figure 13. Equivalent Stress Graph for Different Materials

After performing structural analysis by applying the load on leaf spring, the graph of von-mises stress for three different materials is observed from the Fig. 13.

TABLE II.
RESULTS COMPARISON FOR LEAF SPRING MATERIAL

Material	Total Deformation (mm)	Equivalent Stress (MPa)
Structural Steel	0.30573	85.306
Aluminum Alloy	0.85914	83.971
E-glass Epoxy	0.76766	88.677

From the Table II, it is observed that the maximum total deformation is observed in aluminium alloy and the minimum total deformation is observed in carbon steel material. Maximum von-mises stress is observed in carbon steel and the minimum von-mises stress is observed in aluminium alloy material.

IV. CONCLUSIONS

In this paper, CREO software is used for modelling the leaf spring and analysis of leaf spring with a force of 20322 N is performed by using ANSYS software. Structural analysis is performed on the leaf spring to determine the values of von-mises stress and total deformation of the leaf spring. The effects of material initial residual stresses on the deformation of aluminium alloy are studied and it is the

primary cause for the deformation of the plate. By observing the relationship of total deformation and thickness of the plate, it is suggested to increase the thickness of the plate for aluminium alloy to become best suitable material.

The values of von-mises stress and total deformation of the leaf spring are within the limits. Therefore, modelled leaf spring has long life and safe to use.

REFERENCES

[1] Sunil Chinta and N. Jeevan Kumar, "Design and analysis of a leaf spring," *Global Journal of Computer Science and Technology*, vol. 13, Issue 1, pp. 39–43, 2013.

[2] A. Raveendra and Mohammed Abdul Mubashir, "Design and analysis of leaf spring for heavy weight vehicles using composite materials," *International Journal of Innovative Technology and Exploring Engineering*, vol. 8, Issue 2S, ISSN: 2278-3075, pp. 286–291, December 2018.

[3] D. V. Ramanareddy, B. Subbaratnam, E. Manoj Kumar and Perala Kalyan Praneeth, "Design and analysis of composite leaf spring," *International Journal of Mechanical Engineering and Technology*, vol. 8, Issue 6, ISSN: 0976-6359, pp. 494–500, June 2017.

[4] G. Harinath Gowd and E. Venugopal Goud, "Static analysis of leaf spring," *International Journal of Engineering Science and Technology*, vol. 4, Issue 8, ISSN: 0975-5462, pp. 3794–3803, August 2012.

[5] Pulkit Solanki, and Dr. Ajay Kumar Kaviti, "Study and review on the analyses of leaf spring," *International Journal of Scientific Research and Development*, vol. 3, Issue 9, ISSN: 2321-0613, pp. 637–640, September 2015.

[6] Manash Dey, Sarthak Uniyal, Sagar Singh Dhillon, Kanal Rauthan, and Mudit Sharma, "Design and analysis of leaf spring using ANSYS," *International Journal of Applied Engineering Research*, vol. 14, Issue 10, ISSN:0973-4562,pp. 67–70, 2019.

[7] Amitkumar Magdum, "Dynamic analysis of leaf spring using ANSYS," *International Journal of Modern Trends in Engineering and Research*, vol. 3, Issue 10, ISSN: 2393-8161, pp. 51–59, October 2016.

[8] Ajahar Sayyad, Rahul Kulkarni, Alimoddin Patel and Umesh Jadhav, "Design and analysis of leaf spring by using composite material," *International Research Journal of Engineering and Technology*, vol. 7, Issue 8, ISSN: 2395-0072, pp. 4501–4506, August 2020.

[9] M. Sai Kumar and Dr. C. Bhaskara Reddy, "Modelling and structural analysis of a leaf spring using finite element method," *International Research Journal of Engineering and Technology*, vol. 4, Issue 12, ISSN: 2395-0072, pp. 1155–1161, December 2017.

[10] Ganesh R. Chavan and Pawan V. Chilbule, "Design and analysis of leaf spring using composite materials," *International Journal of Engineering Research& Technology*, vol. 7, Issue 5, ISSN: 2278-0181, pp. 569–576, May 2018.

[11] P.B.Waghmare and R. B.Patil, "Static and modal analysis of leaf spring using FEA," *Imperial Journal of Interdisciplinary Research,* vol. 3, Issue 4, ISSN: 2454-1362, pp. 2036–2044, 2017.

[12] D. Lydia Mahanthi and C. Venkata Siva Murali, "Design and analysis of composite leaf spring for light weight vehicle," *International Journal of Advanced Engineering Research and Science*, vol. 4, Issue 3, ISSN 2349-6495, pp. 147–152, March 2017.

[13] Dev Dutt Dwivedi and V. K. Jain, "Design and analysis of automobile leaf spring using ansys," *International Journal of Current Engineering and Scientific Research,* vol. 3, Issue 1, ISSN: 2393-8374, pp. 100–105, August 2016.

[14] Raja Manas Macherla, and Srikanth Bajaj, "Design and analysis of leaf spring," *International Journal of Professional Engineering Studies*, vol. 9, Issue 2, pp. 223–230, October 2017.

[15] Pankaj Saini, Ashish Goel and Dushyant Kumar, "Design and analysis of composite leaf spring for light vehicles," *International Journal of Innovative Research in Science, Engineering and Technology Research*, vol. 2, Issue 5, ISSN: 2319-8753, pp. 1–10, May 2013.

[16] C. Sai Kiran, M. Ravi Kumar, P. Srinivas Reddy and T. Venkatesh, "Modelling and analysis of brake drum using ansys workbench" *CVR Journal of Science and Technology*, vol. 19, pp. 113-117, December 2020.

[17] C. Sai Kiran, "Design and analysis of shock absorber using ansys workbench" *CVR Journal of Science and Technology*, vol. 17, pp. 144-149, December, 2019.

[18] C. Sai Kiran and J. Sruthi, "Design and structural analysis of scissor jack using ansys workbench" *CVR Journal of Science and Technology,* vol. 15, pp. 101-105, December 2018.

[19] C. Sai Kiran and J. Sruthi, "Design and finite element analysis of domestic lpg cylinder using ansys workbench" *CVR Journal of Science and Technology*, vol. 14, pp. 97-101, June 2018.

[20] C. Sai Kiran, J. Sruthi and S. Chandrahas Balaji "Design and crash analysis of a passenger car using ansys workbench" *CVR Journal of Science and Technology*, vol. 13, pp. 96-100, December 2017.

E-ISSN 2581 – 7957
P-ISSN 2277 – 3916

CVR Journal of Science and Technology, Volume 22, June 2022
DOI: 10.32377/cvrjst2217

Investigation on the Hysteresis Characteristics of Vibration Isolation Devices using Bouc-Wen Model

K. Karthik Selva Kumar[1], R. Brintha[2] and Rajesh Kumar[3]
[1]Asst. Professor, CVR College of Engineering/ Mechanical Engg. Department, Hyderabad, India
Email: kksk88@cvr.ac.in
[2]Asst. Professor, J. P. College of Arts and Science/ IT Department, Ayikudi, India.
Email: brinthaveni@gmail.com
[3]Asst. Professor, CVR College of Engineering/Mechanical Engg. Department, Hyderabad, India
Email: rajeshdenim99@cvr.ac.in

Abstract: **Occurrence of undesirable vibrations in any engineering application leads to the possible damage to the structures, sensitive equipment or components, and machineries. Hence, it is a significant factor to be taken into consideration by avoiding or suppressing such structures and equipment's from the undesirable vibration. Wire rope isolator is considered one of the devices mostly used as an isolation device, because of its excellent performance in vibration and shock isolation. Wire rope isolator shows nonlinear hysteresis behavior when subjected to cyclic and dynamic loading. The hysteresis is due to the rubbing action between the adjacent wires. To model this hysteresis behavior, Bouc-Wen is widely used. In this manuscript, an adapted Bouc-Wen model is employed to analyze the hysteresis characteristics. The characteristic of stiffness along with damping factors of the wire rope isolator are deliberated from the force displacement hysteresis loop. The obtained results show the adapted Bouc-Wen model is useful in developing and analyzing the hysteresis behavior along with an effective identification technique to categorize various influencing parameters. The ratio of effective stiffness along with the ratio of damping observed to be varying with the displacement of the wire rope also shown in the result.**

Index Terms: **Wire rope isolator, Bouc-Wen model, Hysteresis, Vibration control.**

I. Introduction

Vibration can damage sensitive equipment, machinery, or structures. There are various isolation devices to decrease the vibration or isolation of the equipment from the undesirable vibration. Out of so many devices, the Wire Rope Isolator (WRI) is mostly used because of its excellent performance in vibration and shock isolation. WRI has various applications in military defense, railways, marine vessels, aerospace, structures, and sensitive equipment. One of the applications of the WRI is to protect the electronic equipment in the airplane, in which the vibration is generated during takeoff, landing, and due to the turbulence in the air. Another application is during transportation of the sensitive electronic equipment, the equipment had to be isolated from the vibration due to uneven road or terrain condition. Wire Rope Isolator comprises of stranded wire rope, which is held by two metal retainers in a helical shape, one at top and other at the bottom, as shown in Figure 1. Due to the flexibility of the rope, the isolator shows good isolation properties in all three directions. The sliding friction and rubbing between the wire rope, the isolator shows the excellent damping performance. Because of rubbing action between the adjacent wire rope, some portion of the kinetic energy gets converted into heat energy and therefore dissipates vibrational energy.

Figure 1. Wire rope isolator

The Hysteresis is considered one of the nonlinear characteristic phenomena, which is observed to come across in a wide range of method in which the relation among the variables of input and the variables of output engaged in the effects of memory. The comprehensive materialistic modelling of subsequent system is considered a strenuous assignment, and the models developed because of the above issue is more often identified to be a complex in nature for the real time engineering applications in various environment.

The nonlinear hysteresis characteristics of the isolator are developed due to the development of dry friction among the wire ropes. Hysteresis behavior is described by various mathematical models proposed by Bouc-Wen, Preisach, Jiles-Atherton method, etc., [1]. The model is widely used for the hysteresis system is BW model. Because of having a single secondary nonlinear differential equation, the model has the benefit of computational simplicity to describe the hysteretic behavior. With a proper set of suitable parameters, it is realistic to develop the response of the adapted model more or less like the characteristics of an original or real-time hysteresis loop. The BW parameters are evaluated by using the black-box approach, with given input-output experimental data, the Bouc-Wen modal parameters have to adjust such that the model output is close to the experimental data.

Received on 06-10-2021, Revised on 09-11-2021, Accepted on 12-12-2021

Ye et. al. [1] estimated the parameters of the BW model employing a Particle Swarm Optimization technique (PSO). PSO and Genetic Algorithms (GA) performance are compared in terms of parameter efficiency. The result shows that the suggested method shows excellent solutions with better computational efficiency as compared to the GA method. Although the simulated data is contaminated with noise, the suggested PSO shows satisfactory optimal performance. Ismail et. al. [3] carried out a survey containing the research done in the past, the latest development, and execution of the BW model in modeling the hysteresis phenomenon, which has been used substantially. He addressed specific issues like identification, control, modeling, etc., that are organized in sections. Each section represents the author's point of view and contribution related to those specific issues. Wang et. al. [4] proposed an effective modeling method to illustrate the piezoelectric hysteresis phenomenon. The BW model is utilized for a piezoelectric actuator, which has hysteresis behavior. The PSO algorithm is utilized to find out the optimized model parameters. The test data exhibits that the BW along with PSO can be used successfully to illustrate the characteristics of a piezoelectric actuator. The identified results and the experimental outcome proved the effectiveness of the above method. Ye et. al. [5] put-forth an improved algorithm of Particle Swarm Optimization (IPSO) merged with the disorganized map to determine the parameters of the hysteresis model. The precision of identified parameters and the nature of the recreated hysteresis were used to relate the performance of the IPSO with the Genetic Algorithm (GA). The result shows that the put forth method has better performance than GA in identifying the BW model parameters. Balaji et. al. [6] reviewed the research work done on the WRI, which can be utilized effectively to protect the structure from undesirable source of vibration. The WRI is a kind of passive model whose response is observed to be in nonlinear. It is consisting of two metal plates placed between the stranded wire rope with a discrete set of stranded wires. They concluded that the isolation provided by the WRI is observed to be better than the other conventional passive isolator, as the conventional passive isolator shows linear behavior, whereas WRI shows nonlinear behavior. The WRI provides isolation in all three planes.

Zhou et. al. [7] investigated an artificial neural network (ANN)-based hybrid modeling method to model the hysteresis re-establishment force of a helical WRI. At two distinct amplitudes and two frequencies, dynamic tests were performed. The experimental data was used to create a system hybrid model. The technique requires more experimental information to achieve a precise model that can predict the isolator reaction at frequencies and amplitude beyond the appropriate information range. [8] Analyzed the possible application of Nonlinearity in controlling the Passive Vibration in engineering structures. Possible solution with real time application by employing various advanced and innovative techniques was briefly discussed in the article. It concludes certain significant factors such as, the nonlinear is identified to be more effective in the wider bandwidth frequency ratio is compared to the linear isolation systems. Further, the systems are observed to be reducing transmissibility in more efficient manner than the linear system. In addition to the isolation or suppression of vibration and its effects on the engineering structure, there is possible way of converting the bad vibration into energy. There is a greater scope in harvesting energy through the nonlinear energy harvesting system from wide ranges of real time engineering and non-excitations. Some of the devices designed and developed through bio-inspiration models are demonstrated to be more efficient in the isolation of vibration. The design and development of metamaterial based nonlinear vibration isolation system in microstructure level shows a significant improvement in isolation of vibration and in harvesting of energy.

Suman et. al [9] performed a computational study to understand the characteristic behavior of innovative isolation system design; the study shows a significant improvement in the performance of developed system with respect to isolation the chaotic vibration developed during different environment. Various parameters of the QZS system are identified to be significantly enhancing the overall efficiency of the isolation system. So, it is observed that the designed isolation system can be employed in transportation system, especially automobiles at different terrains. [10] CSO performs better than PSO, DA, proposed a new method for parameter estimation, namely, Improved Boundary Chicken Swarm Optimization (IBCSO). They have also analyzed if the estimated accuracy is affected by the time series. The results show that the IBCSO shows better performance with respect to the speed of convergence along with a precision in the convergence than the CSO, PSO, GA. It is also identified to have a shorter time series with better estimation accuracy.

II. Bouc-Wen Model for Hysteresis

The BW model is extensively employed to illustrate the hysteresis characteristics. The Bouc first described the model in 1967, then it was generalized by the Wen in 1976 [11]. Many hysteretic systems were modelled analytically using the generalized BW model. Due to the flexibility of the model, it was possible to model the hysteresis behavior of various systems. This flexibility has some disadvantage such as the number of modeled factors to be identified is increased. As the number of parameters in the model is large, the identification technique will be critical in the BW model applications. Bouc proposed the first model for the hysteresis, and then it was generalized by the Wen. The generalized BW model [11] is as given below

$$Q(x,\dot{x}) = g(x,\dot{x}) + z(x) \tag{1}$$

$$\dot{z} = -\beta|\dot{x}|z^n - \gamma\dot{x}|z|^n + \alpha\dot{x}, \quad n = 1,3,5,.... \tag{2}$$

$$\dot{z} = -\beta|\dot{x}|z^{n-1}|z| - \gamma\dot{x}z^n + \alpha\dot{x}, \quad n = 2,4,6.... \tag{3}$$

Whereas the "Q" represents the restoring force, g is the non-hysteresis component, which is a function of velocity and instantaneous displacement (x), and z (x) is the hysteresis component.

$$\dot{z}(t) = \alpha\dot{x}(\mathrm{t}) - \beta\left|\dot{x}(t)\right|z(t)\left|z(t)\right|^{n-1} - \gamma\dot{x}(t)\left|z(t)\right|^{n} \qquad (4)$$

The Equation (4) is equivalent to Equation (3), Due to the versatility and mathematical tractability of Equation (3), it is extensively used to describe the nonlinear hysteretic characteristics of a system.

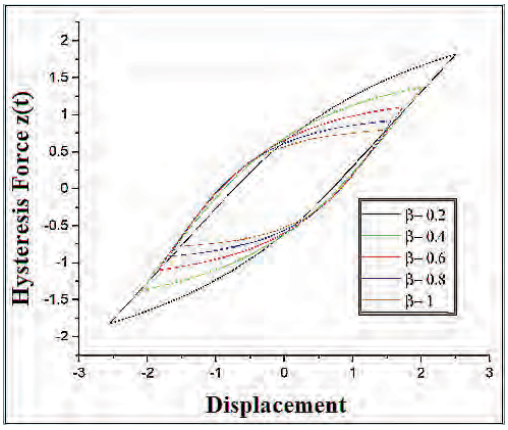

Figure 2. Hysteresis behavior for various β.

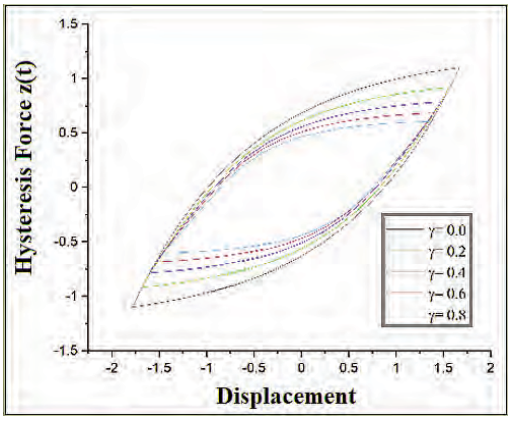

Figure 3. Hysteresis behavior for various γ.

The popularity of the BW model increased after 2004, which can be seen through the increasing number of literature on the BW model. In the literature, the model was used for a wide range of hysteretic systems.

The applications of the BW model are, the parameter identification of MR damper using PSO [12], in [13] analyzed the hysteresis behavior of Magnetorheological dampers, and in [14] did the numerical analysis of the ME damper. The BW model also used for piezoelectric actuators. [15] used the BW model to represent asymmetric hysteresis behavior of PZT, in [16] proposed enhanced the BW model to portray the frequency-dependent hysteresis behavior of a biomorphic PZT actuator, and to model and monitor hysteresis in [17], in [18] for vibration regulation of a smart beam with PZT actuator. Dynamic behavior is studied using the BW model for an O-Type wire cable isolator [19], in [20] a detailed study has been performed on the seismic equipment safety was carried out. Whereas in [21] the study has been concentrated on the safety of the electrical equipment's subjected to the seismic effects were briefly discussed.

A. Parameters influencing the hysteresis behavior

In Equation (4), there are four parameters that have strong control over the hysteresis behavior. Therefore, it is vital to understand the influence of each parameter. Wong et. al. [22] studied the parameters of the BW model. A similar technique is employed here to recognize the influencing factors of the adapted model. In loading-unloading and unloading-reloading, the stiffness difference is 2β. Therefore, the change in stiffness is controlled by β when the sign of velocity changes. The parameters and mainly governing the shape of the hysteresis loop. Various combinations of β and γ leads to different hysteresis loops (Figure 2 and 3).

B. Adapted Bouc-Wen model

Ni et. al. [23] experimentally obtained the hysteresis behavior of the WRI in roll, shear, and tension-compression by performing a cyclic loading test. It was found out that the wire rope isolator shows symmetric hysteresis behavior when subjected to shear and roll mode, while in tension-compression mode, it shows asymmetric hysteresis behavior. They showed that the WRI has softening stiffness for small displacement and for large displacements, it changes to hardening stiffness. This phenomenon is called soft-hardening hysteresis, which an isolator possesses in shear and roll modes. They also have shown that the WRI shows the softening characteristics with respect to the compression along with the tension exhibiting characteristics of hardening; this is the reason for the asymmetric hysteresis behavior and this asymmetric hysteretic loop consists of a portion hardening overlap envelope during loading. Though the BW model represents a large variety of hysteresis by choosing the values of β and γ but it failed to simulate the soft-hardening hysteresis behavior. Therefore, Ni et. al. [23] proposed the two modified BW models to represent the hardening overlap and soft-hardening hysteresis behavior.

$$F(t) = F_2(t)[z(t) + F_1(t)] \qquad (5)$$

$$F_1(t) = k_1 x(t) + k_2\,\mathrm{sgn}(x(t))x(t)^2 + k_3 x(t)^3 \qquad (6)$$

$$F_2(t) = b^{cx(t)} \qquad (7)$$

Where

F (t) = Total restoring Force,

F_1 (t) = Nonlinear spring force,

F_2 (t) = Shaping Function, ensures the hardening overlap

z (t) = Symmetric Loop Hysteresis Force

$\dot{x}$ = velocity of the motion.

The identified parameters for the lateral (shear) and vertical (tension-compression) are shown in Table 1. The IBCSO has successfully identified the modified BW model parameters for both lateral and vertical modes. All nine parameters are identified in one stage.

CVR Journal of Science and Technology, Volume 22, June 2022
DOI: 10.32377/cvrjst2217

III. Results and Discussions

The effective stiffness along with the damping ratio is considered the significant characteristics Phenomenon of the wire rope isolator, and they are calculated from the hysteresis loop. The hysteresis behavior indicates the energy dissipated by the isolator and the stiffness in both loading and unloading direction. In the following, the effective stiffness and damping ratio are given.

A. Effective Stiffness

It is calculated loading and unloading cycle is completed. The effective stiffness is an indicative quantity for understanding the increase or decrease of the WRI stiffness. The equation is given below

$$K_{eff} = \frac{F_{max} - F_{min}}{x_{max} - x_{min}} \tag{8}$$

Where F_{max} and F_{min} are the max positive force and min negative force, where as x_{max} and x_{min} is the max positive displacement, and min negative displacement.

B. The Damping Ratio

The ratio of damping is considered the half of the Energy loss Ratio (ELR). It is an important factor, which determines how effective the WRI is. The ELR is the amount of energy lost due to sliding and development internal friction among the wire rope for the duration of cyclic loading. The higher the value of ELR, the higher the damping capabilities. The equation is given below.

$$ELR = \frac{A_{loop}}{\pi\left(\frac{F_{max} - F_{min}}{2}\right)\left(\frac{x_{max} - x_{min}}{2}\right)} \tag{9}$$

$$\zeta = \frac{ELR}{2} \tag{10}$$

Where A_{loop} the considered to be hysteresis loop area,

TABLE I.
IDENTIFIED PARAMETERS OF THE PROPOSED MODEL

Parameters	Values	
	Lateral (shear)	Vertical(tension-compression)
α	105.5	285.6
β	43.9227	68.1032
γ	-3.211	-4758479
n	0.2516	0.5376
b	0.8259	1.6305
c	0.0301	0.0465
k_1	9.9759	51.7079
k_2	0.215	0.2365
k_3	0.008	0.04

Figure 4-5 shows that the effective stiffness at a range of dislodgment for lateral displacement amplitude and vertical displacement amplitude. The effectiveness of the stiffness coefficient can be deliberated by employing the equation (9). Figure 6-7 shows the damping ratio at different displacement for lateral and vertical displacement amplitude. The damping ratio is calculated using the Equation 10.

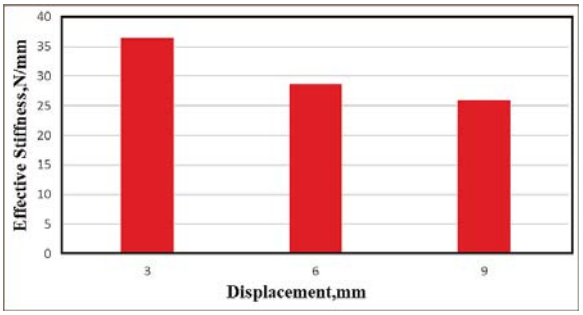

Figure 4. Effective stiffness in vertical directions

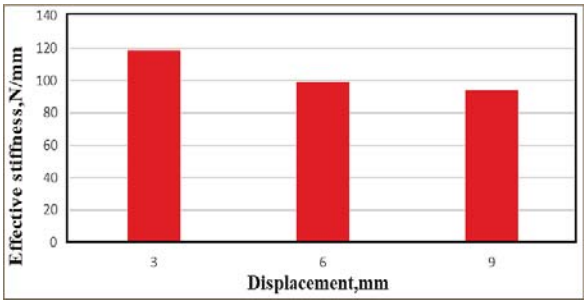

Figure 5. Effective stiffness in lateral directions

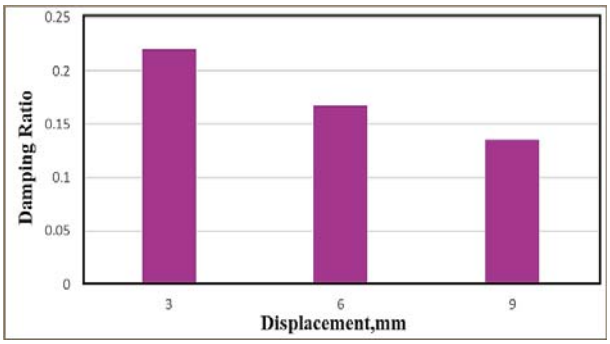

Figure 6. Damping ratio in vertical directions

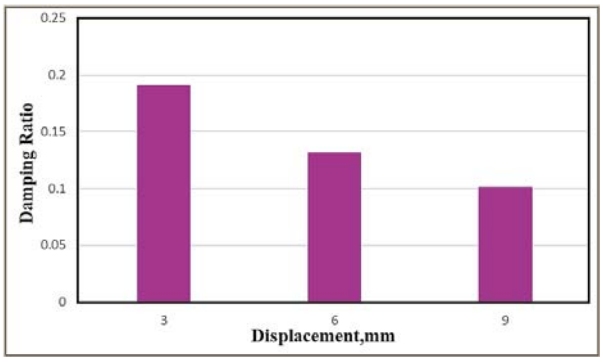

Figure 7. Damping ratio in Lateral directions

IV. Conclusions

The significant contribution and findings of the research were briefly listed out in this section.

- The adapted Bouc-Wen model is effectively employed to illustrate the hysteresis characteristics while shear along with mode of tension and compression.
- The IBCSO is employed to categorize the parameters of the proposed model.
- The hysteresis phenomenon in a loop is found to symmetric for the shear mode and asymmetric for the tension-compression mode.
- The asymmetricity characteristics are identified mainly due to hardening while tension and softening while compression during the mode of tension-compression.
- The effectiveness of the stiffness is identified to be decreased with respect to the increment in the displacement amplitude in both lateral and vertical modes.
- The tension-compression mode has the highest effective stiffness for small displacement.
- The damping ratio is also decreasing with increasing displacement amplitude.
- The shear mode has the highest damping ratio for small displacement.

Acknowledgement

The Authors deeply grateful for the support and facilities provided by CVR College of Engineering

Statement for Conflicts of Interest

The authors assure that, there is no disagreement of interest with respect to publishing this manuscript.

References

[1] M. Ye, X. Wang. "Parameter estimation of the Bouc-Wen hysteresis model using particle swarm optimization", *J. Smart Material and Structures*, Vol 16, pp 2341-2349, 2007.

[2] GGT Series Wire Rope Isolator, *WUXI HONGYUAN DEVFLEX CO.LTD*, China, www.dpflex.com, Ed., ed, 2014.

[3] M. Ismail, F. Ikhouane, J. Rodella. "The Hysteresis Bouc-Wen Model, a Survey", *Arch Comput Methods Eng*, Vol 16, pp. 161–188, 2008.

[4] Z. Y. Wang, J.Q. Mao. "On PSO Bouc-Wen Modeling for Piezoelectric actuator", *Springer Verlag Berlin Heidelberg*, 2010.

[5] M. Ye, X. Wang. "Parameter identification of hysteresis Model with Improved Particle Swarm Optimization", IEEE, 2009.

[6] P. S. Balaji, M. E. Rahman, L. Moussa, H. H. Lau Y. "Wire rope isolators for vibration isolation of equipment and structures – A review", *IOP Conf. Series: Materials Science and Engineering*, Vol 78, pp 012001, 2015.

[7] C. Zhou, X. Zhang, S. Xie, T. Zhou, C. Zhu. "Hybrid modeling of wire cable vibration isolation system through the neural network", *J math Comput Simulation*, Vol 79, pp. 3160-73, 2009.

[8] P. S. Balaji, K. Karthik SelvaKumar. "Applications of Nonlinearity in Passive Vibration Control: A Review", J. *Vib. Eng. Techno*l. Vol 9, pp. 183–213, 2021.

[9] S, Suman, P. S. Balaji, K. Karthik SelvaKumar, et al. "Nonlinear Vibration Control Device for a Vehicle Suspension Using Negative Stiffness Mechanism", *J. Vib. Eng. Techno*l. vol 9, pp. 957–966, 2021.

[10] S. Chen, R. Yang. "A Parameter Estimation Method for Nonlinear System Based on Improved Boundary Chicken Swarm Optimization", *Discrete Dynamics in Nature and Society*, pp. 11, 2016.

[11] Y. K Wen. "Method for random vibration of hysteretic systems", *Journal of Engineering Mechanics Division*, *ASCE,* Vol 102, pp 249-263, 1976.

[12] A. Elsawaf, H. Metered, T. Vampola, Z. Šika. "Parameter identification of Magnetorheological damper using particle swarm optimization", *International Journal of Earthquake Engineering– IJE*, Vol 2(1), 2015.

[13] X. C. Guan, P. F. Guo, J. P. Ou. "Modeling and Analyzing of Hysteresis Behavior of Magneto Rheological Dampers". *Procedia Engineering,* Vol 14, pp 2756-2764, 2011.

[14] M. T. Braz, R. C. Barros. "Experimental Behavior and Analysis of MR Dampers", *15 WCEE*, 2012.

[15] H. Qin, N. Bu, W. Chen and Z. Yin. "An Asymmetric Hysteresis Model and Parameter Identification Method for Piezoelectric Actuator", *Mathematical Problems in Engineering*. Vol 2014, pp 14, 2013.

[16] F. Fujii, K. Tatebatake, K. Morita, T. Shiinoki. "A Bouc-Wen Model-Based Compensation of the Frequency-Dependent Hysteresis of a Piezoelectric Actuator Exhibiting Odd Harmonic Oscillation", *Actuators,* Vol 7, pp 37, 2018.

[17] J. Gan, X. Zhang. "A review of nonlinear hysteresis modeling and control of piezoelectric actuators", *AIP Advances*, Vol 9, pp 040702, 2019.

[18] T. Zhang. "Influence of Hysteresis on the Vibration Control of a Smart Beam with a Piezoelectric Actuator by the Bouc-Wen Model", *Shock and Vibration*, Vol 2020, pp. 11, 2020.

[19] H. X. Wang, X. S. Gong, F. Pan, X. J. Dang. "Experimental Investigations on the Dynamic Behavior of O-Type Wire-Cable Vibration Isolators", *Shock and Vibration*, Vol 2015, pp. 12, 2014.

[20] G. F. Demetriades, M. C. Constantinou and A. M. Reinhorn. "Study of Wire rope systems for seismic protection of equipment in buildings", *Engineering Structures*, Vol 15 pp. 5, 1992.

[21] F. Paolacci, R. Giannini. "Study of the effectiveness of steel cable dampers for the seismic protection of electrical equipment", *14th World Conference on Earthquake Engineering*, 2008.

[22] C. W. Wong, Y. Q. Ni, J. M. Ko. "Steady-State oscillations of hystereric differential model. 11: Performance analysis", *Journal of Engineering Mechanics*, Vol 120, pp. 2299-2325, 1994.

[23] Y Q Ni, J M Ko, C W Wong, and S Zhan. "Modelling and identification of a wire-cable vibration isolator via a cyclic loading test Part 1: experiments and model development", *Proc Instn Mech Engrs*, Vol 213, Part I, 1999.

[24] S. Rashidi, S. Ziaei-Rad. "Experimental and numerical vibration analysis of wire rope isolator under quasi-static and dynamic loading", *Engineering Structures*, Vol 78, pp. 328-339, 2017.

[25] M. Lebloubaa, M.E. Rahmanb, S. Barakata. "Behavior of Polycal wire rope isolators subjected to large lateral deformations", *Engineering Structures*, Vol 191, pp. 117-128, 2019.

[26] F. Tyan, S.-H. Tu, and J. Wu. "An Investigation on Mathematical Models of Wire Rope Isolators", *The 30thNational Conference on Theoretical and Applied Mechanics*, 2006.

[27] A. Hussain, P. S. Balaji. "Stiffness characteristics of a polycal wire rope isolators", *IOP Conf. Series: Materials Science and Engineering*, Vol 402, pp. 012058, 2018.
[28] F. Ikhouanea, V.Mañosaa, J. Rodellara. "Dynamic properties of the hysteretic Bouc-Wen model", *J. Systems & Control Letters*, Vol 56, pp.197–205, 2007.
[29] P.S. Balaji1, L. Moussa, N. Khandoker, T. Yuk Shyh, M.E. Rahman, Lau Hieng Ho. "Experimental study on vertical static stiffnesses of polycal wire rope isolators", *IOP Conf. Series: Materials Science and Engineering*, Vol 217, pp 012032, , 2017.
[30] H. Qin, N. Bu, W. Chen, and Z.g Yin. "Mathematical Problems in Engineering", Vol 2014, Article ID 932974, 2014.
[31] F. Ikhouane, J. E. Hurtado, J.Rodellar,. "Variation of the hysteresis loop with the Bouc–Wen model parameters", *Nonlinear Dynamics*, Vol 48, pp. 361–380, 2007.
[32] Y. Zhao, S.Wang, J. Zhou, C. Li, C. Cheng. "Modeling and identification of the dynamic behavior of stranded wire helical springs", *Journal of VIBROENGINEERING*, Vol 15(1), 2013.
[33] T. ML, C. MA. "Damping phenomena in a wire rope isolation system", *J Sound Vib*, Vol 157(1), pp. 7-18, 1992.
[34] C.W. Wong, Y Q Ni. "Modelling the hysteresis curves of wire-cable isolator", *S Report Dept. of Civil and Structural Eng. Hong Kong Polytechnique*, pp. 644-8, 1994.
[35] P. S. Balaji, 2016. "An analytical and experimental study on wire rope isolator for vibration isolation of equipment and structures". *PhD Thesis, Curtin University*.
[36] W. Schwanen. "Modelling and identificaition of the dynamic brhavior of a wire rope spring", *Master Thesis, Technische Universiteit Eindhoven*, Netherlands, 2004.

E-ISSN 2581 –7957
P-ISSN 2277 – 3916

CVR Journal of Science and Technology, Volume 22, June 2022
DOI: 10.32377/cvrjst2218

Optimization of Turning Parameters of Inconel 718 Alloy using ANOVA in PYTHON

Marripally Ravikumar[1] and Lava Kumar Polisetty[2]
[1]Asst. Professor, CVR College of Engineering/Mechanical Engg. Department, Hyderabad, India
Email: marripallyravikumar@gmail.com
[2] Assoc. Professor, CVR College of Engineering/Mechanical Engg. Department, Hyderabad, India
Email: kumar.lava7023@gmail.com

Abstract: **Every manufacturing industry aims at increasing the production rate. It is very important to optimize cutting parameters for a high production rate. Inconel 718 has high strength and thermal resistance in Nickel-based alloys. It is used in aerospace applications. Due to the extreme toughness and work hardening characteristics of the alloy, machining of Inconel 718 is extremely difficult. This paper deals with the effect of cutting conditions on the machinability of Inconel 718. The present work deals with the optimization of turning parameters for better surface roughness and maximum material removal rate. The design of experiments has been done by using Taguchi L16 orthogonal array. Experiments have been performed on CNC Lathe Machine and results were analyzed by using Python software. ANOVA is performed by using Python software to identify the most influencing factor for MRR and surface roughness. From the analysis of results, it is found that depth of cut is the most influencing factor for MRR and feed is the most influencing factor for surface roughness. An optimum set of turning parameters is found for better surface roughness and maximum MRR.**

Index Terms**: Inconel 718 alloy, Material Removal Rate, Surface Roughness, Taguchi Method, ANOVA, Python.**

I. Introduction

In the present times, mass production of components with less time and good quality to meet customer needs is necessary. In every Manufacturing industry, machining of materials is carried out by one of the fundamental processes like turning. Turning operation is influenced by workpiece material, cutting fluid, cutting tool material, type of insert, Cutting speed, feed and depth of cut. The quality of machining is defined by higher MRR and low surface roughness. In present studies Cutting speed, feed, and depth of cut are selected as the controlled parameters (independent variables) to maximize MRR (dependent variable) and to minimize surface roughness (dependent variable) [1].

Inconel 718 is a high-performance superalloy. It exhibits several key characteristics like excellent mechanical strength at higher temperatures, resistance to thermal creep deformation, good surface stability and resistance to corrosion or oxidation. Inconel 718 alloy is one of the superalloys which find its application in the areas such as gas turbine engines, nuclear power plants, aerospace components, chemical industries and petrochemical plants [4] etc.

II. Objectives

Objectives of this paper are given below

- To analyse the effects of cutting parameters on the Material Removal Rate and Surface Roughness during turning operation of Inconel 718 alloy.
- To optimize the cutting parameters during turning of Inconel 718 alloy for better material removal rate and good surface finish.

III. Experimental Work

A. Experimental Design

As the objective of this research work is to study the effect of cutting parameters on the Material Removal Rate and Surface Roughness during Turning operation of Inconel 718 alloy using carbide cutting inserts by changing the various input machining process parameters, the design variables can be summarized as follows [2]:

- Four levels of speeds to be used because the non-linear behaviour of process parameters can only be studied if more than two levels of a parameter are used.
- Four levels of feed to be used.
- Four levels of depth of cut to be used.

For conducting the experiments, it has been decided to follow the Taguchi method of experimental design and an appropriate orthogonal array is to be selected after taking into consideration the above design variables. The effect of each cutting parameter on the phenomenon of surface modification should be studied to correctly understand its behaviour [3]. Hence, it was decided to conduct experiments with each combination of cutting parameters. Out of the above-listed design variables, the orthogonal array was to be selected for 3 design variables (namely speed, feed and depth of cut) which would constitute the orthogonal array [8].

The effect of many different parameters on the performance characteristic in a condensed set of experiments can be examined by using the orthogonal array experimental design proposed by Taguchi. Knowing the number of parameters and the number of levels, the proper orthogonal array can be selected [9]. Using the array selector, the name of the appropriate array can be found by looking at the column and row corresponding to the number of parameters and number of levels. Once the name has been determined (the subscript represents the number of experiments that must be completed), the predefined array can be looked up. Links are provided to many of the predefined arrays given in the array selector table [10]. These arrays were created using an algorithm Taguchi developed and allows for each variable and set to be tested equally [5].

Received on 29-09-2021, Revised on 22-11-21 Accepted on 25-12-2021.

CVR Journal of Science and Technology, Volume 22, June 2022
DOI: 10.32377/cvrjst2218

TABLE I.
TYPE SIZES MACHINING PARAMETERS AND THEIR LEVELS

S.No.	Process Parameters	Levels			
		1	2	3	4
1	Cutting Speed (mm/min)	40	60	80	100
2	Feed (mm/rev)	0.1	0.15	0.2	0.25
3	Depth of Cut (mm)	0.1	0.2	0.3	0.4

TABLE II.
STANDARD L16 ORTHOGONAL ARRAY

Exp. No.	Speed Level	Feed Level	Depth of Cut Level
1	1	1	1
2	1	2	2
3	1	3	3
4	1	4	4
5	2	1	1
6	2	2	2
7	2	3	3
8	2	4	4
9	3	1	1
10	3	2	2
11	3	3	3
12	3	4	4
13	4	1	1
14	4	2	2
15	4	3	3
16	4	4	4

TABLE III.
INPUT PARAMETERS BASED ON TAGUCHI L16

S. No	Cutting Speed (mm/min)	Feed (mm/rev)	DOC (mm)
1	40	0.1	0.1
2	40	0.15	0.2
3	40	0.2	0.3
4	40	0.25	0.4
5	60	0.1	0.2
6	60	0.15	0.1
7	60	0.2	0.4
8	60	0.25	0.3
9	80	0.1	0.3
10	80	0.15	0.4
11	80	0.2	0.1
12	80	0.25	0.2
13	100	0.1	0.4
14	100	0.15	0.3
15	100	0.2	0.2
16	100	0.25	0.1

A. Work Piece Material

In the present work, Inconel 718 alloy is selected as workpiece material. The following table shows the chemical composition of the alloy.

Inconel 718 is a high-performance superalloy. It exhibits several key characteristics like excellent mechanical strength at higher temperatures, resistance to thermal creep deformation, good surface stability and resistance to corrosion or oxidation [6]. Inconel 718 alloy is one of the superalloys which find its application in the areas such as gas turbine engines, nuclear power plants, aerospace components, chemical industries and petrochemical plants [7] etc.

TABLE IV.
CHEMICAL COMPOSITION OF INCONEL 718 ALLOY

Element	Composition (in weight percentage)
Carbon	0.08 max
Manganese	0.35 max
Phosphorus	0.015 max
Sulphur	0.015 max
Silicon	0.35 max
Chromium	17-21
Nickel	50-55
Molybdenum	2.80-3.30
Columbium	4.75-5.50
Titanium	0.65-1.15
Aluminium	0.20-0.80
Cobalt	1.00 max
Boron	0.006 max
Copper	0.30 max
Tantalum	0.05 max
Iron	Balance

IV. EXPERIMENTAL PROCEDURE

Inconel 718 alloy specimen of 50mm diameter and 100 mm length was used for the experiments. All the experiments were designed based on the Taguchi method and performed on a CNC lathe machine.

The following steps have been followed during the experimentation work:

- Fix the tool to the tool holder and the workpiece to the chuck.
- Fix the centre for a workpiece.
- Set the speed, feed and depth of cut of operation.
- Weight of the workpiece to be recorded before &after each experiment to calculate the material removal rate.
- Machining time is to be recorded for each experiment from CNC Lathe.
- Calculate MRR by using formula and the workpiece is taken out to measure the surface roughness.
- The same experiment was repeated with different speeds, feed and depth of cut combinations.
- Taly-Surf instrument has been used to determine the surface roughness of the workpiece after conducting each experiment.

V. RESULT AND ANALYSIS

The above data has been analyzed by Python software. First, the input parameters are defined in the software as per their corresponding value and then give the responses data to optimize. Here, the main objective of the problem is to minimize the value of surface roughness and maximize the value of Material removal rate. So, ANOVA is performed on the dataset by using statistical models in python software.

CVR Journal of Science and Technology, Volume 22, June 2022
DOI: 10.32377/cvrjst2218

A. Material Removal Rate

The results of MRR for each of the 16 experiments are given in Table 5. The weight of the workpiece before and after each run was measured to calculate the Material removal rate (MRR). The MRR is given by

$$\mathbf{MRR = (W1-W2) \times 60 / (\rho \times t)}$$

Where,
MRR = Material removal rate (cm^3/min)
W1 = Weight of the specimen before the experiment (gm)
W2 = Weight of the specimen after the experiment (gm)
ρ = Density of the specimen (gm/cm^3)
t = Machining time (sec)

TABLE V.
EXPERIMENTAL RESULTS FOR MRR

S. No	Cutting Speed (mm/min)	Feed (mm/rev)	DOC (mm)	MRR (cm3/min)
1	40	0.1	0.1	0.48
2	40	0.15	0.2	1.33
3	40	0.2	0.3	2.25
4	40	0.25	0.4	3.31
5	60	0.1	0.2	1.2
6	60	0.15	0.1	0.69
7	60	0.2	0.4	4.88
8	60	0.25	0.3	4.63
9	80	0.1	0.3	2.3
10	80	0.15	0.4	4.46
11	80	0.2	0.1	1.29
12	80	0.25	0.2	3.94
13	100	0.1	0.4	3.66
14	100	0.15	0.3	4.74
15	100	0.2	0.2	4.27
16	100	0.25	0.1	2.93

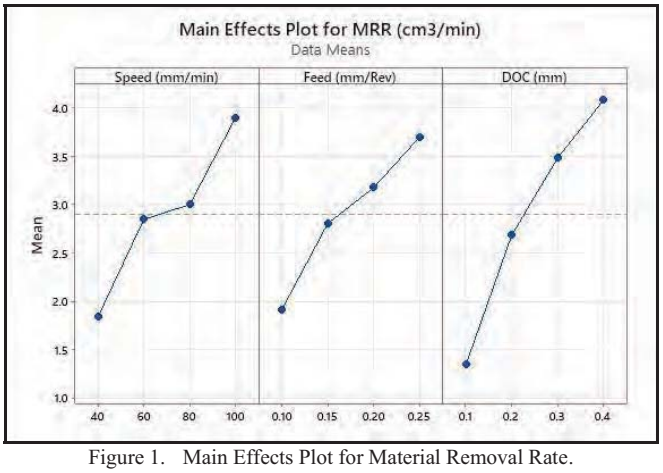

Figure 1. Main Effects Plot for Material Removal Rate.

From Fig.1, Fig.2, Fig.3 and Fig.4, below inferences can be drawn.

- As speed increases, mean MRR increases but the increase MRR is not significant in the speed range of 60 to 80 mm/min.
- As feed increases, mean MRR increases almost linearly.
- As the Depth of cut (DOC) increases, mean MRR increases with decreasing slope.
- By comparing the main effects plot for MRR, it is noticed that the slope of DOC vs. Mean MRR is highest among them. Hence, it can be concluded that Depth of cut (DOC) is the most influencing factor for Material Removal Rate (MRR).

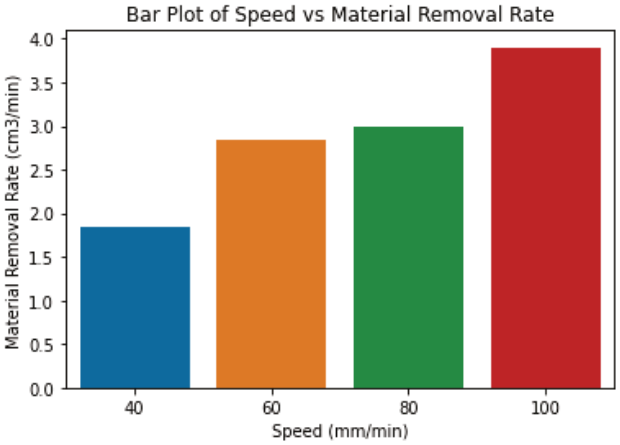

Figure 2. Bar Plot of Speed vs Mean Material Removal Rate

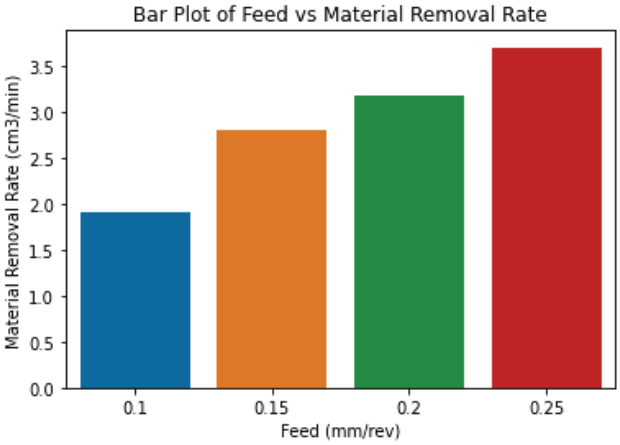

Figure 3. Bar Plot of Feed vs Mean Material Removal Rate.

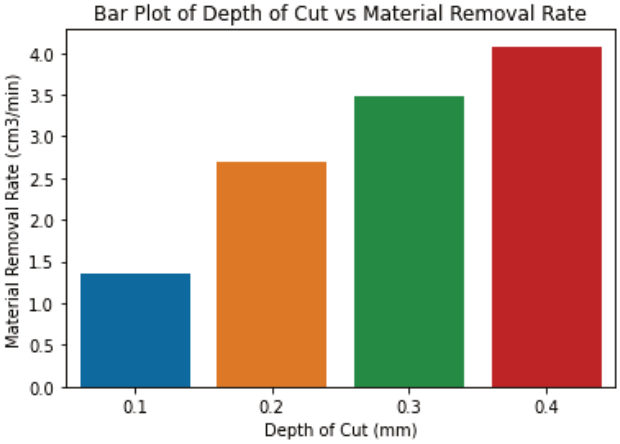

Figure 4. Bar Plot of Depth of Cut vs Mean Material Removal Rate.

B. Surface Roughness

TABLE VI.
EXPERIMENTAL RESULTS FOR SURFACE ROUGHNESS (RA)

S. No	Cutting Speed (mm/min)	Feed (mm/rev)	DOC (mm)	Surface Roughness (Ra)
1	40	0.1	0.1	0.612
2	40	0.15	0.2	0.718
3	40	0.2	0.3	1.357
4	40	0.25	0.4	2.311
5	60	0.1	0.2	0.445
6	60	0.15	0.1	1.057
7	60	0.2	0.4	1.397
8	60	0.25	0.3	2.109
9	80	0.1	0.3	0.226
10	80	0.15	0.4	1.034
11	80	0.2	0.1	1.173
12	80	0.25	0.2	1.976
13	100	0.1	0.4	0.449
14	100	0.15	0.3	0.792
15	100	0.2	0.2	1.522
16	100	0.25	0.1	1.864

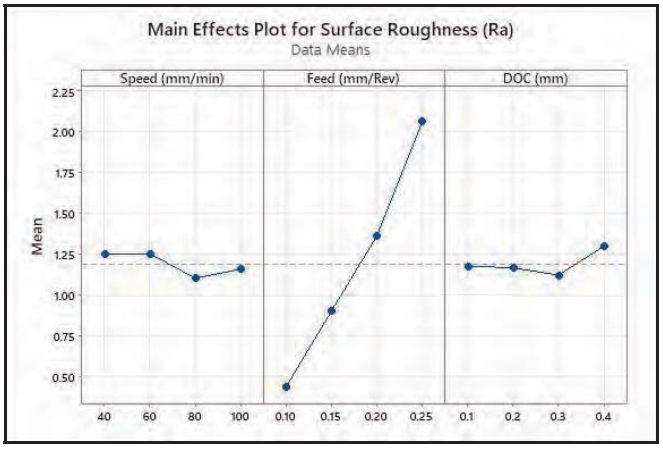

Figure 5. Main effects plot for Surface Roughness (Ra).

From Fig.5, Fig.6, Fig.7 and Fig.8, below inferences can arrive.

- Mean Surface Roughness is not influenced significantly by an increase in speed because the slope of the mean surface roughness vs speed level plot is approaching zero.
- As feed increases, mean Surface Roughness increases with increasing slope.
- Mean Surface Roughness is not influenced significantly with an increase in Depth of Cut (DOC) up to 0.3mm later Mean Surface Roughness increases as DOC increases.
- By comparing the main effects plot for Surface Roughness, it is noticed that the slope of Feed vs. Mean Surface Roughness is highest among them. Hence, it can be concluded that Feed is the most influencing factor for Surface Roughness among all three independent variables.

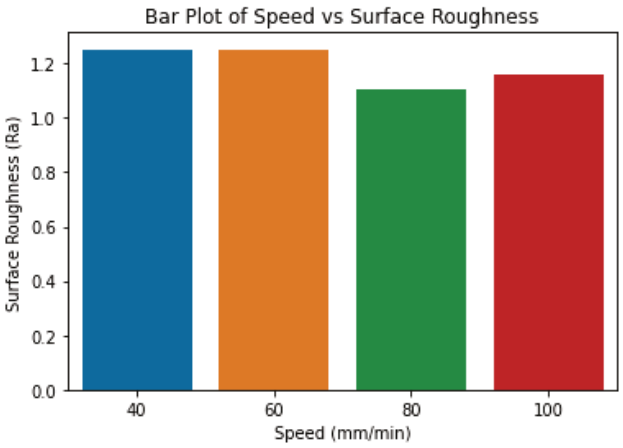

Figure 6. Bar Plot of Speed vs Mean Surface Roughness.

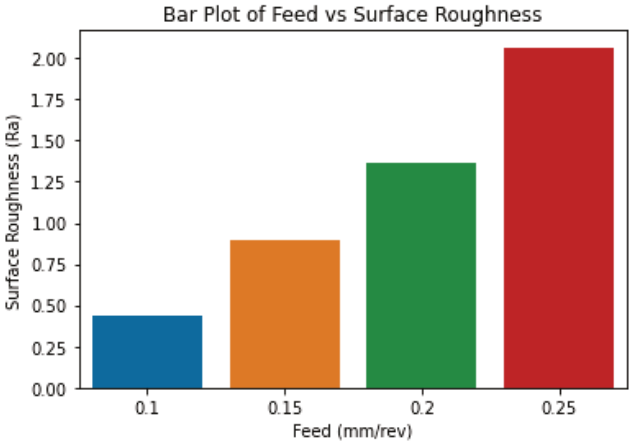

Figure 7. Bar Plot of Feed vs Mean Surface Roughness.

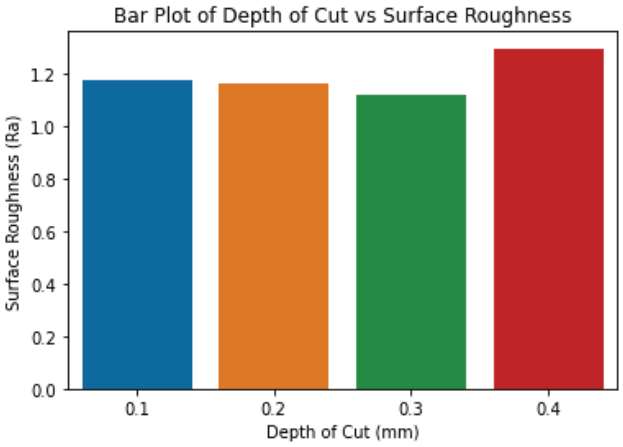

Figure 8. Bar Plot of Depth of Cut vs Mean Surface Roughness.

C . ANOVA for Material Removal Rate

ANOVA Results for Material Removal Rate shows that the "P" value for Depth of Cut (0.013) is less than the significance level (0.05) hence Depth of Cut is the most influencing factor for Material Removal Rate.

CVR Journal of Science and Technology, Volume 22, June 2022
DOI: 10.32377/cvrjst2218

TABLE VII.
ANOVA FOR MATERIAL REMOVAL RATE

Factor	Degrees of Freedom	Sum Squares	Mean Sum Squares	F Ratio	P-Value
Speed	3	8.533	2.844	4.454	0.057
Feed	3	6.841	2.28	3.57	0.086
Depth of Cut	3	16.736	5.579	8.734	0.013
Residual	6	3.832	0.639		

D. ANOVA for Surface Roughness:

TABLE VIII.
ANOVA FOR SURFACE ROUGHNESS

Factor	Degrees of Freedom	Sum Squares	Mean Sum Squares	F Ratio	P-Value
Speed	3	0.0648	0.02159	0.63927	0.61695
Feed	3	5.8092	1.9364	57.345	0.00008
Depth of Cut	3	0.0687	0.02289	0.6778	0.59679
Residual	6	0.2026	0.03377		

ANOVA Results for Surface Roughness shows that the "P" value for feed (0.00008) is less than the significance level (0.05) hence feed is the most influencing factor for Surface Roughness.

E. Correlation between material removal rate and surface roughness

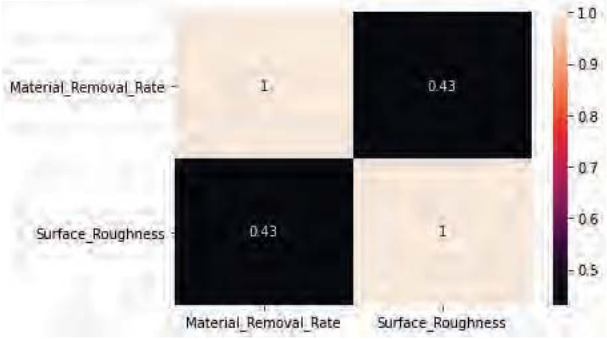

Figure 9. Heat Map between Material Removal Rate and Surface Roughness.

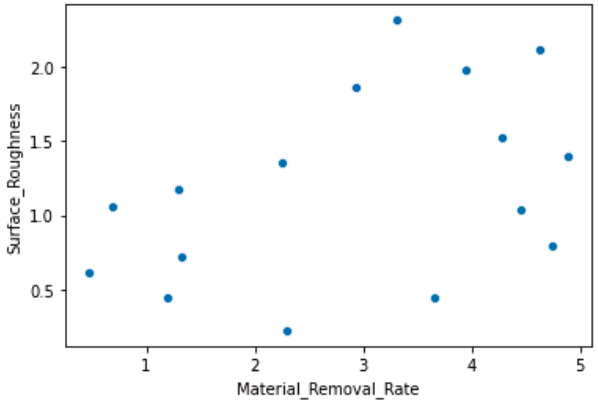

Figure 10. Scatter Plot of Material Removal Rate vs Surface Roughness.

From Fig.9 and Fig.10, it can be noticed that there is a weak positive correlation between them (correlation coefficient = 0.43). Hence, it can be excepted that maximum material removal rate is possible with min or moderate surface roughness with few combinations of input parameters. We aim to know input parameters that provide data points in the right bottom corner (MMR is maximum and Surface Roughness minimum) of the scatter plot. Those parameters are optimum input parameters.

F. Optimum set of input Factors:

From observing main effects plots (Fig 1 & Fig 5), the optimum set of factors for material removal rate and surface roughness are selected in the following way. Input factors should be optimized in such a way that to maximize Material removal rate and minimize surface roughness.

- Optimum cutting speed can be taken as 100 mm/min to maximize MRR and to minimize surface roughness.
- Optimum cutting feed can be taken as 0.15 mm/rev to maximize MRR and to minimize surface roughness.
- Optimum depth of cut can be taken as 0.3 mm to maximize MRR and to minimize surface roughness.

VI. CONCLUSIONS

From the above research work, the below conclusions can arrive

- It is found that Depth of cut is the most influential factor during the turning of INCONEL 718 alloy.
- It is found that Feed is the most influential factor for surface roughness of INCONEL 718 alloy.
- Optimum cutting speed can be taken as 100 mm/min to maximize MRR and to minimize surface roughness.
- Optimum cutting feed can be taken as 0.15 mm/rev to maximize MRR and to minimize surface roughness.
- Optimum depth of cut can be taken as 0.3 mm to maximize MRR and to minimize surface roughness.

REFERENCES

[1] Yang W.H. and Tarng Y.S., (1998), "Design optimization of cutting parameters for turning operations based on Taguchi method," Journal of Materials Processing Technology, 84(1) pp.112–129.
[2] Ali Riza Motorcu "The optimisation of machining parameters using the Taguchi method for surface roughness of AISI 8660 hardened alloy steel" Journal of Mechanical Engineering 56(2010)6, 391-401.
[3] R. Ramanujam et all "Taguchi multi machining characteristics optimisation in turning of Al-15 SiCp composites using desirability function analysis" Journal of studies of manufacturing vol-1-2010/Iss2-3 pp120-125.
[4] J. Paulo Davim Editor "Machining of hard materials" Springer publication, April 2010.
[5] Design of Experiments Using The Taguchi Approach: 16 Steps to Product and Process Improvement BY RANJITH K ROY
[6] Makadia A.J. and Nanavati J.I., (2013), "Optimisation of machining parameters for turning operations based on response surface methodology," Measurement, 46(4) pp.1521-1529.

[7] Neseli S., Yaldiz S. and Turkes E., (2011), "Optimization of tool geometry parameters for turning operations based on the response surface methodology," Measurement, 44(3), pp. 80-587.

[8] Yang W.H. and Tarng Y.S., (1998), "Design optimization of cutting parameters for turning operations based on Taguchi method," Journal of Materials Processing Technology, 84(1) pp.112–129.

[9] Makadia A.J. and Nanavati J.I., (2013), "Optimisation of machining parameters for turning operations based on response surface methodology," Measurement, 46(4) pp.1521-1529.

[10] G. Bharath Reddy and G. Naveen Kumar (2018), "Optimization of cutting parameters for various work-tool combinations in turning operation: An experimental investigation," CVR Journal of Science and Technology, 14, pp.79-85.

E-ISSN 2581 – 7957
P-ISSN 2277 – 3916
CVR Journal of Science and Technology, Volume 22, June 2022
DOI: 10.32377/cvrjst2219

Experimental Investigation and Study of the Influence of Turning Parameters on Al Composite by Taguchi Analysis

Vidyanand Kumar[1], Neeraj Kumar Jha[2]
[1]Asst. Professor, CVR College of Engineering/ Mechanical Engg. Department, Hyderabad, India
Email: vidyanandk75@gmail.com
[2]Assoc. Professor, CVR College of Engineering/ Mechanical Engg. Department, Hyderabad, India
Email : neerajjha.me@gmail.com

Abstract: **Metal cutting actually addresses the biggest class of manufacturing activities where turning is most generally utilized material removal process. In the present research work, the effect of spindle speed, feed rate and depth of cut on material removal rate and surface roughness in turning of AA6061 are investigated by utilizing Taguchi based design of the experiment which includes 9 different control parameters by the combination of L9 orthogonal array. Experiments have been conducted as per DOE designed by Taguchi. The surface roughness and material removal rate are measured after the experimentation. S/N ratio is employed to find the performance characteristic in the turning of Aluminium composite by using carbide insert. ANOVA analysis has been done for both MRR and Ra to find the percentage contribution and significant effect of each control factor on the performance characteristic like volume of material removed and surface quality. Mathematical modeling has been done to find the relationship between input parameters and performance by using regression analysis. The developed regression model can be used to predict the MRR and surface roughness Ra at a confidence level of 95%.**

Index Terms: **ANOVA, Regression analysis, DOE, S/N ratio, Orthogonal array**

I. Introduction

Now a days, quality and customer requirements are the most important objectives for any manufacturing industry [3]. Machining is one of the secondary manufacturing processes in which quality of the desired product depends upon various machining parameters. So proper selection of parameters is very critical task in machining operation. The selected process parameters affect the output or the response of the machined parts. Quality of the finished product should be superior to this various research is carried out with different techniques and multiple ways to produce a defect free product at reduced manufacturing cost. As of now all industries are trying to reduce the cost and simultaneously the quality should match with requirement. The cost is directly proportional to the time of production, so it is required to focus on material removal rate and surface roughness of the product in case of machining. Machining time reduces the overall cost of machining in the form of volume of material removed which is related to different machining parameters like speed, feed, and depth of cut during cutting. The quality of surface also plays an important role in machined parts. Machined surface with good quality shows some improvement in fatigue strength, creep life and corrosion resistance. To increase the productivity and maintaining quality is the main challenge for the manufacturing industries. Turning operation is most widely used machining operation and in present scenario number of research are going on to find the optimal parameters combination to produce sound quality at a very high production rate at lower cost by the utilization of the less energy. Production rate and quality also much affected by the machinability of the material selected as a workpiece. Machinability in turning can be evaluated in terms of various parameters like forces involved, surface finish of the product, tool life and temperature generated during cutting.

Present work focuses on to get the optimal parameters for high production without compromising the surface quality in machining of Aluminium alloy on CNC turning centre. AA6061 alloy is widely used in aircraft structure, Military, aerospace application due to perfect combination of strength, formability, machinability, durability, conductivity, mechanical properties, and its light weight [1]. These alloys are made approximately nearly in size, so this material required to shape in exact dimensions with desired precision. Machining parameters like speed, feed, depth of cut, insert material, use of cutting fluid, machining vibrations involved and influenced the machined parts, so improvement in surface quality at high production of aluminium alloy rate is much important area of research [2,3]. There are three primary factors that affect directly the turning operation such as speed, feed, and depth of cut. Other factors also involved in turning operation, but these factors are the basic factors that involve in any basic machining process. Speed refers the spindle speed or the workpiece. When speed express in revolution per minute(rpm) it shows rotating speed but in case of surface speed or speed is at which the workpiece is moving past the cutting tool. When it is expressed in meter per minute it refers only work piece speed and it is product of rotating speed times the circumference of the workpiece at the starting of cutting. After every pass at a particular depth of cut workpiece show different speed rather than the rotation speed remains the same.

Feed is the rate at which tool advances along the cutting path in every revolution of workpiece. Feed refers to the cutting tool and it is expressed in mm per revolution. Feed rate controls the surface finish of machined part along with various other factors.

Received on 07-09-2021, Revised on 26-10-2021, Accepted on 25-11-2021.

Depth of cut is defined the perpendicular distance from the machined surface to the uncut surface of the workpiece. It is also expressed in other words that the thickness of the material required to remove from the workpiece in a single pass.

AA6061 alloy is most commonly available heat treatable aluminium alloys for commercial use. This alloy primarily composed of aluminium, magnesium and silicon. It is medium to high strength alloy, light weight and very economical material. Due to small amount of chromium its corrosion resistant also improved so it is used in marine application. This is most extensively used in construction material and automotive components [4]. Chorng-Jyh et al. [5] experimentally investigated the turning operation under various parameters by using Taguchi design composed with grey relational analysis and concluded that the main contribution in response was in order depth of cut, cutting speed and feed rate also depth of cut was more influential factor for deciding response in turning operation. Kumar et al. [6] conducted experiment based on RSM box- Behnken design and concluded that depth of cut has a great contribution compared to feed and speed on material removal rate under given parameter condition also feed rate influence more surface roughness of machined parts as compared to speed and depth of cut. Tian-Syung Lan et al. [7] utilizes Taguchi optimization technique L9 orthogonal array with four cutting parameters like speed, feed rate, depth of cut and tool nose runoff at three levels and compared the optimum result with another optimal value for the surface roughness. Dr. Vijay Kumar M. et. al. [8] studied Taguchi optimization for machining of EN19 steel under different process parameters in two condition one is with coolant and without coolant. Finally, concluded that lubrication and depth of cut shows significant effect on surface roughness and material removal rate. In their study utilize L18 orthogonal array and shows feed rate and spindle speed have significant effect on both MRR and surface pattern. S. P. Palaniappan et al. [9] investigated the AA6082 alloy by using Taguchi L27 array for the optimization of CNC turning parameters. In their study concluded that for MRR speed is most significant parameter and simultaneously feed is the great influential factor for surface roughness. In this study, another observation was the temperature generation during turning that is the maximum and minimum value of the temperature is 93.3°C and 50°C respectively. Shunmugesh K. et. al. [10] concentrated on the optimization of turning parameters with carbide tool for surface roughness at various parameter cutting speed range from 135 to 225m/min, feed rate range 0.1 to 0.3 mm/rev. and depth of cut range from 0.5 to 1.5 mm at three different levels by using Taguchi L27 orthogonal array and concluded that feed rate is the most important significant factor that affect surface roughness followed by cutting speed and depth of cut. Y. Hsiao et. al. [11] uses in their study Taguchi based Grey Relational Analysis to optimize the machining parameters and found that feed rate is most influential parameter to control the quality of machined surface. Doreswamy Deepak et. al. [12] utilizes the multi response optimization technique using Taguchi base Grey relational analysis to find the optimal parametric combination for maximum MRR and minimum surface roughness under parameters like speed, feed and depth of cut shows high cutting speed results the more MRR and the better surface finish at lower vale of feed rate and depth of cut. Rao et al. [13] considered the effect of parameters on the cutting force and surface in turning of steel with ceramic inserts. The result shows that feed rate is the most significant parameter for controlling force involved in cutting as well as surface finish produced. Finally, developed a mathematical model for optimum combination of process parameters for minimum cutting force and better surface finish. Vinod et. al. [14] studied the effect of tool overhang on surface pattern. In this study the author has determined the optimum overhung length that surface roughness improved. Though the surface is the most important factor in precision fit, aesthetic aspect, fatigue strength and material removal rate are predominant factors for improvement in productivity. Turning parameters requires proper selection to obtain optimized value of multiple response so Grey Relational analysis is used to solve multiple objective optimizations for multiple response. M.Nataraj et. al [15] utilizes Response surface methodology to optimize the turning parameters for machining of metal matrix composite at various cutting variables as feed rate, speed and depth of cut, tool work interface temperature to get the superior finish. Finally, ANOV test was done to find the contribution of parameter. The author finally concluded that feed and depth of cut was major prominent influential factor for surface roughness. Surface roughness is a key factor in machining process during considering part performance in application and it is the factor that greatly influences manufacturing cost and quality of the product.

II. Experimental Details

A. Material Selection

The experiments were performed on AA6061 alloy according to design of experiment. This material was selected for experimentation due to its light weight and medium to high strength and its application in various industries as well as in aerospace because of high strength to weight ratio. The detail chemical composition and mechanical properties of alloy are shown in table 1 and table 2 respectively.

TABLE I.
Chemical Composition of Work Material

Mg	Si	Fe	Cu	Cr	Mn	Zn	Ti	Al
0.89	0.73	0.45	0.31	0.16	0.09	0.09	0.06	Balance

TABLE II.
Mechanical Properties of Work Material

Ultimate tensile strength	Yield strength	% Elongation	Vicker hardness number (HV)	Reduction in cross-section area
352MPa	301MPa	17.6	105	14.24

CVR Journal of Science and Technology, Volume 22, June 2022
DOI: 10.32377/cvrjst2221

B. Cutting Tool

The cutting tool used for the current research work with all specification is CNMG 120408 carbide insert. A separate insert is used for all experiment to avoid the insert wear and to maintain the surface quality of the product during turning.

Figure 1. Photograph of carbide insert

C. CNC Late Machine

The experiments were conducted on the JOBBER XL CNC lathe designed by Ace designer ltd. The spindle power of machines used is 7.5 KW, and the range of the speed is 40-4000 rpm.

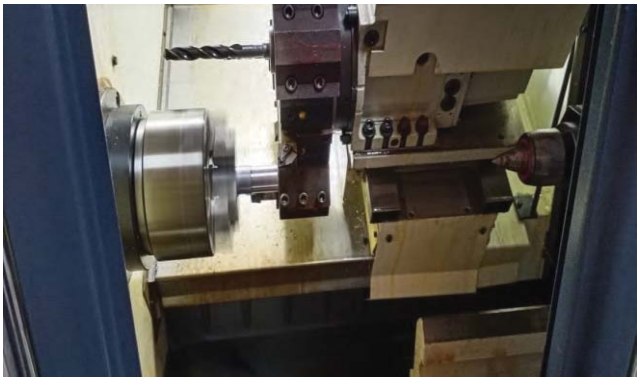

Figure 2. CNC Lathe Jobber XL

D. Design of Experiment

In the current study, experiments were planned according to Taguchi L9 orthogonal array. Three machining parameters were selected as control factor as spindle speed, feed rate and depth of cut at three different levels. The selected process variables with their actual and coded value are mentioned in table 3. Three levels are upper level (3), lower level (1) and the intermediate level (2). Taguchi based design of experiment was used for conducting of experiment because Taguchi experimental design method is very straightforward and very easy to apply many engineering situations simultaneously this method provides the boundary to analyze the different process parameters with a smaller number of experiments. In this research 9 different control variable combination is given by the L9 Array which is shown in table 4 in coded form as well as actual value of process parameters.

TABLE III.
MACHINING PARAMETERS AND THEIR LEVELS

Parameters	Levels		
	Lower level(1)	Intermediate level(2)	Higher level(3)
Speed (rpm)	1000	1500	2000
Feed rate (mm/rev)	0.15	0.25	0.35
Depth of cut(mm)	0.50	0.75	1.0

TABLE IV.
TAGUCHI L9 ORTHOGONAL ARRAY

Sl. No.	Parameters in coded form			Parameters in actual form		
	Spindle speed(N)	Feed rate(f)	Depth of cut(d)	Spindle speed(N)	Feed rate(f)	Depth of cut(d)
1	1	1	1	1000	0.15	0.50
2	1	2	2	1000	0.25	0.75
3	1	3	3	1000	0.35	1.00
4	2	1	2	1500	0.15	0.75
5	2	2	3	1500	0.25	1.00
6	2	3	1	1500	0.35	0.50
7	3	1	3	2000	0.15	1.00
8	3	2	1	2000	0.25	0.50
9	3	3	2	2000	0.35	0.75

III. RESULTS AND DISCUSSION

The experiments are conducted as per design of experiment (DOE) L9 orthogonal array to study and evaluate the effect of each individual and combined process parameters on the output response. The responses are calculated in the form of material removal rate and surface roughness of each experiment individually by varying the parameters. S/N ratio has been calculated for both response Material removal rate (MRR) and Surface roughness (Ra) as per desired requirement that MRR should be larger and surface roughness should be smaller by using MINITAB 17 statistical software. Experimental results and corresponding S/N ratio are shown in table 5 with varying controlled parameters.

TABLE V.
EXPERIMENTAL RESULTS AND S/N RATIO

	Parameters			Response		S/N Ratio	
S.	Speed (N)	Feed rate (f)	Depth of cut (d)	MRR (mm^3/min)	Ra (μm)	MRR	Ra
1	1000	0.15	0.50	6597.3	0.819	76.3874	1.7343
2	1000	0.25	0.75	16493.4	2.079	84.3462	-6.3571
3	1000	0.35	1.00	30787.6	3.614	89.7675	-11.1598
4	1500	0.15	0.75	14844.0	0.856	83.4310	1.3505
5	1500	0.25	1.00	32986.7	2.318	90.3668	-7.3023
6	1500	0.35	0.50	23090.7	3.043	87.2687	-9.6660
7	2000	0.15	1.00	26389.4	1.021	88.4286	-0.1805
8	2000	0.25	0.50	21991.1	1.998	86.8450	-6.0119
9	2000	0.35	0.75	46181.4	3.485	93.2893	-10.8441

As volume of material removed should be maximum so higher the better is desired quality characteristic, it can be seen from the figure 3 that the third level of cutting speed (2000rpm), the third level of feed rate(0.35mm/rev.) and the

CVR Journal of Science and Technology, Volume 22, June 2022
DOI: 10.32377/cvrjst2221

third level of depth of cut(1.0mm) provides the maximum value of material removal during turning. From figure 3, it can also be observed that MRR continuously increases with increase in speed feed and depth of cut respectively.

TABLE VI.
RESPONSE TABLE OF S/N RATIO FOR MRR

Level	Speed(N)	Feed rate(f)	Depth of cut(d)
L1	83.50	82.75	83.50
L2	87.02	87.19	87.02
L3	89.52	90.11	89.52
Delta	6.02	7.36	6.02
Rank	3	1	2

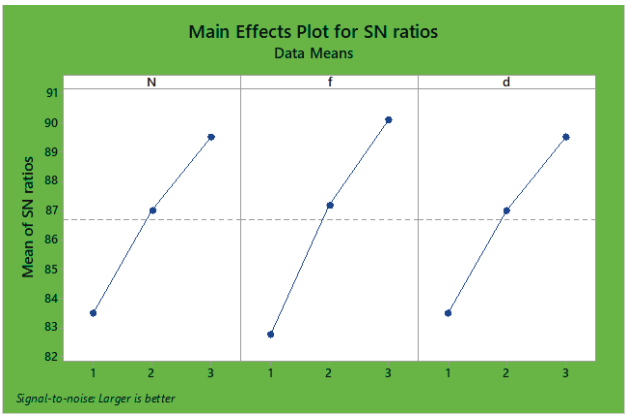

Figure 3. Effect of Parameters on Material Removal Rate

As surface roughness is the major characteristic to identify the sound quality of machining product as the surface finish should be better and surface roughness value should be minimum would reflect the better-quality surface. It can be seen from figure 4 that the third level of spindle speed (2000 rpm), the third level of feed rate(0.35mm/rev.) and the third level of depth of cut(1.0mm) provides lower value of surface roughness and also from figure 3, it can be concluded that surface roughness slightly decreases with increase in spindle speed, continuously decreases with increase in feed rate and also shows some decrement with increase in depth of cut within the given range of process parameters.

TABLE VII.
RESPONSE TABLE OF S/N RATIO FOR SURFACE ROUGHNESS

Level	Speed(N)	Feed rate(f)	Depth of cut(d)
L1	-5.2608	0.9681	-4.6479
L2	-5.2059	-6.5571	-5.2835
L3	-5.6788	-10.5566	-6.2142
Delta	0.4729	11.5247	1.5663
Rank	3	1	2

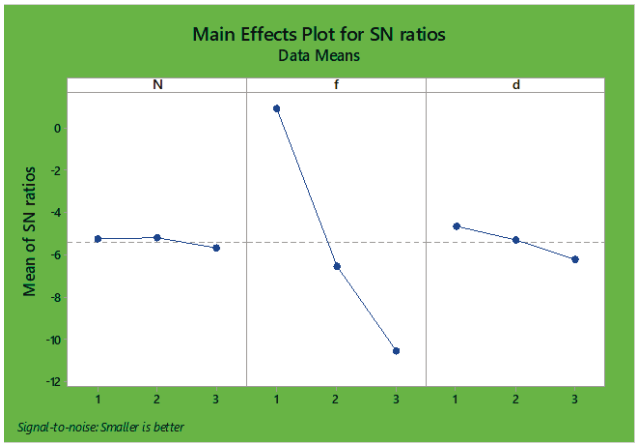

Figure 4. Effect of Parameters on Surface Roughness

From the main effect plot of S/N ratio and response table of S/N ratio reveals that spindle speed, feed rate and depth of cut affecting the variation of surface roughness value. In table rank is allotted based on delta statistics that compare the relative magnitude of control factor effects. Delta is calculated as the highest minus the lowest average for each factor. Software used for analysis purpose Minitab allocates rank according to delta value, the highest delta value shows rank 1, the second highest shows rank 2 and the third on is rank 3. The ranks and delta value show that feed rate has the greatest effect on MRR as well as surface roughness followed by depth of cut and speed.

A. Analysis of Variance(ANOVA)

Using ANOVA technique, it is used to identify the contribution of each individual parameters in output response. As shown in table 8 all three factors are significant factors in MRR. Feed rate has larger contribution of 42.87% followed by speed and depth of cut with a contribution of 28.56% each. Table 9 shows the ANOVA table for surface roughness, in that most significant factor is feed rate with a contribution of 98%, depth of 1.78% and speed has insignificant contribution since the P value is more than 0.05 at the confidence level of 95%.

TABLE VIII.
ANOVA TABLE FOR MRR

Source	DF	Seq. SS	Adj. SS	Adj. M	F-value	P-value	Contribution
N	2	0.72762	0.72762	0.363808	2.48114E+13	0.000	28.56%
f	2	1.09207	1.09207	0.546035	3.72392E+13	0.000	42.87%
d	2	0.72762	0.72762	0.363808	2.48114E+13	0.000	28.56%
Error	2	0.00000	0.00000	0.000000			0.00 %
Total	8	2.54730					100.00%

CVR Journal of Science and Technology, Volume 22, June 2022
DOI: 10.32377/cvrjst2221

TABLE IX.
ANOVA TABLE FOR Ra

Source	DF	Seq. SS	Adj. SS	Adj. MS	F-value	P-value	Contribution
N	2	0.00532	0.00532	0.00266	6.70	0.130	0.19%
f	2	2.72311	2.72311	1.36156	3431.54	0.000	98.0%
d	2	0.04935	0.04935	0.02468	62.19	0.016	1.78%
Error	2	0.00079	0.00079	0.00040			0.03%
Total	8	2.77858					100.0%

B. Mathematical Modeling

The multiple linear regression analysis is used to develop the regression model for correlating the control factors and the performance measurement. In this analysis the regression model is developed for material removal rate and surface roughness by using spindle speed, feed rate and depth of cut as a control factor or predictors with the help of MINITAB 17 statistical software.

The regression equation for MRR

$$MRR = -19426 + 6781\ N + 8705\ f + 6414\ d$$

TABLE X.
ANALYSIS OF VARIANCE TABLE

Source	DF	SS	MS	F	P
Regression	3	977346490	325782163	17.36	0.004
Error	5	93850657	18770131		
Total	8	1071197147			

S= 4332.45, R-sq= 91.24%, R-sq(adj)= 85.98%

The regression equation for surface roughness (Ra)

$$Ra = -0.707 - 0.0013\ N + 1.2410\ f + 0.1822\ d$$

TABLE XI.
ANALYSIS OF VARIANCE TABLE

Source	DF	SS	MS	F	P
Regression	3	9.43960	3.14653	267.33	0.000
Error	5	0.05885	0.19911		
Total	8	9.49846			

S= 0.108491, R-sq= 99.38%, R-sq(adj)= 99.01%

ANOVA results for regression models are presented in table 10 and table 11 for MRR and Ra respectively. It shows that the regression equation for both Material removal rate and surface roughness are statistically significant at 95% confidence level as p valve is less than 0.05. It shows the high value of determination coefficient for both the models that means the developed model is adequate. So, the regression model can be used for the estimation of MRR and Ra value.

IV. CONCLUSIONS

The current study was done to study the effect of control parameters on surface finish and volume of material removed. In view of extension and limitation of the current work, the following conclusion drawn from the CNC Turing operation of AA6061 alloy.

1. The analysis reveals the result that feed rate and depth of cut is the most significant factor for MRR as compared to spindle speed.
2. ANOVA analysis shows that spindle speed, feed rate and depth of cut affect the material removal 42.87%, 28.56%, 28.56% respectively.
3. The optimum parameters level setting for maximum MRR is found to be N3=2000rpm.f3=0.35 mm/rev. and d3=1.0mm.
4. From the ANOVA, it shows that feed rate is the most affecting parameters for surface roughness with a contribution of 98%, compared to depth of cut with contribution of 1.78% and spindle speed with least contribution of 0.19%.
5. The optimum parameters setting for minimum surface roughness N3=2000rpm, f3=0.35mm/rev. and d3=1.0mm.
6. From the present analysis it has been found that the developed mathematical model can be used for the prediction of MRR and surface roughness value at 95% confidence level as its P value < 0.05.

REFERENCES

[1] Narayana B. Doddapattar, Chetana S. Batakurki, “Optimization of Cutting Parameters For Turning Aluminum Alloys Using Taguchi Method,” International Journal of Engineering Research & Technology, Vol. 2 Issue 7, 2013.

[2] Ali A, Rajamony B, “Optimization of cutting parameters for surface roughness in CNC turning machining with aluminum alloy 6061 material,” IOSR Journal of Engineering 10 1-15.

[3] Jayaraman P and Kumar L M , “ Multi-response optimization of machining parameters of turning AA6063 T6 aluminium alloy using grey relational analysis in Taguchi method,” Procedia Engineering 97 197-204.

[4] Narayana B D and Chetana S B, “Optimization of cutting parameters for turning aluminium alloys using Taguchi method,” International Journal of Engineering Research & Technology 2 1399-1407.

[5] Chorng-Jyh Tzeng, Yu-Hsin Lin,Yung-Kuang Yang, Ming-Chang Jeng, “Optimization of turning operations with multiple performance characteristics using the Taguchi method and Grey relational analysis, ”Journal of Materials Processing Technology, 209(6), pp. 2753-2759.

[6] Vidyanand Kumar, Manjeet Kharub, Animesh Sinha, “Modeling and Optimization of Turning Parameters during Machining of AA6061 composite using RSM Box-Behnken Design,” IOP Conf. Series: Materials Science and Engineering 1057, 012058.

[7] Tian-Syung Lan, Ming-Yung Wang, “Competitive parameter optimization of multi-quality CNC turning,” Int J Adv Manuf Technol, 41, 2009, pp.820–826.

[8] Dr. Vijay Kumar M, Kiran Kumar B.J, Rudresha N, "Optimization of Machining Parameters in CNC Turning of Stainless Steel (EN19) By TAGUCHI'S Orthogonal Array Experiments," Materials Today: Proceedings 5, 2018, pp. 11395–11407.

[9] S. P. Palaniappan, K. Muthukumar, R. V. Sabariraj, "CNC turning process parameters optimization on Aluminium 6082 alloy by using Taguchi and ANOVA," Materials Today: Proceedings, https://doi.org/10.1016/j.matpr.2019.10.053.

[10] Shunmugesh K., Panneerselvam K, Pramod M, Amal George, "Optimization of CNC Turning Parameters with Carbide Tool for Surface Roughness Analysis Using Taguchi Analysis," Research Journal of Engineering Sciences, Vol. 3(6), 2014, pp. 1-7.

[11] Y. Hsiao, Y. Tarng, W. Huang, "Optimization of plasma arc welding parameters by using the Taguchi method with the grey relational analysis," Materials and Manufacturing Processes 23, 2007, pp. 51-58.

[12] Doreswamy Deepak, Rajendra Beedu, "Multi Response Optimization of Process Parameters Using Grey Relational Analysis for Turning of Al-6061," IOP Conf. Series: Materials Science and Engineering 225 (2017) 012092.

[13] Rao C. J., D. Nageswara Rao, P. Srihari, "Influence of cutting parameters on cutting force and surface finish in turning operation," International conference on design and manufacturing, Procedia Engineering 64, 2013, pp. 1405 – 1415.

[14] Vinod Mishraa, Gufran S. Khanb, K.D. Chattopadhyaya, Keshva Nanda, RamaGopal V. Sarepakaa, "Effects of tool overhang on selection of machining parameters and surface finish during diamond turning," Measurement, Volume 55, 2014, pp. 353–361

[15] M.Nataraj, K.Balasubramanian, D.Palanisamy, "Optimization of Machining Parameters for CNC Turning of Al/Al_2O_3 MMC Using RSM Approach," Materials Today: Proceedings, Volume 5, Issue 6, Part 2, 2018, pp. 14265-14272.

E-ISSN 2581 – 7957
P-ISSN 2277 – 3916
CVR Journal of Science and Technology, Volume 22, June 2022
DOI: 10.32377/cvrjst2220

Structural Analysis of Wall Joints in Precast Concrete Liquid Retaining Structures using Finite Element Method

B. Shivani[1] and N. Murali Krishna[2]
[1]PG Scholar, CVR College of Engineering/Civil Engg. Department, Hyderabad, India
Email: shivanibanala11@gmail.com
[2]Professor, CVR College of Engineering/Civil Engg. Department, Hyderabad, India
Email: nmuralikrishna1956@gmail.com

Abstract: **In the present-day competitive world, speed is the essence and from civil engineering perspective, fast paced construction is the need of the day. The civil engineering constructions in INDIA are mostly carried-out using reinforced cement concrete material using cast-in-situ construction methods. Cast-in-situ construction of cement concrete structures necessarily need some minimum time-consuming activities like shuttering, formwork centering, concrete setting, curing time etc. In this backdrop, precast cement concrete construction technology has come-up as a viable alternative. In the present project the finite element stress analysis of wall joints in water retaining structures are taken-up. It is proposed to perform the precast joint analysis using ANSYS APDL finite element software. As the panel elements more than one in numbers are to be connected along joints both horizontally and vertically, the joint analysis plays a very significant role. In other words, the integrity of the wall element including near the joint is of utmost importance. The stress concentration all along the joint plays a very important role. For this purpose, 6 different wall joints are analyzed. First model is of 2-Dimensional model and the rest five models are 3-Dimensional models. The 2D model is analyzed using plane strain condition. The vertical section of 1mm length of wall panel from the base of liquid retaining structures till the top is discretized into very many numbers of 4-nodded (Quad elements) plane strain elements subjected to surface traction caused by liquid pressure on the liquid front. In addition, the body forces due to self-weight of the materials are also considered. The rest of all 3-D models are discretized into very many numbers of 8-noded brick elements subjected to surface traction caused by liquid pressure and the body forces due to self-weight of the materials. All the models are analyzed using ANSYS APDL package using the linear static analysis module and the results for stresses and strains are validated.**

Index Terms: **Precast Concrete Walls, Precast Concrete Joints, ANSYS APDL, Liquid retaining Structures, Stresses, Strains**

I. Introduction

Precast structures are becoming popular in developing countries like India to provide housing for all people in a quicker time. This precast technology is an effective workable solution for large scale construction ensuring quality, safety, faster construction with less site disturbance, etc. The precast constructions are mostly carried out using cement concrete materials. The precast cement concrete construction techniques have both advantages and limitations. On the positive front, they facilitate fast pace construction, better quality assurance and better aesthetic appearance and finishing. On the limitations front, they are normally more expensive and need skilled manpower. The challenges posed by precast concrete constructions include: 1. Their feasibility issues, 2. Handling and Transportation difficulties, 3. Difficulty in ensuring leak proof Joints and 4. Difficulty in joining different precast elements. However, all the above limitations are thoroughly offset by the speed of construction. In the precast concrete construction project, the onus is on the structural engineer to proportionate the concrete elements which are transportable, feasible for erection, joints are adequate and finally, the structure shall be feasible duly meeting the safety criteria yet economical to the extent possible. In the present project, the aspect of analyzing the precast concrete element joints is taken up. A precast building structure is consisting of structural elements like footings, columns, beams, walls and slabs. Structural jointing between column-column, beam-beam, column-beam are detailed in IS-2016 (code of practice for precast concrete construction 2016). Depending on the forces acting on different wall/slab elements the precast joint shall be strong enough to remain intact. This can be ensured only by proper structural analysis of precast concrete joint. The analysis proves more challenging if the joint needs to be leak proof. Challenging situations in precast wall joints arise in case of retaining walls and walls of water retaining structures. The present work is taken up to ensure competent, better- quality liquid retaining precast cement concrete structures. As said earlier, such constructions are necessitated due to mass activity with time constrained situations.

Assumption:

All materials are elastic, isotropic and homogeneous. They obey Hook's law.

A. Objectives of the present study

1. The analytical work involves modelling of precast concrete wall to wall vertical joints with the aid of FEM package ANSYS APDL.
2. Finding out the variation of stresses at joints. Pointing out the critical points where the stress is maximum.
3. Validating the stresses and strain values obtained from FEM package ANSYS APDL and comparing

Received on 24-09-2021, Revised on 28-03-2022, Accepted on 25-04-2022.

with the permissible stress and strain values to ensure whether the joints are leak proof or not.

B. Finite Element Method

The FEM (Finite Element Method) is a way of obtaining or finding a solution to a physical problem. It relies on discretizing a continuum domain into finite elements. The accuracy of the solution greatly depends on the number of elements used to represent the physical domain. As we progressively refine the mesh, the solution improves and given enough iterations it converges towards a specific result. FEM allows for detailed visualization and indicates the distribution of stresses and strains inside the body of a structure.

C. Concept of Elements and Nodes

Elements: Basically, in the Finite element method we discretize the structure into smaller shapes called elements. We have 1D, 2D and 3D elements.

1D elements: In 1D analysis we can split a beam of say length L into a number of smaller elements which are nothing but lines. Line elements are bounded by nodes. They may also have additional mid nodes in which case a better solution is obtained.

Example:

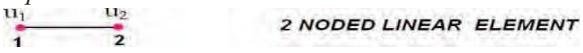

2D elements: A shell element is also called as 2d element. We have two types of 2D elements. 1. The 4 noded element which is also called as quad element and 2. three noded element which is also called as triangular element. We can consider a node as a vertex point. They may also have additional mid nodes in which case a better solution is obtained. At each node we have 2 degrees of freedom.

Example:

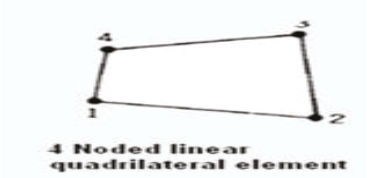

In the present work 2D 4 noded linear quad elements are considered for model-1 plain strain problem.

3D elements: A 3D element is divided into hexahedron element and tetrahedron element. We can consider a node as a vertex point. They may also have additional mid nodes in which case a better solution is obtained. At each node we have 3 degrees of freedom.

Example:

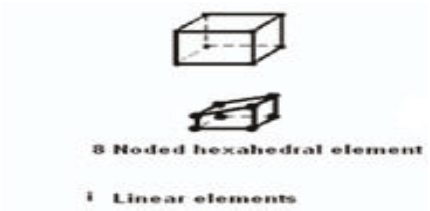

In the present work 3D 8 noded hexahedron elements are considered for model-2,3,4,5 and 6.

Nodes: Nodes are the finite points where the values of the field variable are obtained after the analysis. Variation of the field variable is expressed over an element. For example, in a structural analysis we obtain nodal displacements, strains & stresses are obtained over elements which are called elemental strains and elemental stresses respectively.

D. Two Dimensional Problems

The two-dimensional problems of structural analysis may be categorized as: 1. Plane stress problems, 2. Plane strain problems.

Plane Stress Problem: As the name suggests if the load acting and when the stresses are confined to a plane, then the problem is called the plane stress problem. (Ϭz, Ƈxz, Ƈyz are equal to zero)

Example: compound wall, shear wall, load bearing wall etc.,

Plane Strain Problem: As the name suggests if all the strains are confined to a plane, then the problem is called as a plane strain problem. (єz, ɼxz, ɼyz are equal to zero)

Example: 1. Stress distribution in long cylindrical pipe, 2. Stress distribution in long dams and spill ways, 3. Earthen dams, Gravity dam follow this plain strain principle.

E. Forces Acting on a Body

The kinds of force system, that act on a structure may be categorized as: 1. Body forces, 2. Surface traction forces, 3. Concentrated forces.

1. *Body Forces:* These are the forces which act due to the volume of the body. They may be acting in any direction, but can be resolved in the directions of X, Y and Z for convenience.

The body force acting per unit volume in X- direction may be represented as fbx, fby and fbz represent body forces acting parallel to Y and Z directions respectively.

Example: Self weight of the body, inertial forces etc.,

2. *Surface Traction Forces:* As the name suggests, the forces acting on surface area of the body is called surface traction force. The surface traction force acting per unit area in X- direction is represented as fsx, fsy and fsz represent surface traction forces acting in Y and Z direction.

Example: Liquid pressure, Soil pressure etc.,

Note:

1. External element in a body is subjected to body forces, surface traction forces and point loads.

2. Internal element in a body is subjected to only body forces.

3. Structural analysis is possible only when the body is stable and is in equilibrium.

F. Precast Concrete Joints

The design of joints should be executed as an integral part of the complete wall design. The structural connections between the Precast components will form an essential part of the structural system in the entire precast building. The structural response of the building or structure will depend on the characteristics and the behavior of the connections. To achieve a satisfactory and safe design, the designer should understand about how the connections influence the transfer of forces through a structure under vertical and horizontal loads. The main important purpose of the

structural connections is to transfer forces between the precast elements in order to enable the required structural interaction when the structural system is subjected to load. The Precast concrete wall-to-wall horizontal and vertical connections is very important as it ensures the continuity of load transfer of the connected wall panels. On the other hand, as precast components are fabricated offsite, onsite activity is limited to the assembly of components by lifting equipment. Therefore, the assembly process mainly depends upon the connections between the precast components to ensure secured structural integrity of the complete structure and the safe load transfer between the connected parts. Thus, the connection is regarded as an essential part of the structural system as the stability of the structure mainly relies on the performance of the connection.

G. Stress Concentration

A stress concentration is a place of the mesh where the stress raises above the applied nominal stress. The stress will converge towards a finite value, not infinite, given that the mesh is sufficiently refined. Stress concentration occurs when the load path is deviated by the presence of harder or softer features or a change of geometry. For example, presence of a hole in a plate mesh, around discontinuities, fillet corners, a change of cross-section, etc. contact forces are another common stress concentrations. High stress gradients also occur near the point of contact and rapidly subside as we move away from the contact area. A coarser mesh will not capture local effects such as stress concentrations. The more we refine the mesh, the more accurate the results are.

II. Literature Review

***Sayed Mohammed Arslan Inamdar* (2018)** has stated that, the overall stability of a precast structure mainly depends on connections and the joints between elements of precast structure so, it is important to consider the role of connections and the joints in transferring the loads between its elements of precast structure and to stabilize the foundation [1].

***Ramin Vagheia1 et. al.* (2013)** has done research on the evaluation of precast wall connections subjected to in-plane lateral ground movement [2].

***S. Sudhakar et.al.* (2019)** mentioned about how to choose the right capacity of the connection tools and carried out the research on vertical joint of precast concrete wall panel. This thesis mainly concentrated on connections for vertical joints using bolted connections of precast concrete wall panel [3].

***K. Karthikeyan et. al.* (2019)** did study on the comparing the performance of monolithic wall joints and precast concrete wall joints when subjected to cyclic loading [4].

***Mousa Abdullah Mohammed Hasan et. al.* (2019)** says that, the connection of wall panels is a key factor as it provides the structural integrity and robustness of the overall structural system. Therefore, this study aims to describe and summarize different types of precast concrete wall-to-wall horizontal connections in terms of structural behavior such as embedded length, bonding stress, seismic behavior and modes of failure [5].

III. Methodology

In the present work, I have adopted the Finite Element based analysis to understand the complexity of the stress concentration by analyzing the joints between wall elements and between wall elements with support. Since, the wall elements in liquid retaining structures are predominantly subjected to lateral load due to liquid, the joints are considered to be very vulnerable to stress concentration. The length of wall panels in a liquid retaining structures and their height of liquid retainment can be large. So, the wall panels are divided into smaller elements both for the convenience of transportation and erecting. As the panel elements more than one in numbers are to be connected along joints both horizontally and vertically, the joint analysis plays a very significant role. In other words, the integrity of the wall element including near the joint is of utmost importance. The stress concentration all along the joint plays a very important role. For this purpose, 6 different wall joints are analyzed. First model is of 2-Dimensional model and the rest five models are 3-Dimensional models. For analyzing 2D-model, a small length of wall element extending vertically from the base of the liquid retaining structure till the topmost point is considered. This situation corresponds to plane strain situation. The vertical section of 1mm length of wall panel from the base of liquid retaining structures till the top is discretized into very many numbers of 4-nodded (Quad elements) plane strain elements subjected to surface traction caused by liquid pressure on the liquid front. In addition, the body forces due to self-weight of the materials are also considered. The total 2D model considered in the analysis as described above is fixed at the bottom of the base. Whereas the top end is considered free to get displaced. The second model is the extension of first 2D model, but the analysis carried out is 3-Dimensional. The rest four are also 3D models with different cross section of joints subjected to loading in different directions. These 3D models are discretized into very many numbers of 8-noded brick elements subjected to surface traction caused by liquid pressure on the liquid front. In addition, the body forces due to self-weight of the materials are also considered. In the total 3D models the links or the wall joints which are considered as columns are fixed at the base and the rest of all walls are considered as free. The material of concrete in the wall panel and the material used for jointing the wall panels are all considered to be linearly elastic and isotropic. The model as described above is analyzed using Ansys APDL package using the linear static analysis module and the results for stresses and strains are validated.

IV. Analytical Investigation

A. Stages involved in analyzing the model:

1. Preferences – For defining type of model like structural, thermal etc.,
2. Preprocessor – For defining element type and element behavior.
3. Creating material properties
4. Modelling
5. Assigning material properties
6. Meshing

7. Defining analysis type like static, Harmonic etc.,
8. Creating and assigning boundary conditions
9. Creating and assigning loads at required points
10. Analyze
11. Check output files
12. Plotting results

Analytical model is modelled in ANSYS APDL software for six different types of wall joints. All the precast wall elements and its corresponding joints are modelled with concrete material and steel material where rebars are provided. The figure below shows the 6 different models:

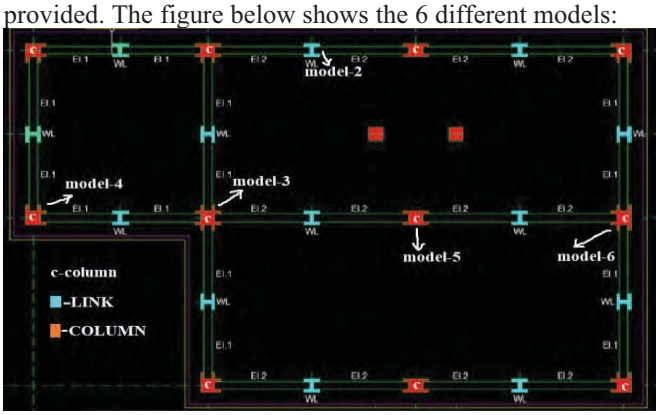

Figure1. Plan of liquid retaining tank

B. Material Properties:

Material used is assumed as structural linear elastic and isotropic.

For concrete:

E = 25e3 N/mm2 (Young's modulus)

μ = 0.2 (Poisson's ratio)

γ = 2.4e-06 kg/mm3 (Density)

For Binder material: (cement mortar, OPC 43 grade, C:S –1:2, W/C – 0.35)

E = 34e3 N/mm2

μ = 0.185

γ = 2.162e-06 kg/mm3

For Steel:

E = 2e5 N/mm2

μ = 0.3

γ = 7.85e-06 kg/mm3

C. Load Function Equation:

As the load applied is water pressure the equation of load is as follows:

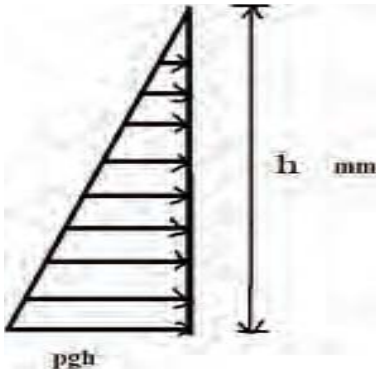

Figure2. Water Pressure (Loading diagram)

9.81×10^{-6}(h-Y) N/mm2

Pressure (P) = ρgh

= 1000 kg/m3 x 9.81 m/s^2 x h m

= 9810 N/m3 x h m

= (9.81 x 10^{-6} N/mm3) x (h – Y) mm

= 9.81 x 10^{-6} x (h – Y) N/mm2

ρ = 1000 kg/m^3 density of water,

g = 9.81 m/s^2 acceleration due to gravity

h = Height

D. Model-1 (2-Dimensional):

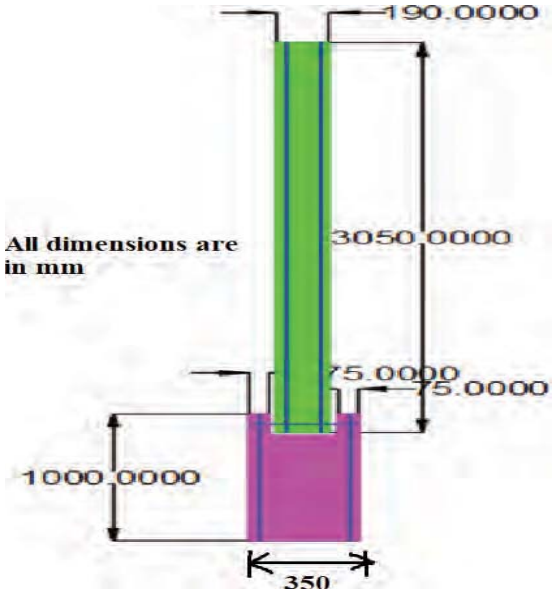

Figure3. Cross section of wall joint

This is a typical plane strain problem. ANSYS Mechanical APDL software is used to analyze it taking ANSYS version 2020 R2. For analyzing 2D-model, a small length of wall element extending vertically from the base of the liquid retaining structure till the top most point is considered. This situation corresponds to plane strain situation. The vertical section of 1mm length of wall panel from the base of liquid retaining structures till the top is discretized into very many numbers of 4-nodded (Quad elements) plane strain elements subjected to surface traction caused by liquid pressure on the liquid front. In addition, the body forces due to self-weight of the materials are also considered. The total 2-D model considered in the analysis as described above is fixed at the bottom of the base. Whereas, the top end is considered free to get displaced

E. 3-Dimensional Model Analysis:

The 3-D models with different cross section of joints subjected to loading in different directions are analyzed. These 3-D models are discretized into very many numbers of 8-noded brick elements subjected to surface traction caused by liquid pressure on the liquid front. In addition, the body forces due to self-weight of the materials are also considered. In the total 3-D models the links or the wall joints which are considered as columns are fixed at the base and the rest of all walls are considered as free. The material of concrete in the wall panel and the material used for jointing the wall panels are all considered to be linearly elastic and isotropic.

E-ISSN 2581 – 7957
P-ISSN 2277 – 3916

DOI: 10.32377/cvrjst2220

F. Model-2 (3-Dimensional):

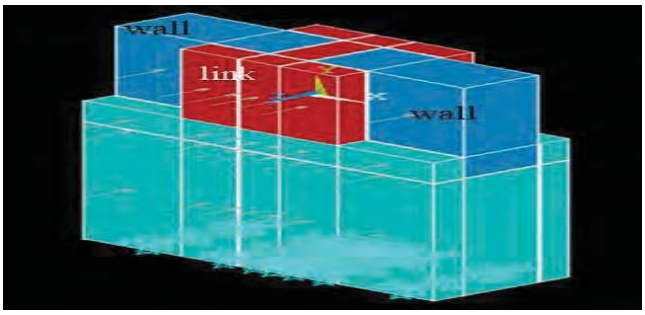

Figure 4. Complete I- link model

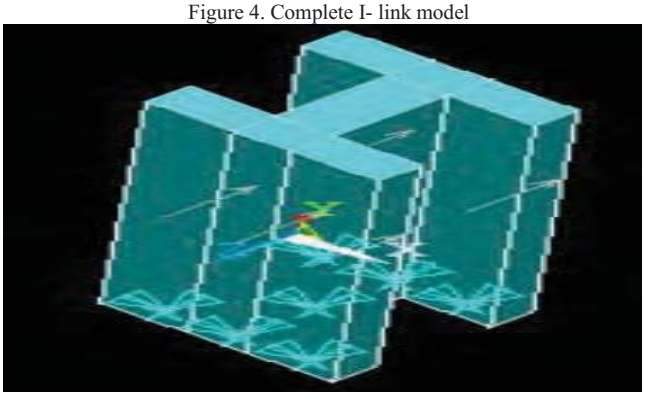

Figure 5. I-Shaped link

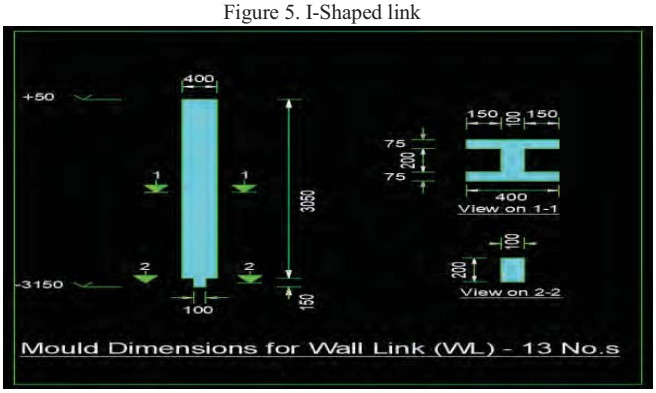

Figure 6. Mould dimensions for wall link

G. Model-3 (3-Dimensional):

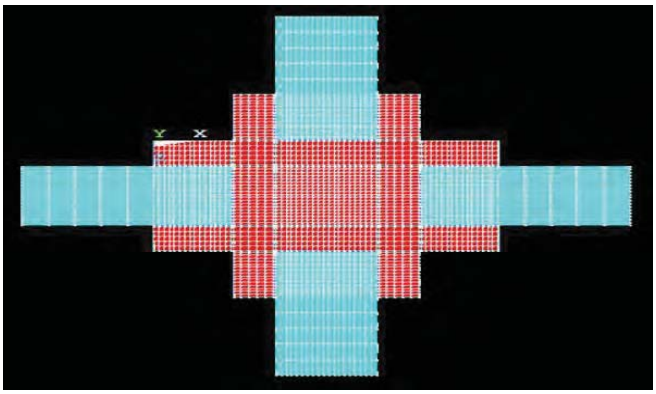

Figure 7. Model-3 Walls on four sides inserted into link (linkhighlighted with red colour and walls in blue)

As this model-3 has four chambers, there will be different cases like: there may be liquid in all the four chambers or any of the one or two or three chambers. So, this model is checked for leak proof for all the possible loading conditions and the critical loading condition is found out. Here the link is a column.

Here, I got 15 cases of different loading conditions and out of which critical loading condition is found out and the results are validated.

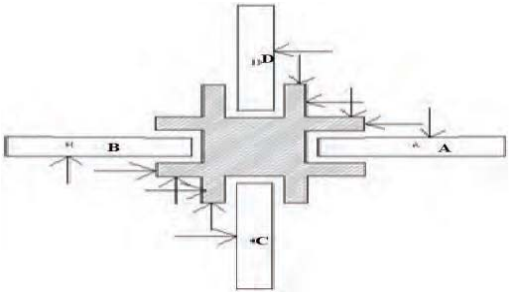

Figure 8. Model-3 I-Shaped link (critical loading condition)

H. Model-4 (3-Dimensional):

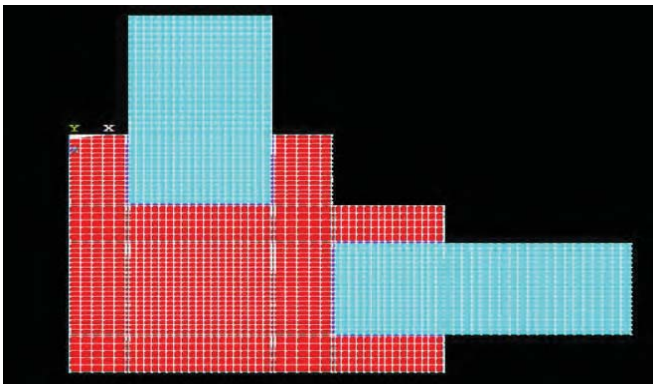

Figure 9. Model – 4 Corner link (link in red colour and it is acolumn and walls in blue)

I. Model-5 (3-Dimensional):

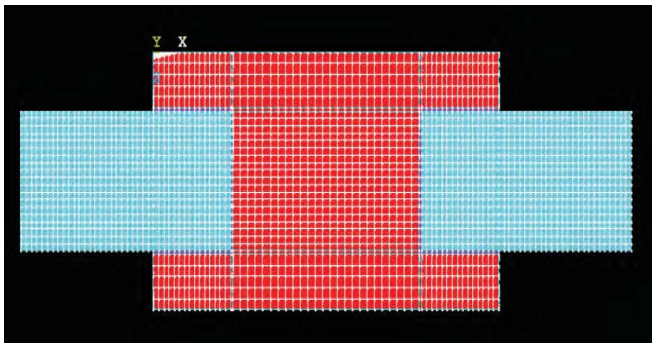

Figure 10. Model – 5 I-link (link in red colour and it is acolumn, walls in blue colour)

This model-5 may have two chambers or one chamber, depending on the location of joint. There will be different cases like: there may be liquid in two chambers or any of the one. So, this model is checked for leak proof for all the possible loading conditions and the critical loading condition is found out. Here the link is a column.

In this model, there are three different cases of loading conditions, and the critical condition is found out accordingly results are validated.

J. Model-6 (3-Dimensional):

This model-6 has two chambers. There will be different cases like: there may be liquid in two chambers or any of the one. So, this model is checked for leak proof for all the possible loading conditions and the critical loading condition is found out. Here the link is a column.

E-ISSN 2581 – 7957
P-ISSN 2277 – 3916

CVR Journal of Science and Technology, Volume 22, June 2022
DOI: 10.32377/cvrjst2220

In this model, there are three different cases of loading conditions, and the critical condition is found out accordingly results are validated.

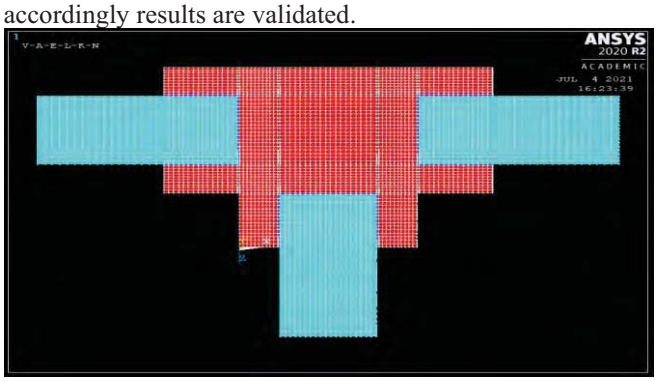

Figure11. Model – 6 link (link in red colour and it is acolumn, walls in blue colour)

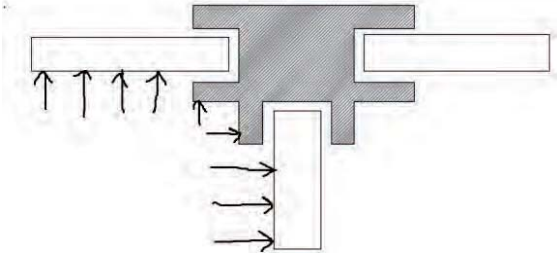

Figure 12. Model-6 (critical loading condition)

V. Results

A. Model-1 (2-Dimensional) Results:

TABLE I.
Results From Model–1 (Cross Section Of Wall(2D) Using Plain Strain Condition)

Maximum intensity of liquid pressure at a depth of 4050 mm height (N/mm2)	Maximum value of Stresses or Strains due to liquid Pressure (N/mm2)		Ultimate value of stress or Strains (N/mm2)		Comment
	Compressive stress or Strain	Tensile Stress or Strain	Compressive stress or Strain	Tensile Stress or Strain	
Stress in concrete with horizontal rebar subjected to Compressive force					
0.039731	21.35	0	25	3.5	Safe
Stress in steel with horizontal rebar subjected to Compressive force					
0.03971	127.133	31.5288	160	415	Safe
Stress at joint in binding material cement mortar					
0.03971	38.9878	0	43	2.5	Safe
Strain values in Concrete					
0.03971	1.16 x 10^{-3}	0	0.0035	0.0035	Safe
Strain values in Steel					
0.03971	0.0005	0.0001	0.0035	0.0035	Safe

From IS-456-2000 clause 38.1 stress-strain curve for concrete, the strain values in concrete are obtained using the above stress values in concrete and from IS-456-2000 clause 38.1 stress-strain curve for steel bar, the strain values in steel bar are obtained using the above stress values in Steel.

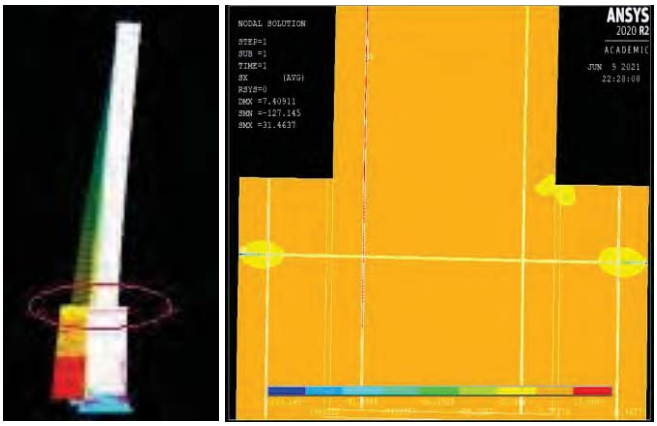

Figure 13. Model-1 (Deformation and Stress visualization)

B. Model-2 (3-Dimensional) Results:

TABLE II.
Results From Model–2 (I-Link Complete 3D Model)

Maximum intensity of liquid pressure at a depth of 4050mm height (N/mm2)	Maximum value of Stresses or Strains due to liquid Pressure (N/mm2)		Ultimate value of stress or Strains		Comment
	Compressive stress or Strain	Tensile Stress or Strain	Compressive stress or Strain	Tensile Stress or Strain	
Stress in concrete					
0.039731	0.17642	0.1572	25	3.5	Safe
Stress at joint in binding material cement mortar					
0.03971	0.102282	0.008924	43	2.5	Safe
Strain values in Concrete					
0.03971	6.31 x 10^{-6}	5.629 x 10^{-6}	0.0035	0.0035	Safe

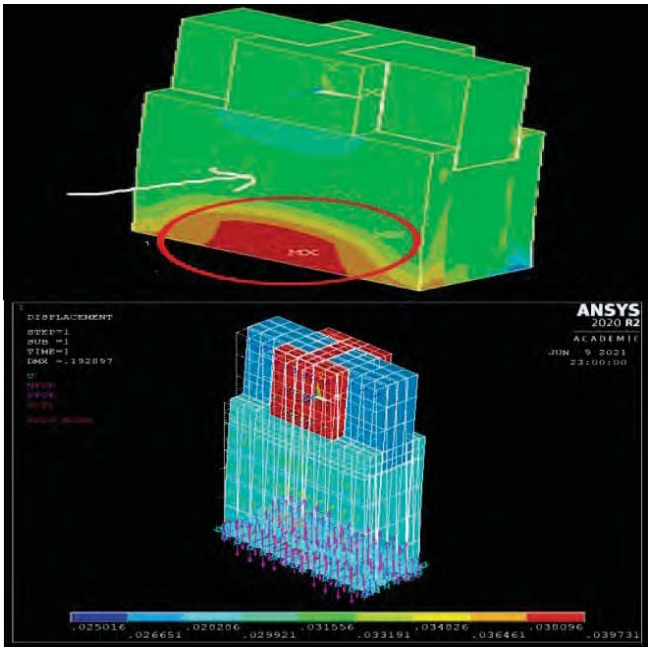

Figure 14. Model-2 (Deformation and Stress visualization)

C. Model-3 (3-Dimensional) Results:

TABLE III.
RESULTS FROM MODEL–3 (FOR 10 MM HEIGHT) CRITICAL MODEL

Maximum intensity of liquid pressure at a depth of 4050 mm height (N/mm2)	Maximum value of Stresses or Strains due to liquid Pressure (N/mm2)		Ultimate value of stress or Strains (N/mm2)		Comment
	Compressive stress or Strain	Tensile Stress or Strain	Compressive stress or Strain	Tensile Stress or Strain	
Stress in concrete					
0.029921	0.89234	2.27002	25	3.5	Safe
Stress at joint in binding material cement mortar					
0.029921	3.264	3.841	43	2.5	Unsafe in tension
Strain values in Concrete					
0.029921	3.32 x 10^{-5}	8.092 x 10^{-5}	0.0035	0.0035	Safe

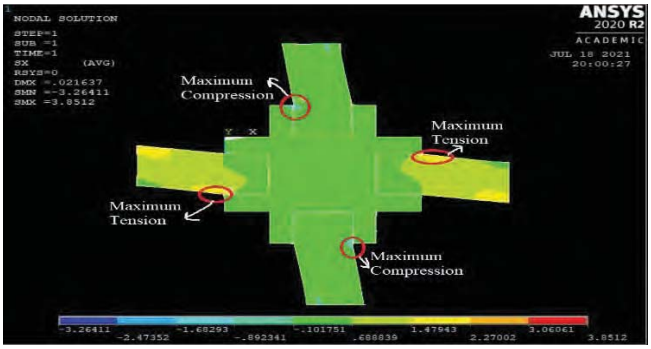

Figure 15. X – Component Stress contour (critical case)

D. Model-4 (3-Dimensional) Results:

TABLE IV.
RESULTS FROM MODEL–4 (FOR 10 MM HEIGHT)

Maximum intensity of liquid pressure at a depth of 4050mm height (N/mm2)	Maximum value of Stresses or Strains due to liquid Pressure (N/mm2)		Ultimate value of stress or Strains (N/mm2)		Comment
	Compressive stress or Strain	Tensile Stress or Strain	Compressive stress or Strain	Tensile Stress or Strain	
Stress in concrete					
0.029921	2.20186	4.75142	25	3.5	Unsafe in tension
Stress at joint in binding material cement mortar					
0.029921	3.07102	3.0131	43	2.5	Unsafe in tension
Strain values in Concrete					
0.029921	1 x 10^{-4}	2.33 x 10^{-4}	0.0035	0.0035	Safe

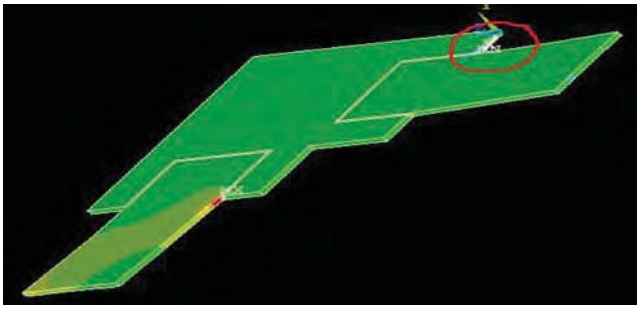

Figure 16. X – Component Stress contour

E. Model-5 (3-Dimensional) Results:

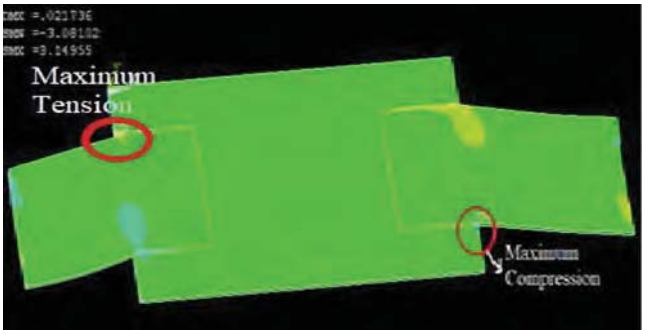

Figure 17. Showing Maximum compressive and Tensile Stress values

TABLE V.
RESULTS FROM MODEL–5 (FOR 10 MM HEIGHT)

Maximum intensity of liquid pressure at a depth of 4050 mm height (N/mm2)	Maximum value of Stresses or Strains due to liquid Pressure (N/mm2)		Ultimate value of stress or Strains (N/mm2)		Comment
	Compressive stress or Strain	Tensile Stress or Strain	Compressive stress or Strain	Tensile Stress or Strain	
Stress in concrete					
0.029921	2.3887	1.0727	25	3.5	Safe
Stress at joint in binding material cement mortar					
0.029921	3.08102	3.14955	43	2.5	Unsafe in tension
Strain values in Concrete					
0.029921	0.8564 x 10^{-4}	0.384 x 10^{-4}	0.0035	0.0035	Safe

F. Model-6 (3-Dimensional) Results:

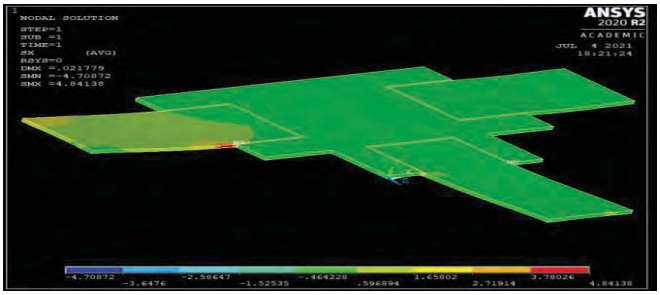

Figure 16. X – Component Stress contour

TABLE VI.
RESULTS FROM MODEL–6 (FOR 10 MM HEIGHT)

Maximum intensity of liquid pressure at a depth of 4050 mm height (N/mm2)	Maximum value of Stresses or Strains due to liquid Pressure (N/mm2)		Ultimate value of stress or Strains (N/mm2)		Comment
	Compressive stress or Strain	Tensile Stress or Strain	Compressive stress or Strain	Tensile Stress or Strain	
Stress in concrete					
0.029921	2.4322	4.43891	25	3.5	Unsafe in tension
Stress at joint in binding material cement mortar					
0.029921	3.29109	2.72113	43	2.5	Unsafe in tension
Strain values in Concrete					
0.029921	0.873 x 10^{-4}	0.158 x 10^{-3}	0.0035	0.0035	Safe

VI. CONCLUSIONS

As it can be seen from the chapter on Results and Discussions, based on the analysis carried-out on five different precast wall joints, following are the list of conclusions made. These are not quantitative conclusions as 1. The numbers of studies carried-out are limited and 2. Limitations imposed on FEA models due to limited software options.

1. The joints are the most critical parts of the precast concrete structures. The stress values near joints are usually very high and no jointing material commercially available can sustain. The present study carried-out demonstrates this phenomenon.
2. The male/female socket type joints ensure better stability in plate bending elements. Better performance is noted when depth of socket is more and width lesser.
3. The magnitude of the stresses in male/female socket joints reduces marginally when mechanical anchors in the form of steel nut/bolt connections are introduced.
4. Finite element modelling done by using plate bending elements for walls/slabs and hexahedron elements for beams/columns would result in more appropriate output.

VII. LIMITATIONS

The study is carried out under certain limitations:

1. All materials of the precast concrete structure are assumed to be linearly elastic which is not true.
2. Plane-strain option is used to model plate elements whereas plate bending option is more appropriate. This option needs superior computational facilities.
3. As the work is carried-out using ANSYS APDL student version with limited software options, the analysis is carried out with reduced number of degrees of freedom.

VIII. SCOPE FOR FUTURE

1. The non-linear behavior of material properties needs to be considered in the finite element analysis.
2. All plate elements shall be modelled using 2D shell elements, beam/column elements with 3D brick elements and jointing material at the interface with 3D brick elements.
3. True boundary conditions shall be used in the analysis by considering soil-structure interaction on the model.

REFERENCES

[1] Iyad ABRAHOIM, "*Connections and joints in precast concrete structures*", Slovak Journal of Civil Engineering, Vol. 28, 2020, No. 1, 49 – 56 DOI: 10.2478/sjce-2020-0007.

[2] Morten A Herfelt, Jorgen Krabbenhoft and Kristian Krabbenhoft, "*Practical design and modelling of precast concrete structures",* ISSN: 2643-6876, DOI: 10.33552/CTCSE.2019.03.000560 current Trends in Civil & Structural Engineering IRIS Publishers July 23, 2019.

[3] Sona P R, Mrs. Jithma T, "*Structural performance of detachable precast composite column and joints using FEA*", International Journal of Engineering Research & Technology (IJERT) ISSN: 2278-0181 IJERTV8IS050516 Vol. 8 Issue 05,May-2019.

[4] S. Sudhakar, G. Srinivasan, "*Behaviour of bolted connection in the vertical joint of precast wall panel*", International Research Journal of Engineering and Technology (IRJET) Volume: 06 Issue: 05 May 2019.

[5] K. Karthikeyan, M. Helen Santhi, *"Experimental investigation on precast wall connections*", Jour of Adv Research in Dynamical & Control Systems, Vol. 11, 06-Special Issue,2019.

[6] Mousa Abdullah Mohammed Hasan, Rahimah Muhamad, *"Wall to wall horizontal connection for precast concrete structures*", International Journal of Recent Technology and Engineering (IJRTE) ISSN:2277-3878, Volume-8 Issue-3S3, November 2019.

[7] E. Brunesi, R. Nascimbene & S. Peloso, "*Evaluation of the seismic response of precast wall connections: experimental observations and numerical modelling*", Journal of Earthquake Engineering, 24:7, 1057-1082 ISSN 07 May 2018.

[8] Sayed Mohammed Arslan Inamdar, "*Joints and connections in precast concrete buildings"*, International Journal of Science and Research (IJSR) ISSN DOI:10.21275/ART20183152, Paper ID: ART20183152, Volume 7 Issue 6, June 2018.

[9] Pouya Seifi, Richard S. Henry and Jason M. Ingham, *"Panel connection details in existing New Zealand precast concrete buildings*", Bulletin of the New Zealand Society for Earthquake Engineering, Vol. 49, No. 2, June 2016.

E-ISSN 2581 – 7957
P-ISSN 2277 – 3916

CVR Journal of Science and Technology, Volume 22, June 2022
DOI: 10.32377/cvrjst2221

Fuzzy Linear Programming Approach to Tank Water Allocation –A Case Study

C. G . Hemamalini
Professor, CVR College of Engineering/Civil Engg. Department, Hyderabad, India.
Email: cghemamalini72@gmail.com

Abstract: **Tanks are small earthen reservoirs constructed across natural drainage basins to impound water during monsoon rains. They are an important source of surface water for minor irrigation and groundwater recharge. Some of these tanks are system tanks that receive supplemental water from nearby streams running through the watershed, in addition to the yield from their own catchment. The remaining non-system tanks are not connected to any river system. Most tank storage lasts only for one season and rarely for two seasons. Therefore, it is necessary to conserve the limited water stored by these tanks and use it in the most efficient manner. The main objective of the study is to maximize the net benefit of the command area with the optimal allocation of tank water. In this study, the linear programming model is developed to optimize the tank water allocation with the objective of maximizing the net benefit of the command area through the allocation of area for different crops for different seasons. Another major objective of the present study is to formulate the fuzzy linear programming model by considering the imprecise inflow variation as the fuzzy set. The net benefit of the command area per annum has arrived such as 12.58 lakhs and 8.02 lakhs for 90% dependability inflow, 13.22 lakhs and 8.67 lakhs for 75% dependability inflow, 13.93 lakhs and 9.39 lakhs for 50% dependability inflow, and 14.20 lakhs and 9.66 lakhs for 40% dependability inflow through the linear programming model analysis. Since the inflow variation is imprecise, the attempt was made to formulate the fuzzy linear programming model and assigned the membership function for different ranges of inflow and analyzed the model. The net benefit of the command area per annum has arrived for three different scenarios such as 13.36 lakhs, 13.30 lakhs, and 13.23 lakhs respectively. It is concluded that wherever the imprecise situation occurs in water resources allocation problems then it is solved with the fuzzy logic concept.**

Index Terms: **Fuzzy linear programming, tank water, irrigation, water allocation**

I. Introduction

A small earthen reservoir formed in depression by constructing an earthen embankment across a natural drainage basin to impound water during monsoon rains is called a tank. These tanks are either system tanks or non-system tanks. If the downstream tanks are connected to upstream tanks by streams/channels, then they are called system tanks. Non-system tanks exist independently and are not connected to upstream tanks. Tanks are the source of a minor irrigation scheme and augment the groundwater recharge. The scheme of irrigation of the tank command area through the tank is called tank irrigation.

Since the tank water storage is directly influenced by the monsoon rains, the optimal allocation of tank water for an irrigable area of various crops grown in the command area for different seasons is the most important task for the water managers. Therefore, the principal objective of any tank irrigation scheme is to maximize the net benefit of its command area through the optimal tank water allocation. There are different constraints which are considered while allocating the water by using any optimization technique, are (i) crop area in each season should not exceed the total area (ii) crop water requirement must be met (iii) total release from the storage should not exceed the storage capacity of the reservoir (iv) tank storage at any period should not exceed the maximum storage (v) tank storage at any period should be maintained above dead storage (vi) minimum area allocated to certain crops such as paddy in different seasons must be fixed.

In this case study, one of the existing tanks named Padianullur tank is taken for applying the linear programming technique for optimal water allocation for various crops grown in the command area. The linear programming model is developed to maximize the net benefit of the Padianallur tank command through the irrigable area allocation for different crops for different seasons. Also, the fuzzy logic [1], [2], [4] is applied to overcome the imprecise tank inflow variation in the problem and the fuzzy linear programming model [1], [3] is developed and compared with the linear programming model. The symmetrical model developed by Zimmermann [1] i.e., the membership function of fuzzy objective of non-decreasing continuous linear function and the membership functions of fuzzy constraints of non-increasing continuous linear functions have been adopted in this study to maximize the net benefit of the command area. The model is formulated with a triangular membership function to maximize the level of satisfaction, so that the linear membership function with a level of satisfaction $\alpha = 1$ for maximum net benefit possible at minimum inflow and $\alpha = 0$ for maximum net benefit possible at maximum inflow is adopted.

Many researchers have used the linear programming technique to obtain optimal cropping patterns for maximizing the net benefit of the command area [5], [6], [7]. Fuzzy logic has been applied in hydrology such as rainfall forecast which grades the rainfall into rareness of rainfall, normality of rainfall, and plenty of rainfall [8] and predicting runoff during the snowmelt season from the combined system of tanks [9]. The water resources allocation has been solved by formulating the fuzzy set of water requirements of a single water user [10]. The fuzzy linear programming model [1], [11] was formulated based on the water requirement of users and minimum flow requirement as fuzzy inputs in the model.

Received on 15-02-2022, Revised on 09-03-2022, Accepted on 25-04-2022.

E-ISSN 2581 – 7957
P-ISSN 2277 – 3916

CVR Journal of Science and Technology, Volume 22, June 2022
DOI: 10.32377/cvrjst2221

II. Study Area

The Padianallur tank is situated in Ponneri taluk, Chengalpattu district of Tamilnadu and its command area is taken as model study area. This tank is a non system tank and having a free catchment area of 3.75 sq.km and intercepted catchment area of 4.45 sq.km. The depth of storage capacity at F.T.L is 0.817 Mcum and water spread area at F.T.L is 97.7 ha. The dead storage of the tank is 0.0017 Mcum.

The command area of the tank extends over 238.41 ha in the three revenue villages of Padianallur, Palavoyal and Theerthakarayanpattu. Water is supplied to these villages through five sluices of the tank. The details of sluices, their location, area commanded and villages commanded are given in the Table 1. The paddy is the major crop grown in the command area in all three seasons. Other than Paddy, Groundnut, Vegetables, Ragi and dry crops (Pulse and Greengram) are grown in second and third seasons and sugarcane is an annual crop which also grows in the command area. Based on the fifty years of data collected from the Redhills rainfall station, the average rainfall for three seasons is taken as (i) First season (Sep-Jan) – 809 mm (ii) Second season (Feb-Apr) – 32 mm and (iii) Third season (May – Aug) – 309 mm. The soil type in the command area is classified as clay loam and sandy loam.

III. Methodology

The methodology of the present study is described in the flow chart and is shown in Fig. 1. The linear programming model is chosen in this study to quantify an optimal allocation of an irrigable area of different crops to maximize the net benefit from the command area. The linear programming model is suitable for the study since the objective function of maximizing the net benefit and the different constraints are the linear functions of irrigated areas of different crops such as decision variables of the model. In the command area of Padinallur tank, the irrigable area of crops depends on the tank water availability in different seasons and major and minor crops grown. So, the constraints are fixed based on the crop selection in different seasons and the minimum irrigable area of the major crop. The fuzzy linear programming model is attempted to maximize the level of satisfaction to arrive at the maximum net benefit from the command area with respect to the imprecise inflow variation.

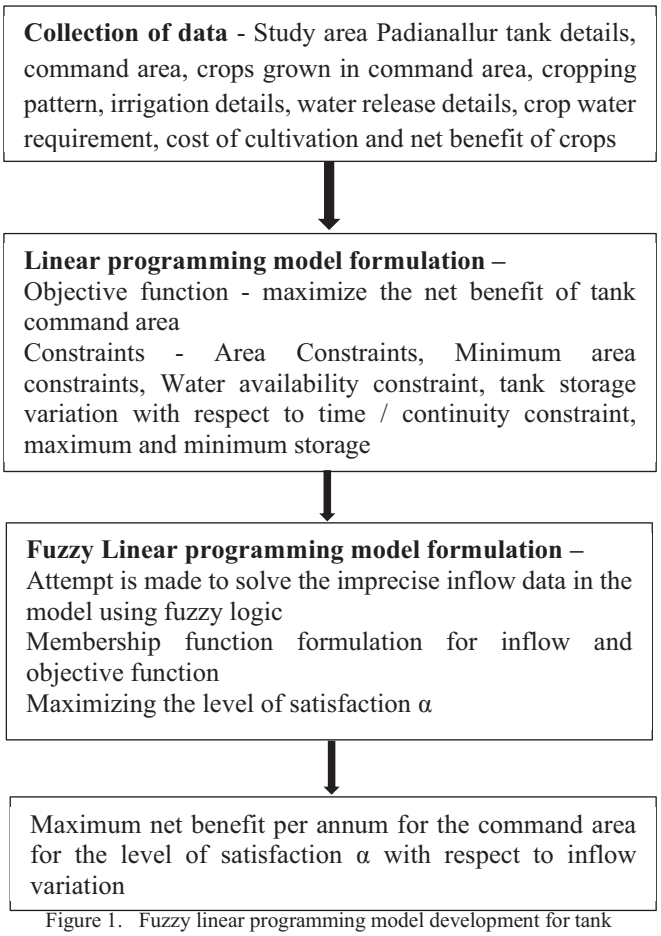

Figure 1. Fuzzy linear programming model development for tank command area

IV. Model Formulation

A. Description of Model Study Area

The parameters which are required to develop the model for optimizing water allocation and maximizing the net benefit of the command area, are crop water requirement, irrigation requirement, effective rainfall, percolation and evaporation loss, inflow to the tank, and the net benefit from each crop. The estimation of crop water requirement of different crops which are grown in the study area [12] is given in Table 2.

TABLE I.
Detail of Sluices

Sluice No.	Location (from Northern end) 'm'	Sill level (with reference to temple B.M.) 'm'		Area commanded 'ha'	Village commanded
		Upper	Lower		
New	358	98.60	98.00	5.98	Padianallur
1	680	97.62	96.95	70.00	Padianallur
2	1166	97.51	96.71	89.15+33.21	Palavoyal and Theerthakarayanpattu
3	1443	97.68	97.08	31.95	Padianallur
4	1771	98.19	98.01	8.12	Padianallur

TABLE II.
Crop Water Requirement

Crop	Season		
	1st	2nd	3rd
	Water Requirement in m		
Paddy	1.061	0.953	1.240
Sugarcane		0.887	0.812
Groundnut		0.491	0.482
Vegetables		0.490	0.490
Ragi		0.486	0.489

The irrigation requirement of the different crops is calculated by subtracting the effective rainfall from the total water requirement of the crop. The total water requirement is the sum of crop water requirement and seepage loss. Tank water requirement at sluice level for each crop is calculated

considering 70% overall efficiency. The effective rainfall is estimated for the study area using monthly average rainfall and monthly average crop water requirement. The percolation loss is taken as 3 mm/day and evaporation loss is taken from the literature [13].

The inflow to the tank is estimated using the Soil and Conservation Services (SCS) method from the available data of 50 years (1942-92) by applying the conditions such as (a) Hydrologic soil group – Group C, (b) Land use description – close seeded legumes, (c) Land use treatment - Straight row (d) Hydrologic condition –Good (e) Antecedent moisture condition – Condition 2 and (f) Curve number – 81. The net benefit from each crop is arrived at based on the data collected from Directorate of Agriculture and Horticulture, Government of Tamilnadu and is given in Table 3.

TABLE III.
COST OF CULTIVATION AND NET BENEFIT OF CROPS

Crop	Yield t/ha	Procurement Values Rs/ha	Cost of Cultivation Rs/ha	Gross benefit Rs/ha	Net Benefit Rs/ha
Paddy 1	4	2000	8000	14000	6000
Paddy 2 & 3	4.5	2000	8000	15750	7750
Groundnut	3	3618	10853	21000	10147
Ragi	2	1286	2571	6000	3229
Vegetables	14.4	1120	16125	35000	18875
Sugarcane	112.5	309	34750	63000	28250

B. Linear Programming Model Formulation

Linear programming (LP) is one of the optimization techniques for optimal allocation of limited resources to arrive at the desired objectives when any study can be described by a mathematical model. The mathematical statement of LP model includes a set of simultaneous linear equations and the linear function. These linear equations represent the conditions / constraints of the problem of study and a linear function represents the objective of the study to be achieved.

In the present study, the Padianallur tank command area is taken as the model study area and the objective is to solve the tank water allocation to irrigable crop areas of various crops grown in different seasons. In this case study, there are ten decision variables that represent the irrigable area of different crops grown in different seasons. The first season (Sep – Jan) crop is Paddy and the crop area is represented by the variable X1. The second season (Feb – Apr) crops are Paddy, Groundnut, Vegetables and Ragi, and the crop area of those crops are represented by X2, X3, X5 and X6 respectively. The third season (May – Aug) crops are Paddy, Groundnut, Vegetables and Ragi, and the crop area of those crops are represented by X7, X8, X9 and X10 respectively and the Sugarcane is grown throughout the year and the crop area is represented by X4.

The constraints which are formulated to solve the problem, are (i) the irrigable crop area of different seasons should not exceed the available command area (ii) the minimum crop area for Paddy in the second and third seasons is fixed to meet the demand of Paddy since the major stable food of people of this command area is rice (iii) sum of the tank water requirement for different crops at different months should not exceed the available tank storage during those months (iv) tank storage at different periods is equal to tank storage at previous period plus inflow to the tank at previous period minus losses minus release minus spill (v) tank storage at different months should be greater than or equal to dead storage (vi) tank storage at different periods should be less than or equal to the storage capacity of the tank and (vii) the area under each crop, storage at any month, spill at any month can not be a negative value.

The objective function of the problem is to maximize the net benefit of the tank command area through the optimal allocation of tank water for different crops.

Maximize $Z = \sum P_i X_i$

Where,
P_i represents the net benefit per hectare of the i^{th} crop
X_i represents the irrigable area of different crops grown in three seasons.

Constraints
(a) Area Constraints
First season >>>→ $X1 + X4 \leq 238.41$
Second season >>>→ $X2 + X3 + X4 + X5 + X6 \leq 238.41$
Third season >>>→ $X7 + X8 + X9 + X10 + X4 \leq 238.41$

(b) Minimum area constraints
$X2 \geq 30$ and $X7 \geq 10$
(c) Water availability constraint

$$\sum_{i=1}^{n} TWRitXi \leq St$$

Where,
TWRit - Tank water requirement for the i^{th} crop during t^{th} month
X_i – Area under i^{th} crop
St – Tank storage at t^{th} month
n – Number of crops grown in a season
t – 1 to 12
(d) Continuity equation

$$S(t+1) = St + It - \sum_{i=1}^{n} TWRitXi - (Pt + Et) - SPt$$

Where,
S(t+1) - Storage at $(t+1)^{th}$ month
It – Inflow at t^{th} month
$\sum_{i=1}^{n} TWRitXi$ - Release at t^{th} month
Pt - Percolation loss at t^{th} month
Et - Evaporation loss at t^{th} month
SPt - Spill at t^{th} month
(e) Minimum water constraint
$S_t \geq$ Smin
Where,
Smin – Tank dead storage
(f) Maximum water constraint
$S_t \leq$ SMax
Where, SMax - Storage capacity of the tank
(g) Non-negativity constarints
$S_t \geq 0$; $X_i \geq 0$; $SP_t \geq 0$.

E-ISSN 2581 – 7957
P-ISSN 2277 – 3916

DOI: 10.32377/cvrjst2221

C. Fuzzy Linear Programming Model Formulation

In operations research, fuzzy set theory has been applied to techniques of linear and non-linear programming, dynamic programming, queueing theory, multiple criteria decision making and group decision making [4].

In the fuzzy linear programming model study, the objective function and the constraints which represent imprecise situations can be solved by fuzzy set theory. The model for the present study is formulated by incorporating the tank inflow variations as a fuzzy set since these values are imprecise in nature. The maximum net benefit possible with maximum and minimum inflows is also represented by means of a fuzzy set of the objective function. The inflow in the continuity equation is represented by its linear membership function with the level of satisfaction $\alpha = 1$ for maximum net benefit possible at minimum inflow and $\alpha = 0$ for maximum net benefit possible at maximum inflow. The objective function is then convoluted as a fuzzy objective constraint. Other constraints such as area constraints, water availability constraint, minimum water requirement, and maximum water requirement are taken as precise constraints. The objective of the fuzzy linear programming model is to maximize the net benefit possible with minimum inflow which implies maximizing α. The membership function for inflow is given below and it is represented in Fig. 2.

$$\mu_I = \begin{cases} 1 & \text{if } I \le I_T \\ I_B - \alpha (I_B - I_T) & \text{if } I_T > I > I_B \\ 0 & \text{if } I \ge I_B \end{cases}$$

Where,
I_T – Upper bound (Maximum dependability inflow)
I_B – Lower bound (Minimum dependability inflow)

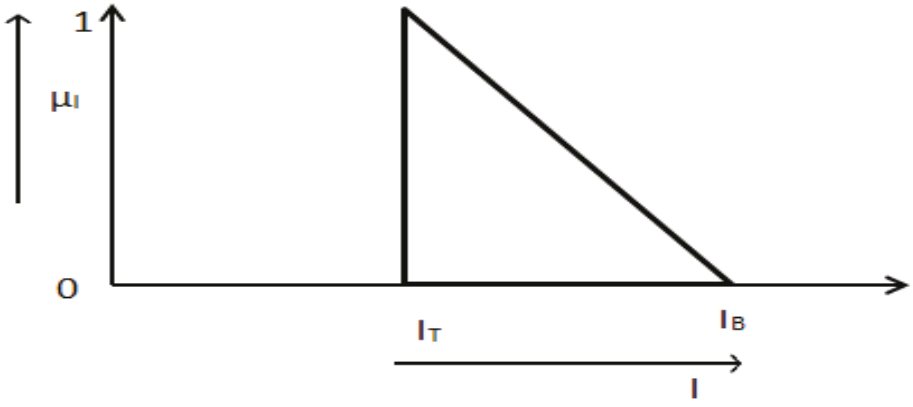

Figure 2. Membership function for inflow

The membership function for objective function is given below and is represented by the Fig. 3.

$$\mu_Z = \begin{cases} 1 & \text{if } Z \le Z_T \\ Z_B - \alpha (Z_B - Z_T) & \text{if } Z_T > Z > Z_B \\ 0 & \text{if } Z \ge Z_B \end{cases}$$

Where,
Z_T = Upper bound (value of objective function for maximum dependability inflow)
Z_B = Lower bound (value of objective function for minimum dependability inflow)

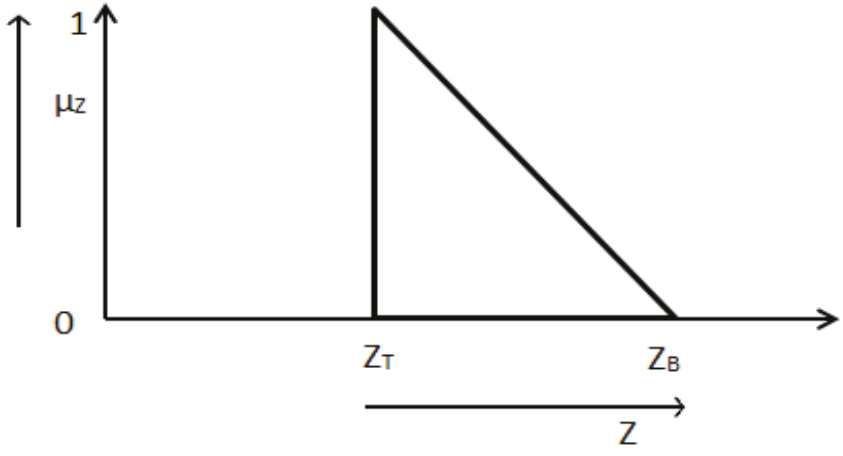

Figure 3 Membership function for objective function

CVR Journal of Science and Technology, Volume 22, June 2022
DOI: 10.32377/cvrjst2221

Maximize α
such that,
$Z \geq Z_B - \alpha (Z_B - Z_T)$
$X1 + X4 \leq 238.41$
$X2 + X3 + X4 + X5 + X6 \leq 238.41$
$X7 + X8 + X9 + X10 + X4 \leq 238.41$
$\sum_{i=1}^{n} TWRitXi \leq St$
$S_{(t+1)} - S_t + P_t + E_t + Sp_t + \sum_{i=1}^{n} TWRitXit = I_B - \alpha (I_B - I_T)$
$S_t \leq SMax$
$S_t \geq Smin$
$\alpha \in (0, 1)$
$S_t \geq 0$; $X_i \geq 0$; $SP_t \geq 0$.

V. Results And Discussion

A. Linear Programming Model Results

The different dependability inflow situations such as 90%, 75%, 50% and 40% are considered to maximize the net benefit in the command area and the results have arrived through linear programming model formulation. Setting the area constraints such as the total available area for cropping in different seasons and minimum area constraint such as minimum paddy cultivation area, continuity constraint and minimum and maximum constraints, and non-negativity constraints, the objective of maximum net benefit at different dependable inflow has been achieved through the linear programming model study. The model run shows that for 90% dependability inflow, the optimal allocated area for paddy for two seasons and net benefit are 130 ha and 12.58 lakhs respectively. Similarly, for different dependability inflow, the maximum net benefit has been achieved as shown in Table .4. It is evident that the maximum net benefit increases with a decrease in the dependability inflow.

TABLE IV.
Inflow Variation and Net Benefit

Dependability Inflow	Scenario	Crops	Area Allocated in three different seasons ha			Net benefit per annum Rs
			1	2	3	
90%	Case (1)	Paddy	104	30	0	12.58 lakhs
		Groundnut	-	0	10.3	
		Vegetables	-	0	16	
		Ragi	-	0	0	
		Sugarcane	-	0	0	
	Case (2)	Paddy	75	30	10	8.02 lakhs
		Groundnut	-	0	4.2	
		Vegetables	-	0	0	
		Ragi	-	0	0	
		Sugarcane	-	0	0	
75%	Case (1)	Paddy	104	30	0	13.22 lakhs
		Groundnut	-	0	16.1	
		Vegetables	-	0	16.2	
		Ragi	-	0	0	
		Sugarcane	-	0	0	
	Case (2)	Paddy	76	30	10	8.67 lakhs
		Groundnut	-	0	10.2	
		Vegetables	-	0	0	
		Ragi	-	0	0	
		Sugarcane	-	0	0	
50%	Case (1)	Paddy	104	30	0	13.93 lakhs
		Groundnut	-	0	23	
		Vegetables	-	0	17	
		Ragi	-	0	0	
		Sugarcane	-	0	0	
	Case (2)	Paddy	76.8	30	10	9.39 lakhs
		Groundnut	-	0	17	
		Vegetables	-	0	0	
		Ragi	-	0	0	
		Sugarcane	-	0	0	
40%	Case (1)	Paddy	104	30	0	14.20lakhs
		Groundnut	-	0	25	
		Vegetables	-	0	17	
		Ragi	-	0	0	
		Sugarcane	-	0	0	
	Case (2)	Paddy	77	30	10	9.66 lakhs
		Groundnut	-	0	19	
		Vegetables	-	0	0	
		Ragi	-	0	0	
		Sugarcane	-	0	0	

CVR Journal of Science and Technology, Volume 22, June 2022
DOI: 10.32377/cvrjst2221

B. Fuzzy Linear Programming Model Results

Using fuzzy logic concept, in first scenario, the inflow variation is given between 75% and 50% dependability inflow. The satisfaction level α = 1 is given to the net benefit achievable at 75% dependability inflow and α = 0 is given to the net benefit achievable at 50% dependability inflow. Similarly, the inflow variation is given between 75% and 40% dependability inflow and the inflow variation is given between 90% and 50% dependability inflow. The fuzzy linear programming model results are arrived for the above scenarios and has shown in the Table.5. Since the dependability inflow is uncertain, instead of giving the crisp dependable inflow, the variation of it, is given with the fuzzy set of (1, 0). Therefore, by setting the maximum and minimum dependability inflow, the optimal allocation of area for different crops is arrived with net benefit.

VI. Conclusions

The case study of Padianallur tank command area is taken to study the optimal water allocation problem with different dependable inflow to get the maximum net benefit from the cultivation in three different seasons. The linear programming model is applied in this problem since the decision variables such as the cropping area taken in the study are linear with respect to independent parameters. The model formulation is done with the objective of achieving the maximum net benefit from the command area and arrived the results. The attempt is made to study the imprecise data such as dependability inflow through fuzzy logic concept. Therefore, the variation of dependability inflow is taken as the fuzzy set in the formulation of the membership function. The maximum net benefit corresponding to the dependability inflow is also taken as the fuzzy set and the membership function is formulated. The fuzzy linear programming model is formulated to achieve the maximum satisfaction level α and has arrived for three different scenarios. The maximum net benefit for different scenarios has arrived at 13.36 lakhs, 13.30 lakhs, and 13.23 lakhs corresponding to the satisfaction level of α = 0.84, 0.9, and 0.57 respectively. Therefore, it is concluded that there is a scope of application of the fuzzy logic concept to solve societal problems such as resource allocation, solid waste management, and water and wastewater quality problems.

TABLE V.
Fuzzy Linear Programming Model Results

Scenario	Crops	Area allocated (ha) in different seasons			α	Net Benefit per Annum Rs
		1	2	3		
1	Paddy	100	0	0	0.84	13.36 Lakhs
	Groundnut	-	0	9		
	Vegetables	-	0	34.2		
	Ragi	-	0	0		
	Sugarcane	-	0	0		
2	Paddy	100	0	0	0.9	13.30 Lakhs
	Groundnut	-	0	9		
	Vegetables	-	0	34		
	Ragi	-	0	0		
	Sugarcane	-	0	0		
3	Paddy	50	0	0	0.57	13.23 lakhs
	Groundnut	-	0	0		
	Vegetables	-	0	54.2		
	Ragi	-	0	0		
	Sugarcane	-	0	0		

References

[1] H. J. Zimmermann, Fuzzy Set Theory and its Applications, Kluwer Academic Publishers, 1991.
[2] Daniel Mcneill and Paul Freiberger, Fuzzy Logic, Simon and Schuster publication,1993.
[3] Kwang H. Lee, First Course on Fuzzy Theory and Applications", Springer, 2004.
[4] YoungJouLai and Ching-Lai Hwang, Fuzzy Mathematical Programming Methods and Applications, Springer, 1992.
[5] Dilip Kanna and Bipin Bihari Lal, "Optimal cropping pattern Vis-A-Via-A case study of Karanja project", Proceedings of National Seminar on Water and Environment, College of Engineering, Kerala, pp.271-278, 1994.
[6] S.G. Mayya and Rama Prasad, "System analysis of tank irrigation:1 crop staggering", Journal of Irrigation and Drainage Engineering, ASCE, Vol 115, No.3, pp.384-403, 1989.
[7] H. Raman and S.Vasudevan, "Application of linear programming techniques for optimal cropping pattern", Irrigation and Power, CBIP, Vol.48, No.4, pp.49-57, 1991.
[8] LI Zuoyong, Zhenpei Chen and Jitao, "A model of weather forecast by fuzzy grade statistics", Fuzzy Sets and Systems, Vol.23, pp.275-281, 1988.
[9] Kazumasa Mizumura, "A new approach to snow melt-runoff fuzzy logic", Proceeding of the Third International Conference on Hydraulic Engineering Software, Massachusetts, USA, 1990.
[10] Janusz Kindler, "Rationalizing water requirements with aid of fuzzy allocation model", Journal of Water Resources Planning and Management, ASCE, Vol.118, No.3, pp.308-323, 1992.
[11] S. Mohan, "A fuzzy linear programming model for water resources allocation", Indian water works association, pp .155-158, 1994.

CVR Journal of Science and Technology, Volume 22, June 2022
DOI: 10.32377/cvrjst2221

[12] S.Subramanian and R Kulandaivelu, Crop water requirement and scheduling irrigation for crops in Tamilnadu state, published by Irrigation Management and Training Institute, Tamilnadu, 1987.
[13] C.R.Shanmugham and R.Sakthivadivel, An action research study on modernising a tank irrigation system in Tamilnadu, CWR, Anna University, 1988.

E-ISSN 2581 – 7957
P-ISSN 2277 – 3916

CVR Journal of Science and Technology, Volume 22, June 2022
DOI: 10.32377/cvrjst2222

Flexural Behavior of Self compacting Concrete Beams Partially replacing Conventional aggregate with Pumice Aggregate

T. Vijay Kumar[1] and N. Ramanjaneyulu[2]
[1] PG Scholar, CVR College of Engineering/Civil Engg. Department, Hyderabad, India
Email: vijaykumarthippani@gmail.com
[2] Asst. Professor, CVR College of Engineering/Civil Engg. Department, Hyderabad, India and
Research Scholar, JNTUA College of Engineering/Anantapuram
Email: rams.613@gmail.com

Abstract: **In the present research work, an attempt was made to study the flexural cracking behavior of self-compacting concrete beams partially replaced with lightweight pumice aggregate with various proportions viz-10%,20%,30%,40% and 50% by its volume of natural coarse aggregate (NCA) and studied fresh properties of lightweight self-compacting concrete (LWSCC). As per the European federation of national associations representing for concrete (EFNARC) guidelines, all results are with in permissible limits. The workability tests utilized in this research work were the flow table, L-box, V-funnel, J-ring tests, which can evaluate the filling ability, passing ability and segregation resistance of self-compacting concrete. This research study studied flexural crack behavior and maximum strength of five beams of size 200*230*1000mm. In addition, observed maximum deflections and peak load also studied the P/ Δcurve. As a result, it was determined that the ultimate load bearing capacity of the lightweight beam flexural elements drops up to 24.5% compared to conventional beam.**

Index Terms: **self-compacting concrete, light weight aggregate, beams.**

I. Introduction

Professor Hajme Okamura's discovery of Self Compacting Concrete (SCC) in 1986 had a big impact on the construction industry because it solved some of the problems with fresh concrete. Worker skill, reinforcing complexity, structural section type and shape, pump capability, segregation resistance, and, most critically, compaction are all addressed by the SCC in its current configuration. It has been proven that self-compacting concrete with high fines content is more durable.

Over the last few decades, self-compacting concrete has become a significant advancement in concrete technology. In the presence of congested reinforcement, SCC is described as a concrete that flows under its own weight without the requirement for vibration for placement and compaction.

Increased productivity, more uniform and cohesive material with few or no honeycombs, improved strength and durability characteristics, good finish, adaptability in congested reinforced sections, reduction in the size of structural members, and so on are some of the benefits of SCC over traditional concrete. SCC improves the workplace environment by removing noise pollution and producing a safe environment for formwork due to the elimination of compaction caused by vibration, resulting in a pleasant working environment.

Light weight concrete

New forms of high-performance concretes, such as self-compacting concrete (SCC) and lightweight concrete (LWC), have been developed to meet some of the building industry's needs. Lightweight concrete has a long history of use and is well-known for its performance and durability. The dead load of a concrete structure is significant in structural applications because it accounts for a significant fraction of the overall load. LWCs provide other advantages over normal-weight concrete, such as greater fire resistance and thermal insulation, due to their lighter weight.

Natural light weight aggregate and artificial light weight aggregate are the two types of light weight aggregate available. Pumice, diatomite, scoria, volcanic cinders, sawdust, and rice husk are examples of natural light weight aggregate. Artificial cinders, coke breeze, foamed slag, bloated clay, inflated shale and slate, sintered fly ash, and exfoliated vermiculate are examples of artificial lightweight aggregate.

Pumice aggregate

Pumice is a common volcanic rock that is utilized as a lightweight aggregate and can be found all over the world. It only retains its useful features when it is young and undamaged. The low density is owing to the fact that their cells have holes generated by gases expanding as pressure is released. It was initially used by the Romans in the second century, when they built 'The Pantheon' out of pumice.

Figure1. Pumice Lightweight Aggregate

Pumice stone is a light, low-specific-gravity aggregate. Because it is a highly porous material, it may absorb up to 55 percent of water. We won't be using the traditional aggregates of sand as fine aggregate and pumice as coarse aggregate; instead, we'll be using pumice stone.

Received on 12-10-2021, Revised on 28-11-2021, Accepted on 21-12-2021.

II. Literature Review

Fiber reinforced pumice aggregate self-compacting concrete by M. I. Kaffetzakis, C.G. Papanicolaou (2011). The goal of this work is to report experimental data related to the creation of self-compacting structural fiber reinforced pumice aggregate concrete. The addition of fibers to lightweight aggregate concrete mixtures mitigates the brittleness associated with this concrete family. The study looks at the impact of several fiber types (polypropylene or steel, with varied aspect ratios) on the material's properties in both the fresh and hardened states, while keeping the fiber content constant. Steel fibers (30 mm and 60 mm long) and polypropylene fibers (25 mm and 50 mm long) were the two types of fibers employed in this investigation. To analyse the toughness properties of all PASCC mixes, four-point bending tests on prismatic specimens (measured 100x100x400mm) were performed (in accordance with the ASTM C1018-97 standard). Both compressive strength and modulus of elasticity were unaltered by fiber addition, as expected. In fiber-free mixes, replacing pumice sand with regular weight sand increases both compressive strength and modulus of elasticity (by 35 percent and 40 percent , respectively). Tests all mixtures measured oven- dry densities less than 1800 kg/m3. With a density 33 percent lower than that of regular weight river sand, the inclusion of 30mm steel fibers and the replacement of pumice sand with normal weight river sand enhance self-compactness, workability retention, and energy absorption capacity. SCC [1].

Mechanical and fresh properties of fiber reinforced self- compacting lightweight concrete by T. Gonen (2015),. Fiber Reinforced Self-Compacting Lightweight Concrete (FRSCLC) workability and mechanical properties were explored in this study. Steel fiber with low and high carbon content was used to make concrete samples. The fluidity of FRSCLC was tested using two types of flow ability: fresh concrete property and viscosity. Short and long-term tests, including compressive and flexural strength at 3, 7, 28, and 365 days, were used to determine the mechanical performance of the concrete mixes. According to the findings, adding fibres to self-compacting lightweight concrete mixtures reduces their workability. Compressive strength, on the other hand, did not improve as much as flexural strength did. As a result, by adding fibre at 28 days, the compressive and flexure strength of SCLWC's rose by 30 and 43 percent, respectively. [2].

Basic Properties of Pumice Aggregate by R S Muralitharan AND V Ramasamy (2015) Because of its advantages over ordinary concrete, the use of lightweight concrete for construction projects has exploded in recent years. Pumice breccias are proposed to be used as the coarse aggregate in this experiment. The primary goal of structural grade light weight concrete is to minimise self-weight and make it easier to build larger precast units. Pumice can be used to make light weight concrete with a dry density of 1200 kg/m3 to 1450 kg/m3. At this time, there has been a significant amount of effort done to investigate the mechanical properties of lightweight aggregate concrete. For all types of lightweight aggregate concrete and at various ages of curing, compressive strength, splitting tensile strength, acid resistances, and heat resistances were examined. Reduced mass, increased thermal and acoustic insulation capabilities, and optimal strength maintenance are all advantages of lightweight concrete. The many engineering qualities of pumice, as well as material test findings, must be investigated. [3].

Flexural behaviour of self-compacting concrete beams by R Manju, Dr. J. Premalatha, R Shanthi, V Aishwaryalakshmi(2017) The combined influence of cementitious materials (Fillers) on the fresh and hardened properties of Self Compacting Concrete is investigated in depth in this article (SCC). The study involves a mixture of Ordinary Portland Cement (OPC) and Fly Ash (FA), in which OPC is partially substituted with a percentage of FA (25 percent, 30 percent, 35 percent, 40 percent, and 45 percent). Ordinary Portland Cement (OPC) was replaced with 20% Fly Ash (FA) by the weight of OPC in the Control mixture. The use of fillers (FA) lowered cement hydration and improved concrete cohesiveness. For all of the mixtures, a total binder content of 550 kg/m3 and a water binder ratio of 0.34 were used as constants. The experimental research of fresh properties such as Slump flow test, L Box, U Box, V funnel, and T50 time, as well as hardened properties such as Compressive strength, Split tensile strength, and Flexure strength of beams for all the mixtures were presented in this work. Based on the findings, the optimal FA replacement percentage as well as the flexural behaviour of beams was investigated. The blend with 35% FA, on the other hand, outperforms all other mixes. [4].

III. Experimental Programme

This experimental program is aimed to find out the behavior of self-compacting concrete produced using pumice lightweight aggregate replacing 10%, 20%, 30%, 40% and 50% of normal coarse aggregate. Fresh properties and the flexural strength behavior of light weight self-compacting beams at 28 days are investigated for M40 grade SCC.

Objectives

- To design SCC mix M40 by partially replacing the coarse aggregate with Pumice aggregate.
- To find out the fresh and hardened properties of LWSCC (lightweight aggregate self-compacting concrete).
- To study the flexural behaviour of reinforced SCC beam and compared with partially replaced pumice aggregate reinforced SCC beam.
- To reduce the self-weight and density of the structures.

IV. Material and Properties

Cement

Ordinary Portland cement of 53 grades available in local market was used in this present investigation which conforms IS 12269-1987". The cement used for the mix is tested for various properties based on IS: 4031-1988 and for all the tests the cement is taken from the same batch and with a specific gravity of 3.1 conformed to IS 8112-2013.

CVR Journal of Science and Technology, Volume 22, June 2022
DOI: 10.32377/cvrjst2222

Fine aggregates

River Sand used is locally available and was conforming to zone II with Specific gravity as 2.59. Moisture content and water absorption is 0.1% and 1.0% respectively.

Coarse aggregates

Locally available crushed angular coarse aggregate having the maximum size of 20 mm is used. The specific gravity of coarse aggregate is 2.64. Moisture content and water absorption is 0.5% and 2.0% respectively.

Fly ash

Fly ash is a by-product of pulverized coal combustion product that is composed of the particular (fine particles of burned fuel) that are driven out of coal-fired boilers together with the flue gases. Ash that falls to the rock bottom of the boiler's combustion chamber (commonly known as firebox) is named as bottom ash. Fly ash with specific gravity is 2.1.

Super plasticizer

Super plasticizers are the high range water reducers which are used to improve the workability of concrete at lower water cement ratios. Addition of super plasticizers to the concrete mix reduces water-cement ratio, increases strength, improves the flow of concrete and avoid segregation. In the present study, the super plasticizer used is "CONPLAST SP 430." Conplast SP 430 which helps in reducing water content Specific gravity is 1.2.

Water

Potable tap water is used for the preparation of specimens and for curing specimens.

V. Mix Proportions and Mix Designations

The mix proportions for M40 grade concrete is as shown below.

TABLE I.
MIX DESIGN DETAILS

Description	Quantity (Kg/m^3)	Ratio
Cement	468	1
Fly ash	350	0.745
Fine aggregate	885	1.891
Coarse aggregate	700	1.495
Water	240	0.512
Sp	12.2	0.026

TABLE II.
DESIGNATIONS OF MIXPROPORTIONS

MC	Control mix
MP10	Beam with 10% pumice (By volume of CA)
MP20	Beam with 20% pumice (By volume of CA)
MP30	Beam with 30% pumice (By volume of CA)
MP40	Beam with 40% pumice (By volume of CA)
MP50	Beam with 50% pumice (By volume of CA)

VI. Experimental Test Procedure

Based on the requirements of the rational mix design approach, the mix is created for M40 grade concrete. The many cases of mix proportions are as follows. In MP10, MP20, MP30, MP40, and MP50, pumice replaces coarse aggregate in 10 percent, 20 percent, 30 percent, 40 percent, and 50 percent of the time, respectively. The specimens are casted and cured for 28 days in water. The specimens were then put through their paces on a load frame machine to determine flexural strength, load vs. deflection curves, and crack behavior.

Methods of Evaluation of Workability of SCC

Workability tests for conventional concrete mixes are insufficient for determining the workability of Self-Compacting Concrete mixes since they are not sensitive enough to determine all of the requirements. To characterize the fresh qualities of SCC blends, various test procedures were devised. To date, no one method for assessing relevant workability requirements has been available. As a result, the SCC mixes must be examined using many tests to determine various workability characteristics. The test techniques listed below can be used to characterize desirable workability requirements and to finish new Self-Compacting Concrete mixtures.

Slump flow test and T50 cm test

The slump flow test is used to ascertain the free flow of Self Compacting Concrete without obstructions.

Figure 2. Slump Flow T50 cm test

J-ring test

This test method provides a procedure to determine the passing ability of self-compacting concrete mixtures

Figure 3. J-Ring test

L-box test

The test is for assessing the flow of the SCC and the blocking resistance.

Figure 4. L-Box test

V-funnel test

This test is performed to determine the filling ability (flow ability) of the Self-Compacting Concrete.

Figure 5V-Funnel test

Flexural strength test

Flexural strength is to measure the tensile strength of concrete which helps in assessing the failure of beam or slab in bending. It is measured by applying a load of 100kN on 200mmx230mmx1000mm specimen. For this research work, I have used the load frame of capacity 1000KN (100 tons) axial jack and 200KN (20 tons) lateral with LVDT arrangements

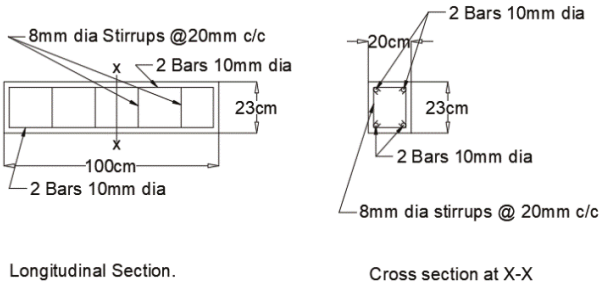

Figure 6. Reinforcement details in beams

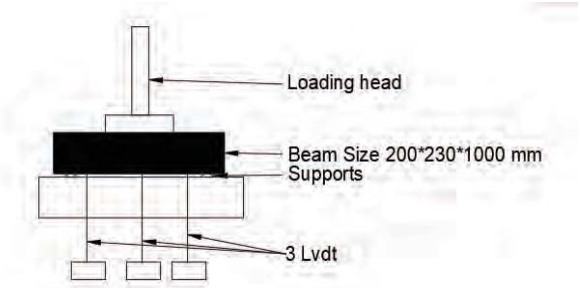

Figure 7 Experimental set up for flexure test of beams

VII. Results and Discussons

TABLE III.
Fresh Concrete Properties of Pumice Aggregate Concrete

Description	Slump flow (mm)	T50 (sec)	J-Ring(cm)	L-Box	V-Funnel (sec)	T5 (sec)
Limits	**650*800**	**2-5**	**0-10**	**0.8-1**	**6-12**	**9-15**
MC	780*770	4.25	9.8	0.98	6.51	9.75
MP10	770*770	4.49	9.5	0.96	6.83	11.32
MP20	750*750	5.07	9.2	0.94	10.72	13.25
MP30	700*700	5.45	9	0.93	10.99	14.16
MP40	690*710	6.5	8.6	0.88	11.12	14.56
MP50	670*650	9.92	8.4	0.85	12.35	15.3

TABLE IV.
Peak Loads for Beams Obtained from Load Frame

Beam	Peak load(KN)
MC	209.7
MP10	195.4
MP20	181.9
MP30	179.4
MP40	172.1
MP50	158.4

From the table we can observe that with increase in the percentage of pumice aggregate content there is reduction in the maximum load carrying capacity of beams.

TABLE V.
Stiffness Values for Beams

Beam	Stiffness value(KN/mm) at centre	Stiffnessvalue(KN/mm) 200mm from right	Stiffnessvalue(KN/mm) 200mm from left
MC	19.78	12.55	14.46
MP10	15.26	9.77	11.842
MP20	9.328	5.334	6.942
MP30	7.834	4.485	5.805
MP40	5.295	3.749	4.197
MP50	5.245	3.729	4.168

From the table it is observed that with increase in pumice content in the RC beams there is gradual reduction in the values of P/Δ due to the increased deflections in the pumice replaced self-compacting concrete beams.

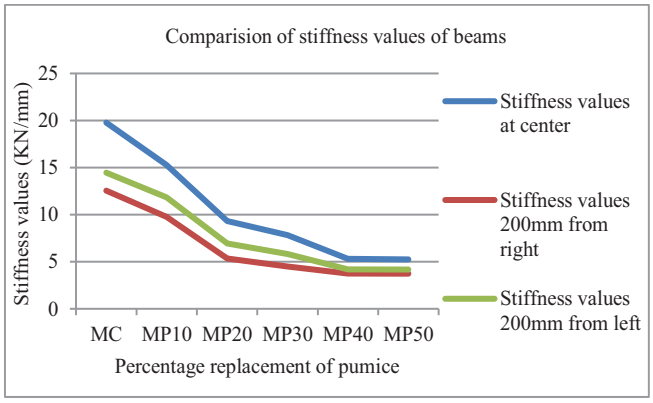

Figure 8.Comparision of stiffness values of beams

CVR Journal of Science and Technology, Volume 22, June 2022
DOI: 10.32377/cvrjst2222

Load vs. deflection curves

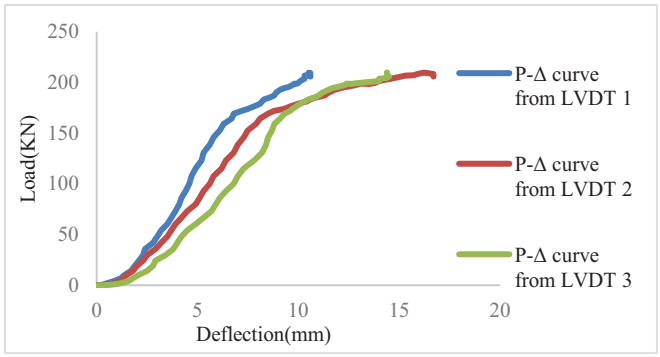

Figure 9. Load vs. deflection curves for MC beam

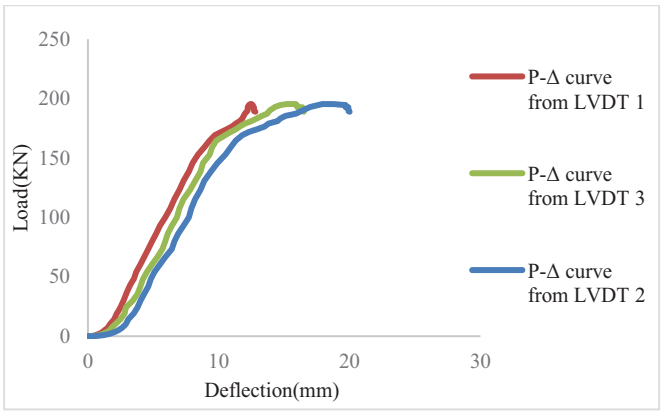

Figure 10. Load vs. deflection curves for MP10 beam

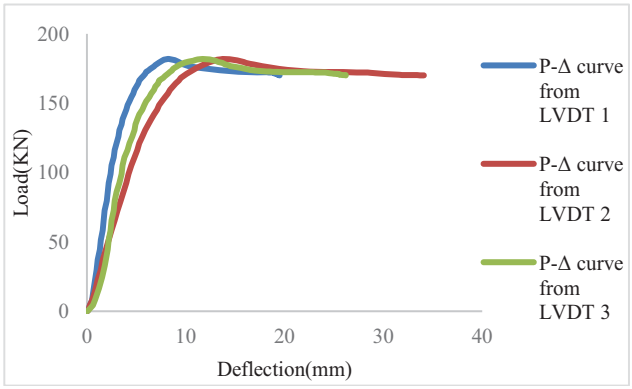

Figure 11. Load vs. deflection curves for MP20 beam

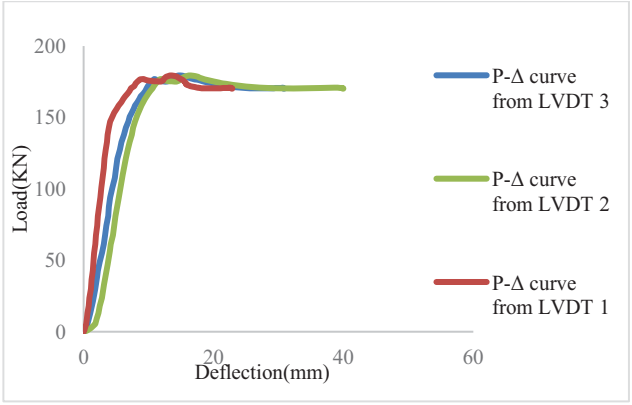

Figure 12. Load vs. deflection curves for MP30 beam

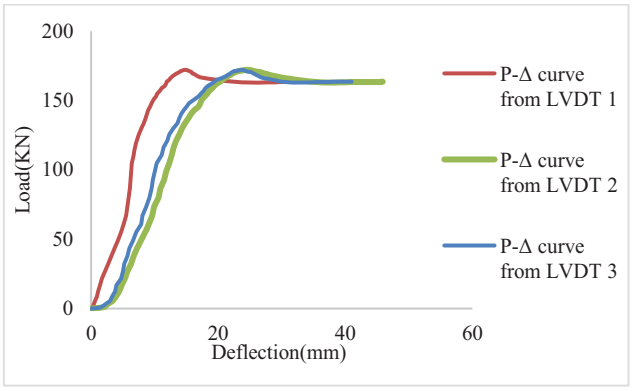

Figure 13. Load vs. deflection curves for MP40 beam

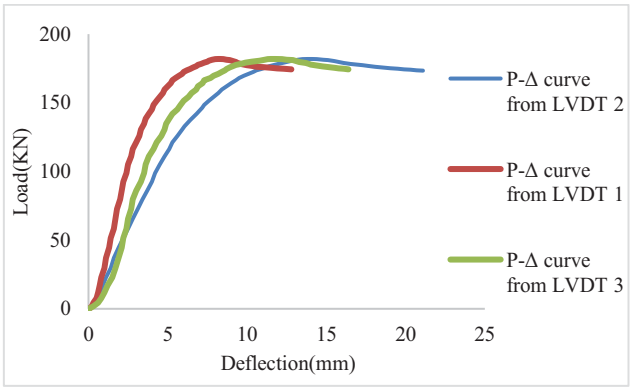

Figure 14. Load vs. deflection curves for MP50 beam

Load vs deflection curves shows that with increase in the percentage of pumice replacement in self compcting concrete beams there is reduction in the maximum load carrying capacity of beams and increase in the delection of beams.

TABLE VI.
DENSITIES OF PUMICE REPLACED CONCRETE

Beam	Density(Kg/m^3)
MC	2305
MP10	2256
MP20	2205
MP30	2156
MP40	2105
MP50	2056

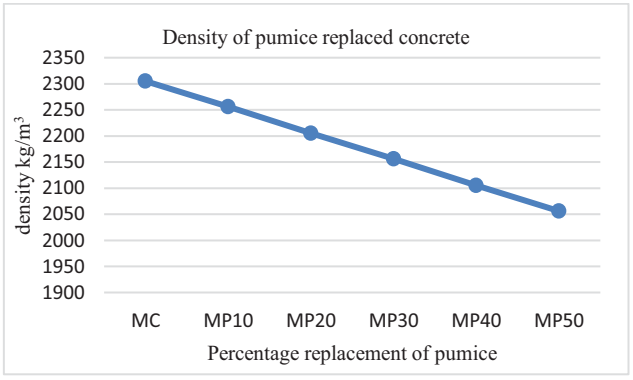

Figure 15. Densities of pumice replaced concrete

CVR Journal of Science and Technology, Volume 22, June 2022
DOI: 10.32377/cvrjst2222

From the graph it was found that the densities of self-compacting concrete reduced gradually with 10%, 20%, 30%, 40% and 50% replacement ofcoarse aggregate with pumice aggregate. This is due to the less weight of pumice aggregate compared to normal coarse aggregate.

Cracking pattern of beams

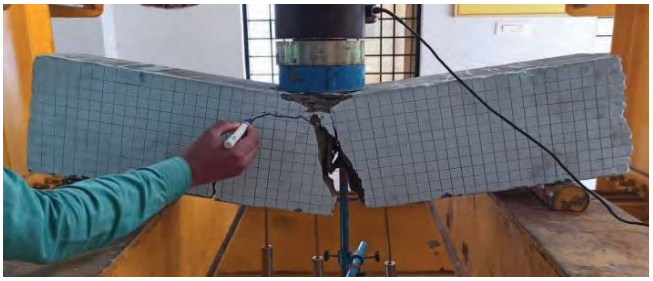

Figure 16. Crack pattern of beam MC

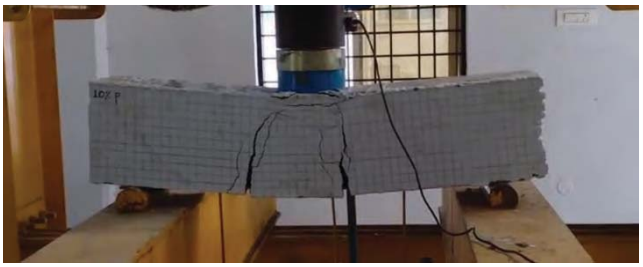

Figure 17. Crack pattern of beam MP10

Figure 18. Crack pattern of beam MP20

Figure 19. Crack pattern of beam MP30

Figure 20. Crack pattern of beam MP40

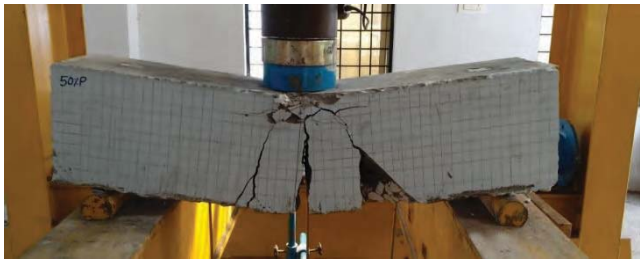

Figure 21. Crack pattern of beam MP50

From the figures we can observe that only flexure cracks and flexure shear cracks were developed. There were no web shear cracks developed in beams.

TABLE VII.
CRACK WIDTH VALUES

Beam	Width of crack (mm)
MC	1
MP10	1
MP20	1.25
MP30	1.55
MP40	1.75
MP50	2

From the table we can observe that width of crack was increased with increase in percentage replacement of pumice aggregate because of the less load carrying capacity of beams.

VII. CONCLUSIONS

- The filling ability, passing ability and segregation resistance of all SCC mixes with Pumice conform to EFNARC guidelines.
- The results obtained found that the densities of self-compacting concrete reduced gradually with 10%, 20%, 30%, 40% and 50% replacement of coarse aggregate with pumice aggregate.
- The reduction in density of lightweight self-compacting concrete is about 10.8% compared to density of conventional self-compacting concretefor 50% replacement.
- The increase in percentage of pumice lightweight coarse aggregate is shown reduction in the flexural strength of concrete.
- The result determined that the ultimate load-bearing capacity of the light weight beam flexural elements drops up to 24.5% compared to conventional beam for 50% replacement.
- Width of cracks increased with increase in percentage replacement of pumice aggregate.

REFERENCES

[1] M.I.Kaffetzakis,C.G.Papanicolaou,“Fiber reinforced pumice aggregate self compacting concrete”
[2] T. Gonen(2015), “Mechanical and fresh properties of fiber reinforced self- compacting lightweight concrete”

[3] Romildo Dias Toledo Filho, GuilhermeChagasCordeiro, ThiagoMeloGrabois(2016), " Fresh and hardened-state properties of self-compacting light weight concrete reinforced with steel fibers"
[4] Hugo Costa,Dina A. Esteves,Eduardo Julio, Tiago Simoes(2012), "Design and characterization of self compacting fibre-reinforced light weight aggregate concrete"
[5] HanaaFares;HoussamToutanji,; Kristopher Pierce, and Albert Noumowé (2015), "Lightweight Self-Consolidating Concrete Exposed to Elevated Temperatures", American Society of Civil Engineers.
[6] ShahidIqbala,AhsanAli,KlausHolschemacher,Thomas A. Bier (2015), "Mechanical properties of steel fiber reinforced high strength light weight self- compacting concrete(SHLSCC)"
[7] H.Mazaheripour,S.Ghanbarpour,S.H.Mirmoradi,I.Hosseinpour (2011), "The effect of polypropylene fibers on the properties of fresh and hardened lightweight self- compacting concrete"
[8] N. Bozkurt (2014), "The High Temperature Effect On Fibre Reinforced Self Compacting Lightweight Concrete Designed with Single and Hybrid Fibres"
[9] R.Vengadesan, S.Divya, S.Vijipriya, R.Anbarasi (2016), "Experimental Study on Flexural Behavior of Self Compacting Concrete using Steel Fiber"
[10] R S MURALITHARAN AND V RAMASAMY (2015) "Basic Properties of Pumice Aggregate"
[11] SlametWidodo, ImanSatyarno, Sri Tudjono (2014) "Experimental study on the potential use of pumice breccia as coarse aggregate in structural lightweight concrete"
[12] Shijumon. V, Nalanth. N (2019) "Flexural Behaviour of Self Compacting Concrete Beams Modified using Recycled Concrete Waste Aggregates"

E-ISSN 2581 – 7957
P-ISSN 2277 – 3916

CVR Journal of Science and Technology, Volume 22, June 2022
DOI: 10.32377/cvrjst2223

The Productivity of Compost in Drums with Varying Proportions of Food Waste Along with Bulking Agents

K. Ravi Chandra Reddy
Asst. Professor, CVR College of Engineering/ Civil Engg. Department, Hyderabad, India.
Email: krc.reddy@cvr.ac.in

Abstract: **Composting is a form of waste disposal where organic waste decomposes naturally under oxygen-rich conditions. Once the waste items are placed in a pile, the composting process commences. Organic materials are broken down naturally by bacteria, earthworms, and other organisms. In this paper, an attempt is made to make the compost from the food waste generated from the Cafeteria, CVR College of Engineering. Composting Study is performed on vegetable waste, fruit waste, and tree leaves. All the sources of waste are from the Canteen, CVR College of Engineering Campus. The composting study was conducted on a rotary drum composter by finding the physical and chemical characteristics of the compost. Experiments are conducted to find out the Nitrogen (N), Phosphorous (P), and Potassium (P) (NPK) values, Electrical conductivity, moisture content of the final product i.e., Compost. Temperatures are observed throughout the work to identify the better combinations of compost (i.e., fruit waste, cattle dung, and sawdust) to produce the quality compost. and temperatures are observed to identify the better combinations of compost to produce the quality compost.**

Index Terms: Compost, Food waste, Organic matter, Cafeteria's waste, Manure, Mixed Waste.

I. Introduction

Every day, around 1.13 million tons of Food Waste (FW) are thrown globally [1]. As a result, there are a variety of FW repercussions on the environment, economy, and community, including GHG emissions and groundwater contamination [2,3]. Animal feeding, anaerobic/aerobic digestion, composting, pyrolysis, gasification, incineration, and landfill disposal are just a few of the treatment options for FW [4-9]. Landfills and composting are the most common treatment options in developing nations, accounting for 90–96 percent of total FW disposal [10].

The efficiency and quality of the composting process are influenced by several factors, including the properties of the starting materials, operational circumstances, and maturation time [11].

II. Materials and Methods:

A. Sampling:

Organic waste generated from the Canteen of CVR College consists of food waste, vegetable waste, and fruit peelings. Dried leaves and sawdust are added to the food waste and fruit peelings and together called mixed waste (MW).

B. Design of drum:

The composting was carried out in four plastic drums of 100 L capacity. Four drums are modified for free air circulation by providing 1 cm diameter holes are made over the drum with a distance of 5cm apart from the supply of oxygen into the drum. A 10cm square window has been made over the drum in order to input the organic waste and to monitor regularly. Concrete blocks were placed on the ground with an equidistance of 30cm and drums are placed on the blocks which make it easy for turning the drums. Leachate collection is also provided at the bottom of the drum to collect the wastewater generated from the pile. The image of the modified drum is shown in Figure 1.

Figure 1. Image of the modified drum

C. Composting process:

The experiment was carried out in the open space located at the back of the Environmental Engineering laboratory, CVR College of Engineering. The drums were placed on the concrete blocks and plastic tray provided below the drum to collect the leachate. In this study, around 50kg of food waste was used in the drums with varying mixed proportions along with the bulking agent. In the Drum-1, it was mixed with 15kg of MW along with 5kg of sawdust (bulking agent). In the Drum-2, it was mixed with 20kg of MW along with 5kg of sawdust. In the Drum-3, 10kg of MW along with 2.5kg of sawdust and mixed 2.5kg of cow dung as an accelerator to speed up the process. In the Drum-4, 12kg of MW along with 3kg sawdust.

Mixed waste for the drums is selected based on the moisture content. It is observed from the literature that moisture content between 40-60% is good for composting

Received on 27-10-2021, Revised on 28-02-2022, Accepted on 24-03-2022

CVR Journal of Science and Technology, Volume 22, June 2022
DOI: 10.32377/cvrjst2223

process. Moisture content is important because it reduces the odor from the waste pile in turn reduces the flies around it. The moisture content of the waste sample is the key indicator for choosing the waste proportions. Laboratory sample and field sample Mixed proportion values are mentioned in Tables I and II.

TABLE I.
LABORATORY SAMPLE RESULTS

Waste quantity	Moisture Content	Suitable/ Not suitable
10g crushed rice	71%	Not Suitable
10g mixed food waste	65%	Suitable
8g rice+ 2g dried leaves	57%	suitable
80g rice+20g dried leaves	62.5%	Suitable
80g rice+ 20g sawdust	60.7%	Suitable

TABLE II.
FIELD SAMPLE RESULTS

Waste Quantity	Mix Proportion	Drum
15kg mixed waste and 5kg sawdust	3:1	Drum 1
20kg mixed waste and 5kg sawdust	4:1	Drum 2
10kg mixed waste, 2.5kg sawdust and 2.5kg cow dung	4:1:1	Drum 3
12kg mixed waste, 3kg sawdust	4:1	Drum 4

III. LITERATURE REVIEW

Ashok and Santhosh More analyzed that the addition of additives was to help enhance the composting process [12]. Gonawala and Hemali found out that compost has many benefits such as reducing the landfill space, reducing surface and groundwater contamination, and also reducing methane emissions [13]. Jara and Murica showed that compost obtained was the absence of phototoxicity and appropriate agronomic properties for their use as fertilizers and compost obtained has significant economic value in nutrients that could be internalized in the final compost price [14]. Manu and Garg studied the kinetics of the compost and found out that regular turning of waste is an important activity to achieve better microbial degradation of a biodegradable waste fraction [15].

IV. METHODOLOGY

In the present work, food waste is shredded into small pieces, small pieces are added to the drum with different waste proportions and allowing sufficient time to obtain the maturity of the compost. In the end, conducting laboratory tests to analyze the quality of the final product i.e., compost. The whole process is explained in Figure 2.

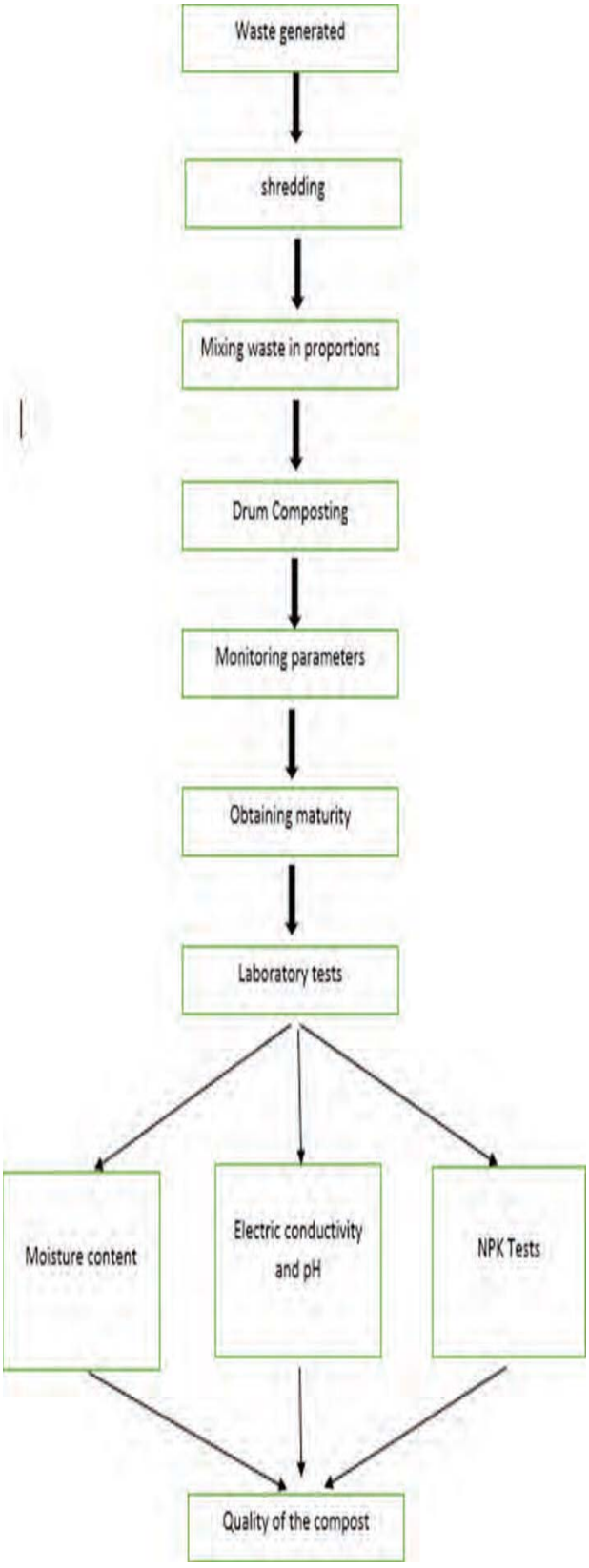

Figure 2. Methodology

E-ISSN 2581 – 7957
P-ISSN 2277 – 3916

DOI: 10.32377/cvrjst2223

V. Results and Discussion

A. Temperature:

Composting process is regularly monitored, and the temperature of the compost bed is recorded daily using a thermometer. The details of the temperature of each drum for the 30 days period are mentioned in table III.

TABLE III.
DAILY TEMPERATURE IN DRUMS

Day	Drum 1	Drum 2	Drum 3	Drum 4
01	28ºC	28ºC	35ºC	35ºC
05	50ºC	44ºC	50ºC	50ºC
10	51ºC	49ºC	41ºC	53ºC
15	59ºC	46ºC	38ºC	39ºC
20	47ºC	50ºC	40ºC	35ºC
25	41ºC	40ºC	32ºC	32ºC
30	34ºC	35ºC		

A square window of 10cm is made on the drum to measure temperature daily using a thermometer. In this experiment, four drums are used and each one of the drums is measured daily. The addition of mixed waste and bulking agents have shown significant improvement in achieving the compost quickly. It can be noticed in drum 3 and drum 4 from table III. The results of all the drums are shown in Figure 3.

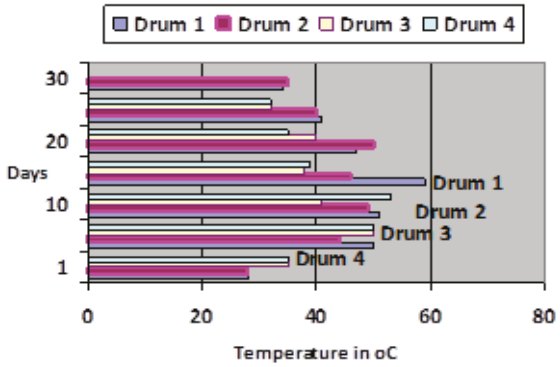

Figure 3. Temperature in the drums

B. pH:

pH is one of the factors affecting the compost. The pH of all the drums compost was measured using a pocket pH meter and the values are mentioned in Table IV. Generally, the compost pH range is between 5-8. Soils having pH values between 6-7.5 are good for cultivating agricultural crops. pH values for drum 3 and drum 4 were optimum i.e., nearer to neutral, and shown in Figure 4.

TABLE IV.
PH VALUES OF THE COMPOST

Drum	pH readings
1	7.6
2	7.7
3	7.4
4	7.2

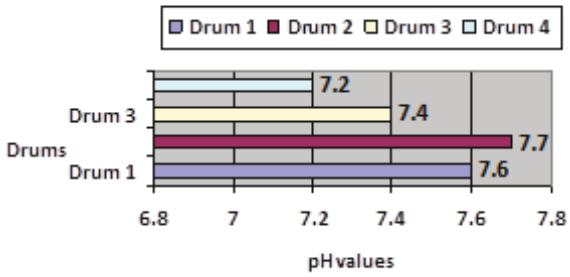

Figure 4. pH Values in the drums

C. Electrical Conductivity:

Electrical Conductivity (EC) is a measure of the number of salts in compost. It is an important indicator of compost health. Electrical conductivity values of the compost were shown in table V. Optimum Electrical Conductivity of the soil is between 115-570 milli Siemens per meter (mS/m). Too low EC values indicate low availability of nutrients and too high EC values indicate an excess of nutrients in the compost. The results of the compost drums are shown in Figure 5.

TABLE V.
ELECTRICAL CONDUCTIVITY OF COMPOST

Drum	Electrical Conductivity (mS/m)
1	470
2	462
3	466
4	399

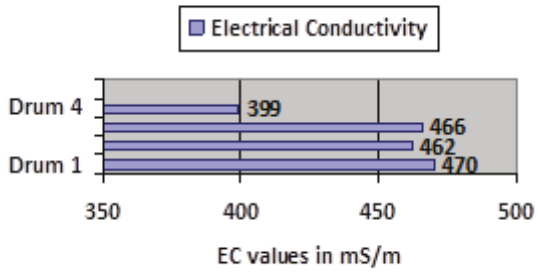

Figure 5. EC of the Compost

D. *Moisture Content:*

Moisture content is an indicator of the amount of water available in the soil. Moisture meters give the values immediately, but they are said to be lack accuracy. So, it is preferred to measure using oven drying. The moisture content of the compost values is mentioned in table VI. Values were calculated by drying the compost at 110ºC for 24 hours and the same results were shown in Figure 6.

TABLE VI.
MOISTURE CONTENT OF COMPOST IN THE DRUMS

Drum	Moisture Content (%)
1	51
2	49
3	57
4	52

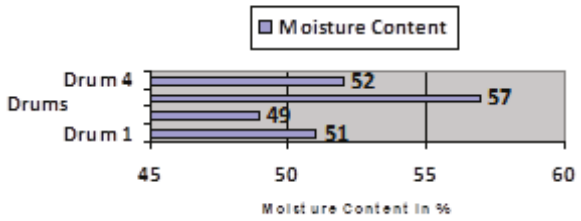

Figure 6. Moisture Content of the Compost

E. NPK Value test:

NPK value test is very important to determine the quality of the compost as Nitrogen, Potassium, and Phosphorous values in the compost are important for plant growth. In this experiment, the NPK test is conducted by using a soil doctor plus kit. Nitrogen is part of chlorophyll. Nitrogen makes plants green and is a key component in photosynthesis. It's vital for stem and leaf development, converting the energy of the Sun into sugars and overall plant growth. Compost NPK values are mentioned in Table VII. The NPK results of the compost drums were shown in Figure 7.

TABLE VII.
NPK VALUES OF THE COMPOST

Drum	NPK ratio
1	1.5:0.75:1.75
2	1.5:0.35:3.75
3	2:0.5:1.5
4	1.5:1:2

Figure 7. NPK Soil doctor kit

F. Comparisons and Observations:

- Drum 3 has obtained the compost in less time because cow dung acted as an accelerator.
- Drum 1 & 2 has the longest processing time as the bulking agent was not shredded.
- All the drums have a pH in the range of 5.5-8.0 indicating the compost is neutral in nature.
- All the drums have less electrical conductivity indicating less salinity which is suitable for plant growth.
- Drums 1 & 2 have less phosphorous content due to improper shredding and mixing of agents which is a poor substitute for a balanced fertilizer.
- Drums 3 & 4 have the proper NPK ratio due to proper mixing and shredding of bulking agents.

VI. CONCLUSIONS

An effort has been made to convert the mixed food waste into Compost from the Cafeteria of CVR College of Engineering. Physical parameters of the compost i.e., temperature, moisture content, etc., are monitored regularly to ensure the quality of the compost. It was observed that food waste along with the bulking agents and regular turning of the drum improved the efficiency of the compost. The addition of Cow dung accelerated the process of composting, and the compost has been achieved in less time with superior quality.

.

REFERENCES

[1] Chen, C., Chaudhary, A., Mathys, A "Nutritional and environmental losses embedded in global food waste". Resour. Conserv. Recycl. (2020)
[2] Malamis, D., Bourka, A., Stamatopoulou, E., Moustakas, K., Skiadi, O., Loizidou, M "Study and assessment of segregated biowaste composting: the case study of Attica municipalities". J. Environ. Manag. (2017)
[3] Scherhaufer, S., Moates, G., Hartikainen, H., Waldron, K., Obersteiner, G "Environmental impacts of food waste in Europe". Waste Management (2018).
[4] Mo, W.Y., Man, Y.B., Wong, M.H "Use of food waste, fish waste and food processing waste for China's aquaculture industry: needs and challenge". Sci. Total Environ(2018).
[5] Wainaina, S., Awasthi, M.K., Sarsaiya, S., Chen, H., Singh, E., Kumar, A., Ravindran, B., Awasthi, S.K., Liu, T., Duan, Y "Resource recovery and circular economy from organic solid waste using aerobic and anaerobic digestion technologies". Bioresource. Technol(2020).
[6] Cesaro, A., Conte, A., Belgiorno, V., Siciliano, A., Guida, M "The evolution of compost stability and maturity during the full-scale treatment of the organic fraction of municipal solid waste". J. Environ. Management (2019).
[7] Kim, S., Lee, Y., Lin, K.-Y.A., Hong, E., Kwon, E.E., Lee, J "The valorization of food waste via pyrolysis: a review". J. Clean. Prod(2020).
[8] You, S., Wang, W., Dai, Y., Tong, Y.W., Wang, C.H "Comparison of the co-gasifi- cation of sewage sludge and food wastes and cost-benefit analysis of gasification-and incineration-based waste treatment schemes". Bioresour. Technol(2016).

[9] Goodman-Smith, F., Mirosa, M., Skeaff, S "A mixed-methods study of retail food waste in New Zealand". Food Policy(2020)
[10] Thi, N.B.D., Kumar, G., Lin, C.Y "An overview of food waste management in de- veloping countries: current status and future perspective". J. Environ. Management (2015).
[11] Soto-Paz, J et al. "Influence of mixing ratio and turning frequency on the co-composting of biowaste with sugarcane filter cake: a mixture experimental design". Waste and Biomass Valorization(2019b).
[12] Ashok More, Santosh More "Enriched Rapid Composting Techniques for Agro Industrial Organic Solid Waste". IJITEE(2019)
[13] Suhas S. Gonawala and Hemali Jardosh "Organic Waste in Composting:A brief review" . IJCET(2018).
[14] Jara-Samaniego et al "Development of organic fertilizers from food market waste and urban gardening by composting in Ecuador". PLoS One(2017).
[15] M.K. Manu, R. Kumar, A. Garg "Drum Composting of Food Waste: A Kinetic Study" ,Procedia Environmental Sciences(2016).

E-ISSN 2581 – 7957
P-ISSN 2277 – 3916
CVR Journal of Science and Technology, Volume 22, June 2022
DOI: 10.32377/cvrjst2224

Assessment of Pre and Post Retrofitting Performance of a RCC Framed Building

Siricilla Spandana[1] and Tangudu Manoj[2]
[1]PG Scholar, CVR College of Engineering/ Civil Engg. Department, Hyderabad, India
Email: Spandanasiricilla12@gmail.com
[2]Asst. Professor, CVR College of Engineering/Civil Engg. Department, Hyderabad, India
Email: Manoj.tangudu03@gmail.com

Abstract: **Most of the structures constructed were found to have a seismic imbalance. They do not satisfy the present-day codes. In multistoried buildings, the lateral forces caused by seismic activities constitute severe thrift. Structural elements such as beams and columns can only resist the vertical loads effectively, but they cannot sustain heavy lateral loads. Demolishing the existing structure and constructing the seismic-resistant system with the present code of requirements is impossible as it is uneconomical and undesirable. Hence the existing structure needs to be strengthened by alternative methods instead of demolition. One such way is seismic retrofitting.**

This project, an existing G+13 storied building, is modeled using structural analysis and design software ETABS. The seismic approaches such as response spectrum analysis and time history analysis are performed. Based on the response spectrum and time history analysis, the weak areas of existing buildings are to be identified, and retrofitting is done. Seismic retrofitting using shear walls and different bracing systems at other locations of weak areas based on the response spectrum analysis and time history analysis is proposed for the safety of the existing building. The project focuses on examining the seismic responses in terms of various parameters such as base shear, story displacement, and the effect of forces on the structure with the help of dynamic analysis. The performance of the building to satisfy the current code requirements is checked based on the results obtained from the seismic analysis. The study also incorporates strengthening an existing deficient building using shear walls and bracings at different locations. Further, the effectiveness of the bracings and shear wall in enhancing the structure is studied.

Index Terms: **Moment resistance, Shear Wall, Bracing, Base Shear, Performance Point, Storey displacements, story Drift ratios, Global Stiffens, dynamic analysis, response spectrum analysis, time history analysis & ETABS.**

I. Introduction

Some buildings with multiple stories constructed years back are seismically weak to resist unexpected earthquakes and wind loads in the present scenario. Hence it is necessary to take specific remedies by checking the performance of those secondary structures. It is mandatory to incorporate strength regaining techniques into the existing buildings. Retrofitting techniques are the strength-regaining techniques.

In the past few decades, most people have invested in multistoried buildings, but they are not strong enough to withstand earthquakes for many reasons. As the number of stories increases, the seismic activity effect, i.e., lateral forces effect, also increases. In addition to that, the building may also be subjected to heavy wind loads. We hear the news that heavy rains, winds, or unexpected earthquakes have destroyed the buildings and led to the loss of lives as the buildings are not strong enough to withstand those loads. It may happen if used old construction practices during construction. Due to the frequent occurrence of natural disasters, there is a need to develop new codes. Most existing structures fail to satisfy the present-day regulations and are called seismic deficient structures. Reducing human and material loss can be avoided by redesigning the structure to resist the threats from unexpected lateral loads and other loads. The method used to strengthen the existing seismically deficient structures are seismic retrofitting techniques.

A. Seismic retrofitting

Seismic retrofitting is the method in which the strength is given to the existing seismic deficient structures so that they can resist seismic activities, ground motions, and soil failures caused due to earthquakes. In present times seismic retrofitting is one of the strengths incorporating solutions to the deficient structures prone to different environmental forces. The method of adding new features to existing old structures is also called retrofitting. When Retrofitting techniques are applied to existing structures, the extent of damage due to seismic activity can be reduced. The main objective of Retrofitting is to strengthen the structures in relevance to the present-day codal provisions. Retrofitting procedures are applied to provide longevity and sustainability to the structures. Retrofitting helps increase the structure's strength, stiffness, resistivity, and overall lifespan.

Retrofitting method is adopted to:

1. Increase the lateral strength of the structure.
2. Increase the ductility of the structure.
3. Increase the overall stiffness of the building.

Different retrofitting techniques that are used and discussed in the paper are given below:

1. Retrofitting the structure with the shear wall.
2. Retrofitting with efficient bracings at different Locations.

B.Shear wall

A concrete wall with reinforcement is known as a shear wall in engineering designs. It is similar to the beam. It is simply called a vertical beam. The shear wall resists both the

Received on 16-02-2022, Revised on 10-03-2022, Accepted on 25-04-2022.

vertical and lateral loads from seismic activities. The columns in the RC buildings resist the primary gravity loads coming on the structure. The retrofitted Shear walls help strengthen the existing structure and impart stiffness to the building. Therefore, the lateral sway of the building reduces. In turn, it reduces the damage to the elements of the structure. Shear walls can be effectively used to control the displacement and drift against a load of earthquakes that operate on them.

The shear wall should be located to provide high strength and stiffness to the existing building. The optimum location of the shear wall is decided by placing the shear wall at different locations and analyzing it. The various locations of the shear walls are the staircase area, lift area, core areas, corners, and the periphery of the building, depending on the requirements.

C.Bracings

Bracing is one of the structural systems used to resist the lateral forces in the structures. Seismic deficient structures need to be strengthened by retrofitting with bracings so that the lateral resistance of the structure can be increased. Bracings reduce the columns' bending moments and shear forces, and the loads are transferred safely to the foundation through axial action. Bracings provide the required strength and stiffness to the structures, and the displacements are also decreased. It improves the displacement capacity of the structure.

D.Objective of the study

1. Improving the performance of an existing G+13 storey unsymmetrical building which is seismically deficient by using structural analysis and design software ETABS.

2. The failure areas of an existing building are identified, and its strength is to be increased by incorporating shear walls and bracings into the existing structure.

3. Building responses in terms of story displacement, story drift ratio, story shear, and time periods are compared for different locations of shear wall and bracings to decide the best retrofitting technique and retrofitting locations. The values are compared with allowable values.

4. The responses of the buildings are also compared for the static method, response spectrum method, and time history method to show the variation in those methods and their level of accuracy.

II. Literature Review

Bharat Diliprao Daspute and L. G. Kalurkar (2020). This paper focuses on the concepts of retrofitting structures against seismic activities. This paper studied the functionality of the buildings, various retrofitting techniques used, and their effectiveness.

Akansha Dwivedi and B.S Tyagi (2020) studied the effect of the presence of shear walls in RCC G+19 buildings. The structure is analyzed based on storey displacement, drift, stiffness, lateral force, and base shear. They concluded that in the presence of the shear wall, the story responses were reduced by approx.—40%.

Priyanka Kosare and Deepti Hazari (2019) have studied that the shear wall provided along the periphery of the structure is more efficient than all other types of shear walls.

Sylviya B and P. Eswaramoorthi (2018) have found that the structural walls should be provided for the structure's total height for best earthquake resistance. Placing the structural walls towards the building center allows flexibility for buildings to undergo torsion as the first mode of oscillation, which is not desirable. It is concluded that structural walls, when placed at the periphery of the building, show more effective results.

M. Tamim. A Tanwer (2013) has carried out a study on Structural Configuration Optimization of a Multi-storey Building by Optimum Positioning of Shear Wall (2012). In the case of mass center and stiffness center coincide with each other; at that time, the distance of the shear wall from the mass center also plays a vital role in the shear contribution of the shear wall.

III. Methodology

A. Description of the Building

An existing unsymmetrical G+13 storied building located in the zone -II is taken and studied in the project. The performance of the existing building is analyzed by using seismic analysis methods such as linear response spectrum and nonlinear time history analysis.

1. Utility of Buildings: Residential Building
2. No of Storey: 14 Stories (G+13Building)
3. Grade of concrete: M40 for columns, shear wall
   M35 for beams, slabs
4. Grade of Reinforcing steel: Fe-415, Fe-500
5. Type of construction: RCC framed structure
6. Dimensions of beam: 230mm*450mm,
   230mm*500mm
   230mm*600mm
7. Dimensions of the column: 300mmX900mm
8. The thickness of the slab: 150mm
9. Thickness of Shear wall: 250mm
10. Loads considered: Dead loads, Live loads, floor loads
    Earthquake loads, wind load
11. Seismic Zone: Zone II
12. Zone factor: 0.1
13. Site type: II
14. Importance factor: 1.2
15. Response reduction factor: 3
16. Time history function: El Centro time history function
17. Structure class: B
18. Terrain category: II
19. Basic wind speed: 44m/s

B. Steps involved in analyzing the models

1. Forming a grid and storey setup
2. Defining the material and section properties
3. Defining the mass, source, diaphragms, load

combinations, and response spectrum function or a time history function

4. Creating beams, columns, floors, and shear walls or bracings
5. Assigning dead, live loads, earthquake loads, and wind loads
6. Check the building
7. Analysis of the building
8. Design the concrete frames
9. Checking output results

C. Cases considered

Case-1: Modelling and analysis of an existing building.

Case-2: Modelling and analysis of an existing building retrofitted with a shear wall at the staircase and lift area. (Height of the shear wall up to top floor)

Case-3: Modelling and analyzing an existing building retrofitted with a shear wall at the staircase, lift area, and corners.

Case-4: Modelling and analysis of an existing building retrofitted with X-bracings at the staircase, lift area, and corners (Bracings up to the top floor)

Case-5: Modelling and analysis of an existing building retrofitted with V-bracings at the staircase, lift area, and corners (Bracings up to the top floor)

Case-6: Modelling and analysis of an existing building retrofitted with bracings at corners and shear wall at the core (composite)

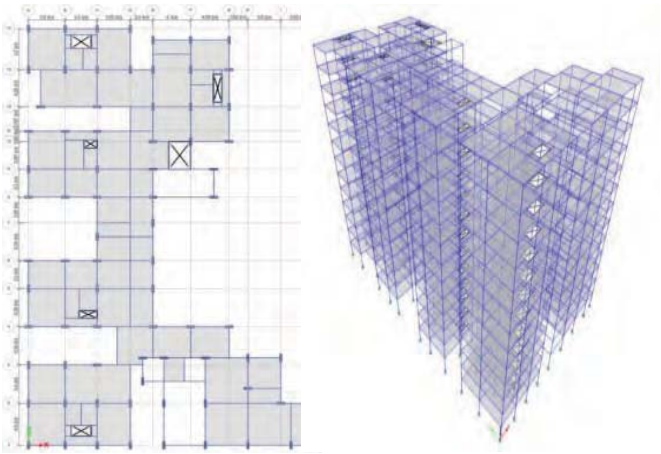

Figure 1. Plan and Isometric view of case-1(Existing building plan)

From the analysis and design results of the response spectrum and time history analysis, it was observed that 55 weak columns are not cable of taking the maximum loads coming on the structure. Fifty-five concrete frames (columns) of an existing building are overstressed beyond their capacity and failed. Hence it was concluded that the existing building is seismically inadequate. It cannot sustain or be capable of taking unexpected earthquake or wind loads in addition to gravity loads. The columns that are overstressed and failed after the analysis and design in etabs are C7, C24, C27, C33, C34, C38, C42, C60, C8, and C72.

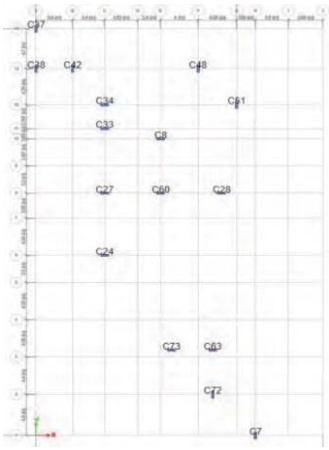

Figure 2. Plan of an existing structure showing the failed columns which are overstressed

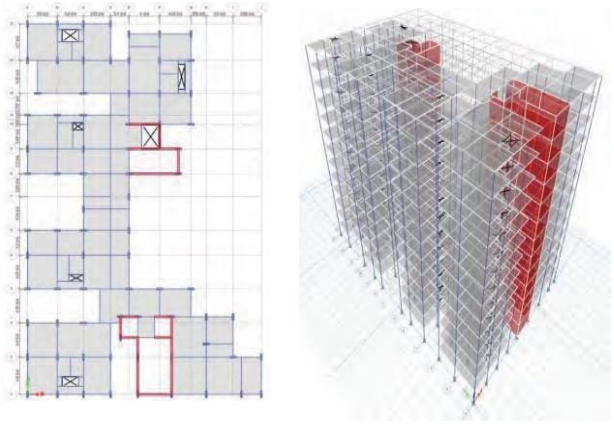

Figure 3. Plan and Isometric view of case-2

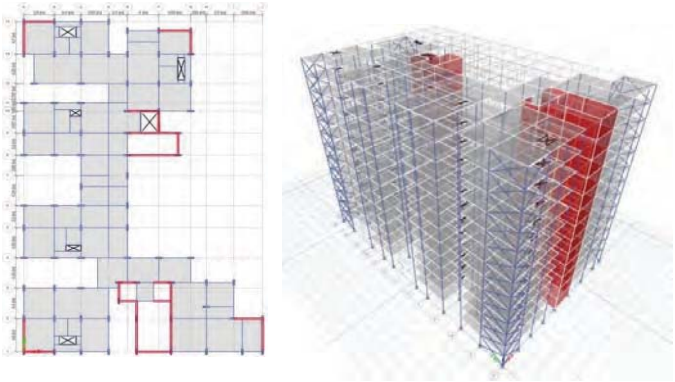

Figure 4. Plan and Isometric view of case-3

E-ISSN 2581 – 7957
P-ISSN 2277 – 3916

CVR Journal of Science and Technology, Volume 22, June 2022
DOI: 10.32377/cvrjst2224

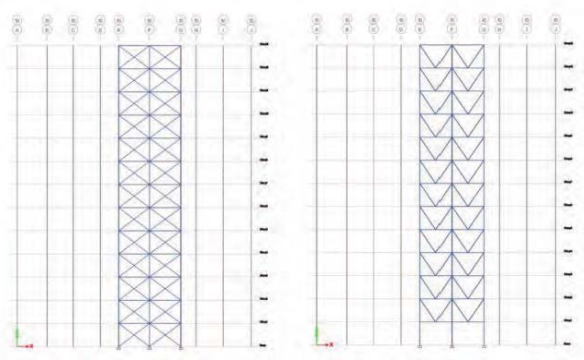

Figure 5. Elevation view of case-4 and case-5

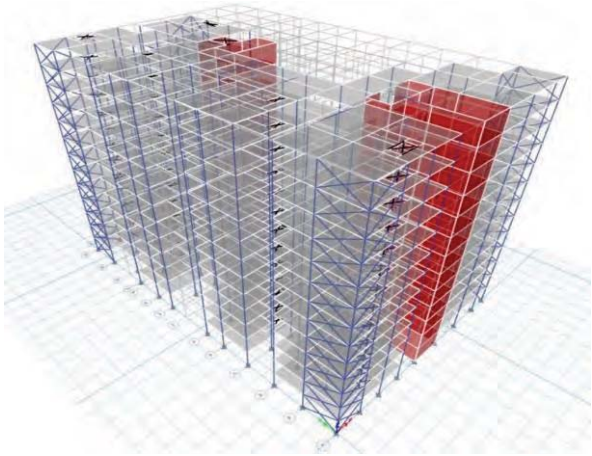

Figure 6. Isometric view of case-6

IV. Analytical Study

The factors studied in this project are story displacement, story shear, story drifts, and Time periods. Based on the results obtained from the various retrofitting methods, the responses are observed, such as story displacements, story shear, the story drifts. Time periods are presented herein. Based on the obtained results, the optimum location and the method of retrofitting are identified. A comparison between the various analysis methods, i.e., static, response spectrum, and time history analysis, is done.

A. Comparison of parameters for different cases considered

TABLE I.
Comparison Of Storey Displacement And Storey Drift For Different Cases

CASE	STOREY DISPLACEMENT	STOREY DRIFT RATIO
case-1	262.451	0.0092
case-2	76.038	0.0026
case-3	42.778	0.0014
case-4	146.649	0.0048
case-5	135.305	0.00421
case-6	68.158	0.00225

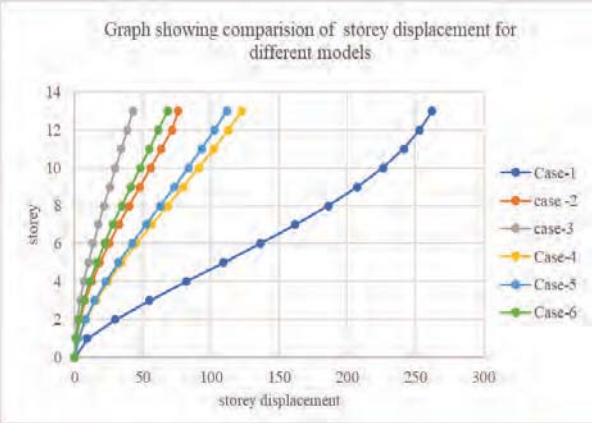

Graph 1. Showing comparison of story displacements for different cases

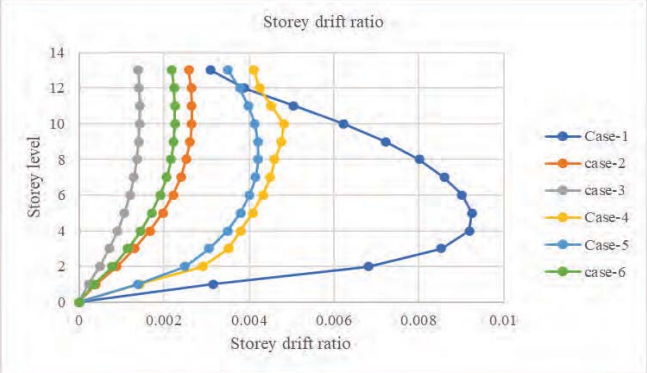

Graph 2. Showing comparison of story drift ratio for different cases

TABLE II.
Comparison Of Story Shear For Different Cases

CASES	X	Y
Case-1	9686.7695	11317.8506
Case-2	10539.0637	12313.656
Case-3	11039.4577	12898.3075
Case-4	9783.5587	11430.9373
Case-5	9805.1012	11456.1072
Case-6	10545.6835	12321.3905

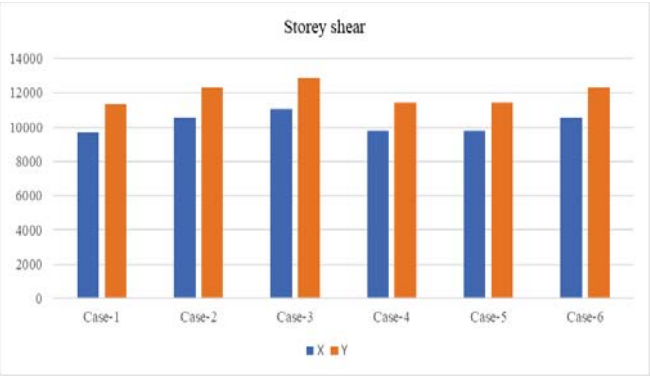

Graph 3. Showing comparison of story shear for different Cases

E-ISSN 2581 – 7957
P-ISSN 2277 – 3916

CVR Journal of Science and Technology, Volume 22, June 2022
DOI: 10.32377/cvrjst2224

TABLE III.
COMPARISON OF TIME PERIODS FOR DIFFERENT CASES

case-1	case-2	case-3	case-4	case-5	case-6
.84	1.29	1.02	1.81	1.65	1.20

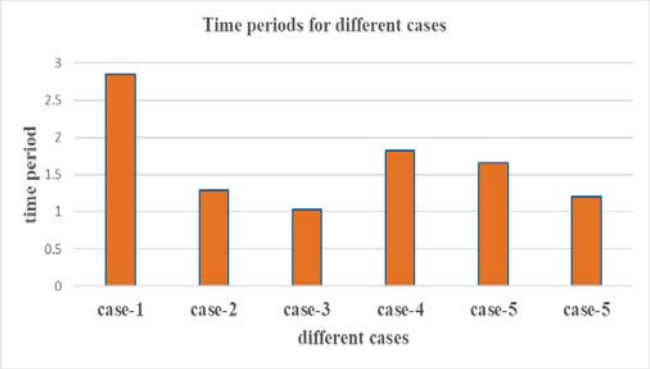

Graph 4. Comparison of time periods for different Cases.

B.Comparison of parameters between different methods of analysis

TABLE IV.
COMPARISON OF STOREY DISPLACEMENT FOR DIFFERENT METHODS OF ANALYSES

Case	EQX	RSM	THM
Case-1	170.718	134.312	101.578
Case-2	48.729	43.349	26.39
Case-3	30.409	28.101	14.731
Case-4	73.634	60.995	59.25
Case-5	66.687	56.28	55.45
Case-6	42.0155	40.206	39.186

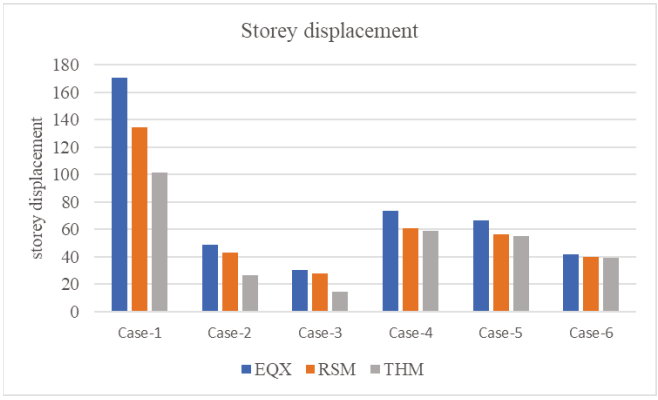

Graph 5. Comparison of Storey Displacements for Different Methods of Analyses

TABLE V.
COMPARISON OF STOREY DRIFT RATIO FOR DIFFERENT METHODS OF ANALYSIS

Case	EQX	RSM	THM
Case-1	0.00604	0.005923	0.0043
Case-2	0.001615	0.001392	0.001
Case-3	0.001126	0.000932	0.0002
Case-4	0.002008	0.0023	0.0022
Case-5	0.00208	0.00175	0.002
Case-6	0.0014	0.00127	0.001

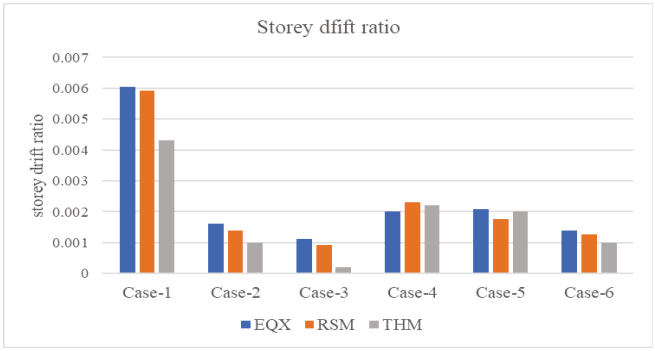

Graph 6. Comparison of Storey Displacements for Different Methods of Analysis

TABLE VI.
COMPARISON OF STOREY SHEAR FOR DIFFERENT METHODS OF ANALYSES

Case	EQX	RSM	THM
Case-1	6457.846	5489.166	5408.468
Case-2	7026.042	5972.137	5971.406
Case-3	7359.63	6255.694	6235.989
Case-4	6522.37	5544.01	5471.4
Case-5	6536.73	5556.22	5521.64
Case-6	7030.45	6132.75	6105.14

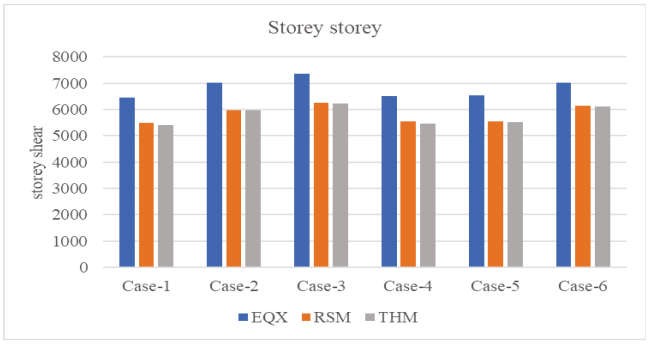

Graph 7. Comparison of Storey shear for Different Methods of Analysis

As per IS 1893(part-1):2016, cl. 7.11.1 the maximum allowable displacement should not exceed L/500, i.e.,3000*13/500=78mm, and the story drift ratio should not exceed 0.004. from the below values, case 2, case-3, and case-6 show good results.

When compared to the codal allowable values, the displacements and drift ratio values are high, which is undesirable. It was observed that the allowable displacement is 78mm, and for cases 4 and 5, the values are high, and the drift values for those cases are also more than allowable, i.e., 0.004. Case-2, Case-3, and Case-6 satisfied the serviceability criteria, whereas case-4 and case-5 failed to fulfill the serviceability criteria. Hence, we can conclude or justify that the shear located in the core and core-plus corners and the combination of the shear wall at the core and bracings at corners satisfy both strength and serviceability criteria.

When the shear wall and bracings are added to the existing building, the structure's self-weight increases, due to to which the storey shear increases. It was observed that storey shear increases for all cases considered. Bracings add less self-weight than shear walls; hence cases-2, case-3, and case-5 show high storey shear. In terms of storey shear, as its value is low, bracings provide good results, but the shear wall offers good results when it comes to deflection point of view.

From IS 1893(part-1):2016, cl.no.7.1 of table 5, it was said that a building is said to be torsionally irregular when the fundamental torsional mode (Rz) is greater than the first two translation modes (Ux and Uy) in each of the principal plan directions. When an existing structure is retrofitted with shear at the core and corners(case-3), it was found that the building is structurally safe without any torsion effect. The torsion effect is taken care of by the corner shear wall more effectively than the core location of the shear wall.

V. Conclusions

1. The analysis and design results concluded that retrofitting an existing seismically inadequate building with a shear wall at the core and corners(case-3) and retrofitting with a shear wall at the core and bracings at the corners (case-6) made the structure seismic resistant and strong.

2. Adding shear walls to the building reduced storey responses by around 83%, whereas adding bracings to the building has reduced storey responses by 44%. Compared to shear walls, bracings had not attained the required criteria.

.

3. Adding Shear walls is found to be more effective as they have a more significant effect in reducing storey displacements and storey drift ratios when compared to that of bracing. The torsional irregularity is also avoided by adding shear walls. The combination of bracings and shear wall was also found to be effective in the same way

4. From all considerations, case-3 and case-6 are the best retrofitting cases in the existing building.

References

[1] Bharat Dilip Rao daspute, L.G. kalurkar(2020), "Seismic Retrofitting of RC Structures with Exterior Shear Walls and Bracing," International Journal Of Engineering Research & Technology (IJERT) VOLUME 09, ISSUE 08.

[2] Akansha Dwivedi, B.S Tyagi (2020), "Seismic Analysis of Building with and Without Shear Wall for Building with RCC and Composite Column," International Journal of Engineering Research and Technology, Volume 09, Issue 06.

[3] Dr. Victor Babu Neela Professor (2019), "Earthquake resistant building design by considering bracings and shear wall system in e-tabs software," Paideuma Journal Issn No: 0090-5674

[4] Donthireddy Raja Shekar Reddy, Joshi Sreenivasa Prasad (2019), "Seismic Behaviour of The Building with Shear Walls of Four Different Shapes in All Zones," International Journal of Engineering Research & Technology (IJERT)Volume 08, Issue 07.

[5] Sylviya B, P. Eswaramoorthi (2018), "Analysis of RCC Building with Shear Walls at Various Locations and In Different Seismic Zones," International Journal of Innovative Technology and Exploring Engineering (IJITEE), Volume-8, Isuue2-s.

[6] Sumit Ghangus, Prof. Sangeet Kumar Gupta (2018), "Typical Structural System of Tall RCC Buildings in India," International Research Journal of Engineering and Technology (IRJET) Volume: 05 Issue: 05.

[7] Chandana Kurma, G. Siva Vignan, T. Sai Krishna Teja (2018) "Nonlinear Analysis of Multistoried Building with and without Shear Wall," International Journal of Engineering Research & Technology (IJERT) Volume 07, Issue 01.

[8] Fazal U Rahman Mehrabi, Dr.D. Ravi Prasad (2017) "Effects of Providing Shear wall and Bracing to Seismic Performance of Concrete Building," International Research Journal of Engineering and Technology (IRJET) Volume: 04 Issue: 02.

[9] Subodh.S. Patil, Chetan.R. Shah, Rahul.A. Patil, Sunil.D. Bedege(2017) has carried out a study on "push over-analysis of the multi-storied building," International Journal of Modern Trends in Engineering and Science Volume 04 Issue 03, 2017.

[10] ResearchGate (https://www.researchgate.net/publication/315471642)

E-ISSN 2581 – 7957
P-ISSN 2277 – 3916

CVR Journal of Science and Technology, Volume 22, June 2022
DOI: 10.32377/cvrjst2225

Common Fixed-Point theorem for Self maps of S-Metric Spaces with A Weak S-Metric

G.Vijaya Lakshmi
Asst. Professor, CVR College of Engineering/ H & S Department(/Maths),Hyderabad, India.
Email: garishevijayalakshmi@cvr.ac.in

***Abstract*:**
In this paper, we introduced the notation of a *Weak S-metric* on a S-metric space and established a common fixed-point theorem for two self-maps of a S-metric space with a weak S-metric. Also, we deduce a common fixed point theorem and proved in metric spaces from our results.

Index Terms:S-metric space, Weak S-metric, Common fixed point

AMS Mathematical Subject Classifications: **54H25, 47H10**

I. Introduction

In view of the importance of the metric space theory both in mathematics and in applied sciences, several researchers have generalized the metric spaces. Although Gahler [5] and Dhage [3] have introduced *2-metric spaces* and *D-metric spaces* respectively and initiated their study ,later investigators (see [10]-[12]) have pointed out that these attempts are not valid.
As modifications to D-metric spaces ,new structures of generalized metric spaces –such as *G-metric spaces* by Mustafa and Sims [8], *D*-metric spaces* by Sedghi, Shobeand Zhou [13] .

Very recently Sedghi, Shobe and Aliouche [14] introduced S – metric space as a generalization of metric space and several researchers have proved fixed point theorems for self-maps of such spaces. In 1996, Kadaet.al [7] defined the concept of a weak distance in metric space, using which Ume and Yi [16] proved a common fixed point theorem for self-maps of metric spaces with weak distance.
Also several fixed point theorems for self maps of S-metric spaces were established in recent years .For examples, see [1],[2],[9],[14] and [15].

In this we deal with S-metric spaces defined in [14] (Definition 2.1) as follows.

Definition 1.1

Let X be a non empty set. A S-metric on X in a function $S: X * X * X \to [0,\infty)$ satisfying the conditions below for each $x, y, z, a \in X$:

(a) $S(x,y,z) \geq 0$
(b) $S(x,y,z) = 0$ *if and only if* $x = y = z$
(c) $S(x,y,z) \leq S(x,x,a) + S(y,y,a) + S(z,z,a)$. A set X with a S-metric defined on it is called a *S-metric space* and is denoted by (X,S).

Examples 1.2

(i) Let (X,d) be a metric space. Define $S_\alpha: X * X * X \to [0,\infty)$ by $S_\alpha(x,y,z) = d(x,z) + d(y,z)$ for $x,y,z \in X$ and verify that (X, S_α) is a S-metric space.

(ii) Suppose $X_0 = \left\{\frac{1}{n}; n \geq 1\right\} \cup \{0\}$ and define S: $X_0 * X_0 * X_0 \to [0,\infty)$ by $S(x,y,z) = x + y + 2z$ for $x,y,z \in X_0$.

Then (X_0, S) is a S-metric space

(iii) If X=R^n and $\|.\|$ is a norm on X then $S: X * X * X \to [0,\infty)$ defined by

$S(x,y,z) = \|y + z - 2x\| + \|y - z\|$ for $x,y,z \in X$

is a S-metric on X giving the S-metric space (R^n, S) .

For other examples see [14].

Definition 1.3 ([14],Definition 2.8)

Let (X,S) be a S-metric space .A sequence $\{x_n\}$ is said to

(i) *Converge to* $x \in X$ if to each $\epsilon > 0$ there is a natural number n_0 such that $S(x_n, x_n, x) < \epsilon$ for all $n \geq n_0$. In this case we write $\lim_{n\to\infty} x_n = x$.

(ii) be a *Cauchy sequence* if to each $\epsilon > 0$ there is a natural number n_0 such that $S(x_n, x_n, x_m) < \epsilon$ for all n,m $\geq n_0$.

It has been proved in [14] (Lemma2.10 and Lemma2.11) that every sequence in (X,S) that converges is a Cauchy sequence and has unique limit x.

Definition 1.4

A S-metric space (X,S) is said to be *Complete* if every Cauchy sequence in it converges.

If (X,S) is a S-metric space then it is proved in [14] that

(1.5) $S(x,x,y) = S(y,y,x)$ for all $x,y \in X$ ([14], Lemma 2.5)
and
(1.6) If $\{x_n\}$ and $\{y_n\}$ in X are converging respectively to x and y in X then $\lim_{n\to\infty} S(x_n, x_n, y_n) = S(x,x,y)$ ([14], Lemma 2.12).

In 1996, Kada et.al [7] introduced the concept of a weak distance in a metric space(X,d) using which Ume and Yi [16] have proved common fixed point theorems for self maps on complete metric spaces with weak distance.

The purpose of this paper is to define the notion of a *Weak S-metric* on a S-metric space and establish a Common fixed point theorem for two self maps of a S-metric space with a

Received on 31-03-2022, Revised on 19-04-2022, Accepted on 05-05-2022

weak S-metric. Also we show that a theorem proved in [16] can be deduced from our results.

II. Weak S–Metric on a S-Metric Space

Definition 2.1

Suppose (X,S) is a S-metric space. A *Weak S-metric* on X is a function $p: X*X*X \to [0,\infty)$ satisfying the condition given below:

(a^1) $p(x,y,z) \le p(a,a,x) + p(a,a,y) + p(a,a,z)$ for $x,y,z,a \in X$

(b^1) For each $x \in X$, $p(x,x.): X \to [0,\infty)$ is lower semi continuous in the third variable. That is, for each $\{y_n\} \in$X that converges to y in (X,S),we have

$$\liminf_{n\to\infty} p(x,x,y_n) \le p(x,x,y)$$

(c^1) For each $\in > 0$ there is a $\delta > 0$ such that

$p(a,a,x) < \delta$, $p(a,a,y) < \delta$ and $p(a,a,z) < \delta$ for some $a \in X$ imply that $S(x,y,z) < \in$.

Example 2.2

(i)If (X,S) is a S-metric space then $p: X*X*X \to [0,\infty)$ defined by $p(x,y,z) = S(x,y,z)$ for $x,y,z \in X$ is a weak S-metric. That is, every S-metric is a weak S-metric.

In fact, (a^1) holds in view of Definition 1.1 *(c)* and (1.5); (b^1) holds in view of (1.6).

Finally, for given $\in > 0$ take $\delta = \frac{\in}{3}$ and observe that (c^1) holds in view of Definition 1.1 *(a)*.

(ii) Let (X_0,S) be the S-metric space given in Example 1.2(ii). Define $p: X*X*X \to [0,\infty)$ by $p(x,y,z) = y + 2z$ for $x,y,z \in X_0$.Then p is a weak S-metric .To verify this for $x,y,z,a \in X_0$, note that

$$p(a,a,x) + p(a,a,y) + p(a,a,z) = 2(x+y+z) + 3a \ge y + 2z = p(x,y,z)$$

which gives (a^1); if $\{y_n\} \to y$ as $n \to \infty$ in (X_0,S) then $\lim_{n\to\infty} p(x,x,y_n) = \lim_{n\to\infty}(x+2y_n) = x + 2y = p(x,x,y)$ shows(b^1) holds;

and finally for given $\in > 0$ take $\delta = \frac{\in}{3}$ we find that$p(a,a,x) < \delta, p(a,a,y) < \delta$ and $p(a,a,z) < \delta$

imply $2(x+y+z) + 3a < 3\,\delta < \in$

So that $S(x,y,z) = x + y + 2z < \in$ proving (c^1).

Remark 2.3

For a weak S-metric p on S-metric space(X,S), $p(x,y,z) = 0$ need not imply $x = y = z$. Therefore $p(x,x,y)$ and $p(y,y,x)$ need not be equal for $x,y \in X$.

For instance, in Example 2.2(ii) notice that $p(a,0,0) = 0$ for any $a \in X_0$,

Some properties of a weak S-metric are given below:

Lemma 2.4

Suppose (X,S) is a S-metric space p is a weak S-metric on X. Let $\{x_n\}$ and $\{y_n\}$ be sequence in X; $\{\alpha_n\}$ and$\{\beta_n\}$ be sequences in $[0,\infty)$ such that $\lim_{n\to\infty}\alpha_n = \lim_{n\to\infty}\beta_n = 0$ and $x,y,z \in X$.

Then $p(x_n,x_n,y) \le \alpha_n$ *and* $p(x_n,x_n,z) \le \beta_n$ for every n implies $y = z$.

Inparticuler $p(x,x,y) = p(x,x,z)$implies $y = z$

(i) $p(x_n,x_n,y_n) \le \alpha_n$ and $p(x_n,x_n,z) \le \beta_n$ for every n implies that $\{y_n\}$ converges to z in (X,S).

(ii) $p(x_n,x_n,x_m) \le \alpha_n$ for all $m > n \ge 1$ implies $\{x_n\}$ Cauchy sequence in (X,S).

(iii) $p(y,y,x_n) \le \alpha_n$or every $n \ge 1$ implies $\{x_n\}$Cauchy sequence in (X,S).

Proof:

For any $\in > 0$ choose $\delta > 0$ satisfying(c^1) of Definition 2.1 and find a natural number n_0 such that $\alpha_n < \delta$ and $\beta_n < \delta$ whenever $n \ge n_0$.

(i) For $n \ge n_0$ we get $p(x_n,x_n,y) < \delta$ and

$p(x_n,x_n,z) < \delta$ so that by (c^1), $S(y,y,z) < \in$ .Since $\in$ is arbitrary it follows that $S(y,y,z) = 0$ giving $y = z$

(ii) For $n \ge n_0$ we get in this case, $p(x_n,x_n,y_n) < \delta$ and $p(x_n,x_n,z) < \delta$ so that by (c^1) gives

$S(y_n,y_n,z) < \in$ showing $\{y_n\} \to z$ as $n \to \infty$ in (X,S).

(iii) In this $p(x_n,x_n,x_m) < \delta$ for $n \ge n_0$. In particular $p(x_{n_0},x_{n_0},x_m) < \delta$ and $p(x_{n_0},x_{n_0},x_k) < \delta$ where

$m > k \ge n_0$ which implies $S(x_m,x_m,x_k) < \in$ for

$m > k \ge n_0$ proving $\{x_n\}$ is a Cauchy sequence in (X,S).

(iv) For $n \ge n_0$we have $p(y,y,x_n) < \delta$ so that for

$m > n \ge n_0$ we have $p(y,y,x_n) < \delta$ and $p(y,y,x_m) < \delta$ and hence $S(x_m,x_m,x_n) < \in$ proving $\{x_n\}$is a Cauchy sequence in (X,S).

III. Main Results

First we prove the following:

Theorem3.1

Let (X,S) be a S-metric space with a Weak S-metric $p$onit. Suppose f and g are self maps of X ,and $\varphi: X \to [0,\infty)$ are such that

(A) $g(X) \subseteq f(X)$

(B) there is a $z \in X$ and$r \in [0,1)$ suchthat $p(gx,gx,z) \le rp(fx,fx,z) + M[\varphi(fx) - \varphi(gx)]$ for all $x \in X$, where $M \in [0,\infty)$ is a fixed number.

(C) For every sequence $\{x_n\}$ in X with $\lim_{n\to\infty} p(fx_n,fx_n,z) = \lim_{n\to\infty} p(gx_n,gx_n,z) = 0$

we have with $\lim_{n\to\infty} \max\{p(fx_n,fx_n,z), p(gx_n,gx_n,z),$

$p(fgx_n,fgx_n,gfx_n)\} = 0$

and

(D) For each $u \in$X with $u \ne fu$ or $u \ne g$ u we have $inf\{p(fx,fx,u) + p(gx,gx,u) + p(fgx,fgx,gfx): x \in X\} > 0$.

Then z is the unique common fixed point of f and g.

Proof:

Let $x_0 \in X$. Then by (A), there is a sequence $\{x_n\}$ in X such that $g\,x_{n-1} = fx_n$ for $n \geq 1$

Now for $z \in X$ satisfying (B) note that

$$p(fx_{n+1}, fx_{n+1}, z) = p(gx_n, gx_n, z) \leq rp(fx_n, fx_n, z) + M[\varphi(fx_n) - \varphi(gx_n)]$$

$$= rp(fx_n, fx_n, z) + M[\varphi(fx_n) - \varphi(fx_{n+1})]$$

and therefore

$$\sum_{n=0}^{N} p(fx_{n+1}, fx_{n+1}, z) \leq r \cdot \sum_{n=0}^{N} p(fx_n, fx_n, z) + M \sum_{n=0}^{N} [\varphi(fx_n) - \varphi(fx_{n+1})]$$

from which we get

$$(1-r)\sum_{n=1}^{N} p(fx_n, fx_n, z) \leq r \cdot p(fx_0, fx_0, z) + M\,[\varphi(fx_0) - \varphi(fx_{N+1})]$$

So that

$$\sum_{n=1}^{N} p(fx_n, fx_n, z) \leq \frac{r}{(1-r)} \cdot p(fx_0, fx_0, z) + \frac{M}{(1-r)}\varphi(fx_0).$$

That is ,the series $\sum_{n=1}^{\infty} p(fx_n, fx_n, z)$ is convergent and hence $\lim_{n\to\infty} p(fx_n, fx_n, z) = 0$.Similarly we can prove that $\lim_{n\to\infty} p(gx_n, gx_n, z) = 0$.

Therefore, by (C),

$\lim_{n\to\infty} \max \{p(fx_n, fx_n, z), p(gx_n, gx_n, z), p(fgx_n, fgx_n, gfx_n)\} = 0$

We now claim that $fz = gz = z$.

If possible, either $fz \neq z$ or $gz \neq z$ in which case by (D) and(C)

We get $0 < inf\,\{p(fx, fx, z) + p(gx, gx, z) + p(fgx, fgx, gfx): x \in X\}$

$\leq inf\{p(fx_n, fx_n, z) + p(gx_n, gx_n, z) + p(fgx_n, fgx_n, gfx_n): n \geq 1\}$

$= 0,$

a contradiction. Hence $fz = gz = z$.

To prove the uniqueness of z, suppose $u \in X$ is such that $fu = gu = u$.

Then, by (B),

$$p(u,u,z) = p(gu, gu, z) \leq rp(fu, fu, z) + M[\varphi(fu) - \varphi(gu)]$$

$= rp(u,u,z)$

and

$$p(u,u,u) = p(gu, gu, u) \leq rp(fu, fu, u) + M[\varphi(fu) - \varphi(gu)]$$

$= rp(u,u,u)$

Form which we get $p(u,u,z) = 0 = p(u,u,u)$

since $0 \leq r < 1$.

Therefore by (i) of Lemma 2.4,it follows u = z.

Hence the theorem.

Definition 3.2

Suppose (X, S) is a S-metric space. Two self maps f and g of X are said to be *Compatible* if for every sequence $\{x_n\}$ in S with $\lim_{n\to\infty} x_n = x$ in (X, S) (see Definition 1.3(i))

We have $\lim_{n\to\infty} S(fgx_n, fgx_n, gfx_n) = 0$

It is trivial that every pair of commuting self-maps of X are Compatible but not conversely.

Remark 3.3

If (X, S) is a S-metric space and $p = s$ then condition (C) of Theorem 3.1 shows f and g are Compatible and the condition (D) holds always. Therefore, we can restate Theorem 3.1 in the case $p = s$ as follows:

Theorem 3.4

Let (X, S) be a S-metric space. Suppose f and g are self maps of X and $\varphi: X \to [0, \infty)$ are

Such that

(A^1) $g(X) \subseteq f(X)$

(B^1) there is a $z \in X$ and $r \in [0,1)$ suchthat

$S(gx, gx, z) \leq r\,S(fx, fx, z) + M[\varphi(fx) - \varphi(gx)]$

for all x ∈ X and

(C^1) f and g are Compatible.

Then z is the unique common fixed point of f and g.

In [6], Jungck defined Compatibility of two self maps f and g on a metric space (X, d) as follows:

Definition 3.5

A pair of self maps f and g on a metric space (X, d) is said to be *Compatible* if for every sequence $\{x_n\}$ in X with $\lim_{n\to\infty} x_n = z$ we have

$\lim_{n\to\infty} d\,(f\,gx_n, gfx_n) = 0.$

The following Common fixed point theorem due to Dien [4] (Theorem 2.2) is a consequence of Theorem 3.4

Corollary 3.5

Suppose (X, d) is a metric space. Suppose f and g are self maps of X and $\varphi: X \to [0, \infty)$ are Such that

(A^{11}) $g(X) \subseteq f(X)$

(B^{11}) there is a $z \in X$ and $r \in [0,1)$ suchthat

$d(gx, z) \leq rd(fx, z) + \varphi(fx) - \varphi(gx))$

for all $x \in X$ and

(C^{11}) f and g are Compatible.

Then z is the unique Common fixed point of f and g.

Proof:

Given the metric space (X, d), define $S_\alpha: X * X * X \to [0, \infty)$ by $S_\alpha(x, y, z) = d(x, z) + d(y, z)$ for $x, y, z \in X$. Then (X, S_d) is a S-metric space (see Example 1.2(i)).

Also $S_\alpha(x, y, z) = 2\, d(x, y)$ for $x, y \in X$. Therefore (A^{11}),(B^{11}) and (C^{11}) respectively given

(A^1), (B^1) and (C^1) for the S-metric space (X, S_d) with $M = \frac{1}{2}$.

Hence, by Theorem 3.4,

f and g have z as unique Common fixed point.

ACKNOWLEDGEMENT

The author would like to thank University Grants Commission, Govt. of India, New Delhi for sanctioning the Minor Research Project No.112.

Under which the present research is carried out.

The author would like to thank V. SIVA RAMA PRASAD, Retired Professor, Osmania University, for his continuous support and guidance.

REFERENCES

[1] Afra,J.M.,Fixed point type theorem in S-metric space, Middle-East J.Scientific Research 22(6)(2014),864-869.
[2] Choustan.P. and Neeraj Malaviya, A Common unique fixed point theorem for expansive type mappings in S-metric spaces, International Math.Forum,vol.8(2013) no.26,1287-1293.
[3] Dhage,B.c.,Generalized metric spaces mappings with fixed point, Bull.Calcutta Math.Soc.84(1992),329-336.
[4] Dien,N.H, Some remarks on Common fixed point theorems ,J.Math.Anal.Appl.187(1994), no.1,76-90.
[5] Gahler,S,2-metrische Raume and ihertopoloischestruktr, Math.Nachr.26 (1963), 115-148.
[6] Jungck,G,Commuting mappings and fixed points, Amer.Math.Monthly83(1976) no.4, 261-263.
[7] Kada, O.,T.Suzuki and W.Takahashi, NonConvex minimization theorems and fixed point theorems in completemetricspaces,Math.Japon.44(1996),no.2,381-391.
[8] Mustafa,Z.andB.Sims, A new approach to generalized metric spaces, J.Nonlinear Convex Anal.7(2006),289-297.
[9] Nabil M. Mlaiki ,$\alpha - \psi$- Contractive mapping on S-metric space, Math.Sci, Letters,4 no.1(2015),9-12.
[10] Naidu,S.V.R.,K.P.R.Rao and N.SrinivasRao, On the topology of D-metric spaces and the generation of D –metric spaces from metric spaces, Intl.J.Math.Math.Sci .2004(2004)no.51,2719-2740.
[11] Naidu,S.V.R,.,K.P.R.Rao and N.Srinivas Rao, On the concept of balls in D-metric space,c spaces ,Intl. J.Math.Math.Sci .2005(2005),133-141.
[12] Naidu,S.V.R,K.P.R.Rao and N.Srinivas Rao, On convergent sequences and fixed point theorems in D-metric spaces, Intl.J.Math.Math.Sci .2005(2005),1969-1988.
[13] Sedghi,S.,N.Shobe and H.Zhou, A Common fixed point theorem in D*-metric spaces, Fixed point theory Appl.Vol.2007 Article ID 27908,13pages.
[14] Sedghi,S.,N.Shobe and A.Aliouche, A generalization of fixed point theorems in S-metric spaces ,Mat.Vesnik 64.3(2012)258-266.
[15] Sedghi, S.,N.V.Dung, Fixed point theorems on S-metric spaces,Mat.Vesnik.66,1(2014),113-124.
[16] Ume,J.S, and S.Yi, Common fixed point theorems for a weak distance in complete metric spaces, Intl.J.Math& Math.Sci.30(10),2002,605-611.

In the next issue (Vol. 23, December 2022)

1.	*Strength and durability studies on light weight self compacting concrete partially replacing coarse aggregate with sintered fly ash aggregate.*	*K.Raju, N. Ramanjaneyulu, Dr.M.V. Seshagiri Rao*
2.	*Travel Time and Congestion Analysis of Heterogeneous Traffic Condition, A Case Study on Kothapet Signal to Nalgonda X-Road Signal Road*	*Kona Mahesh, Gunda Sharanya*
3.	*A Study on Dynamic Response of High-Rise Buildings Using Lead Rubber Bearing Isolator*	*S Mallikarjun, A Shruthi*
4.	*Augmented Corvus Search Optimization for Image Retrieval in Content Based Images*	*Dr. A. Srinivasa Reddy*
5.	*IoT Based Smart Power Management in Public Areas Along with Public Traffic Monitoring*	*V. Shilpa, Dr. Humaira Nishat*
6.	*Advanced Coal Mine Safety Monitoring and Auto Alert System using LoRa Technology*	*N. Lakshmipathi, Dr. Amit Arora*
7.	*Deep Learning Model to Predict the Risk of Developing Diabetic Retinopathy*	*P Prathyusha, A Mallareddy, Dr. S V Suryanarayana*
8.	*Survey on Driver Drowsiness Detection using Convolutional Neural Networks*	*S. Nikhila, V. Sidda Reddy*
9.	*Modelling and Analysis of Domestic Windmill Turbine Blade*	*Mada Rukmini Sai Rupa Sri*
10.	*Mechanical Characterization and evaluation of effects of Epoxy in Lamination for Kevlar Composites*	*A. Suresh*
11.	*Synthesis of New Benzothiazole Derivatives as Potential Antimicrobial Agents*	*Dr. Swapna Ponnampalli*

E-ISSN 2581 – 7957
P-ISSN 2277 – 3916
CVR Journal of Science and Technology, Volume 23, December 2022
DOI: 10.32377/cvrjstxxxx

Template for the Preparation of Papers for Publication in CVR Journal of Science and Technology

First A. Author[1] and Second B. Author[2]
[1]Designation, Name of Institution/Department, City, Country
Email: first.author@hostname1.org
[2]Designation, Name of Institution/Department, City, Country
Email: second.author@hostname2.org

Abstract: **These instructions give you basic guidelines for preparing camera-ready papers for CVR College journal Publications. Your cooperation in this matter will help in producing a high-quality journal.**

Index Terms: **first term, second term, third term, fourth term, fifth term, sixth term**

I. Introduction

Your goal is to simulate the usual appearance of papers in a Journal Publication of the CVR College. We are requesting that you follow these guidelines as closely as possible. It should be original work. Format must be done as per the template specified. Diagrams with good clarity with relevant reference within the text are to be given. References are to be cited within the body of the paper. Number of pages must not be less than five with minimum number of 4000 words and not exceeding eight pages. The journal is published in colour. Colours used for headings, subheadings and other captions must be strictly as per the template given in colour.

A. Full-Sized Camera-Ready (CR) Copy

Prepare your CR paper in full-size format, on A4 paper (210 x 297 mm or 8.27 x 11.69 in). No header or footer, no page number.

Type sizes and typefaces: Follow the type sizes specified in Table I. As an aid in gauging type size, 1 point is about 0.35 mm. The size of the lowercase letter "j" will give the point size. Times New Roman has to be the font for main text. Paper should be single spaced.

Margins: Top and Bottom = 24.9mm (0.98 in), Left and Right = 16 mm (0.63 in). The column width is 86mm (3.39 in). The space between the two columns is 6mm (0.24 in). Paragraph indentation is 3.7 mm (0.15 in).

Left- and right-justify your columns. Use tables and figures to adjust column length. On the last page of your paper, adjust the lengths of the columns so that they are equal. Use automatic hyphenation and check spelling. Digitize or paste down figures.

For the Title use 24-point Times New Roman font, an initial capital letter for each word. Its paragraph description should be set so that the line spacing is single with 6-point spacing before and 6-point spacing after. Use two additional line spacings of 10 points before the beginning of the double column section, as shown above.

TABLE I.
TYPE SIZES FOR CAMERA-READY PAPERS

Type size (pts.)	Appearance		
	Regular	Bold	Italic
6	Table caption, table superscripts		
8	Tables, table names, f irst letters in table captions, figure captions, footnotes, text subscripts, and superscripts		
9	References, authors' biographies	Abstra ct	
10	Section titles ,Authors' affiliations, main text, equations, first letters in section titles		Subheading
11	Authors' names		
24	Paper title		

Each major section begins with a Heading in 10 point Times New Roman font centered within the column and numbered using Roman numerals (except for REFERENCES), followed by a period, two spaces, and the title using an initial capital letter for each word. The remaining letters are in SMALL CAPITALS (8 point). The paragraph description of the section heading line should be set for 12 points before and 6 points after.

Subheadings should be 10 point, italic, left justified, and numbered with letters (A, B, …), followed by a period, two spaces, and the title using an initial capital letter for each word. The paragraph description of the subheading line should be set for 6 points before and 3 points after.

For main text, paragraph spacing should be single spaced, no space between paragraphs. Paragraph indentation should be 3.7mm/0.21in, but no indentation for abstract & index terms.

II. Helpful Hints

A. Figures And Tables

Position figures and tables at the tops and bottoms of columns. Avoid placing them in the middle of columns. Large figures and tables may span across both columns. Leave sufficient room between the figures/tables and the main text. Figure captions should be centered below the figures; table captions should be centered above. Avoid placing figures and tables before their first mention in the

Received on xx-xx-xxxx, Revised on xx-xx-xxxx, Accepted on xx-xx-xxxx.

text. Use the abbreviation "Fig. 1," even at the beginning of a sentence.

To figure axis labels, use words rather than symbols. Do not label axes only with units. Do not label axes with a ratio

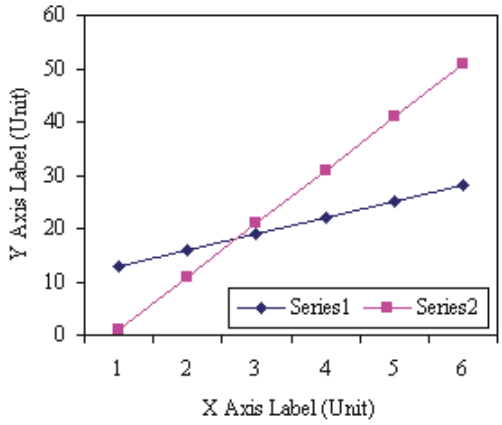

Figure 2. Note how the caption is centered in the column.

of quantities and units. Figure labels should be legible, about 8-point type.

All figures, tables and references must be cited in the text.

Please indicate the broad area/specializations into which the research paper falls, in the covering letter/mail to the Editor, so that reviewers with those specializations may be identified.

B. References

Number citations consecutively in square brackets [1]. Punctuation follows the bracket [2]. Use "Ref. [3]" or "Reference [3]" at the beginning of a sentence:

Give all authors' names; use "et al." if there are six authors or more. Papers that have not been published, even if they have been submitted for publication, should be cited as "unpublished" [4]. Papers that have been accepted for publication should be cited as "in press" [5]. In a paper title, capitalize the first word and all other words except for conjunctions, prepositions less than seven letters, and prepositional phrases. Good number of references must be given.

Latest references in the area must be included and every refence must be cited in the text of the research article.

C. Footnotes

Number footnotes separately in superscripts [1, 2, ⋯]. Place the actual footnote at the bottom of the column in which it was cited, as in this column. See first page footnote as an example.

D. Abbreviations and Acronyms

Define abbreviations and acronyms the first time they are used in the text, even after they have been defined in the abstract. Do not use abbreviations in the title unless they are unavoidable.

E. Equations0

Equations should be left justified in the column. The paragraph description of the line containing the equation should be set for 6 points before and 6 points after. Number equations consecutively with equation numbers in parentheses flush with the right margin, as in (1). Italicize Roman symbols for quantities and variables, but not Greek symbols. Punctuate equations with commas or periods when they are part of a sentence, as in

$$a + b = c\,. \tag{1}$$

Symbols in your equation should be defined before the equation appears or immediately following. Use "(1)," not "Eq. (1)" or "equation (1)," except at the beginning of a sentence: "Equation (1) is ..."

F. Other Recommendations

Use either SI (MKS) or CGS as primary units. (SI units are encouraged.) If your native language is not English, try to get a native English-speaking colleague to proofread your paper. Do not add page numbers.

III. Conclusions

The authors can conclude on the topic discussed and proposed, future enhancement of research work can also be briefed here.

References

[1] G. Eason, B. Noble, and I. N. Sneddon, "On certain integrals of Lipschitz-Hankel type involving products of Bessel functions," Phil. Trans. Roy. Soc. London, vol. A247, pp. 529–551, April 1955.

[2] J. Clerk Maxwell, *A Treatise on Electricity and Magnetism*, 3rd ed., vol. 2. Oxford: Clarendon, 1892, pp.68–73.

[3] I. S. Jacobs and C. P. Bean, "Fine particles, thin films and exchange anisotropy," in *Magnetism*, vol. III, G. T. Rado and H. Suhl, Eds. New York: Academic, 1963, pp. 271–350.

[4] K. Elissa, "Title of paper if known," unpublished.

[5] R. Nicole, "Title of paper with only first word capitalized", *J. Name Stand. Abbrev.*, in press.

[6] Y. Yorozu, M. Hirano, K. Oka, and Y. Tagawa, "Electron spectroscopy studies on magneto-optical media and plastic substrate interface," *IEEE Transl. J. Magn. Japan*, vol. 2, pp. 740–741, August 1987 [Digests 9th Annual Conf. Magnetics Japan, p. 301, 1982].

[7] M. Young, *The Technical Writer's Handbook*. Mill Valley, CA: University Science, 1989.

[8] T. Ali, B.K. Subhash and R.C. Biradar, "A Miniaturized Decagonal Sierpinski UWB Fractal Antenna", PIERS C, vol. 84, pp. 161-174, 2018.

ABOUT THE COLLEGE

CVR College of Engineering, an autonomous institution under the UGC was established in the Year 2001, the first college in Telangana to be promoted by NRI technology professional resident in the USA. The NRI promoters are associated with cutting-edge technologies of the computer and electronics industry. They also have strong associations with other leading NRI professionals working for world-renowned companies like IBM, Intel, Cisco, Facebook, AT & T, Google, and Apple who have agreed to associate with the College with a vision and passion to make the College a state-of-the-art engineering institution.

The college has been ranked 155 by the National Institutional Ranking Framework among the Engineering colleges of the country. All the seven eligible courses of B. Tech and M. Tech - Structural Engineering and VLSI System Design are NBA accredited. New GEN funds of Rs. 60 lakhs have been received for the current year for 20 projects and are in progress.

A Number of Faculty Development Programmes and workshops for students have been conducted. Publications by faculty have increased in quality and numbers. Students have won prizes in various events; trophies own by girl students in Basketball and Throwball in inter-collegiate tournaments deserve a special mention. Students have done exceedingly well in obtaining placements in reputed organizations with high salaries.

Dr. K. Lal Kishore, Dean – Research was honoured with the Lifetime Achievement Award by the ISTE in April 2021 for a meritorious career in the field of education.

Faculty members are working on Rupees One crore worth projects with funding from AICTE, UGC and ISRO. 30 Projects worth Rs. 2.54 Crores have been completed thus far. The current number of patents published is 29.

The AICTE sanctioned Rs. 2 lakhs to students and faculty of CE and ME for a study tour of ATAL tunnel and Rs. 1 lakh towards activities under scheme for Promoting Interests, Creativity and Ethics among Students (SPICES).

The college has been creating records year after year. With more than 100 companies visiting CVR and 1600+ placements for the 2021 - 2022 academic year, it is the highest among the peer group of colleges. The highest offer of **Rs. 44 Lakhs PA** was bagged by 3 students and close to **60 students** got offers higher than **Rs. 10 Lakhs PA**. About **500 offers** are higher than **Rs. 5 Lakhs PA** and another **300 offers** are higher than **Rs. 7 Lakhs PA**. With this, CVR became the leading college in entire Telangana in terms of the offers with higher salaries. CVR has made huge progress in a short span of time and was preferred by the students and parents during the EAMCET counseling this year and is among the **top 3 colleges** in the state.

In keeping with the current global emphasis on green and eco-friendly energy generation, 360kW Solar PV plant has been installed on the campus to meet the power requirements of the college to a significant extent.

CALL FOR PAPERS:

Papers in Engineering, Science and Management disciplines are invited for Publication in our Journal. Authors are requested to mail their contributions to Editor, CVR Journal of Science and Technology (Email Id: journal@cvr.ac.in). Authors can also submit their papers through our online open journal system (OJS) www.ojs.cvr.ac.in or www.cvr.ac.in/ojs. Papers are to be written using a Standard Template, which may be obtained on request from the Editor. It is also available on the college website www.cvr.ac.in

CVR JOURNAL OF SCIENCE AND TECHNOLOGY

CVR COLLEGE OF ENGINEERING

(UGC Autonomous- Affiliated to JNTU Hyderabad)
Mangalpalli (V), Ibrahimpatnam (M),
R.R. District, Telangana - 501510
http://cvr.ac.in